Geophysical Characteristics of Oceanic Transform Faults

Dissertation

zur Erlangung des Doktorgrades an der

Mathematisch-Naturwissenschaftlichen Fakultät der
Christian-Albrechts-Universität zu Kiel

vorgelegt von

YU REN

Kiel, Januar 2025

Erster Gutachter:.....Prof. Dr. Ingo Grevemeyer

Zweite Gutachterin: .....Prof. Dr. Heidrun Kopp

Tag der mündlichen Prüfung: 12.02.2025

Zum Druck genehmigt:.....12.02.2025

……..

Der Dekan

Hiermit erkläre ich, dass ich die vorliegende Doktorarbeit selbständig und ohne Zuhilfenahme unerlaubter Hilfsmittel erstellt habe. Weder diese noch eine ähnliche Arbeit wurde an einer anderen Abteilung oder Hochschule im Rahmen eines Prüfungsverfahrens vorgelegt, veröffentlicht oder zur Veröffentlichung vorgelegt. Ferner versichere ich, dass die Arbeit unter Einhaltung der Regeln guter wissenschaftlicher Praxis der Deutschen Forschungsgemeinschaft entstanden ist. Ich versichere, dass mir noch kein akademischer Titel entzogen wurde.

Kiel, den……...

Yu Ren

ABSTRACT

Among the most prominent features in ocean basins, oceanic transform faults (OTFs), offsetting mid-ocean ridges by tens to hundreds of kilometers, are intrinsically associated with plate motion on a spherical Earth, tracing small circles around a pole of rotation. Plate tectonics traditionally define OTFs as conservative strike-slip plate boundaries where lithosphere is neither created nor destroyed. This conceptual framework has fostered an oversimplified interpretation that has dominated for six decades. However, increasing near-field observations have unveiled complexities in their geophysical characteristics, indicating dynamics far more intricate than previously assumed. In this thesis, I present global analyses of OTF morphology, residual mantle Bouguer anomalies, and mantle rheology, along with local seismicity studies of the Oceanographer, Blanco, and Mendocino transform fault systems, to address the following research questions: How does the surface expression of OTFs vary on a global scale? How does mantle rheology influence the gravity signals and surface expressions of OTFs? How does crustal thickness vary between tectonic features within an OTF system? How many faulting styles exist within OTF systems, and what are their possible causes? How do OTFs interact with far-field and local-field stresses?

A global analysis of the geometric parameters reveals a robust relationship that transform valleys get deeper and wider with increasing age offset, links surface deformation to tectonic extension predicted by geodynamic simulations. However, the correlation between parameterized morphology and spreading rate is found to be weak, unlike the well-received spreading rate dependence of mid-ocean ridge morphology. Gravity analyses, supported by three-dimensional geodynamic modelling, highlight systematic crustal thickness variations between OTFs and their adjacent fracture zones. The results show thinner crust beneath transform valleys due to cross-transform extension, while their adjacent fracture zones exhibit thicker crust as a result of multi-stage magmatic accretion and hydrothermal alteration.

Local seismicity studies of the Oceanographer transform fault in the Atlantic and the Blanco and Mendocino transform fault system in the northeast Pacific further elucidate their fault structure, slip mode, evolution and segmentation. Bathymetric and seismicity analyses of the Oceanographer transform fault reveal a combination of strike-slip motion and tectonic extension, with normal faulting and widespread seismicity concentrated near inside corners, and strike-slip faulting dominant along the transform fault farther from ridge-transform intersections. The Blanco transform fault system shows a similar combination of strike-slip and extensional dynamics but is highly segmented due to changes in plate motion. Its eastern segment reflects a mature plate boundary undergoing steady-state deformation,

whereas its western segment remains immature, adapting to regional tectonic forces. Additionally, a machine-learning-based microseismicity catalog for the Mendocino transform fault provides evidence for the reactivation of spreading-related faults and the development of mantle shear zones. These processes are driven by a combination of north-south compression and plate-bending extension, in response to the northward migration of the Mendocino triple junction.

Synthesizing these results, this thesis provides systematic evidence for tectonic extension and multi-stage magmatic accretion at OTF systems, fundamentally challenging the conventional view of OTFs as purely strike-slip, conservative plate boundaries. Moreover, significant deformation arises when OTFs are influenced by far-field and local-field stresses, adding further complexity to their geophysical characteristics.

KURZFASSUNG

Unter den markantesten Merkmalen der Ozeanbecken gehören ozeanische Transformstörungen (OTFs), die mittelozeanische Rücken über Distanzen von einigen Dutzend bis mehreren Hundert Kilometern versetzen. Sie sind untrennbar mit der Plattenbewegung auf einer kugelförmigen Erde verbunden und folgen kleinen Kreisen um einen Rotationspol. In der Plattentektonik werden OTFs traditionell als konservative Blattverschiebungsgrenzen definiert, an denen keine Lithosphäre erzeugt oder zerstört wird. Dieses konzeptionelle Modell hat über sechs Jahrzehnte hinweg eine stark vereinfachte Interpretation gefördert. Neuere Beobachtungen in der Nähe von OTFs haben jedoch Komplexitäten in ihren geophysikalischen Eigenschaften aufgedeckt, die weit über das bisher angenommene Maß hinausgehen. In dieser Dissertation präsentiere ich globale Analysen der OTF-Morphologie, residualer Mantel-Bouguer-Anomalien und der Mantelrheologie sowie lokale seismologische Untersuchungen der Oceanographer-, Blanco- und Mendocino-Transformstörungen, um folgende Forschungsfragen zu adressieren: Wie variiert die Oberflächenmorphologie von OTFs global? Wie beeinflusst die Mantelrheologie die Schwerefeldsignale und Oberflächenmorphologie von OTFs? Wie variieren die Krustendicken zwischen tektonischen Strukturen innerhalb eines OTF-Systems? Wie viele Verformungsstile gibt es innerhalb von OTF-Systemen und welche möglichen Ursachen haben sie? Wie interagieren OTFs mit Fern- und Nahfeldspannungen?

Eine globale Analyse der geometrischen Parameter zeigt eine starke Korrelation: Mit zunehmendem Altersversatz werden die Transformtäler tiefer und breiter, was die Oberflächenverformung mit der durch geodynamische Simulationen vorhergesagten tektonischen Dehnung verknüpft. Die Korrelation zwischen der parametrisierten Morphologie und der Spreizungsrate ist jedoch schwach und weicht von der etablierten Abhängigkeit der Morphologie mittelozeanischer Rücken von der Spreizungsrate ab. Schwerefeldanalysen, unterstützt durch dreidimensionale geodynamische Modellierungen, zeigen systematische Variationen der Krustendicke zwischen OTFs und ihren angrenzenden Bruchzonen. Die Ergebnisse weisen auf dünnere Kruste unter den Transformtälern hin, die durch Querverlängerung entstanden ist, während die angrenzenden Bruchzonen aufgrund mehrstufiger magmatischer Akkretion und hydrothermaler Alteration dickere Kruste aufweisen.

Lokale seismologische Studien der Oceanographer-Transformstörung im Atlantik sowie der Blanco- und Mendocino-Transformstörungen im Nordostpazifik liefern weitere Einblicke in ihre Störungsstruktur, ihre Verformungsmodi, Entwicklung und Segmentierung. Bathymetrische und seismologische Analysen der Oceanographer-Transformstörung zeigen eine Kombination aus Blattverschiebungsbewegung und tektonischer Dehnung, wobei normale Verwerfungen und weit

verbreitete seismische Aktivität in der Nähe der inneren Ecken konzentriert sind, während Blattverschiebungsaktivität entlang der Transformstörung weiter entfernt von Rücken-Transform-Kreuzungen dominiert. Das Blanco-Transformstörungssystem zeigt eine ähnliche Kombination aus Blattverschiebungs- und Dehnungsdynamik, ist jedoch aufgrund von Änderungen der Plattenbewegung stark segmentiert. Sein östliches Segment repräsentiert eine reife Plattengrenze mit stationärem Deformationszustand, während das westliche Segment weiterhin unreif ist und sich an regionale tektonische Kräfte anpasst. Darüber hinaus liefert ein auf maschinellem Lernen basierender Mikroseismizitätskatalog für die Mendocino-Transformstörung Hinweise auf die Reaktivierung von aus der Spreizung resultierenden Verwerfungen sowie die Entwicklung von Mantelscherzonen. Diese Prozesse werden durch eine Kombination aus Nord-Süd-Kompression und Plattenbiege-Dehnung angetrieben, als Reaktion auf die nordwärts gerichtete Migration des Mendocino-Dreifachknotenpunkts.

Die Synthese dieser Ergebnisse liefert systematische Belege für tektonische Dehnung und mehrstufige magmatische Akkretion in OTF-Systemen und stellt damit die traditionelle Sichtweise von OTFs als rein konservative Blattverschiebungsgrenzen grundlegend in Frage. Darüber hinaus zeigt die Analyse, dass signifikante Verformungen auftreten, wenn OTFs von Fern- und Nahfeldspannungen beeinflusst werden, was ihre geophysikalischen Eigenschaften weiter verkompliziert.

Contents

CHAPTER 1

INTRODUCTION

1.1 Motivation

The segmentation of mid-ocean ridges (MORs) is one of the most striking features of terrestrial plate tectonics. Oceanic transform faults (OTFs), offsetting MORs by tens to several hundreds of kilometers, represent first-order ridge-axis discontinuities (Macdonald et al., 1988). They leave long scars on the seafloor, known as fracture zones (FZs), which extend across ocean basins.

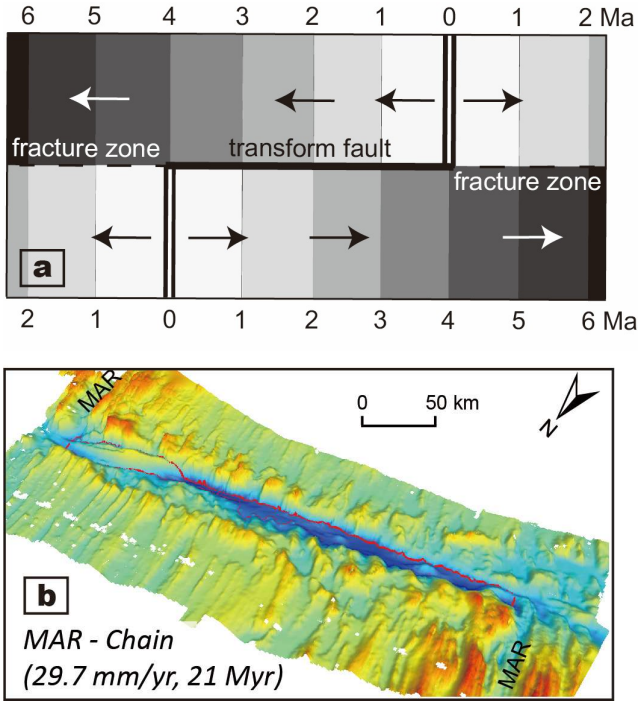

Figure 1. (**a**) Schematic illustration of the traditional conceptual model for OTF geometry. The example OTF features an age offset of 4 Myr, with arrows indicating the relative plate motion. (**b**) Three-dimensional perspective view of the Chain transform fault offsetting the Mid-Atlantic Ridge (MAR). The active deformation zone within the transform valley is delineated by the red polygon. Seafloor bathymetric data are from Harmon et al. (2018).

Since the seminal introduction of transform fault by J. T. Wilson (1965), OTFs have been traditionally regarded as geometrically simple, conservative strike-slip plate boundaries (Figure 1a), a paradigm that has shaped thinking for the past six decades. Early investigations into the surface expression of OTFs primarily relied on towed seismic surveys (e.g., Detrick et al., 1973; MacDonald et al., 1986), sidescan

sonar (e.g., Searle & Laughton, 1977; Searle, 1986), and singlebeam echosounders (e.g., MacDonald et al., 1979). Although limited in resolution and coverage, these studies identified deep transform valleys along some OTFs, indicating morphological complexities beyond initial assumptions. The transform length was the first geometric parameter which have been systematically investigated (Sandwell, 1986), as the intersections between ridge segments and OTFs can, to some extent, be discerned from satellite altimeter data. Among OTFs analyzed, transform lengths range from 0 to 922 km, with an average of approximately 120 km. Notably, no correlation has been observed between transform length and either the spreading rate or ridge segment length.

Recent advances in survey technologies, particularly the use of high-resolution multibeam sonar systems, have revolutionized the detailed mapping of OTFs (e.g., Dauteuil, 1995; Ligi et al., 2002; Okino et al., 2015; Maia et al., 2016). Figure 1b illustrates a ship-based multibeam bathymetric map of the Chain transform fault (Harmon et al., 2018), which offsets the Mid-Atlantic Ridge, slips at a rate of 29.7 mm/yr, and exhibits an age offset of 21 Myr. The three-dimensional perspective clearly delineates the active deformation zone and reveals that the transform valley is significantly deeper than any adjacent features within the OTF system. Furthermore, the seafloor bathymetry highlights distinct tectonic features within the valley, such as submarine volcanoes and transpressive ridges, underscoring the precision and high-resolution capabilities of contemporary survey techniques. Continued high-resolution seafloor mapping has progressively unveiled the structural variability of OTFs, prompting detailed analyses of their morphological parameters on a global scale (e.g., Fox & Gallo, 1984; Dauteuil et al., 2002; Mishra & Gordon, 2016; Wolfson-Schwehr & Boettcher, 2019; Grevemeyer et al., 2021). Analogue models applied to 24 OTFs (Dauteuil et al., 2002) suggested that the transform deformation zone gets wider with a smaller offset, which generally corresponds to a higher spreading rate of the adjacent MOR. The authors further inferred that fault patterns in the transform deformation zone are governed by lithospheric strength and influenced by geometric parameters, including transform length, spreading rate, and regional heat flow. A global analysis of OTF azimuths (Mishra & Gordon, 2016) found an average deviation of ~0.46° from the predicted relative plate motions. This deviation, likely resulted from the widening of transform valleys, contradicts the rigid-plate hypothesis (e.g., Wilson, 1965; Korenaga, 2007). Furthermore, Grevemeyer et al. (2021), using a compilation of ship-based bathymetric data from 44 OTF systems, demonstrated that transform valleys are consistently deeper than their associated FZs. This finding contradicts the predictions of thermal subsidence due to plate cooling (Davis & Lister, 1974), as the older seafloor within FZs is observed to become shallower rather than deeper. While earlier studies (e.g., Barth, 1994; Fornari et al., 1989; Gallo et al., 1986) associated J-shaped ridges extending across ridge–transform intersections (RTIs) with fast spreading rates, Grevemeyer et al. (2021) identified these J-shaped ridges as an intrinsic feature occurring across all spreading rates, providing further evidence of episodic magmatic activity at OTF systems.

Steadily increasing near-field observations have revealed a remarkable variability in the structure and tectonics of OTF systems, adding complexity to their geophysical characteristics. For instance, anomalously shallow, transform-parallel transverse ridges are widely observed within deep transform valleys (e.g., Bonatti, 1978; Pockalny et al., 1988; Pockalny, 1997; Embley & Wilson, 1992; Maia, 2019; Wolfson-Schwehr & Boettcher, 2019). The formation of these transverse ridges is likely not the result of excess volcanism but rather of tectonic uplift of upper mantle and crustal blocks, driven by a component of extension or compression commonly induced by changes in plate motions (Bonatti, 1978; Kastens et al., 1998). Moreover, mantle Bouguer anomalies over the transverse ridge of the Blanco transform fault system in the northeast Pacific revealed a low-density body, possibly related to serpentine intrusions, which contributes to the uplift of the Blanco Ridge (Dziak et al., 2000). In addition, numerous gravity studies (e.g., Abrams et al., 1988; Prince & Forsyth, 1988; Escartín & Cannat, 1999; Brink et al., 2002) revealed exceedingly thin crust within transform valleys, consistent with findings from seismic refraction and reflection experiments (e.g., Cormier et al., 1984; Ambos & Hussong, 1986; Whitmarsh & Calvert, 1986). A global analysis of residual mantle Bouguer anomalies (RMBA) across 19 OTF systems (Gregg et al., 2008) further indicated that OTFs at slow-spreading ridges exhibit thinner crust compared to adjacent MOR segments, whereas OTFs offsetting intermediate- and fast-spreading ridges are associated with thicker crust relative to their neighboring MOR segments. It was further suggested that three-dimensional magma accretion may occur near intermediate- and fast-slipping OTFs.

A limited number of passive seismic experiments have also been conducted to investigate the seismotectonics of OTFs. However, early studies on local seismicity predominantly focused on specific localized features rather than the entire transform fault system. Among the most heavily studied tectonic features within OTF systems are the ridge-transform intersections (RTIs), where transform-fault shear stress interacts with spreading-axis tensile stress (Morgan & Parmentier, 1984). In the eastern RTIs of the St. Paul (Francis et al., 1978), Oceanographer (Cessaro & Hussong, 1986), Kane (Wilcock et al., 1990), Atlantis (Collins et al., 2012), and Romanche (Yu et al., 2021) transform faults, as well as the western RTI of the Vema transform fault (Rowlett and Forsyth, 1984; Louden et al., 1986), seismic activity has been observed across a broad area of the inside corner while little activity occurs near the RTI along the transform fault. Together with normal faulting evident from focal mechanisms, these studies demonstrate extensional or dip-slip tectonics within OTF systems. However, the potential causes of this extension remain a subject of debate (e.g., Wilcock et al., 1990). More recent studies, leveraging large-scale ocean-bottom-seismometer (OBS) experiments, revealed significant along-strike variations in fault structure and slip mode of the fast-slipping Quebrada-Discovery-Gofar transform fault system (McGuire et al., 2012; Wolfson-Schwehr et al., 2014; Gong et al., 2022; 2023), intermediate-slipping Blanco transform fault system (Kuna, 2020), and slow-slipping Chain transform fault (Schlaphorst et

al., 2023). These findings highlight the complex interactions between OTF systems and plate spreading dynamics, a relationship that remains poorly understood.

Numerical simulations have significantly advanced our understanding of transform dynamics. Within OTF systems, the presence of adjacent old and cold lithosphere reduces the temperature in the wedge of asthenosphere rising beneath the ridge axis (Collette, 1974; Fox & Gallo, 1984). This lateral cooling and heat conduction generate thermal stress across the transform, influencing the structure of OTFs (Turcotte, 1974; Morgan & Forsyth, 1988). Based on thermal models, Collette (1974) proposed that OTFs function as contraction cracks that relieve thermal stress, leading to the shrinkage of opposing lithospheric plates. This mechanism could explain the presence of wide and deep valleys within ridge-transform systems (Sandwell, 1986). Moreover, thermal models (Furlong et al., 2001) and geodynamic flow simulations (Grevemeyer et al., 2021) suggest the presence of an oblique shear zone at depth, indicating an extensional component within the transform domain. These models associate extensional tectonics at OTFs with oblique faulting at shallow depths, mantle upwelling, and/or crustal thinning along the transform, which collectively contribute to the widening and deepening of OTFs (Furlong et al., 2001; Grevemeyer et al., 2021; Tian et al., 2024).

Plate tectonics traditionally define OTFs as conservative strike-slip plate boundaries that adjust almost instantaneously to changes in plate motions without undergoing significant deformation. However, increasing near-field observations have unveiled complexities in their geophysical characteristics, indicating dynamics far more intricate than previously assumed. While advanced geodynamic models have recently suggested that extensional tectonics are an integral component of OTF systems, geological and geophysical observations, particularly on a global scale, are essential to validate these predictions. Consequently, in this thesis, I present global analyses of OTF morphology, RMBA, and mantle rheology, along with local seismicity studies of the Oceanographer, Blanco, and Mendocino transform fault systems, to address the following research questions:

(I) How does the surface expression of OTFs vary on a global scale?
(II) How does mantle rheology influence the gravity signals and surface expressions of OTFs?
(III) How does crustal thickness vary between tectonic features, including transform deformation zone, FZs, spreading segments, and inside and outside corners, within an OTF system?
(IV) How many faulting styles exist within OTF systems, and what are their possible causes?
(V) How do OTFs interact with far-field (e.g., changes in plate motion) and local-field (e.g., nearby hotspots) stresses?

1.2 Thesis outline

This thesis comprises eight chapters, including stand-alone articles that have been published (Chapters 2, 3, 4, and 6; Appendix), submitted (Chapter 5), or are ready for submission (Chapter 7) to peer-reviewed journals. Chapters 2, 6, 7, and the Appendix represent scientific articles that I led as the first author. Chapters 3, 4, and 5 are collaborative scientific articles to which I contributed as part of my PhD project, with my role recognized as a co-author. In Chapter 8, I summarize the key findings from the presented articles and provide an outlook on unresolved questions and future research directions.

Chapter 1 provides an overview of the motivation and objectives behind this doctoral thesis.

Chapter 2 explores the morphological characteristics of global oceanic transform faults (OTFs) and their controlling factors using a quantitative approach. In this chapter, shipborne multibeam bathymetric data from open-access databases and various research cruises were compiled and merged. By leveraging the most advanced global dataset on OTF morphology, key geometric features of OTFs, including length, width, depth, area, perimeter, and their associated uncertainties, were parameterized. This chapter highlights the morphological variability of global OTFs and examines its relationship with related tectonic parameters, providing new insights that benchmark the extensional tectonics at OTFs predicted by geodynamic simulations.

Authors' contributions: *I. Grevemeyer and J. Geersen supervised the study. Y. Ren was responsible for data compiling and processing. Y. Ren and J. Geersen drafted the initial manuscript, and all authors contributed to the discussion of the results and the final editing of the paper.*

Chapter 2 has been published in *Geophysical Research Letters* as:
Ren, Y., Geersen, J., and Grevemeyer, I., (2022), *Impact of spreading rate and age-offset on oceanic transform fault morphology*, Geophysical Research Letters, 49, e2021GL096170.

Chapter 3 examines the variations in gravity signals of OTF systems. In this chapter, high-resolution multibeam bathymetry, satellite gravity data, and geodynamic models were integrated to calculate residual mantle Bouguer anomalies (RMBAs) for OTFs across the full spectrum of spreading rates. The RMBA differences, serving as a proxy for crustal thickness variations, reveal generally thinner crust beneath active transform valleys and relatively thicker crust beneath their associated FZs. This chapter offers fundamental insights into the accretionary processes of OTFs, supporting the presence of tectonic extension and multi-stage accretion at oceanic transform plate boundaries.

Authors' contributions: *L. H. Rüpke and I. Grevemeyer conceptualized and designed the study. Z. Guo and S. Liu processed the integrated dataset, and Y. Ren contributed to geological interpretations. Z. Guo and S. Liu wrote the initial manuscript, with all authors contributing to the discussion of results and the final editing of the paper.*

Chapter 3 has been published in *Geology* as:
Guo, Z., Liu, S., Rüpke, L. H., Grevemeyer, I., Morgan, J. P., Lange, D., Ren, Y., and Tao, C., (2023), *Disparate crustal thicknesses beneath oceanic transform faults and adjacent fracture zones revealed by gravity anomalies*, Geology, 51(3): 300–304.

Chapter 4 investigates the impact of mantle rheology on the RMBA values computed in Chapter 3. Various rheological models of OTF systems were applied to perform lithospheric thermal gravity corrections. The differences in the RMBA values derived from these models were compared with key features of OTFs, revealing that the RMBA changes, driven by different rheology-dependent thermal solutions, correlate with spreading rate under mid-ocean ridges and vary systematically with age offset in other tectonic compartments. This chapter underscores the sensitivity of gravity anomalies to the rheology-dependent thermal structures of OTFs and advocates for the inclusion of a more realistic nonlinear viscoplastic mantle rheology in the steps of lithospheric thermal gravity corrections.

Authors' contributions: *L. H. Rüpke supervised the study. S. Liu and Z. Guo processed the integrated dataset, and Y. Ren contributed to geological interpretations. S. Liu and Z. Guo wrote the initial manuscript, with all authors contributing to the discussion of results and the final editing of the paper.*

Chapter 4 has been published in *Earth and Planetary Science Letters* as:
Liu, S., Guo, Z., Rüpke, L. H., Morgan, J. P., Grevemeyer, I., Ren, Y., and Li, C., (2023), *Sensitivity of gravity anomalies to mantle rheology at mid-ocean ridge – transform fault systems*, Earth and Planetary Science Letters, 622, 118420.

Chapter 5 presents a case study on the morphology, seismicity, and deformation of the Oceanographer transform fault on the Mid-Atlantic Ridge near 35°N. Recently acquired multibeam bathymetry and passive OBS data from research cruises M170 and M175 indicate more complex dynamics than previously anticipated. Near the RTI, widespread seismicity extends across the inside corner, with normal faulting observed parallel to the transform fault. Away from the RTIs, strike-slip motion aligns with predictions based on plate tectonics. This chapter provides seismological evidence for tectonic extension and magmatic additions at OTFs by uncovering systematic changes in stress patterns along the fault system. Additionally, it offers new insights into the segmentation of OTFs.

Authors' contributions: *I. Grevemeyer conceptualized and designed the study. I. Grevemeyer and D. Lange processed the seismological data, and I. Klaucke contributed to morphological interpretations. I. Grevemeyer drafted the initial manuscript, and all authors contributed to the discussion of the results and the final editing of the paper.*

Chapter 5 has been submitted to *Journal of Geophysical Research: Solid Earth*.

Chapter 6 concentrates on the seismotectonics and evolution of a highly segmented OTF system in the northeast Pacific. In this chapter, a dense OBS network, combined with multibeam bathymetry, gravity, and aeromagnetic data, was utilized to study recent faulting and deformation within the Blanco transform fault system (BTFS) northwest off the coast of Oregon. Distinct magnetic, morphological, and seismological features were observed at the western and eastern RTIs, suggesting that the impact of spreading episodes of the adjacent spreading ridges on the OTFs is weaker in the east compared to the west. While stresses at the eastern BTFS align closely with plate motion, those in the west are skewed clockwise, indicating ongoing reorganization of the fault system. Based on multidisciplinary observations, a revised kinematic model was developed to reveal the development of transform faults and ridge segments since the formation of the BTFS. This chapter highlights seismotectonic behaviors of the highly segmented BTFS as an immature transform plate boundary and provides new insights into the evolution of OTFs in response to plate motion changes and ridge propagation events.

Authors' contributions: *I. Grevemeyer and D. Lange supervised the study. D. Lange accessed the seismological dataset and constructed a preliminary earthquake catalog. Y. Ren manually picked P- and S-phase onsets and first-motion polarities for the local events and conducted further analysis. Y. Ren drafted the initial manuscript, and all authors contributed to the discussion of the results and the final editing of the paper.*

Chapter 6 has been published in *Journal of Geophysical Research: Solid Earth* as:
Ren, Y., Lange, D., and Grevemeyer, I., (2023), *Seismotectonics of the Blanco transform fault system, northeast Pacific: Evidence for an immature plate boundary*, Journal of Geophysical Research: Solid Earth, 128, e2022JB026045.

Chapter 7 focuses on micro-seismicity offshore central and southern Cascadia in the northeast Pacific, a region encompassing diverse plate boundaries, including the JdF and Gorda ridges, the Blanco and Mendocino transform fault systems, and the Cascadia subduction zone. This area serves as a natural laboratory for studying the interactions between MORs, OTFs, and SZs. In this chapter, deep-learning algorithms were applied to detect and locate micro-earthquakes using massive OBS data from the

Cascadia Initiative. This approach revealed detailed seismic activity around active tectonic features, which were largely absent in previous investigations. The well-constrained source parameters provide seismological evidence for reactivated spreading-related faults near the deformation front and mantle shear zones beneath the Mendocino transform fault. This chapter highlights the structural and deformation characteristics from ridge to trench and offers new seismological insights into the interactions between OTFs and their surrounding tectonic features.

Authors' contributions: *Y. Ren accessed seismological data from various temporary offshore networks and generated a high-quality micro-earthquake catalog using advanced machine-learning-based algorithms. I. Grevemeyer and D. Lange supervised the study, refined its overall scope, and provided input on the interpretation and discussion of the results. Y. Ren drafted the initial manuscript, and all authors contributed to editing the manuscript.*

Chapter 7 is ready for submission to *Nature Communications*.

Chapter 8 synthesizes the key findings from the preceding chapters and outlines future research directions to address unresolved questions related to mid-ocean ridge and transform dynamics, and machine-learning-facilitated seismic event detection.

In addition, the ***Appendix*** explores innovative approaches to scientific data representation by incorporating artistic methodologies. Through spectrum analysis and dynamic imaging techniques, seismic data presented in Chapters 6 and 7 were transformed into visually engaging and scientifically stimulating artworks. This interdisciplinary effort not only paves the way for new modes of scientific investigation and communication but also fosters enhanced public engagement with complex geophysical phenomena.

Authors' contributions: *Y. Ren and T. Wu conceptualized and designed the study. Y. Ren extracted multiple soundtracks from seismological datasets presented in previous chapters and conducted spectral analysis. T. Wu and P. Yao incorporated artistic methodologies to transform the extracted soundtracks into art videos. Y. Ren drafted the initial manuscript, and all authors contributed to discussing the results and editing the final version of the paper.*

The Appendix has been published in *iScience* as:
Ren, Y., Wu, T., Li, C., Yao, P., and Ding, W., (2024), *Bridging Science and Art: Auralization and Visualization of Ocean Soundscape*, iScience, 27(9), 110696.

1.3 References

Abrams, L. J., Detrick, R. S., & Fox, P. J. (1988). Morphology and crustal structure of the Kane Fracture Zone Transverse Ridge. *Journal of Geophysical Research*, 93(B4), 3195–3210. https://doi.org/10.1029/JB093iB04p03195.

Ambos, E. L., & Hussong, D. M. (1986). Oceanographer transform fault structure compared to that of surrounding oceanic crust: Results from seismic refraction data analysis. *Journal of geodynamics*, 5(1), 79–102. https://doi.org/10.1016/0264-3707(86)90024-4

Barth, G.A. (1994). Oceanic crust thickens approaching the Clipperton Fracture Zone. *Marine Geophysical Researches*, 16, 51–64. https://doi.org/10.1007/BF01812445

Bonatti, E. (1978). Vertical tectonism in oceanic fracture zones. *Earth and Planetary Science Letters*, 37(3), 369–379. https://doi.org/10.1016/0012-821X(78)90052-3

Brink, U. S., Coleman, D. F., & Dillon, W. P. (2002). The nature of the crust under Cayman Trough from gravity. *Marine and Petroleum Geology*, 19(8), 971–987. https://doi.org/10.1016/S0264-8172(02)00132-0

Cessaro, R. K., & Hussong, D. M. (1986). Transform seismicity at the intersection of the oceanographer fracture zone and the Mid-Atlantic Ridge. *Journal of Geophysical Research*, 91(B5), 4839–4853. https://doi.org/10.1029/JB091iB05p04839

Collette, B. (1974). Thermal contraction joints in a spreading seafloor as origin of fracture zones. *Nature*, 251, 299–300. https://doi.org/10.1038/251299a0

Collins, J. A., Smith, D. K., & McGuire, J. J. (2012). Seismicity of the Atlantis Massif detachment fault, 30°N at the Mid-Atlantic Ridge. *Geochemistry, Geophysics, Geosystems*, 13, Q0AG11. https://doi.org/10.1029/2012GC004210.

Cormier, M. H., Detrick, R. S., & Purdy, G. M. (1984). Anomalously thin crust in oceanic fracture zones: New seismic constraints from the Kane fracture zone. *Journal of Geophysical Research*, 89(B12), 10249-10266. https://doi.org/10.1029/JB089iB12p10249

Dauteuil, O. (1995). Fault pattern from seabeam processing: The western part of the Blanco Fracture Zone (NE pacific). *Marine Geophysical Researches*, 17, 17–35. https://doi.org/10.1007/BF01268049

Dauteuil, O., Bourgeois, O., & Mauduit, T. (2002). Lithosphere strength controls oceanic transform zone structure: insights from analogue models. *Geophysical Journal International*, 150(3), 706–714. https://doi.org/10.1046/j.1365-246X.2002.01736.x

Davis, E. E., & Lister, C. R. B. (1974). Fundamentals of ridge crest topography. *Earth and Planetary Science Letters*, 21(4), 405–413. https://doi.org/10.1016/0012-821X(74)90180-0

Detrick, R. S., Mudie, J. D., Luyendyk, B. P., & Macdonald, K. C. (1973). Near-bottom Observations of an Active Transform Fault (Mid-Atlantic Ridge at 37°N). *Nature Physical Science*, 246, 59–61. https://doi.org/10.1038/physci246059a0

Dziak, R., Fox, C., Embley, R., Nábělek, J., Braunmiller, J., & Koski, R. (2000). Recent tectonics of the Blanco Ridge, eastern Blanco transform fault zone. *Marine Geophysical Researches*, 21, 423–450. https://doi.org/10.1023/A:1026545910893

Embley, R. W., & Wilson, D. S. (1992). Morphology of the Blanco Transform Fault Zone-NE Pacific: Implications for its Tectonic Evolution. *Marine Geophysical Researches*, 14, 25–45. https://doi.org/10.1007/BF01674064

Escartín, J., & Cannat, M. (1999). Ultramafic exposures and the gravity signature of the lithosphere near the Fifteen-Twenty Fracture Zone (Mid-Atlantic Ridge, 14°–16.5°N). *Earth and Planetary Science Letters*, 171(3), 411–424. https://doi.org/10.1016/S0012-821X(99)00169-7

Fornari, D. J., Gallo, D. G., Edwards, M. H., Madsen, J. A., Perfit, M. R., & Shor, A. N. (1989). Structure and topography of the Siqueiros transform fault system: Evidence for the development of intra-transform spreading centers. *Marine Geophysical Researches*, 11(4), 263–299. https://doi.org/10.1007/BF00282579

Fox, P. J., & Gallo, D. G. (1984). A tectonic model for ridge transform ridge plate boundaries: implications for the structure of oceanic lithosphere. *Tectonophysics*, 104, 205–242. https://doi.org/10.1016/0040-1951(84)90124-0

Francis, T. J. G., Porter, I. T., & Lilwall, R. C. (1978). Microearthquakes near the eastern end of St Paul's Fracture Zone. *Geophysical Journal International*, 53(2), 201–217. https://doi.org/10.1111/j.1365-246X.1978.tb03738.x

Furlong, K. P., Sheaffer, S. D., & Malservisi, R. (2001). Thermal-rheological controls on deformation within oceanic transforms. *Geological Society, London, Special Publications*, 186, 65–83. https://doi.org/10.1144/GSL.SP.2001.186.01.05

Gallo, D. G., Fox, P. J., & Macdonald, K. C. (1986). A Sea Beam investigation of the Clipperton transform fault: The morphotectonic expression of a fast-slipping transform boundary. *Journal of Geophysical Research*, 91, 3455–3467. https://doi.org/10.1029/JB091iB03p03455

Gong, J., Fan, W., & Parnell-Turner, R. (2022). Microseismicity indicates atypical small-scale plate rotation at the Quebrada transform fault system, East Pacific Rise. *Geophysical Research Letters*, 49(3), e2021GL097000. https://doi.org/10.1029/2021GL097000

Gong, J., Fan, W., & Parnell-Turner, R. (2023). Machine learning-based new earthquake catalog illuminates on-fault and off-fault seismicity patterns at the Discovery Transform Fault, East Pacific Rise. *Geochemistry, Geophysics, Geosystems*, 24(9), e2023GC011043. https://doi.org/10.1029/2023GC011043

Grevemeyer, I., Rüpke, L. H., Morgan, J. P., Iyer, K., & Devey, C. W. (2021). Extensional tectonics and two-stage crustal accretion at oceanic transform faults. *Nature*, 591, 402–407. https://doi.org/10.1038/s41586-021-03278-9

Harmon, N., Rychert, C., Agius, M., Tharimena, S., Le Bas, T., Kendall, J. M., & Constable, S.

(2018). Marine geophysical investigation of the Chain Fracture Zone in the equatorial Atlantic from the PI-LAB experiment. *Journal of Geophysical Research: Solid Earth*, 123(11), 11016–11030. https://doi.org/10.1029/2018JB015982

Kastens, K., Bonatti, E., Caress, D., Carrara, G., Dauteuil, O., Frueh-Green, G., et al. (1998). The Vema transverse ridge (central Atlantic). *Marine Geophysical Researches*, 20, 533–556. https://doi.org/10.1023/A:1004745127999

Korenaga, J. (2007). Thermal cracking and the deep hydration of oceanic lithosphere: A key to the generation of plate tectonics? *Journal of Geophysical Research*, 112, B05408. https://doi.org/10.1029/2006JB004502.

Kuna, V. M. (2020), Investigation of Slip and Tectonics of the Blanco Transform Fault Using High-resolution Ocean Bottom Seismic Data. *Ph.D. thesis*, Oregon State University.

Ligi, M., Bonatti, E., Gasperini, L., & Poliakov, A. N. B. (2002). Oceanic broad multifault transform plate boundaries. *Geology*, 30(1), 11–14. https://doi.org/10.1130/00917613(2002)030<0011:Obmtpb>2.0.Co;2

Louden, K. E., White, R. S., Potts, C. G., & Forsyth, D. W. (1986). Structure and seismotectonics of the Vema fracture zone, Atlantic Ocean. *Journal Geological Society London*, 143, 795–805, https://doi.org/10.1144/gsjgs.143.5.0795

MacDonald, K. C., Kastens, K., Spiess, F. N., & Miller, M. (1979). Deep tow studies of the Tamayo transform fault. *Marine Geophysical Researches*, 4, 37–70. https://doi.org/10.1007/BF00286145

Macdonald, K. C., Castillo, D. A., Miller, S. P., Fox, P. J., Kastens, K. A., & Bonatti, E. (1986). Deep-Tow Studies of the Vema Fracture Zone. 1. Tectonics of a Major Slow Slipping Transform Fault and its Intersection with the Mid-Atlantic Ridge. *Journal of Geophysical Research*, 91, 3334–3354. https://doi.org/10.1029/JB091iB03p03334

Macdonald, K., Fox, P., Perram, L., Eisen, M., Haymon, R., , et al. (1988). A new view of the mid-ocean ridge from the behaviour of ridge-axis discontinuities. *Nature*, 335, 217–225. https://doi.org/10.1038/335217a0

Maia, M., Sichel, S., Briais, A., Brunelli, D., Ligi, M., Ferreira, N., et al. (2016). Extreme mantle uplift and exhumation along a transpressive transform fault. *Nature Geoscience*, 9(8), 619–623. https://doi.org/10.1038/Ngeo2759

Maia, M. (2019). Topographic and morphologic evidences of deformation at oceanic transform faults: far-field and local-field stresses. In: *Transform Plate Boundaries and Fracture Zones*, Duarte, J. C. (ed), pp. 61–87. Elsevier, Amsterdam. https://doi.org/10.1016/B978-0-12-812064-4.00003-7

McGuire, J. J., Collins, J. A., Gouédard, P., Roland, E., Lizarralde, D., Boettcher, M. S., et al. (2012). Variations in earthquake rupture properties along the Gofar transform fault, East Pacific Rise. *Nature Geoscience*, 5(5), 336–341. https://doi.org/10.1038/ngeo1454

Mishra, J. K., & Gordon, R. G. (2016). The rigid-plate and shrinking-plate hypotheses: Implications for the azimuths of transform faults. *Tectonics*, 35, 1827–1842.

https://doi.org/10.1002/2015TC003968

Morgan, J.P., & Parmentier, E.M. (1984). Lithospheric stress near a ridge-transform intersection. *Geophysical Research Letters*, 11, 113–116. https://doi.org/10.1029/GL011i002p00113

Morgan, J. P., & Forsyth, D. W. (1988). Three-dimensional flow and temperature perturbations due to a transform offset: Effects on oceanic crustal and upper mantle structure. *Journal of Geophysical Research*, 93(B4), 2955–2966. https://doi.org/10.1029/JB093iB04p02955.

Okino, K., Nakamura, K., & Sato, H. (2015). Tectonic Background of Four Hydrothermal Fields Along the Central Indian Ridge. In: *Subseafloor Biosphere Linked to Hydrothermal Systems*, Ishibashi, J., Okino, K., Sunamura, M. (Eds), pp. 133–146. Springer, Tokyo. https://doi.org/10.1007/978-4-431-54865-2_11

Pockalny, R. (1997). Evidence of transpression along the Clipperton Transform: implications for processes of plate boundary reorganization. *Earth and Planetary Science Letters*, 146, 449–464. https://doi.org/10.1016/S0012-821X(96)00253-1.

Pockalny, R. A., Detrick, R. S., & Fox, P. J. (1988). Morphology and tectonics of the Kane Transform from Sea Beam bathymetry data. *Journal of Geophysical Research*, 93(B4), 3179–3193. https://doi.org/10.1029/JB093iB04p03179

Prince, R. A., & Forsyth, D. W. (1988). Horizontal extent of anomalously thin crust near the Vema fracture zone from the three-dimensional analysis of gravity anomalies. *Journal of Geophysical Research*, 93(B7), 8051–8063. https://doi.org/10.1029/JB093iB07p08051

Rowlett, H. (1981). Seismicity at intersection of spreading centers and transform faults: recent faulting and microearthquakes at the intersection of the Vema Fracture zone and the Mid Atlantic Ridge. *Journal of Geophysical Research*, 86(B5), 3815–3820. https://doi.org/10.1029/JB086iB05p03815.

Schlaphorst, D., Rychert, C. A., Harmon, N., Hicks, S. P., Bogiatzis, P., Kendall, J. M., & Abercrombie, R. E. (2023). Local seismicity around the Chain Transform Fault at the Mid-Atlantic Ridge from OBS observations. *Geophysical Journal International*, 234(2), 1111-1124. https://doi.org/10.1093/gji/ggad124

Searle, R. C., & Laughton, A. S. (1977). Sonar studies of the Mid-Atlantic Ridge and Kurchatov fracture zone. *Journal of Geophysical Research*, 82(33), 5313–5328. https://doi.org/10.1029/JB082i033p05313

Searle, R. C. (1986). GLORIA investigations of oceanic fracture zones: comparative study of the transform fault zone. *Journal of the Geological Society*, 143(5), 743–756. https://doi.org/10.1144/gsjgs.143.5.0743

Tian, X., Behn, M. D., Ito, G., Schierjott, J. C., Kaus, B. J. P. & Popov, A. A. (2024). Magmatism controls global oceanic transform fault topography. *Nature Communications*, 15, 1914. https://doi.org/10.1038/s41467-024-46197-9

Turcotte, D. L. (1974). Are transform faults thermal contraction cracks? *Journal of Geophysical Research*, 79(17), 2573–2577. https://doi.org/10.1029/JB079i017p02573

Yu, Z., Singh, S. C., Gregory, E. P. M., Maia, M., Wang, Z., & Brunelli, D. (2021). Semi-brittle seismic deformation in high-temperature mantle mylonite shear zone along the Romanche transform fault. *Science Advances*, 7(15), eabf3388. https://doi.org/10.1126/sciadv.abf3388

Whitmarsh, R. B., & Calvert, A. J. (1986). Crustal structure of Atlantic fracture zones — I. The Charlie-Gibbs Fracture Zone. *Geophysical Journal International*, 85(1), 107–138. https://doi.org/10.1111/j.1365-246X.1986.tb05174.x

Wilcock, W. S. D., Purdy, G. M., & Solomon, S. C. (1990). Microearthquake evidence for extension across the Kane Transform Fault. *Journal of Geophysical Research*, 95(B10), 15439–15462. https://doi.org/10.1029/JB095iB10p15439

Wilson, J. T. (1965). A new class of faults and their bearing on continental drift. *Nature*, 207, 343–347. https://doi.org/10.1038/207343a0

Wolfson-Schwehr, M., Boettcher, M. S., McGuire, J. J., & Collins, J. A. (2014). The relationship between seismicity and fault structure on the Discovery transform fault, East Pacific Rise. *Geochemistry, Geophysics, Geosystems*, 15(9), 3698–3712. https://doi.org/10.1002/2014GC005445

Wolfson-Schwehr, M., & Boettcher, M. S. (2019). Global Characteristics of Oceanic Transform Fault Structure and Seismicity. In: *Transform Plate Boundaries and Fracture Zones*, Duarte, J. C. (ed), pp. 21–59. Elsevier, Amsterdam. https://doi.org/10.1016/B978-0-12-812064-4.00002-5

CHAPTER 2

MANUSCRIPT #1

Impact of spreading rate and age-offset on oceanic transform fault morphology

Yu Ren [(1)], Jacob Geersen [(2)], and Ingo Grevemeyer [(1)]

(1) GEOMAR Helmholtz Centre for Ocean Research Kiel, Kiel, Germany
(2) Institute of Geosciences, University of Kiel, Kiel, Germany

Published in 2022 in *Geophysical Research Letters*, 49, e2021GL096170

This chapter contains a manuscript published in *Geophysical Research Letters* in its original form. Please note that the publication contains its own reference list and refers to its own figure and page numbers. The manuscript is reproduced with permission of the John Wiley and Sons.

Geophysical Research Letters

RESEARCH LETTER
10.1029/2021GL096170

Key Points:

- We compiled multibeam bathymetric data of 94 oceanic transform faults (OTFs) to quantify their morphological characteristics
- Morphology of OTFs is dominated by age-offset rather than spreading rate
- Transform valleys get systematically deeper and wider with increasing age-offset, implying extensional tectonics at OTFs

Supporting Information:

Supporting Information may be found in the online version of this article.

Correspondence to:

Y. Ren,
yren@geomar.de

Citation:

Ren, Y., Geersen, J., & Grevemeyer, I. (2022). Impact of spreading rate and age-offset on oceanic transform fault morphology. *Geophysical Research Letters*, *49*, e2021GL096170. https://doi.org/10.1029/2021GL096170

Received 29 NOV 2021
Accepted 10 JAN 2022

Impact of Spreading Rate and Age-Offset on Oceanic Transform Fault Morphology

Yu Ren[1], Jacob Geersen[2], and Ingo Grevemeyer[1]

[1]GEOMAR Helmholtz Centre for Ocean Research Kiel, Kiel, Germany, [2]Institute of Geosciences, University of Kiel, Kiel, Germany

Abstract Oceanic transform faults (OTFs) are an inherent part of seafloor spreading and plate tectonics, whereas the process controlling their morphology remains enigmatic. Here, we systematically quantify variations in transform morphology and their dependence on spreading rate and age-offset, based on a compilation of shipborne bathymetric data from 94 OTFs at ultraslow- to intermediate-spreading ridges. In general, the length, width and depth of OTFs scale systematically better with age-offset rather than spreading rate. This observation supports recent geodynamic models proposing that cross-transform extension scaling with age-offset, is a key process of transform dynamics. On the global scale, OTFs with larger age-offsets tend to have longer, wider, and deeper valleys. However, at small age-offsets (<5 Myr), scatters in the depth and width of OTFs increase, indicating that small age-offset OTFs with weak lithospheric strength are easily affected by secondary tectonic processes.

Plain Language Summary In the past 5 decades, studies on oceanic transform faults (OTFs) have revealed significant complexity in their morphology, which calls for detailed quantitative analysis to study the processes controlling the morphology of OTFs. Using the most complete and advanced compilation of bathymetric data from ultraslow- to intermediate-spreading ridges, we parameterized the morphological characteristics of OTFs and extracted length, width and depth for each transform fault from the compiled bathymetric data. Moreover, correlations between these morphological parameters and related tectonic factors (e.g., spreading rate, age-offset) were investigated in this study. We find that correlations between morphological features and spreading rate are rather weak. Comparison of correlations suggests that age-offset scales better with the morphological parameters, along with scatters mostly at small age-offsets, indicating small-age-offset OTFs are unstable due to their weak lithospheric strength. Our observation evidences extensional tectonics at OTFs.

1. Introduction

Oceanic transform faults (OTFs) are prominent linear features in the ocean-basins, offsetting mid-ocean ridges by tens to several hundreds of kilometers and hence juxtaposing oceanic lithosphere of contrasting age (Fox & Gallo, 1984; Wilson, 1965). They are usually located in remote oceanic regions where coverage from high-resolution shipborne bathymetric data is often rather poor. In the past decades, the quantity and quality of shipborne bathymetric surveys mapping the remote seafloor has, however, steadily increased (Gallo et al., 1986; Pockalny et al.,1988; Ryan et al., 2009). The new data revealed an enormous variability with respect to the morphology of global OTFs, calling for updated tectonic models on the origin of OTFs and their role in plate tectonics (Furlong et al., 2001; Gerya, 2012; Searle, 1986; Wolfson-Schwehr & Boettcher, 2019).

Unfortunately, even more than 5 decades after Wilson (1965) published his landmark paper on OTFs, we have a limited understanding of the processes controlling their morphological variability. Conceptually, they are simple conservative strike-slip faults and inherent to the spreading process (Sandwell, 1986; Sykes, 1967; Wilson, 1965). However, the strike-slip fault of a transform system often runs along a transform valley (Wolfson-Schwehr & Boettcher, 2019) which is several kilometers wide (e.g., Searle, 1986) and processes shaping these valleys are poorly understood. In addition, small changes in plate motion may result in either extension across OTFs, curving J-shaped abyssal hills at the ridge-transform intersections (Fornari et al., 1989; Tucholke & Schouten, 1988), widening the valley, the formation of transverse ridges (Pockalny et al., 1996), or causing compressive features within the transform valley (Harmon et al., 2018; Maia, 2019). However, recent observations suggest that the formation of transform valley might be inherently related to extensional tectonics at OTFs (Grevemeyer et al., 2021).

Geodynamic modeling suggests that the nonlinear viscoplastic rheology of oceanic lithosphere governs deformation below the rectilinear strike-slip plate boundaries, causing extension and thinning of the crust and hence wide and deep valleys (Grevemeyer et al., 2021).

Such geodynamic models require observational evidence to benchmark them (Ito, 2021). A previous statistical study has indicated that the length of OTFs is poorly correlated to spreading rate (Sandwell, 1986). More recent statistical compilations have shown that the width of OTFs may increase with spreading rate (Dauteuil et al., 2002) and age-offset (Luo et al., 2021) or that the depth of transform valleys scales with spreading rate and age-offset (Grevemeyer et al., 2021). However, it should be noted that observational studies of transform morphology and their dependence on related tectonic features generally suffer from poor data quality, coverage and/or lacked resolution (Text S1 in Supporting Information S1) and thus may bias our perception of ridge-transform dynamics (Luo et al., 2021).

The objective of this paper is to quantify variations in the morphology of global OTFs and to systematically study their dependence on related tectonic parameters, including spreading rate and age-offset. We collected and analyzed multibeam bathymetric data of 94 OTFs (Figure 1a) from ultraslow- to intermediate-spreading ridges. OTFs corresponding to higher spreading rates were excluded because their morphology and segmentation are often rather complex and thus may not allow a simple quantification (e.g., Dauteuil et al., 2002; Fox & Gallo, 1984). Our results provide new insights into the systematic variation of transform morphology and parameters governing key features like the width and depth of transform valleys.

2. Data and Methods

We compiled and merged shipborne multibeam bathymetric data from the Global Multi-Resolution Topography (GMRT) synthesis (Ryan et al., 2009) and the Japan Agency for Marine-Earth Science and Technology (JAMSTEC). Data from these databases were complemented with bathymetric information from several individual research cruises which were carried out in the region of the Bouvet triple junction (Ligi et al., 1999), along the Romanche (Ligi et al., 2002), St. Paul (Maia et al., 2016), and Chain (Harmon et al., 2018) transforms, as well as along the Central Indian Ridge (Okino et al., 2015). All the data were quality checked and regridded to a 100-m cell size for further processing and analyzing by using the ArcGIS Desktop software. Based on this compilation, we were able to generate maps of shipborne bathymetry for 94 OTFs, including 8 OTFs from the ultraslow-spreading Southwest Indian Ridge, 30 OTFs from the slow-spreading Central Indian Ridge and Mid-Atlantic Ridge, and 56 OTFs from the intermediate-spreading Southeast Indian Ridge, Chile Rise, Pacific Antarctic Ridge, Juan de Fuca Ridge, and Galapagos Ridge (Figure 1a).

We used the merged bathymetric datasets to study the systematics of OTFs, including length, width, depth, and their standard deviation. Figures 1b–1e illustrate characteristic structural elements of OTFs for the Chain transform (Figures 1b–1d) and the Chiloe transform (Figure 1e). At mid-ocean ridges, an active OTF is bounded by the two ridge-transform intersections (RTIs), where the tectonic stresses rotate over tens of degrees from ridge normal extension to strike-slip motion along the OTF (Figure 1b). Thus, the length of an OTF can be best defined by the distance between the two RTIs. Unfortunately, most OTFs and adjacent mid-ocean ridges lack high-resolution magnetic data to define seafloor ages along OTFs (Text S2, Figure S1, and Table S1 in Supporting Information S1). We therefore defined the age-offset as the transform fault length divided by the half-spreading rate derived from MORVEL (DeMets et al., 2010). While the length of an OTF can readily be derived, the rugged morphology of transform domains calls for a robust definition of key parameters like depth and width. At intermediate, slow and ultraslow spreading rates, the transform fault generally runs along a deep transform valley, which is usually flanked by the abyssal hills, transverse ridges, or oceanic core complexes developing at inside corner setting. From both bounding walls, the seafloor slopes steeply down into the transform valley. The slope map of the Chain transform (Figure 1c) highlights the transition from the steep slopes of the flanking valley walls to the flat seafloor of the valley. We used this characteristic feature to derive the outline or perimeter of the valley, including additional tectonic features such as submarine volcanos or flower structures (Figure 1b) in the deep valley. Thus, we calculated the slope gradient of the seafloor and manually defined a polygon (in red color, Figure 1b) at the toe of the steep slope of the valley walls where the seabed grades into a flat or gently sloping floor within the valley. Toward the RTIs, the polygon is truncated by two parallel lines perpendicular to the long axis of the transform fault, at a distance of 5–15 km from the RTIs to avoid morphological edge effects (DeMets

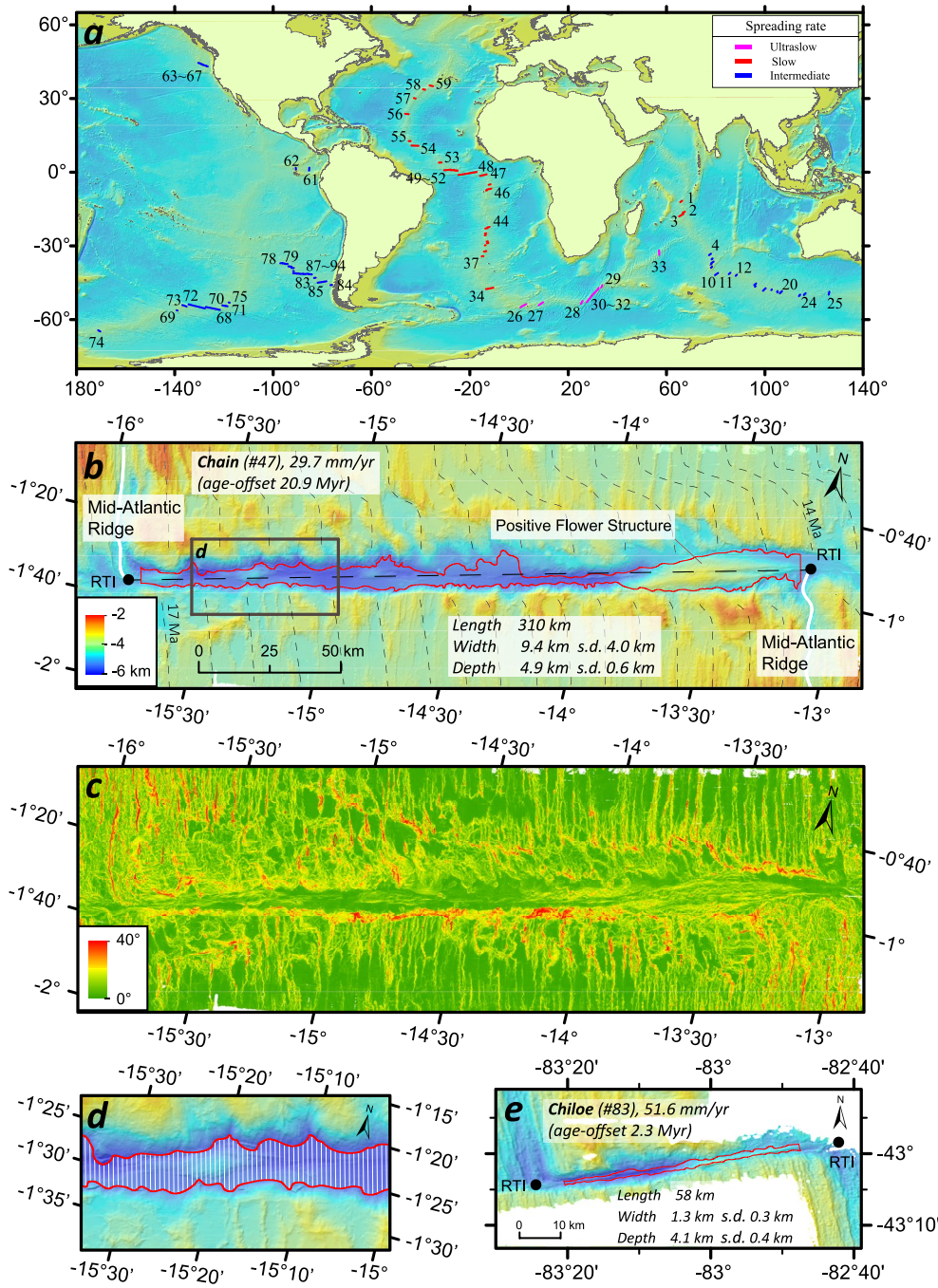

Figure 1. (a) Locations of the 94 oceanic transform faults (OTFs) investigated in this research. Numbering is as in column 1 of Table S2 in Supporting Information S1. (b) Bathymetry (from Harmon et al., 2018), (c) Slope map and (d) Zoomed bathymetric view of the Chain transform. Dashed lines on the opposite plates are age contours at 1 Ma interval from global age grid (Seton et al., 2020). Location of the Chain transform can be traced in panel (a) with its numbering (#47). Black box: the region shown in the zoomed view in (d). The white parallel lines at 1 km spacing which trend perpendicular to the long axis of the OTF (black dashed line in b) are used to derive the width of the transform. They are truncated on both sides by the outline of the transform valley (red lines). (e) Bathymetry (from GMRT synthesis, Ryan et al., 2009) of the Chiloe transform (#83). Color scale is the same as in panel (b). RTI, ridge-transform intersection; s.d., standard deviation.

et al., 2010; Grevemeyer et al., 2021). In the case of Chain transform fault, ridge axis at the RTI curves into the deep valley, causing J-shaped abyssal curvatures within a distance of ~5 km from the RTI. Thus, the polygon outlining valley wall scarps was truncated by two vertical lines of the transform axis at a distance of 5 km from

both RTIs (Figure 1b). To derive the width of the transform valley, we used parallel lines at 1 km spacing which trend perpendicular to the transform axis. The lines are truncated on both sides by the outline of the transform valley (red lines, Figure 1d). The width is then defined as the mean length of these truncated lines, from which the standard deviation is also measured. Using ArcGIS, data points from the bathymetry inside of the polygon were extracted and used to derive mean depth and its standard deviation. Besides, the area, perimeter and area/perimeter ratio of the outline of the transform valley were also measured in this study.

3. Results

A summary of the morphologic parameters for each OTF is presented in Table S2 in Supporting Information S1. Spreading rate across the 94 investigated OTFs varies from 14.1 to 83.1 mm/yr. The related age-offset ranges from 0.6 to 62.2 Myr. From the OTFs, 92 (97.9%) have an age-offset of less than 30 Myr and only two exceed 55 Myr (Andrew Bain W, 62.2 Myr; Romanche, 58.0 Myr). The length of OTFs varies from 21 to 847 km, with an average of ∼118 km. The longest one is the Romanche transform at the equatorial Mid-Atlantic ridge. From all transforms studied, 86 OTFs (91.5%) are shorter than 250 km. The width of the OTFs varies from 0.9 to 15.1 km, with an average of ∼3.7 km. The Vema transform, also at the equatorial Mid-Atlantic ridge, is the widest known OTF on Earth. From the investigated OTFs, 75 (79.8%) are narrower than 5 km. The mean water depth of the OTFs varies from 2.3 to 5.6 km, with an average of ∼3.8 km. Again, the Romanche transform has the deepest seafloor within the transform valley, up to ∼7,860 m.

An interesting feature is the large variability of morphologic parameters (especially the width) at slow spreading rates (Figures 2a–2c, Figures S2a–S2c and S3 in Supporting Information S1). Length, width, and depth ranges of OTFs at ultraslow-spreading Southwest Indian Ridge are 91–438 km, 4.3–10.5 km, 3.9–5.6 km, respectively. Table S3 in Supporting Information S1 documents the average morphologic variations subdivided into OTFs from ultraslow- (0–20 mm/yr), slow- (20–50 mm/yr) and intermediate- (50–90 mm/yr) spreading ridges. OTFs from ultraslow-spreading ridges share the largest mean values in age-offset (26.2 Myr), length (189.7 km), width (7.1 km) and depth (5.1 km), while the intermediate-slipping OTFs have the lowest mean values in transform parameters (3.2 Myr, 100.7 km long, 2.4 km wide, 3.5 km deep). To investigate their specific dependence on spreading rate and age-offset, we systematically plotted the length, width and depth of all OTFs against the spreading rate (Figures 2a–2c) and age-offset (Figures 2d–2f), and calculated the weighted linear fits with 95% confidence intervals.

We observed large scatters in Figures 2a–2c. Slopes of the linear fits are all negative. For length and width, this feature is superimposed by an inverse and hence positive trend (increase) for OTFs that share a similar age-offset (same color in the plot). This increase is most obvious for OTFs with age-offsets above 5 Myr whereas below 5 Myr a large scatter prohibits the identification of robust patterns (Figures 2a and 2b). With respect to the depth (Figure 2c), there seems to be an overall decrease in average water depth with increasing spreading rate, which is more obvious compared to the length and the width. However, a systematic increase in depth for OTFs with similar age-offsets, as observed for width and length, is not evident from the plot. Values of the coefficient of determination (R^2) are all small, indicating that correlations between morphologic parameters and spreading rate are rather weak.

The length, width, and depth patterns are different if plotted against the age-offset (Figures 2d–2f). Transform length increases with increasing age-offset on a global scale as well as almost linearly if considered for OTFs originating at the same spreading ridge. Both width and depth increase at OTFs with age-offsets above 5 Myr (Figures 2h and 2i). The improved R^2 value suggests that correlations between morphologic parameters and age-offset are reasonably stronger. Furthermore, width scales with age-offset better than depth, according to the R^2. The scatter discussed above for small-age-offset (<5 Myr) OTFs is, however, still visible (Figures 2e, 2f, and 3a–3c). The width of small-age-offset OTFs varies from 0.8 to 5.1 km, while the width of large-age-offset (>5 Myr) OTFs ranges from 1.7 to 15.1 km. The average water depth of small- and large-age-offset OTFs varies from 2.3 to 4.8 km and 2.6–5.6 km, respectively. Furthermore, large age-offset OTFs tend to slip at slow rates (Figure 3d, Figure S6 in Supporting Information S1), which agrees with the simplified calculation of age-offset by dividing transform length by half-spreading rate.

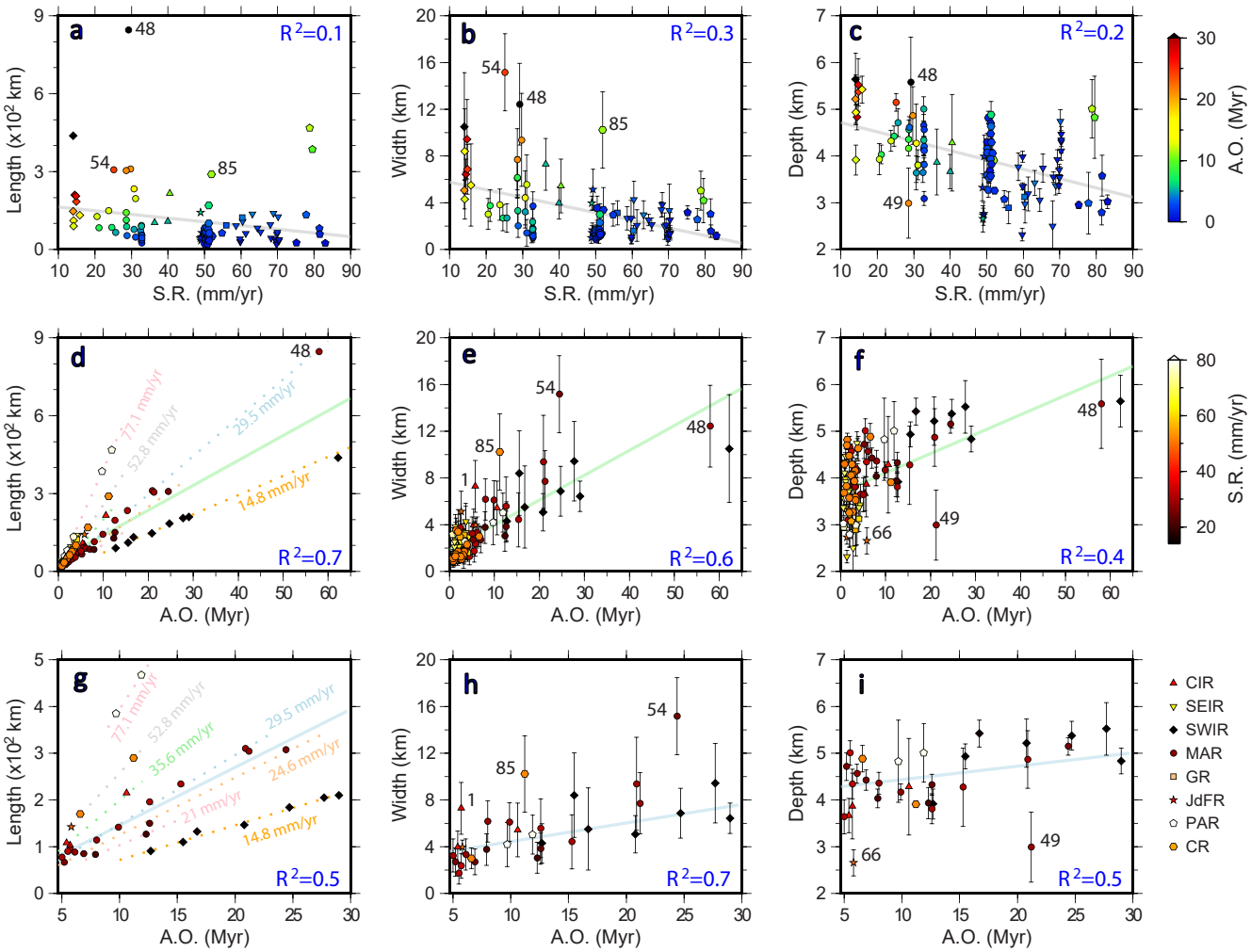

Figure 2. Morphological variability of global oceanic transform faults (OTFs). (a–f) Length, mean width, and mean water depth of OTF versus spreading rate and age-offset, respectively. (g–i) Zoomed views of (d–f). Thick lines show weighted linear fits. In figures (h–i) OTFs labeled (Table S5 in Supporting Information S1) which have undergone obvious secondary processes discussed were excluded during calculating their linear fits. A.O., age-offset; S.R., spreading rate. CR, Chile Rise; PAR, Pacific Antarctic Ridge; JdFR, Juan de Fuca Ridge; GR, Galapagos Ridge; MAR, Mid-Atlantic Ridge; SWIR, Southwest Indian Ridge; SEIR, Southeast Indian Ridge; CIR, Central Indian Ridge. 1, CIR 12S; 48, Romanche; 49, St Paul A; 54, Vema; 66, Blanco D; 85, Guafo.

4. Discussion

4.1. Comparison With Previous Statistics on the Morphology of OTFs

In an early study, Sandwell (1986) used bathymetry and satellite altimeter data to measure the length of global OTFs, and only found a weak correlation between transform length and spreading rate. The width of 24 OTFs was studied by Dauteuil et al. (2002) and they suggested that width correlates with spreading rate, despite a high variability resulting from secondary processes affecting the local lithospheric strength. Using a compilation of 41 well-mapped OTFs, Grevemeyer et al. (2021) revealed that the depth of transform valleys is generally much deeper at slow- and ultraslow-spreading rates than at intermediate- and fast-spreading rates. Such observations are also supported by a recent study (Luo et al., 2021), suggesting that the width and depth of OTFs decrease with increasing spreading rate. However, Luo et al. (2021) reported only 44 width estimates and their approach used the SRTM15+ bathymetry (Tozer et al., 2019) instead of using swath-mapping data and hence their estimates might be biased by including predicted seafloor bathymetry. Furthermore, they defined the width by the distance between the crests of the flanking walls of the OTF instead of using the width of the transform valley floor. Consequently, their estimates are two to three times wider than our estimates and values reported by Mishra and Gordon (2016) (Figure S5 in Supporting Information S1). Further, Luo et al. (2021) defined the width by a single

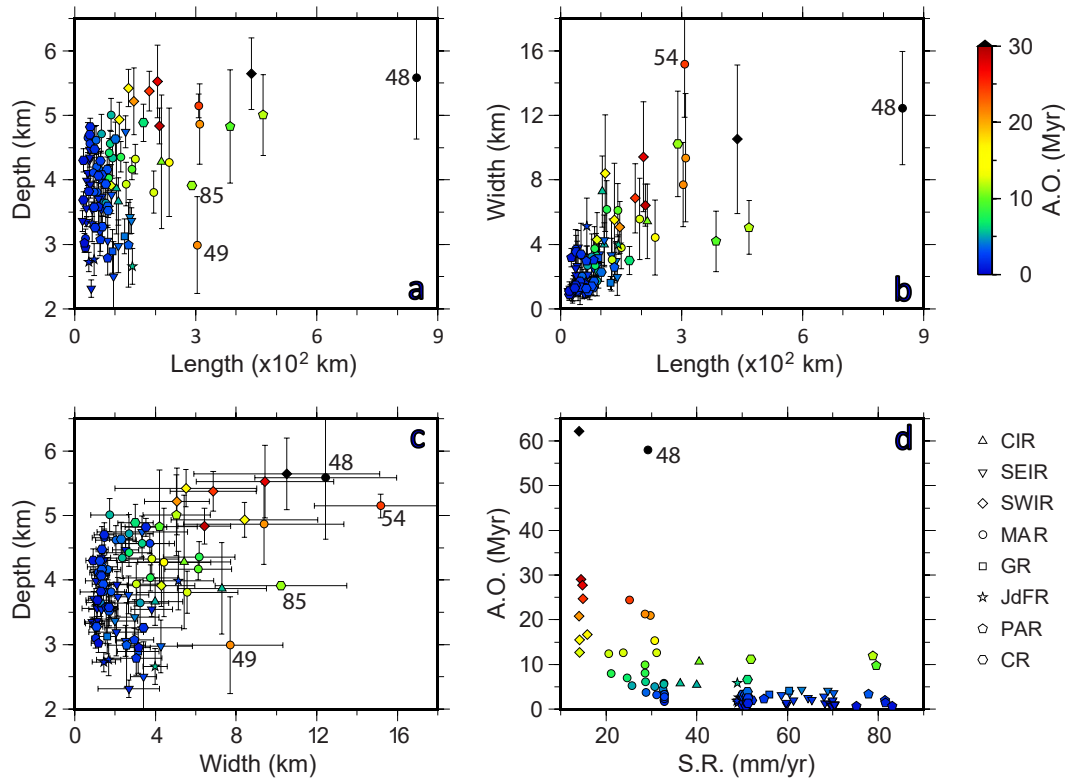

Figure 3. Correlations between morphologic parameters of global oceanic transform faults (OTFs). (a) Depth versus length. (b) Width versus length. (c) Depth versus width. (d) Age-offset versus spreading rate. Numbering is consistent in Figures 1a and 2.

measurement at the center of the OTF and Mishra and Gordon (2016) used the width of a best fitting rectangular instead of using a statistically robust approach (e.g., our polygon outlining the shape of transform valley). Similar simplifications not only governed width but also depth estimates of most previous approaches (Text S1 in Supporting Information S1). Therefore, statistically robust estimates from this study are needed to further explore transform tectonics.

4.2. Spreading Rate and Age-Offset Dependence of Transform Morphology

Our documented spreading rate dependence of transform morphology is consistent with the above-mentioned studies. Slow spreading rates correspond to large age-offsets as well as long, wide, and deep valleys. However, the low values of the coefficient of determination (R^2) for the length, width, and depth suggest that their correlations with spreading rate are reasonably weak, as they are superimposed by a high degree of scattering (Figures 2a–2c). It is worth noting that the scatters in our data also comply with previous studies (Dauteuil et al., 2002; Grevemeyer et al., 2021; Luo et al., 2021; Sandwell, 1986), indicating that other processes further affect transform morphology.

Correlations between age-offset and transform morphology are more robust. The age-offset is derived from transform length and spreading rate. It is therefore obvious, that an increase in age-offset corresponds to a linear increase in transform length, for a given spreading rate (Figure 2d). However, the high R^2 (0.7) for length could be biased by the cluster at small age-offsets, since the R^2 decreases at larger age-offsets (Figure 2g). For width and depth, R^2 values increase at age-offsets above 5 Myr (Figures 2h and 2i). OTFs with large age-offsets tend to slip at lower rates, corresponding to long, wide, and deep valleys. With respect to other statistical studies (Text S1 in Supporting Information S1), our data set shows a more consistent and clearer age-offset dependence of transform morphology (Figure S5 in Supporting Information S1). Using the most complete and advanced data set on transform morphology compiled so far, we confirm that morphological parameters correlate well with age-offset, indicating that the age-offset plays an important role in the ridge-transform dynamics. The fact that the spreading

rate and transform length are used for calculating the age-offset explains the long-wavelength dependence of transform morphologic parameters on spreading rate (Figures 2a–2c) or transform length (Figures 3a and 3b) despite the obvious large scatters.

4.3. Implications for the Transform Dynamics

Previous geophysical studies uncovered that thinning and stretching represent typical tectonic process within OTFs. For example, seismic refraction (Whitmarsh & Calvert, 1986) and gravity studies (Brink et al., 2002; Escartín & Cannat, 1999) revealed very thin crust along the transform valley. Moreover, normal faulting and stretching within OTFs was directly observed in several microseismicity studies (Cessaro & Hussong, 1986; Wilcock et al., 1990; Yu et al., 2021). Global analysis of the azimuths of OTFs suggested that transforms do not precisely parallel plate motion (Mishra & Gordon, 2016), thus their deformation could partly be accommodated by stretching along the OTFs.

Numerical simulations further revealed extensional tectonics within transforms. Within the ridge-transform system, the adjacent old and cold lithosphere lowers the temperature in the wedge of asthenosphere rising beneath the ridge axis (Collette, 1974; Fox & Gallo, 1984). The lateral cooling and heat conduction result in thermal stress across the transform, which in turn affects the structure of OTFs (Morgan & Forsyth, 1988; Turcotte, 1974). According to results from thermal models, Collette (1974) suggested that OTFs are contraction cracks relieving thermal stress, causing the shrinkage of opposite lithospheric plates. This might be responsible for the wide and deep valley within the ridge-transform system (Sandwell, 1986). Further, thermal (Furlong et al., 2001) and geodynamic flow models (Grevemeyer et al., 2021) proposed the existence of an oblique shear zone at depth, which infers an extensional component within the transform domain. The extensional tectonics at OTFs correspond to oblique faulting at shallow depth (Mishra & Gordon, 2016), mantle upwelling and/or crustal thinning along the transform, and hence widening and deepening of OTFs (Furlong et al., 2001; Grevemeyer et al., 2021). Further, geodynamic models predict that the cross-transform extension, a key process of transform dynamics, scales with the age-offset (Grevemeyer et al., 2021).

In this study, the robust correlation between transform morphology and age-offset, especially for large-age-offset OTFs, links the extension predicted by geodynamic simulations to the surface deformation pattern. The overall increase in the morphological parameters of global OTFs with increasing age-offset as well as the robust R^2 values support the hypothesized extensional tectonics at OTFs (Grevemeyer et al., 2021) in a statistical manner. The cross-transform extension, scaling with age-offset and predicted by thermal contraction, is an important process acting on oceanic transform plate boundaries. However, the large variability revealed in the cross plots (Figures 2e, 2f, and 3a–3c) supports that both width and depth of transform valleys are affected by secondary tectonic processes that may act independently.

4.4. Processes Affecting Transform Morphology

Another key observation with respect to transform morphology is the fact that width and depth show significantly more scatters for small-age-offset (<5 Myr) OTFs than for OTFs with age-offsets above 5 Myr (Figures 2e, 2f, and 3a–3c). One explanation for the scattering at small age-offsets is the time-delay until a tectonic process is reflected in surface morphology which can actually take hundred-thousand to millions of years (Gerya, 2010, 2013). Considering the extensional effect of OTFs, it may thus take a certain time until widening and deepening of the transform valley has reached a threshold that can be identified in seafloor morphology (Sandwell, 1986). Especially considering that the morphology of newly generated lithosphere that becomes subject to transform related processes, may differ between different spreading segments.

In addition, we also observed (Figure 3d and Figure S6 in Supporting Information S1) that the majority of small-age-offset OTFs slip at faster rates, while most transforms with large age-offsets correspond to slower spreading rates. Moreover, analogue and numerical models (Dauteuil et al., 2002; Furlong et al., 2001) have indicated that small-age-offset transforms tend to be hotter and more ductile to accommodate the higher spreading rate than OTFs with large age-offsets. Therefore, OTFs with small age-offsets are more likely altered by secondary tectonic processes, which can be caused by the stress field adjustment, or the regional variations in mantle temperature or composition. In the following, we evaluate secondary processes which may alter transform morphology.

Properties of OTFs might be affected by regional features, like hotspots, which may increase the melt supply and by this generate warmer thermal conditions at nearby transform faults. This may lead to anomalous thickening of the crust and thus shallower transform valleys (Dauteuil et al., 2002; Ito et al., 2003; Maia, 2019). For example, the distance between the Hollister transform and the nearest Louisville hotspot is approximately 400 km. The depth of the small age-offset (3.4 Myr) Hollister transform at the Pacific-Antarctic Ridge is only 2.99 km, which is significantly shallow among the compiled OTFs (Figure S7 in Supporting Information S1). The shallow valley nearly disappears around the ridge-transform intersections (Figure S8a in Supporting Information S1), which may be caused by the redistribution of plume flux from the nearby Louisville hotspot (Small, 1995). Figure S7 in Supporting Information S1 shows the effect of nearby hotspots. Some OTFs (e.g., Blanco D, Hollister, etc.) seem to be affected by nearby hotspots, as expressed in the shallow depth likely due to crustal thickening. However, we also observed some deep transforms (e.g., Ter Tholen, Bouvet, Shaka, etc.) that are close to hotspots, suggesting a relatively weak impact of nearby hotspots, which may correspond to low plume flux (e.g., Sibrant et al., 2019). Besides, there are also a number of shallow transforms (e.g., SEIR 96E W, Raitt W) without any nearby hotspot (within 1,000 km), indicating that the impact of a nearby hotspot is not systematic.

Further, changes in plate motion may affect the structure of transform faults. Previous observation suggested that OTFs do not precisely parallel plate motion (Mishra & Gordon, 2016). Therefore, small variations in spreading direction may cause an additional component of either compression or extension acting along an OTF, which, in turn, may affect either estimation of depth or width and thus contribute to the profound scatters observed in statistics. For example, in some cases, shallow transforms show indications for transpressive tectonics (Figures S8c–S8d in Supporting Information S1), which may result from intense deformation in response to the reorientation of the spreading center (Carbotte & Macdonald, 1994; Maia et al., 2016; Pockalny, 1997; Wolfson-Schwehr & Boettcher, 2019). Positive flower structures, for example, developed along the Chain transform (Figure 1b), result from transpression along the fault (Harmon et al., 2018) and thus may induce uplift of the seafloor along the axis of the transform valley leading to shallow overall depths. Furthermore, changes in plate motion can also create transtension across the transform (Bonatti et al., 2005; Tucholke & Schouten, 1988; Wolfson-Schwehr & Boettcher, 2019). Along the Kane transform, Pockalny et al. (1996) suggested that changes in plate motion caused transtension, contributing to the widening of the valley and formation of transverse ridges flanking the transform by flexural response. In addition, a recent study (Zhang et al., 2022) on OTFs at Pacific Antarctic Ridge indicated that, in response to plate rotation, off-transform normal faults and rift zones might even take place, adding to the complexity in the morphology of transform systems.

The key feature of most OTFs is a deep valley extending along the active strike-slip fault (Wolfson-Schwehr & Boettcher, 2019). Our statistical analysis shows the spreading rate and age-offset dependence of the morphological characteristics of OTFs. The correlation between transform morphology and spreading rate turns out to be weak, while a more robust relationship that transform valleys get deeper and wider with increasing age-offset, links the surface deformation to the cross-transform extension predicted by numerical models, as discussed above. The larger age-offset causes greater extension at OTFs (Furlong et al., 2001; Grevemeyer et al., 2021) and consequently wider and deeper valleys as revealed by our statistical approach.

5. Conclusions

Morphological variability of global oceanic transform faults derived from shipborne bathymetric data and its dependence on related tectonic parameters were systematically analyzed in this study. Our statistical results suggest that

1. OTFs from ultraslow- and slow-spreading ridges tend to have large-age-offset, long, wide, and deep valleys, while at intermediate-spreading ridges, transforms show mostly small age-offsets, where morphology demonstrates high complexities. However, correlations between morphological parameters and spreading rate are weak.
2. Age-offset is the key feature governing transform morphology rather than spreading rate, as age-offset scales better with morphological parameters. At a global scale, larger age-offsets correspond to longer, wider, and deeper valleys. Thus, it is indicated that, in addition to strike-slip motion, cross-transform extension is an important process acting on oceanic transform plate boundaries.

3. Scatters observed in the correlations between morphological characteristics and age-offset indicate that, in addition to the extension, there are also secondary processes affecting transform morphology, such as nearby hotspots and changes in plate motion.

Data Availability Statement

Bathymetric data compiled from open sources are available at http://doi.org/10.5281/zenodo.4774185.

Acknowledgments
The authors thank Kyoko Okino, Marcia Maia, Marco Ligi, and Nicholas Harmon, who kindly contributed additional bathymetric data to this research. Colin Devey, Yuhan Li, Ingo Klaucke, and Anouk Beniest provided helpful feedback during the completion of this work. This manuscript benefited greatly from constructive reviews by three anonymous referees. Yu Ren thanks funding from the China Scholarship Council (201904910466). Open access funding enabled and organized by Projekt DEAL.

References

Bonatti, E., Brunelli, D., Buck, W. R., Cipriani, A., Fabretti, P., Ferrante, V., et al. (2005). Flexural uplift of a lithospheric slab near the Vema transform (Central Atlantic): Timing and mechanisms. *Earth and Planetary Science Letters*, *240*, 642–655. https://doi.org/10.1016/j.epsl.2005.10.010

Brink, U. S., Coleman, D. F., & Dillon, W. P. (2002). The nature of the crust under Cayman Trough from gravity. *Marine and Petroleum Geology*, *19*(8), 971–987. https://doi.org/10.1016/S0264-8172(02)00132-0

Carbotte, S. M., & Macdonald, K. (1994). Comparison of seafloor tectonic fabric at intermediate, fast, and super fast spreading ridges: Influence of spreading rate, plate motions, and ridge segmentation on fault patterns. *Journal of Geophysical Research*, *99*(B7), 13609–13631. https://doi.org/10.1029/93JB02971

Cessaro, R. K., & Hussong, D. M. (1986). Transform seismicity at the intersection of the oceanographer fracture zone and the Mid-Atlantic Ridge. *Journal of Geophysical Research*, *91*(B5), 4839–4853. https://doi.org/10.1029/JB091iB05p04839

Collette, B. (1974). Thermal contraction joints in a spreading seafloor as origin of fracture zones. *Nature*, *251*, 299–300. https://doi.org/10.1038/251299a0

Dauteuil, O., Bourgeois, O., & Mauduit, T. (2002). Lithosphere strength controls oceanic transform zone structure: Insights from analogue models. *Geophysical Journal International*, *150*(3), 706–714. https://doi.org/10.1046/j.1365-246X.2002.01736.x

DeMets, C., Gordon, R. G., & Argus, D. F. (2010). Geologically current plate motions. *Geophysical Journal International*, *181*(1), 1–80. https://doi.org/10.1111/j.1365-246X.2009.04491.x

Escartín, J., & Cannat, M. (1999). Ultramafic exposures and the gravity signature of the lithosphere near the fifteen-twenty fracture zone (mid-Atlantic ridge, 14°–16.5°N). *Earth and Planetary Science Letters*, *171*(3), 411–424. https://doi.org/10.1016/S0012-821X(99)00169-7

Fornari, D. J., Gallo, D. G., Edwards, M. H., Madsen, J. A., Perfit, M. R., & Shor, A. N. (1989). Structure and topography of the Siqueiros transform fault system: Evidence for the development of intra-transform spreading centers. *Marine Geophysical Researches*, *11*(4), 263–299. https://doi.org/10.1007/BF00282579

Fox, P. J., & Gallo, D. G. (1984). A tectonic model for ridge transform ridge plate boundaries: Implications for the structure of oceanic lithosphere. *Tectonophysics*, *104*, 205–242. https://doi.org/10.1016/0040-1951(84)90124-0

Furlong, K. P., Sheaffer, S. D., & Malservisi, R. (2001). Thermal-rheological controls on deformation within oceanic transforms. *Geological Society, London, Special Publications*, *186*, 65–83. https://doi.org/10.1144/GSL.SP.2001.186.01.05

Gallo, D. G., Fox, P. J., & Macdonald, K. C. (1986). A Sea Beam investigation of the Clipperton transform fault: The morphotectonic expression of a fast-slipping transform boundary. *Journal of Geophysical Research*, *91*, 3455–3467. https://doi.org/10.1029/JB091iB03p03455

Gerya, T. V. (2010). Dynamical instability produces transform faults at mid-ocean ridges. *Science*, *329*, 1047–1050. https://doi.org/10.1126/science.1191349

Gerya, T. V. (2012). Origin and models of oceanic transform faults. *Tectonophysics*, *522–533*, 34–54. https://doi.org/10.1016/j.tecto.2011.07.006

Gerya, T. V. (2013). Three-dimensional thermomechanical modeling of oceanic spreading initiation and evolution. *Physics of the Earth and Planetary Interiors*, *214*, 35–52. https://doi.org/10.1016/j.pepi.2012.10.007

Grevemeyer, I., Rüpke, L. H., Morgan, J. P., Iyer, K., & Devey, C. W. (2021). Extensional tectonics and two-stage crustal accretion at oceanic transform faults. *Nature*, *591*, 402–407. https://doi.org/10.1038/s41586-021-03278-9

Harmon, N., Rychert, C., Agius, M., Tharimena, S., Le Bas, T., Kendall, J. M., & Constable, S. (2018). Marine geophysical investigation of the Chain fracture zone in the equatorial Atlantic from the PI-LAB experiment. *Journal of Geophysical Research: Solid Earth*, *123*(11), 11016–11030. https://doi.org/10.1029/2018JB015982

Ito, G. (2021). Oceanic fault zones reconstructed. *Nature*, *591*, 376–377. https://doi.org/10.1038/d41586-021-00639-2

Ito, G., Lin, J., & Graham, D. (2003). Observational and theoretical studies of the dynamics of mantle plume–mid-ocean ridge interaction. *Reviews of Geophysics*, *41*, 1017. https://doi.org/10.1029/2002RG000117

Ligi, M., Bonatti, E., Bortoluzzi, G., Carrara, G., Fabretti, P., Gilod, D., et al. (1999). Bouvet triple junction in the south Atlantic: Geology and evolution. *Journal of Geophysical Research: Solid Earth*, *104*(12), 29365–29385. https://doi.org/10.1029/1999JB900192

Ligi, M., Bonatti, E., Gasperini, L., & Poliakov, A. N. B. (2002). Oceanic broad multifault transform plate boundaries. *Geology*, *30*(1), 11–14. https://doi.org/10.1130/0091-7613(2002)030<0011:Obmtpb>2.0.Co;2

Luo, Y., Lin, J., Zhang, F., & Meng, W. (2021). Spreading rate dependence of morphological characteristics in global oceanic transform faults. *Acta Oceanologica Sinica*, *40*(5), 1–64. https://doi.org/10.1007/s13131-021-1722-5

Maia, M. (2019). Topographic and morphologic evidences of deformation at oceanic transform faults: Far-field and local-field stresses. In J. C. Duarte (Ed.), *Transform plate boundaries and fracture zones* (pp. 61–87). Elsevier. https://doi.org/10.1016/B978-0-12-812064-4.00003-7

Maia, M., Sichel, S., Briais, A., Brunelli, D., Ligi, M., Ferreira, N., et al. (2016). Extreme mantle uplift and exhumation along a transpressive transform fault. *Nature Geoscience*, *9*(8), 619–623. https://doi.org/10.1038/Ngeo2759

Mishra, J. K., & Gordon, R. G. (2016). The rigid-plate and shrinking-plate hypotheses: Implications for the azimuths of transform faults. *Tectonics*, *35*, 1827–1842. https://doi.org/10.1002/2015TC003968

Morgan, J. P., & Forsyth, D. W. (1988). Three-dimensional flow and temperature perturbations due to a transform offset: Effects on oceanic crustal and upper mantle structure. *Journal of Geophysical Research*, *93*(B4), 2955–2966. https://doi.org/10.1029/JB093iB04p02955

Okino, K., Nakamura, K., & Sato, H. (2015). Tectonic background of four hydrothermal fields along the Central Indian ridge. In J. Ishibashi, K. Okino & M. Sunamura (Eds.), *Subseafloor biosphere linked to hydrothermal systems* (pp. 133–146). Springer. https://doi.org/10.1007/978-4-431-54865-2_11

Pockalny, R. (1997). Evidence of transpression along the Clipperton transform: Implications for processes of plate boundary reorganization. *Earth and Planetary Science Letters*, *146*, 449–464. https://doi.org/10.1016/S0012-821X(96)00253-1

Pockalny, R., Gente, P., Buck, R. (1996). Oceanic transverse ridges: A flexural response to fracture-zone-normal extension. *Geology*, *24*(1), 712–n. https://doi.org/10.1130/0091-7613(1996)024<0071:otrafr>2.3.co;2

Pockalny, R. A., Detrick, R. S., & Fox, P. J. (1988). Morphology and tectonics of the Kane transform from sea beam bathymetry data. *Journal of Geophysical Research*, *93*(B4), 3179–3193. https://doi.org/10.1029/JB093iB04p03179

Ryan, W. B. F., Carbotte, S. M., Coplan, J. O., O'Hara, S., Melkonian, A., Arko, R., et al. (2009). Global multi-resolution topography synthesis. *Geochemistry, Geophysics, Geosystems*, *10*, Q03014. https://doi.org/10.1029/2008GC002332

Sandwell, D. T. (1986). Thermal stress and the spacings of transform faults. *Journal of Geophysical Research: Solid Earth*, *91*(B6), 6405–6417. https://doi.org/10.1029/JB091iB06p06405

Searle, R. C. (1986). GLORIA investigations of oceanic fracture zones: Comparative study of the transform fault zone. *Journal of the Geological Society*, *143*(5), 743–756. https://doi.org/10.1144/gsjgs.143.5.0743

Seton, M., Müller, R. D., Zahirovic, S., Williams, S., Wright, N. M., Cannon, J., et al. (2020). A global data set of present-day oceanic crustal age and seafloor spreading parameters. *Geochemistry, Geophysics, Geosystems*, *21*, e2020GC009214. https://doi.org/10.1029/2020GC009214

Sibrant, A. L. R., Maia, M., Mittelstaedt, E., & Graham, D. W. (2019). Variable crustal production originating from mantle source heterogeneity beneath the South East Indian Ridge and Amsterdam-St. Paul Plateau. *Geochemistry, Geophysics, Geosystems*, *20*, 4635–4653. https://doi.org/10.1029/2019GC008419

Small, C. (1995). Observations of ridge-hotspot interactions in the Southern Ocean. *Journal of Geophysical Research*, *100*(B9), 17931–17946. https://doi.org/10.1029/95JB01377

Sykes, L. R. (1967). Mechanism of earthquakes and nature of faulting on the mid-oceanic ridges. *Journal of Geophysical Research*, *72*(8), 2131–2153. https://doi.org/10.1029/JZ072i008p02131

Tozer, B., Sandwell, D. T., Smith, W. H. F., Olson, C., Beale, J. R., & Wessel, P. (2019). Global bathymetry and topography at 15 arc sec: SRTM15+. *Earth and Space Science*, *6*, 1847–1864. https://doi.org/10.1029/2019EA000658

Tucholke, B., & Schouten, H. (1988). Kane fracture zone. *Marine Geophysical Researches*, *10*, 1–39. https://doi.org/10.1007/BF02424659

Turcotte, D. L. (1974). Are transform faults thermal contraction cracks? *Journal of Geophysical Research*, *79*(17), 2573–2577. https://doi.org/10.1029/JB079i017p02573

Whitmarsh, R. B., & Calvert, A. J. (1986). Crustal structure of Atlantic fracture zones — I. The Charlie-Gibbs fracture zone. *Geophysical Journal International*, *85*(1), 107–138. https://doi.org/10.1111/j.1365-246X.1986.tb05174.x

Wilcock, W. S. D., Purdy, G. M., & Solomon, S. C. (1990). Microearthquake evidence for extension across the Kane transform fault. *Journal of Geophysical Research*, *95*(B10), 15439–15462. https://doi.org/10.1029/JB095iB10p15439

Wilson, J. T. (1965). A new class of faults and their bearing on continental drift. *Nature*, *207*, 343–347. https://doi.org/10.1038/207343a0

Wolfson-Schwehr, M., & Boettcher, M. S. (2019). Global characteristics of oceanic transform fault structure and seismicity. In J. C. Duarte (Ed.), *Transform plate boundaries and fracture zones* (pp. 21–59). Elsevier. https://doi.org/10.1016/B978-0-12-812064-4.00002-5

Yu, Z., Singh, S. C., Gregory, E. P. M., Maia, M., Wang, Z., & Brunelli, D. (2021). Semi-brittle seismic deformation in high-temperature mantle mylonite shear zone along the Romanche transform fault. *Science Advances*, *7*(15), eabf3388. https://doi.org/10.1126/sciadv.abf3388

Zhang, F., Lin, J., Zhou, Z., Yang, H., & Morgan, J. P. (2022). Mechanism of progressive broad deformation from oceanic transform valley to off-transform faulting and rifting. *Innovation*, *3*(1), 100193. https://doi.org/10.1016/j.xinn.2021.100193

References From the Supporting Information

Morgan, W. J., & Morgan, J. P. (2007). Plate velocities in the hotspot reference frame. In G. R. Foulger & D. M. Jurdy (Eds.), *Plates, plumes and planetary processes: Geological society of America special paper 430* (pp. 65–78). The Geological Society of America. https://doi.org/10.1130/2007.2430(04)

Tebbens, S. F., Cande, S. C., Kovacs, L., Parra, J. C., LaBrecque, J. L., & Vergara, H. (1997). The Chile ridge: A tectonic framework. *Journal of Geophysical Research*, *102*(B6), 12035–12059. https://doi.org/10.1029/96JB02581

Geophysical Research Letters

Supporting Information for

Impact of spreading rate and age-offset on oceanic transform fault morphology

Yu Ren [(1)], Jacob Geersen [(2)], and Ingo Grevemeyer [(1)]

(1) GEOMAR Helmholtz Centre for Ocean Research Kiel, Kiel, Germany
(2) Institute of Geosciences, University of Kiel, Kiel, Germany

Text S1. Comparison with recent statistics on transform morphology

After the discovery of OTFs in the mid-1960s (Wilson, 1965), it has been recognized that OTFs show a vast variability in their morphology, which is partly related to advances in the quality and quantity of seafloor mapping. Previous statistical investigations of transform morphology usually focused on the length (Sandwell, 1986; Luo et al., 2021), width (Searle, 1986; Dauteuil et al., 2002; Mishra & Gordon, 2016; Luo et al., 2021), and depth (Luo et al., 2021; Grevemeyer et al., 2021) of OTFs. However, it should be noted that most previous approaches to systematically quantify transform morphology suffer from the incompleteness of shipborne bathymetric datasets putting limitations to (A) the number of analyzed cases, (B) the exact shape of the structural elements, and (C) the quantification of morphological variations within one transform system including the robust assignment of uncertainties (e.g. standard deviation).

For example, the most recent and up-to-date analysis of transform morphology conducted by Luo et al. (2021), is based on the SRTM15+ grid (Tozer et al., 2019) which interpolates sparse ship-based bathymetric soundings with bathymetric predictions from gravity models at 15 arc-seconds spatial resolution. As a consequence, the width of 44 OTFs (all with a relatively simple morphology) was extracted exclusively for the mid-point of the transform valley, ignoring any along-transform variation. Furthermore, the depth of some OTFs was derived from predicted bathymetry (e.g., Charlie Gibbs, Doldrums, Jan Mayen, Marie Celeste, etc.) by averaging depth values along a profile, which cannot resolve short-wavelength depth variation within the transform. Another recent study, which was based exclusively on shipborne data (Grevemeyer et al., 2021), indicated that transform depth correlates with spreading rate and age-offset, but the number of investigated cases (41) was smaller compared to this study (94).

In Figure S5 we systematically compared our results to the above-mentioned statistical datasets on transform morphology from Mishra & Gordon (2016), Luo et al. (2021), and Grevemeyer et al. (2021). The misfit between the different datasets is significant with respect to the width (Figures S5c-d). The width estimates from Luo et al. (2021) are much larger, resulting from the fact that they included the walls of the transform valley, which are generally not considered when investigating the transform deformation zones (e.g., Searle, 1986; Mishra & Gordon, 2016; Grevemeyer et al., 2021). Furthermore, their single width estimates, which were exclusively done for the central point of the transform valleys, do not account for any along transform changes. However, Mishra & Gordon (2016) derived the width based on a rectangle to approximate the shape of transform deformation zone, producing a dataset that has a similar range but shows larger scatters, when compared to our width estimation. Grevemeyer et al. (2021)

fitted relatively simple polygons to the transform valleys, most of which were rectangles. Therefore, our approach of using well-defined polygons to outline the shape of transform valley, from which we extracted the width and depth, as well as their standard deviations, is clearly superior and more advanced than any previous estimation.

With respect to the depth of the floor of the transform valley, our data show clearer trends at larger age-offsets and less scatter compared to Luo et al. (2021) (Figure S5b). While our depth estimates show a similar trend compared to those from Grevemeyer et al. (2021), it has to be noted that their values for the large age-offset Andrew Bain and Romanche transform faults were different (Figure S5b). The latter results from the incompleteness of coverage of shipborne bathymetric data used in their study. For example, the complied bathymetry of Romanche in Grevemeyer et al. (2021) only provided coverage of the east domain, where the transform valley is much deeper. However, our compilation included additional bathymetric data from Ligi et al. (2002) covering the whole transform zone, which resulted in a shallower average depth for the entire transform valley. The same was the case for the Andrew Bain, where Grevemeyer et al. (2021) used a more limited dataset only covering the southern portion of the transform fault.

Therefore, we concluded that our compilation of high-resolution bathymetric data of global OTFs and well-constrained parameterization enables us to present the most complete and advanced dataset on the spreading rate and age-offset dependence of the morphology of OTFs (Table S2; Figure 2).

Text S2. Estimation of the age-offset across OTFs

The lack of high-resolution magnetic data around most OTFs, induces some uncertainties with respect to oceanic crustal ages, that need to be considered when estimating the age offset across a transform fault. Using a global dataset of present-day oceanic crustal ages (e.g. Seton et al., 2020), it is possible to directly derive the age-offset. This method, however, suffers from the above-mentioned incompleteness of magnetic data and may incorporate some gridding artefacts along transform faults and fracture zones (Seton et al., 2020). Alternatively, it is also possible to derive the age offset by dividing the transform length by the half-spreading rate (e.g., Furlong et al., 2001; Luo et al., 2021; Grevemeyer et al., 2021).

To validate and cross-check both methods we first checked the fine-scale quality of the recently published age grid from Seton et al. (2020) for each OTFs. From the investigated 94 OTFs, only 33 show a fine consistency between their geometry and the shapes of the seafloor isochrons. For these 33 cases we extracted the age offset for the two ridge-transform intersections (RTIs) from the Seton et al. (2020) data (Table S1) and compared it to the calculated values from dividing the transform length by the half-spreading rate (Figure S1). The good correlation (Figures S1, S3) between estimated and measured age-offset allows the calculation of age-offset for all OTFs in this study.

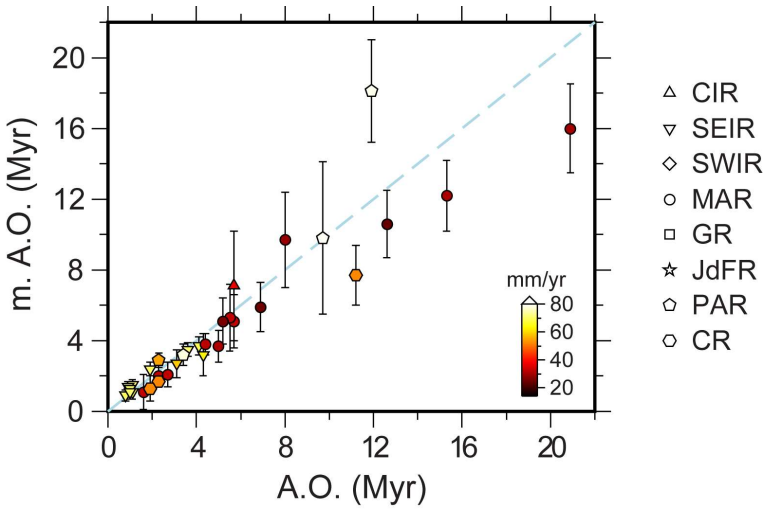

Figure S1. Age-offset from global age model versus calculated age-offset used in the main text. m. A.O., offset in seafloor age across the transform, measured from the global crustal age model (Seton et al., 2020); A.O., offset in seafloor age across the transform, calculated as the transform length divided by half-spreading rate.

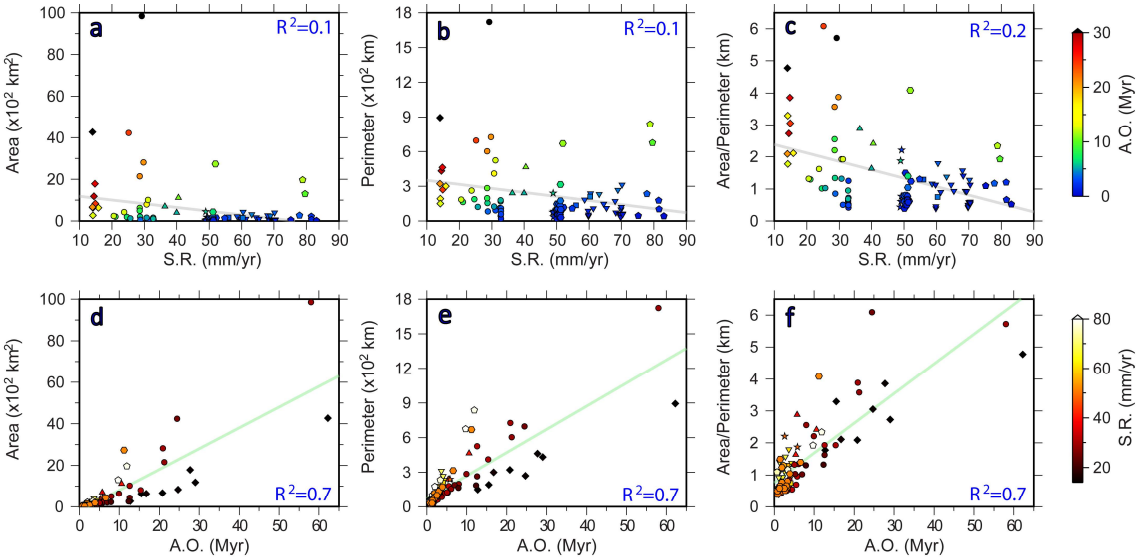

Figure S2. Variations in area, perimeter and area/perimeter ratio of the transform valleys (red polygon in Figure 1b). A.O., age-offset; S.R., spreading rate.

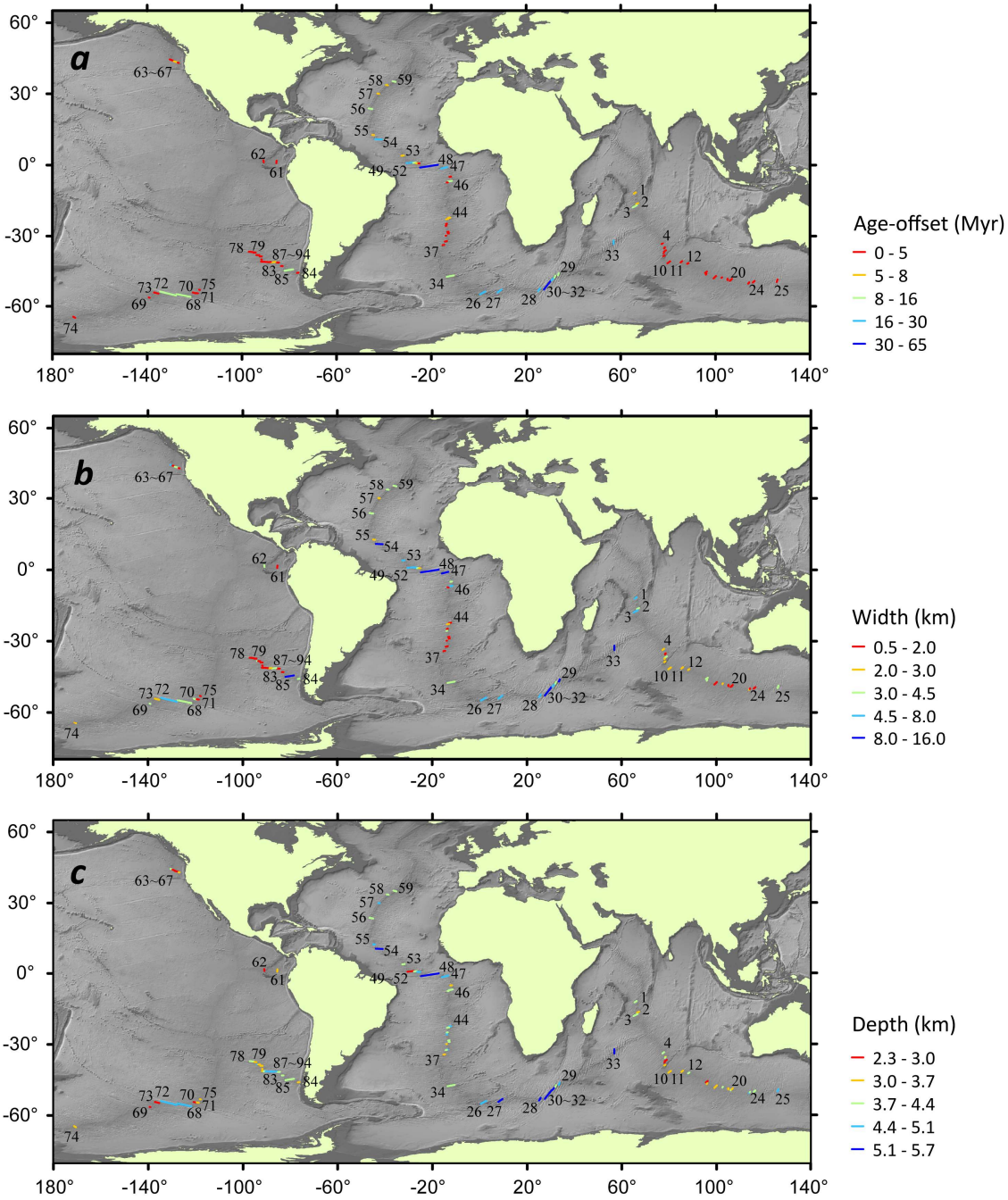

Figure S3. Variation in age-offset, and major morphological parameters (width and depth) of global OTFs. The length of colored lines scales with the length of their corresponding transform faults. Numbering is as in column 1 of Table S2.

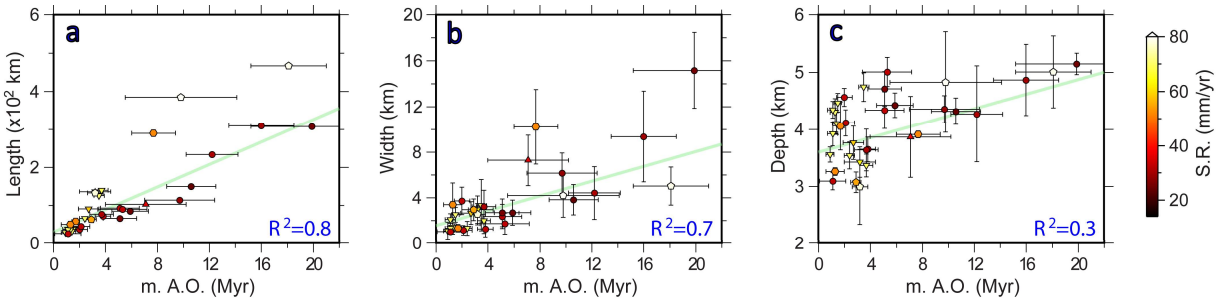

Figure S4. Length, width, and depth of OTFs versus age-offset measured from the global crustal age model (Seton et al., 2020). Only 33 OTFs were shown in the plots due to the quality of global age grids. m. A.O., age-offset measured from global crustal age model.

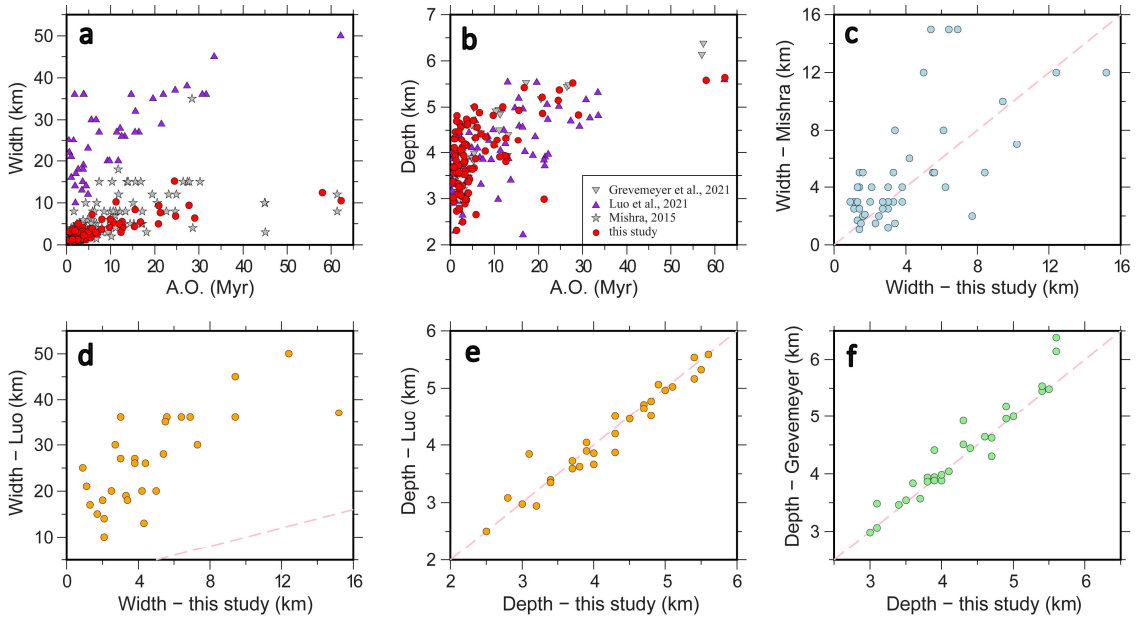

Figure S5. Cross plots of the recent statistical studies (Mishra & Gordon, 2016; Luo et al., 2021; Grevemeyer et al., 2021) and our datasets on the width and depth of OTFs. Dashed pink lines show one-to-one relationship between different datasets.

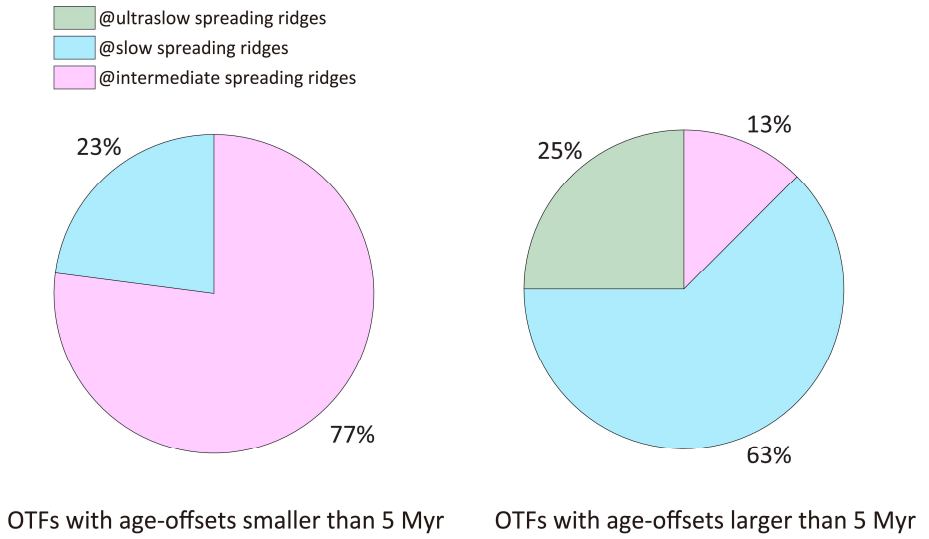

Figure S6. Percentage of different spreading rates for small and large age-offset OTFs, respectively.

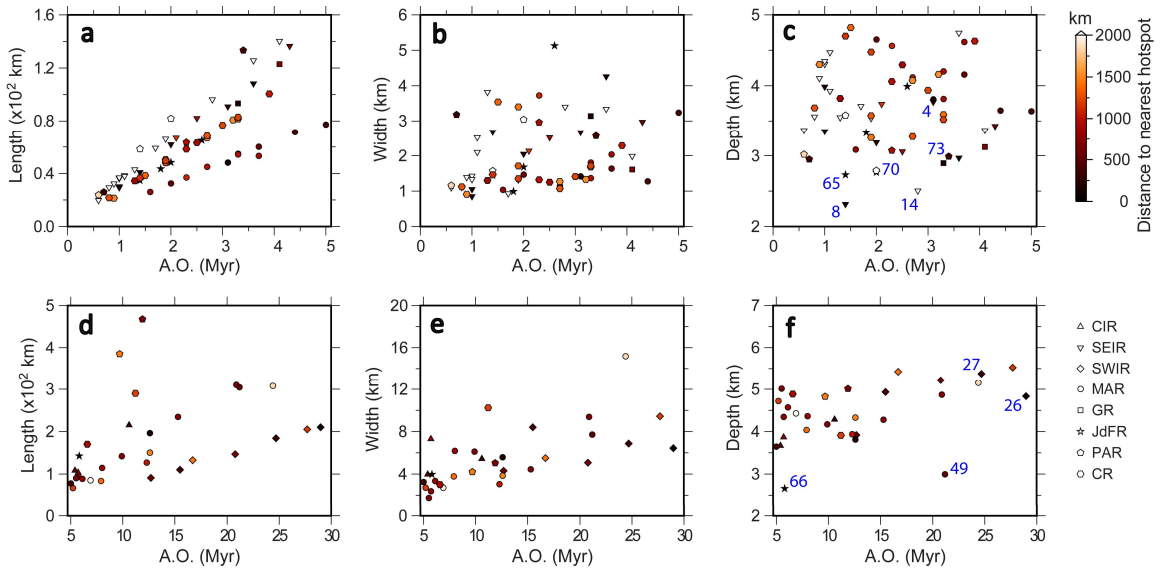

Figure S7. Variations in morphological parameters of OTFs with respect to the effect from nearby hotspot. Hotspot locations were compiled in Table S6. 4, Ter Tholen; 8, Boomerang; 14, SEIR 96E W; 26, Bouvet; 27, Shaka; 49, St Paul A; 65, Blanco C; 66, Blanco D; 70, Raitt W; 73, Hollister.

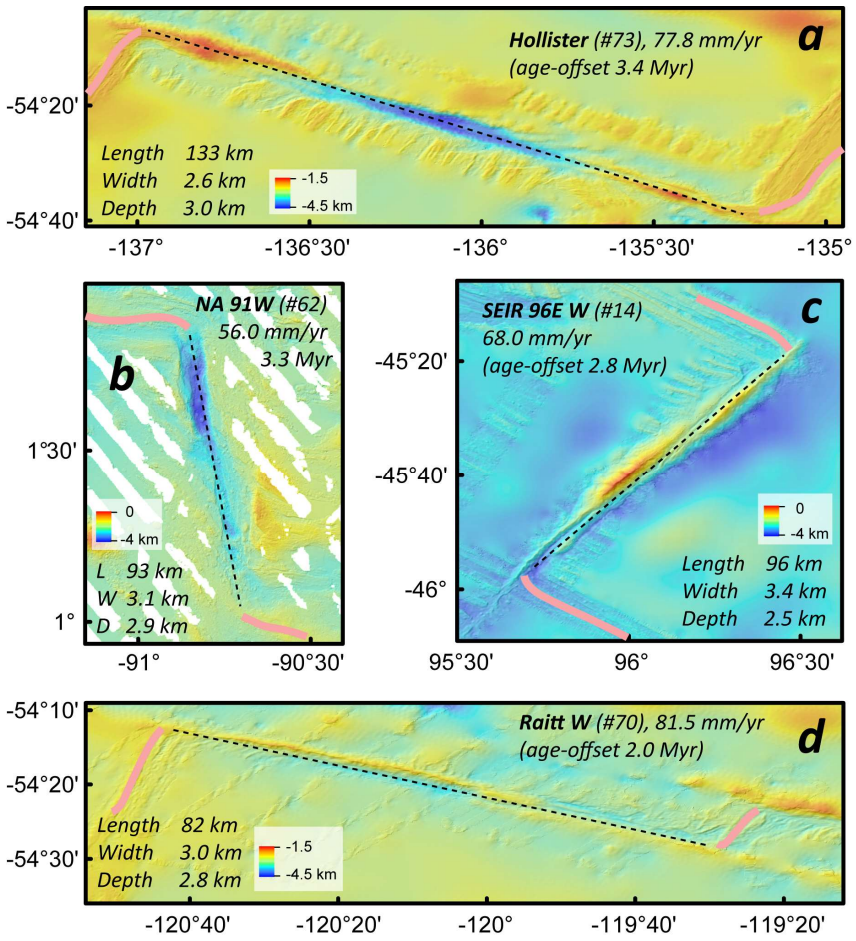

Figure S8. Bathymetric maps of **a,** Hollister (#73), **b,** NA 91W (#62), **c,** SEIR 96E W (#14) and **d,** Raitt W transforms (#70). Locations of the OTFs can be traced in Figure 1a, according to their numbering. Pink thick lines indicate mid-ocean ridges segmented by transform faults. Black dashed lines show the long axis of the OTFs.

Table S1. Age-offset across OTFs from global age model (Seton et al., 2020).

OTFs	AO A[a] (Myr)	Unc. A[b] (Myr)	AO B[c] (Myr)	Unc. B[d] (Myr)	Avg. AO[e] (Myr)	Avg. unc.[f] (Myr)
CIR 12S	6.03	2.39	8.07	3.72	7.05	3.06
Ter Tholen	2.87	0.52	2.56	1.02	2.72	0.77
Vlamingh	2.86	1.48	3.51	0.88	3.19	1.18
SEIR 100E	3.83	0.43	3.64	0.48	3.74	0.46
SEIR 103E	1.08	0.34	1.06	0.35	1.07	0.35
SEIR 105E W	0.83	0.33	0.86	0.31	0.85	0.32
SEIR 106E E	1.71	0.38	3.11	0.38	2.41	0.38
Zeehaen W	2.08	0.31	0.82	0.32	1.45	0.32
Zeehaen E	1.67	0.32	1.09	0.36	1.38	0.34
Heemskerck W	1.58	0.34	0.98	0.36	1.28	0.35
Heemskerck E	1.03	0.36	1.16	0.36	1.10	0.36
Euroka	3.34	0.36	3.72	0.41	3.53	0.39
Falkland	11.45	1.05	12.92	2.88	12.19	1.97
MAR 34S	4.77	0.41	2.76	0.77	3.77	0.59
MAR 2945S	1.20	1.15	1.06	0.86	1.13	1.01
MAR 2550S	1.64	0.61	2.34	0.51	1.99	0.56
MAR 25S	2.14	0.56	2.08	0.74	2.11	0.65
MAR 22S W	5.08	2.54	5.18	0.44	5.13	1.49
MAR 22S E	4.88	1.32	5.72	2.42	5.30	1.87
Chain	17.81	2.02	14.11	3.05	15.96	2.54
Strakhow	11.94	3.84	7.36	1.45	9.65	2.65
Vema	19.37	6.52	20.44	2.91	19.91	4.72
Marathon	5.63	1.35	6.09	1.51	5.86	1.43
Kane	9.51	2.34	11.77	1.46	10.64	1.90
Atlantis	5.38	1.06	4.78	1.46	5.08	1.26
MAR5S	3.75	0.96	3.67	0.84	3.71	0.90
Heezen	13.15	5.63	6.53	2.89	9.84	4.26
Tharp	15.43	0.93	20.83	4.88	18.13	2.91
Hollister	3.17	0.91	3.20	0.3	3.19	0.61
Pitman	2.89	0.46	2.91	0.28	2.90	0.37
Chiloe	1.67	0.31	1.62	0.18	1.65	0.25
Darwin	1.52	0.86	1.13	0.53	1.33	0.70
Guafo	7.43	2.09	8.00	1.25	7.72	1.67

[a] Age-offset measured at one RTI

[b] Uncertainty of the age-offset in [a]

[c] Age-offset measured at the other RTI

[d] Uncertainty of the age-offset in [b]

[e] Mean value of age-offsets estimated at the two RTIs

[f] Averaged uncertainty for the age-offset

Table S2. Morphological characteristics of global oceanic transform faults.

No.	OTF	S.R.	A. O.	Length	Width	Width STD	Depth	Depth STD	Nearest hotspot
Central Indian Ridge									
1	CIR 12S	36.3	5.7	103.00	7.284	2.208	3.870	0.707	Rodriguez
2	CIR 16S	40.0	5.4	108.06	3.977	1.367	3.667	0.367	Rodriguez
3	Marie Celeste	40.5	10.6	215.37	5.423	2.304	4.280	1.034	Rodriguez
Southeast Indian Ridge									
4	Ter Tholen	58.6	3.1	90.88	2.670	1.005	3.769	0.294	Christmas
5	Zeewolf E	59.8	1.0	29.39	0.854	0.374	3.350	0.078	Christmas
6	Zeewolf W	59.8	1.0	30.21	1.050	0.527	3.985	0.117	Christmas
7	Amsterdam	60.5	3.6	108.34	4.260	1.574	2.972	0.406	Amsterdam
8	Boomerang	59.7	1.4	40.91	2.677	1.527	2.316	0.133	Amsterdam
9	Hillegoms Hole	61.3	2.0	61.94	2.054	1.349	3.190	0.364	Amsterdam
10	Vlamingh	63.1	4.3	136.41	2.968	1.214	3.427	0.268	Amsterdam
11	Geelvinck E	64.5	2.5	82.17	2.518	0.475	3.058	0.242	Christmas
12	SEIR 88E	65.4	2.1	67.06	2.141	0.550	3.740	0.300	NAN
13	SEIR 96E E	68.2	1.3	42.92	3.821	1.035	3.548	0.113	NAN
14	SEIR 96E W	68.0	2.8	96.30	3.403	0.651	2.503	0.542	NAN
15	SEIR 100E	68.9	4.1	140.18	1.987	1.137	3.367	0.199	NAN
16	SEIR 103E	69.3	1.1	38.40	2.095	0.492	3.924	0.208	NAN
17	SEIR 105E W	69.7	0.8	29.31	1.113	0.750	3.562	0.133	NAN
18	SEIR 105E E	69.7	0.6	19.66	1.100	0.297	3.363	0.162	NAN
19	SEIR 106E W	69.8	1.7	59.11	0.928	0.263	3.712	0.114	NAN
20	SEIR 106E E	69.9	1.9	66.18	1.321	0.623	3.542	0.236	NAN
21	Zeehaen W	70.4	1.1	37.78	2.522	0.654	4.470	0.166	NAN
22	Zeehaen E	70.4	0.9	32.25	1.387	0.346	4.107	0.196	NAN
23	Heemskerck W	70.4	1.0	36.20	1.428	0.626	4.304	0.239	NAN
24	Heemskerck E	70.4	1.0	36.89	1.330	0.435	4.345	0.146	NAN
25	Euroka	70.2	3.6	125.57	3.344	2.247	4.744	0.249	NAN
Southwest Indian Ridge									
26	Bouvet	14.5	29.0	209.91	6.429	1.309	4.834	0.276	Bouvet
27	Shaka	14.9	24.7	184.37	6.862	2.141	5.375	0.309	Shona
28	Du Toit	15.9	16.7	132.74	5.510	3.512	5.421	0.288	NAN
29	Marion	14.2	15.5	110.29	8.414	3.628	4.934	0.269	Marion
30	Andrew Bain W	14.1	62.2	438.24	10.516	4.612	5.645	0.553	Marion
31	Andrew Bain M	14.1	20.8	146.96	5.061	1.603	5.217	0.520	Marion
32	Andrew Bain E	14.2	12.7	90.51	4.285	1.671	3.913	0.323	Marion
33	Atlantis II	14.8	27.7	204.89	9.430	3.403	5.522	0.563	NAN
Mid-Atlantic Ridge									
34	Falkland	30.7	15.3	234.21	4.426	2.318	4.272	0.838	Gough
35	Cox W	32.7	3.7	60.31	1.643	0.637	4.159	0.153	Tristan
36	Cox E	32.7	2.0	32.42	1.469	0.597	4.655	0.236	Tristan
37	MAR34S	32.5	4.4	71.57	1.282	0.714	3.651	0.219	Tristan

Table S2. (continued)

No.	OTF	S.R.	A. O.	Length	Width	Width STD	Depth	Depth STD	Nearest hotspot
38	MAR2945S	32.8	1.6	26.09	1.036	0.198	3.092	0.149	Tristan
39	MAR29SB	32.8	3.3	54.92	1.806	0.656	3.815	0.146	Tristan
40	Rio Grande	32.8	3.3	54.42	1.368	0.735	4.207	0.210	Tristan
41	MAR2550S	32.8	2.3	36.94	3.729	1.203	4.565	0.157	Tristan
42	MAR25S	32.8	2.7	45.05	1.151	0.414	4.118	0.231	St. Helena
43	MAR22S W	32.7	5.7	93.25	2.352	1.068	4.342	0.319	St. Helena
44	MAR22S E	32.7	5.5	89.62	1.731	0.931	5.007	0.256	St. Helena
45	Ascension W	31.1	3.1	48.15	1.419	1.153	3.812	0.169	Ascension
46	Ascension E	31.1	12.6	196.19	5.578	2.511	3.811	0.323	Ascension
47	Chain	29.7	20.9	310.03	9.374	3.976	4.866	0.620	Ascension
48	Romanche	29.2	58.0	846.73	12.443	3.507	5.587	0.951	Fernando
49	St Paul A	28.6	21.2	303.78	7.709	2.611	2.990	0.750	Fernando
50	St Paul B	28.6	9.9	142.06	6.116	1.658	4.170	0.169	Fernando
51	St Paul C	28.7	6.1	88.03	3.333	1.335	4.564	0.206	Fernando
52	St Paul D	28.8	3.7	53.37	2.044	1.009	4.620	0.224	Fernando
53	Strakhow	28.6	8.0	113.80	6.166	1.778	4.358	0.237	Fernando
54	Vema	25.2	24.4	307.61	15.174	3.295	5.147	0.185	NAN
55	Marathon	24.6	6.9	84.80	2.693	1.098	4.424	0.214	NAN
56	Kane	23.8	12.6	150.38	3.823	1.339	4.323	0.227	NAN
57	Atlantis	25.7	5.2	66.31	2.686	1.210	4.713	0.299	NAN
58	Hayes	21.1	7.9	83.48	3.755	1.351	4.031	0.201	NAN
59	Oceanographer	20.6	12.3	126.92	3.049	1.326	3.934	0.335	Azores
60	MAR5S	30.7	5.0	77.36	3.238	1.412	3.640	0.364	Ascension
Galapagos Ridge									
61	NA85W	60.3	4.1	123.01	1.613	0.408	3.124	0.270	Galapagos
62	NA91W	56.0	3.3	93.31	3.139	1.036	2.893	0.340	Galapagos
Juan de Fuca Ridge									
63	Blanco A	49.3	2.6	65.17	5.131	1.751	3.991	0.455	Cobb
64	Blanco B	49.1	2.0	48.23	1.677	0.593	2.764	0.246	Cobb
65	Blanco C	49.0	1.4	34.71	1.448	0.577	2.731	0.150	P. Jackson
66	Blanco D	48.9	5.8	142.84	3.981	0.601	2.658	0.279	P. Jackson
67	Blanco E	48.8	1.8	43.44	0.993	0.471	3.329	0.290	P. Jackson
Pacific Antarctic Ridge									
68	Heezen	79.5	9.7	384.89	4.195	1.880	4.829	0.878	NAN
69	Herron	75.2	0.7	25.99	3.179	0.570	2.952	0.077	Louisville
70	Raitt W	81.5	2.0	81.75	3.044	1.282	2.791	0.264	NAN
71	Raitt E	81.6	1.4	58.33	1.570	0.538	3.579	0.435	NAN
72	Tharp	78.8	11.9	467.31	5.046	1.665	5.006	0.626	Louisville
73	Hollister	77.8	3.4	133.34	2.573	0.942	2.992	0.657	Louisville
74	Pitman	54.8	2.3	63.44	2.959	0.951	3.075	0.180	Scott
75	Vacquier	83.1	0.6	23.85	1.165	0.338	3.021	0.146	NAN

Table S2. (continued)

No.	OTF	S.R.	A. O.	Length	Width	Width STD	Depth	Depth STD	Nearest hotspot
Chile Rise									
76	Challenger A	50.1	3.2	80.68	1.334	0.535	4.160	0.197	NAN
77	Challenger B	50.1	2.7	66.86	1.272	0.440	4.076	0.188	NAN
78	Challenger C	50.1	0.9	21.39	0.909	0.357	4.300	0.180	NAN
79	Challenger D	50.1	3.3	81.50	1.684	0.419	3.588	0.328	NAN
80	CR38S W	50.4	1.5	38.43	3.537	1.033	4.818	0.138	NAN
81	CR38S E	50.4	2.7	68.49	1.072	0.331	3.275	0.156	NAN
82	CR39S	50.6	3.3	83.04	1.708	0.343	3.522	0.107	NAN
83	Chiloe	51.6	2.3	58.40	1.324	0.329	4.062	0.422	J. Fernandez
84	Darwin	52.1	1.9	50.39	3.405	1.905	3.261	0.066	NAN
85	Guafo	51.9	11.2	290.19	10.224	3.272	3.912	0.059	NAN
86	UN_Chile	50.9	0.8	21.56	1.118	0.574	3.685	0.133	NAN
87	Valdivia A	51.1	1.9	47.98	1.710	0.417	3.576	0.288	NAN
88	Valdivia B	51.1	3.0	76.76	1.410	0.542	3.933	0.133	NAN
89	Valdivia C	51.1	1.9	49.68	1.348	0.303	4.473	0.356	NAN
90	Valdivia D	51.1	1.4	36.66	1.461	0.493	4.699	0.088	NAN
91	Valdivia E	51.2	3.9	100.48	2.295	0.578	4.632	0.262	J. Fernandez
92	Valdivia F	51.2	6.6	170.20	3.011	0.873	4.884	0.286	J. Fernandez
93	Valdivia G	51.3	2.5	63.24	1.255	0.325	4.293	0.148	J. Fernandez
94	Valdivia H	51.3	1.3	34.31	1.297	0.330	3.822	0.244	J. Fernandez

Table S3. Averaged morphological parameters of the 94 transform faults from ultraslow- to intermediate-spreading ridges.

Type	Spreading Rate (mm/yr)	Age-offset (Myr)	Length (km)	Width (km)	Depth (km)
Ultraslow	14.6	26.2	189.7	7.1	5.1
Slow	39.1	6.7	117.4	4.1	3.8
Intermediate	63.0	3.2	100.7	2.4	3.5

Table S4. The summary statistics of weighted linear fits in Figure 2. L, length; W, width; D, depth; SR, spreading rate; AO, age-offset; R^2, coefficient of determination; Adjusted R^2, adjusted coefficient of determination; RMSE, root mean squared error; SSE, sum of squares due to error.

Correlations	R^2	Adjusted R^2	RMSE	SSE
L vs. SR	0.05	0.04	114.89	1.21e+06
W vs. SR	0.25	0.24	3.37	1.05e+03
D vs. SR	0.22	0.21	0.40	14.61
L vs. AO	0.69	0.69	65.74	3.98e+05
W vs. AO	0.58	0.58	2.52	584.78
D vs. AO	0.39	0.38	0.35	11.46
L vs. AO (> 5 Myr)	0.54	0.53	108.73	3.55e+05
W vs. AO (> 5 Myr)*	0.69	0.68	2.30	143.34
D vs. AO (> 5 Myr)*	0.49	0.47	0.28	2.24

*OTFs that have undergone obvious secondary processes with numbering (Table S4) were excluded in the calculation, as mentioned in Figures 2k-l.

Table S5. Parameters and secondary processes of the obvious outliers in Figures 2h-i. PMC, plate-motion change.

OTFs	AO (Myr)	Width (km)	Depth (km)	Tectonic features
CIR 12S (#1)	7.1	7.284	3.870	Nearby Rodriguez hotspot (triple junction)
St Paul A (#49)	17.7	7.709	2.990	Nearby Fernando hotspot; PMC (Maia et al., 2016)
Vema (#54)	19.0	15.174	5.147	Transtension caused by PMC (Bonatti et al., 2005)
Blanco D (#66)	5.8	3.981	2.658	Nearby P. Jackson hotspot; PMC (Wilson, 1993)
Guafo (#85)	7.5	10.224	3.912	Transtension possibly from PMC (Tebbens et al., 1997)

Table S6. Location of the hotspots used in this paper (modified from the "Compleate Hot Spot Table" via *http://www.mantleplumes.org/CompleateHotspotTable.xls*, and Morgan & Morgan, 2007).

Hotspot	Lon. (º)	Lat. (º)	Hotspot	Lon. (º)	Lat. (º)	Hotspot	Lon. (º)	Lat. (º)
Afar	39.5	7.0	E. Australia	146.0	-40.8	Marqueses	-139.0	-10.5
Aitutaki	-159.8	-18.9	Eifel	6.7	50.2	Martin	-28.8	-20.5
Amsterdam	77.0	-37.0	Erebus	167.2	-77.5	Massif Central	2.7	45.1
Anyuy	166.0	67.0	Etna	15.0	37.8	Meteor	1.0	-51.4
Arago	-150.7	-23.4	Fernando	-32.4	-3.8	Mt. Rungwe	33.9	-8.3
Arnold	-25.0	-18.0	Foundation	-111.1	-37.7	New England	28.0	-32.0
Ascension	-14.3	-7.9	Galapagos	-91.6	-0.4	North Austral	-143.3	-25.6
Azores	-26.0	37.9	Gough	-10.0	-40.3	Ob-Lena	40.0	-52.2
Baikal	101.0	51.0	Great Meteor	28.0	30.0	Peter I	-90.6	-68.8
Baja	-114.5	27.7	Guyana	-61.0	5.0	Pitcairn	-129.3	-25.4
Balleny	164.8	-67.6	Hainan	110.0	20.0	P. Jackson	-127.7	42.5
Bermuda	-64.3	32.6	Hawaii	-155.2	19.0	Rarotonga	-159.0	-21.5
Bouvet	3.4	-54.4	Heard	73.5	-53.1	Raton	-104.1	36.8
Bowie	-134.8	53.0	Hoggar	5.6	23.3	Reunion	55.7	-21.2
Cameroon	5.1	-2.0	Hollister	-219.0	-54.0	Rodriguez	63.5	-19.6
Canary	-18.0	28.2	Iceland	-17.3	64.4	Sala Gomez	-109.0	-27.0
Cape Verde	-24.0	16.0	Jan Mayen	-8.2	71.1	Samoa	-169.1	-14.5
Caroline	164.4	4.8	Jebel Marra	24.2	13.0	San Felix	-80.1	-26.4
Christmas	80.0	-35.0	Juan de Fuca	231.0	45.0	Scott	-178.8	-68.8
Circe	-9.0	-8.0	J. Fernandez	-81.8	-33.9	Shimada	-117.5	16.9
Cobb	-130.1	46.0	Karisimbi	29.4	-15	Shona	6.0	-52.0
Cocos	94.5	-17.0	Kerguelen	69.0	-49.6	Socorro	-111.0	18.7
Comores	43.3	-11.5	Kilimanjiro	37.5	-3.0	St. Helena	-9.5	-16.5
Corner	-51.5	36.5	Lord Howe	159.8	-34.7	Tahiti/Society	-148.4	-18.2
Crough	-114.6	-26.9	Louisville	-140.6	-53.6	Tasmanid	155.5	-40.4
Crozet	50.2	-46.1	Macdonald	-140.3	-29.0	Tibesti	17.5	20.8
Darfur	24.0	13.0	Madeira	-17.3	32.6	Tristan	-12.3	-37.2
Discovery	-2.7	-43.0	Maria	-154.0	-22.2	Vema	6.3	-32.1
East Africa	34.0	6.0	Marion	37.6	-46.9	Yellowstone	-110.4	44.5
Easter	-106.5	-26.4	M.-Gilbert	-153.5	-21.0			

CHAPTER 3

MANUSCRIPT #2

Disparate crustal thicknesses beneath oceanic transform faults and adjacent fracture zones revealed by gravity anomalies

Zhikui Guo [1,2], Sibiao Liu [2], Lars Rüpke [2], Ingo Grevemeyer [2], Jason P. Morgan [3], Dietrich Lange [2], Yu Ren [2], and Chunhui Tao [1,4]

(1) Second Institute of Oceanography, MNR, Hangzhou, China
(2) GEOMAR Helmholtz Centre for Ocean Research Kiel, Kiel, Germany
(3) Southern University of Science and Technology, Shenzhen, China
(4) School of Oceanography, Shanghai Jiao Tong University, Shanghai, China

Published in 2023 in *Geology*, 51(3), 300–304

GEOLOGY | THE GEOLOGICAL SOCIETY OF AMERICA®

https://doi.org/10.1130/G50429.1

Manuscript received 23 May 2022
Revised manuscript received 28 October 2022
Manuscript accepted 29 October 2022

Published online 7 February 2023

Disparate crustal thicknesses beneath oceanic transform faults and adjacent fracture zones revealed by gravity anomalies

Zhikui Guo[1,2], Sibiao Liu[2], Lars Rüpke[2]*, Ingo Grevemeyer[2], Jason P. Morgan[3], Dietrich Lange[2], Yu Ren[2] and Chunhui Tao[1,4]*
[1]Key Laboratory of Submarine Geosciences, Second Institute of Oceanography, MNR, 310012 Hangzhou, China
[2]GEOMAR, Helmholtz Centre for Ocean Research Kiel, Wischhofstrasse 1-3, 24148 Kiel, Germany
[3]Southern University of Science and Technology, Xueyuan Avenue 1088, 518055 Shenzhen, China
[4]School of Oceanography, Shanghai Jiao Tong University, 1954 Huashan Road, Shanghai 200030, China

ABSTRACT

Plate tectonics describes oceanic transform faults as conservative strike-slip boundaries, where lithosphere is neither created nor destroyed. Therefore, seafloor accreted at ridge-transform intersections should follow a similar subsidence trend with age as lithosphere that forms away from ridge-transform intersections. Yet, recent compilations of high-resolution bathymetry show that the seafloor is significantly deeper along transform faults than at the adjacent fracture zones. We present residual mantle Bouguer anomalies, a proxy for crustal thickness, for 11 transform fault systems across the full range of spreading rates. Our results indicate that the crust is thinner in the transform deformation zone than in either the adjacent fracture zones or the inside corner regions. Consequently, oceanic transform faulting appears not only to thin the transform valley crust but also leads to a secondary phase of magmatic addition at the transition to the passive fracture zones. These observations challenge the concept of transform faults being conservative plate boundaries.

INTRODUCTION

Plate tectonics theory considers oceanic transform faults (TFs; Fig. 1A) to be conservative strike-slip plate boundaries that offset mid-ocean ridge (MOR; Fig. 1A) segments along small circles of plate motion (Morgan, 1968). Oceanic fracture zones (FZs; Fig. 1A), the passive extensions of active TFs, are visible as thousands-of-kilometer-long scars on the ocean floor. As lithosphere would be neither created nor destroyed in pure strike-slip motion, ocean plates sliding past one another along TFs should follow a similar age-dependent subsidence curve in response to plate cooling as does "normal" oceanic lithosphere away from ridge-transform intersections (RTIs, Fig. 1A; Stein and Stein, 1992). Yet, thermal contraction induced by cooling of the oceanic lithosphere causes a horizontal shrinking component in plates (Turcotte, 1974; Kumar and Gordon, 2009), which can potentially lead to azimuths of transform faults that differ from predictions that assume plates to be rigid (Mishra and Gordon, 2016). In addition, a recent systematic analysis of seafloor topography along TFs and FZs indicates that the topography of the TF is always deeper (up to 1.6 km) than its adjacent FZs (Grevemeyer et al., 2021). By combining bathymetric observations with 3-D geodynamic flow models, Grevemeyer et al. (2021) hypothesized that the deeper seafloor along the TF is linked to extension in the inside corner region (IC in Fig. 1A) of the RTI. The shoaling of the seafloor at the TF to FZ transition may, in turn, be related to magmatic addition, a hypothesis that is corroborated by characteristic magmatic features such as J-shaped ridges and magmatic flows visible in bathymetric data. If correct, this evolution scenario implies that the crust along TFs is systematically thinner than that along their associated FZs. This corollary can be tested using residual mantle Bouguer gravity anomalies (RMBA) under the common assumption that they can be interpreted as a proxy for crustal thickness variations (Lin and Morgan, 1992). Previous gravity studies revealed that crustal accretion becomes asymmetric toward segment ends of slow-spreading ridges, with IC crust being systematically thinner than crust of the outside corner (OC, Fig. 1A; Escartín and Lin, 1995). Likewise, Gregg et al. (2007) found that the crust beneath slow-spreading ridge segments tends to be thicker than the crust beneath their connecting TF, while intermediate to fast-slipping TFs appear to have a mass deficit with respect to the adjacent ridge segment that may originate from having a thicker, more porous, and/or more altered transform crust.

The differences between the gravity signals of FZs and their connecting TFs where they were "born" have never been systematically explored. While the inference that transform faults could be non-conservative can be deduced from prior works (e.g., Turcotte, 1974; Mishra and Gordon, 2016; Sasajima and Ito, 2017), this hypothesis has rarely been explicitly proposed. Hence, more robust observational evidence is still needed to answer the first-order question of whether TFs are conservative strike-slip boundaries in a "classic" plate tectonics sense, or whether transform faulting itself modulates crustal thickness by tectono-magmatic processes in a non-conservative way. We address this question by integrating high-resolution multibeam bathymetry from 11 TFs (Fig. 1; Table S2 in the Supplemental Material[1]), satellite gravity data, and 3-D geodynamic models to compute RMBA differences between the TF and their associated FZs ($\Delta RMBA_{TF-FZ}$). Our analysis reveals systematically positive $\Delta RMBA_{TF-FZ}$ values, which suggests that tectonics and magmatism at the TF cause a disparity between crustal thicknesses beneath oceanic FZs and TFs.

*E-mails: lruepke@geomar.de; taochunhui@sio.org.cn

[1]Supplemental Material. Details on the geodynamic model, thermal correction, and additional results of all 11 transform faults. Please visit https://doi.org/10.1130/GEOL.S.21899406 to access the supplemental material, and contact editing@geosociety.org with any questions.

CITATION: Guo, Z., et al., 2023, Disparate crustal thicknesses beneath oceanic transform faults and adjacent fracture zones revealed by gravity anomalies: Geology, v. 51, p. 300–304, https://doi.org/10.1130/G50429.1

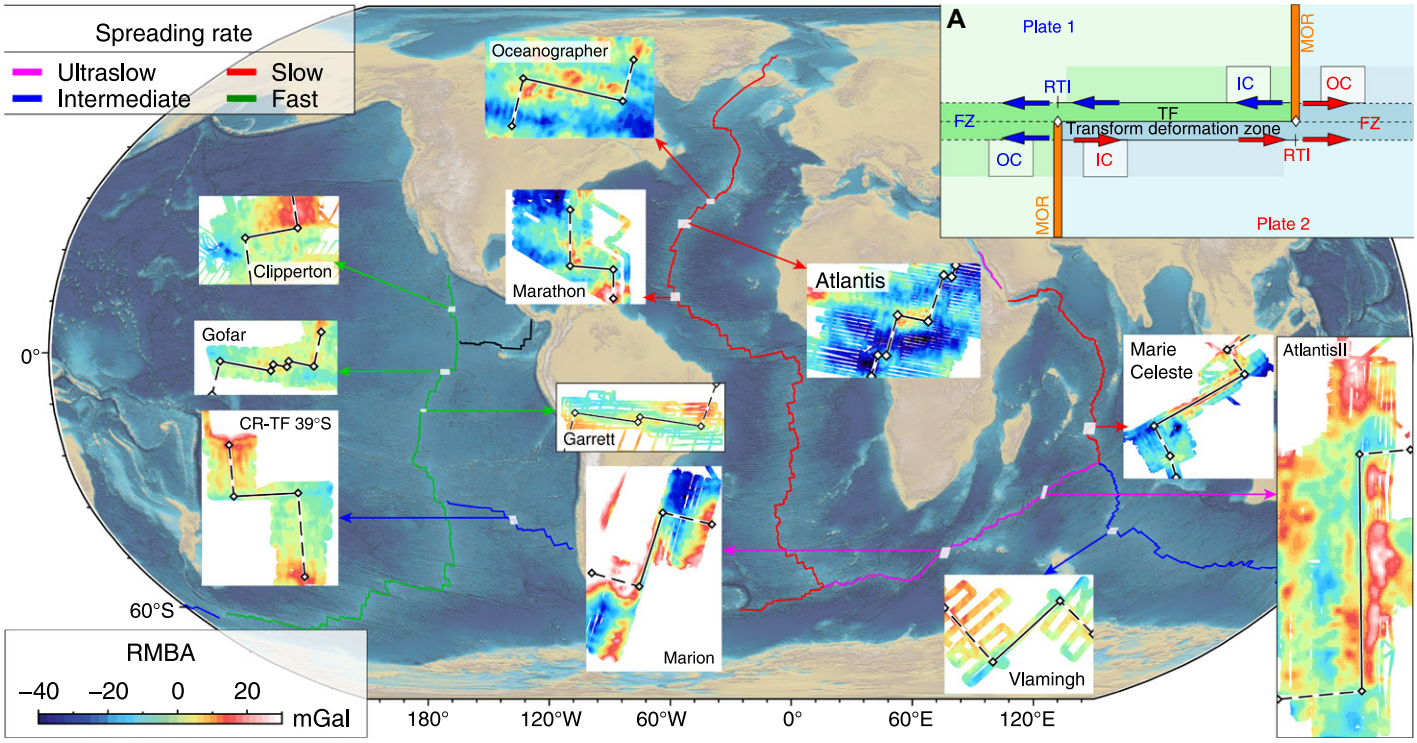

Figure 1. Global map showing transform faults (TFs) included in this study and their residual mantle Bouguer anomaly (RMBA). Colors of the ridges represent different spreading rates (see legend). Dashed black lines are spreading ridge segments; solid black lines are TFs; diamonds are ridge-transform intersections (RTIs). CR-TF 39°S is the transform fault near 39°S offsetting the Chile Ridge. (A) Inset shows the basic geometry and magmatic-tectonic elements of a transform fracture-zone system. FZ—fracture zone; OC—outside corner; IC—inside corner; MOR—mid-ocean ridge.

DATA AND METHOD

We used RMBA as a proxy for crustal thickness variations following the method of Prince and Forsyth (1988). We first calculated the mantle Bouguer anomaly (MBA) from satellite free-air anomaly data (Sandwell et al., 2014) with Parker's method (Parker, 1973) using high-resolution multibeam bathymetric data in combination with the global ETOPO1 bathymetric data set (NOAA National Geophysical Data Center, 2009) as needed to fill data gaps. After removing the gravitational effects of the water-crust and crust-Moho interface with an assumed 6 km normal crustal thickness, the MBA mainly reflects variations in crustal thickness and the thermally induced density structure of the mantle. The RMBA is then determined by removing the thermally induced mantle density effects from the MBA. The thermal correction is based on an accurate gravity forward method of a prism (Nagy, 1966), and temperature-induced density anomalies are estimated from 3-D geodynamic models following the approaches of Grevemeyer et al. (2021) and Behn et al. (2007). See Table S1 and Figs. S1 and S2 in the Supplemental Material for more detail. In contrast to MBA, RMBA is mainly caused by anomalous crustal thickness variations and/or mantle density effects that are not resolved by the thermal correction model.

To investigate RMBA changes between TF domains and their associated FZs, we defined the mean difference $\Delta RMBA_{TF-FZ} = RMBA_{TF} - (RMBA_{FZ1} + RMBA_{FZ2})/2$ based on the approach proposed by Gregg et al. (2007), where $RMBA_{TF}$, $RMBA_{FZ1}$, and $RMBA_{FZ2}$ are mean RMBA values along the TF domain and the two associated fracture zones FZ1 and FZ2, respectively. $RMBA_{TF}$ was calculated by averaging the values over a 10-km-wide rectangular box covering the TF (red box in Fig. 2). The length of the box was 90% of the TF length. At some places, like the East Pacific Rise, where TFs are wider due to internal segmentation, we used separate boxes for each transform segment identified from bathymetric data (Fig. S13). $RMBA_{FZ1}$ and $RMBA_{FZ2}$ were calculated by averaging RMBA values in a 10-km-wide box that starts at the RTI and extends along the FZ. The box length depends on the coverage of the multibeam bathymetric data that characterize the FZ (blue boxes in Fig. 2). Note that resolution tests show that variations in box length affected the results by less than 5% (Fig. S16).

RESULTS

The 11 transform systems and their RMBA maps are shown in Figure 1. The seafloor bathymetry, MBA, thermal correction, and RMBA map of each TF-FZ system are shown in Figs. S3–S13. Results indicate a correlation between the spreading rate and the RMBA value of a spreading segment, with positive anomalies at intermediate- and fast-spreading ridges and negative anomalies at slow- and ultraslow-spreading ridges. This feature (Fig. S15) results in a similar trend of the spreading rate versus RMBA difference between the TF and the associated ridge segments, as reported by Gregg et al. (2007).

Figure 2 illustrates the workflow for computing the RMBA for the Atlantis TF. The bathymetry in Figure 2A shows that the transform valley is deeper than its adjacent FZs. A positive RMBA anomaly centered around the transform valley suggests relatively thin crust in the transform deformation zone with respect to the FZs and MORs. This relative variation of crustal thickness (Fig. 2F) can be inverted from the RMBA map based on Parker-Oldenburg's algorithm (Gómez-Ortiz and Bhrigu, 2005).

The systematic analysis of the $\Delta RMBA_{TF-FZ}$ shows that it is positive for almost all of the transform systems studied regardless of spreading rate (Fig. 3A). The vertical error bars refer to the RMBA variation between two FZs ($|RMBA_{FZ1} - RMBA_{FZ2}|$) of the transform system. The magnitude of $\Delta RMBA_{TF-FZ}$ appears to decrease with increasing spreading rate. It is interesting to note that the Atlantis II transform with the largest age offset (~30 m.y.) appears to have an anomalously low $\Delta RMBA_{TF-FZ}$, which could be caused by additional effects unrelated to crustal thickness variation, such as mantle

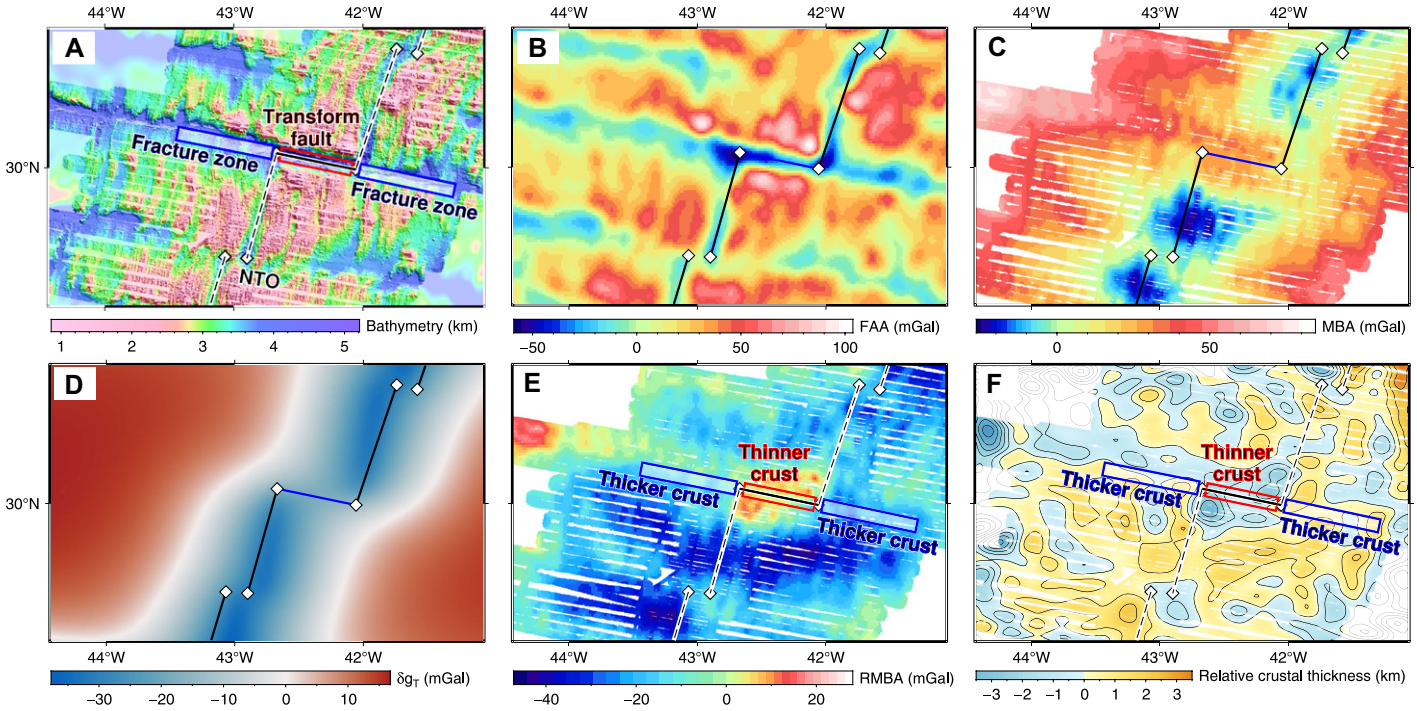

Figure 2. Results for the Atlantis transform on the Mid-Atlantic Ridge. (A) Seafloor topography merged from multibeam bathymetric data and ETOPO1 (NOAA National Geophysical Data Center, 2009). NTO—non-transform offset. The other symbols are as in Figure 1. (B) Free-air anomaly (FAA) derived from satellite. (C) Calculated mantle Bouguer anomaly (MBA). (D) Gravity anomaly of thermal contribution estimated from a 3-D viscoplastic mantle upwelling model. (E) Calculated residual mantle Bouguer anomaly (RMBA). (F) Map of gravity-derived relative variation of crustal thickness with contours of 1 km. All gravity anomalies are relative to the average value of the transform fault zone (red box). Blue and red boxes indicate regions where mean RMBA values were calculated for the fracture zone and transform fault, respectively.

serpentinization (~10%) and increased rock porosity (~10%) in the crust (Fig. S19). The geological and geophysical evidence seems to support thin crust (~2.7 km) and a highly fractured and serpentinized lower layer beneath the Atlantis II transform valley (Detrick et al., 1993; Muller et al., 2000), which implies that the crustal thickness-related $\Delta RMBA_{TF-FZ}$ of Atlantis II could be closer to the overall trend.

DISCUSSION

The gravity field at ridge–TF–FZ systems reveals distinct and characteristic differences between the active TF domain, the adjacent FZs, and the ridge segments. Particularly striking are the systematically higher RMBA values in the transform domain with respect to the RMBA along the adjacent FZs. A key question is whether this is a consequence of transform faulting-related thermo-magmatic processes, or of the aforementioned asymmetry between the inside corner (IC) and outside corner (OC) crust at MOR segment ends (Severinghaus and Macdonald, 1988; Escartín and Lin, 1995), in which case the $RMBA_{TF}$ should be close to $RMBA_{IC}$ and $RMBA_{FZ}$ and in between $RMBA_{IC}$ and $RMBA_{OC}$, with $0.5(RMBA_{IC} + RMBA_{OC})$ being a reasonable baseline. To discriminate, Figure 3B shows the RMBA differences between IC and OC, and Figure 3C shows the differences between $\Delta RMBA_{TF-FZ}$ and $0.5\Delta RMBA_{IC-OC}$. The latter is nearly always positive, with values of up to 20 mGal. To test which crustal configurations are compatible with this observation, we performed synthetic tests with differing OC, IC, TF, and FZ crustal thicknesses (Figs. S17 and S18). Figure 3D shows that the crust in the transform fault must also be thinner than IC crust on the order of 0–1.5 km to make $\Delta RMBA_{TF-FZ} - 0.5\Delta RMBA_{IC-OC}$ positive.

Thin TF crust was previously proposed to explain the deep transform valley (e.g., Morgan and Forsyth, 1988). The thinner crust could result from perturbations in melt generation and migration caused by the lower upwelling rates near the transform and the depth of the permeability barrier at the base of the thermal boundary layer (Morgan and Forsyth, 1988; Gregg et al., 2009). Melt segregation and migration are controlled by the thermal structure of the lithosphere and magma budget along ridge segments (Morgan and Forsyth, 1988; Sparks and Parmentier, 1991), and these factors are spreading rate-dependent, i.e., the depth of the isothermal surface (e.g., 700 °C) is deepening, and the magma supply is attenuating at slower spreading rates (Chen, 1988; Furlong et al., 2001).

We favor an alternative but complementary view in which the thin transform crust is the result of extension (Grevemeyer et al., 2021; Ren et al., 2022). In this scenario, the difference in plate strength (a consequence of the age offset) results in an increasingly oblique plate boundary at depth, which causes extension and mantle upwelling (Furlong et al., 2001; Grevemeyer et al., 2021). This proposed extension may therefore be an inherent feature of transform faulting and is consistent with extensional focal mechanisms observed along the Kane (Wilcock et al., 1990) and Oceanographer (Cessaro and Hussong, 1986) transforms on the Mid-Atlantic Ridge. Although gravity data alone cannot discriminate between the contributions of tectonic extension and lower melt supply to crustal thinning, it does suggest that the systematically positive, spreading rate-dependent RMBA along the active transform domain is plausibly due to crustal thinning, whose relative importance tends to diminish as the spreading rate increases.

As the gravity data support relatively thicker crust beneath FZs than beneath their adjacent TF, we interpret the observed shoaling of the young FZ seafloor at RTIs (Grevemeyer et al., 2021) as being related to the magmatic addition and/or preferential asymmetric crustal accretion toward the OC. Evidence for thermal rejuvenation in combination with magmatic addition was first reported for the fast-slipping Clipperton transform (northern East Pacific Rise; Gallo et al., 1986; Barth, 1994) and recently, based on high-resolution bathymetric data, for transform systems of all spreading rates (Grevemeyer et al., 2021). A complementary view is that of "dueling" ridge tips that would occasionally propagate beyond the TF (Pollard and

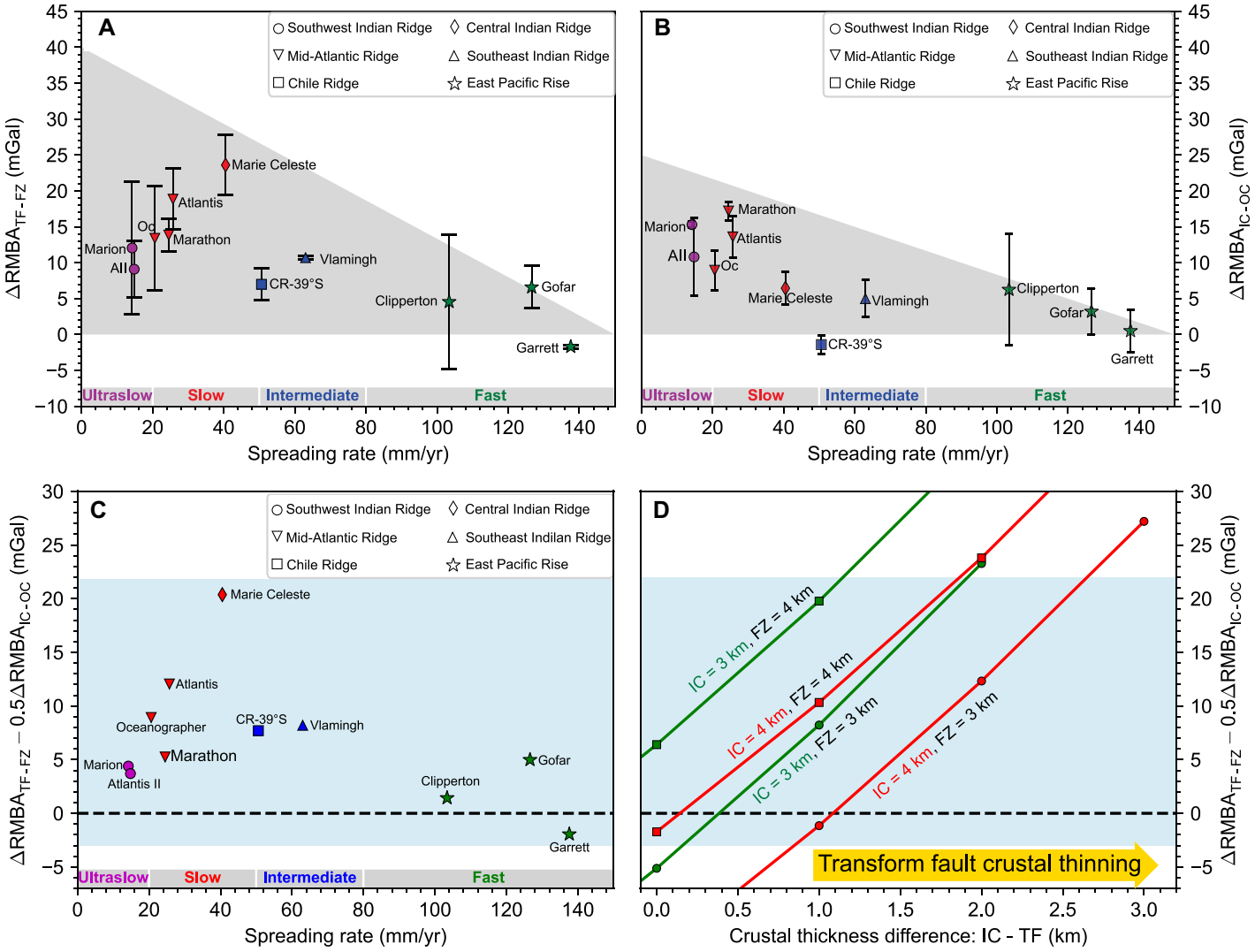

Figure 3. Gravity analysis results. Variation of ΔRMBA$_{TF–FZ}$ (A) and ΔRMBA$_{IC–OC}$ (B) as a function of spreading rate. TF—transform fault; FZ—fracture zone; OC—outside corner; IC—inside corner. Gray shaded areas outline the approximate variations in the shown values. (C) Difference between ΔRMBA$_{TF–FZ}$ and 0.5ΔRMBA$_{IC–OC}$. Different symbols indicate the associated spreading ridges. All—Atlantis II; Oc—Oceanographer. (D) Synthetic model results of ΔRMBA$_{TF–FZ}$ − 0.5ΔRMBA$_{IC–OC}$ as a function of transform fault crustal thinning relative to the IC. The *x*-axis shows extra thinning of transform crust with respect to the IC, and the red and green lines show predictions of the synthetic models. The blue shaded area is the observed range of differences between ΔRMBA$_{TF–FZ}$ and 0.5ΔRMBA$_{IC–OC}$ that needs to be explained (red and green curves need to be in the blue shaded region). The crustal thickness of the OC in this synthetic model calculation is 5 km. Additional details of the theoretical model calculation and results with an OC crustal thickness of 6 km and 7 km can be found in Figs. S17 and S18 (see footnote 1).

Aydin, 1984). In this view, magmatic addition would be more dynamic and unnecessary in a stable transform-to-fracture-zone transition. Despite these uncertainties, the systematic trend in ΔRMBA$_{TF–FZ}$ shown in Figure 3A indicates that the magmatic addition is particularly pronounced at ultraslow to slow spreading rates.

The RMBA is typically interpreted in terms of crustal thickness variations. However, it cannot discriminate between additional density-changing processes such as variations in porosity, mantle serpentinization, and temperature states not resolved by the mantle-flow model. When combined with other independent observations, the systematically positive ΔRMBA$_{TF–FZ}$ in our results does point to thinner crust along the TF domains compared to their adjacent FZs. For ultraslow- to slow-spreading systems, crustal thinning and seafloor deepening in the TF domain have been inferred from geomorphology, gravity data, and seismic data (Fox et al., 1976; Muller et al., 2000). At fast-slipping TF systems, seismic studies indicate that the crust below the TF is slightly thinner than normal oceanic crust (Van Avendonk et al., 2001) and that it thickens beneath the FZ (Barth, 1994; Van Avendonk et al., 1998). This feature is consistent with the slightly positive RMBA in our study (Fig. 3; Fig. S6). Furthermore, thin crust along transform domains correlates with the observed systematic deepening of transform valleys that is seen in the statistics of a recent compilation of 41 transform systems (Grevemeyer et al., 2021). Therefore, the observed positive ΔRMBA$_{TF–FZ}$ could be induced by both crustal thinning along TFs and the thicker crust in their adjacent FZs that is being created when transform seafloor passes by the opposing ridge tip at the ridge-transform intersection. This oceanic transform-related mode of deformation and multi-stage accretion has significant implications for the composition and hydrothermal state of crust and lithosphere along FZs, material that has generally been inferred to represent altered and hydrated crust and mantle (Detrick et al., 1993). Instead, FZs may actually contain magmatically accreted crust (Marjanović et al., 2020; Growe et al., 2021) that has experienced two distinct phases of accretion and hydrothermal alteration at an active spreading center, which has implications for the possibility

of systematic compositional and evolutionary differences between FZs and their adjacent oceanic lithosphere. Therefore, the fractured and hydrated lithosphere of oceanic transform faults will be magmatically overprinted by RTI magmatism, revealing the accretionary nature of oceanic transform faults and hence contradicting the idea that transform faults are conservative plate boundaries.

ACKNOWLEDGMENTS

We thank the National Natural Science Foundation of China (grant 42127807), the Scientific Research Fund of the Second Institute of Oceanography, Ministry of Natural Resources, China (grant SZ2201), and the China Ocean Mineral Resources R&D Association (grant DY135-S1–01–01) for funding support, and Norddeutscher Verbund für Hoch- und Höchstleistungsrechnen for parallel computing support. We thank the editor and the reviewers (Richard G Gordon, Mark Behn, and three anonymous reviewers) for their constructive comments, which helped to improve the manuscript.

REFERENCES CITED

Barth, G., 1994, Oceanic crust thickens approaching the Clipperton Fracture Zone: Marine Geophysical Researches, v. 16, p. 51–64, https://doi.org/10.1007/BF01812445.

Behn, M.D., Boettcher, M.S., and Hirth, G., 2007, Thermal structure of oceanic transform faults: Geology, v. 35, p. 307–310, https://doi.org/10.1130/G23112A.1.

Cessaro, R.K., and Hussong, D.M., 1986, Transform seismicity at the intersection of the Oceanographer Fracture Zone and the Mid-Atlantic Ridge: Journal of Geophysical Research: Solid Earth, v. 91, p. 4839–4853, https://doi.org/10.1029/JB091iB05p04839.

Chen, Y., 1988, Thermal model of oceanic transform faults: Journal of Geophysical Research: Solid Earth, v. 93, p. 8839–8851, https://doi.org/10.1029/JB093iB08p08839.

Detrick, R., White, R., and Purdy, G., 1993, Crustal structure of North Atlantic fracture zones: Reviews of Geophysics, v. 31, p. 439–458, https://doi.org/10.1029/93RG01952.

Escartín, J., and Lin, J., 1995, Ridge offsets, normal faulting, and gravity anomalies of slow spreading ridges: Journal of Geophysical Research: Solid Earth, v. 100, p. 6163–6177, https://doi.org/10.1029/94JB03267.

Fox, P.J., Schreiber, E., Rowlett, H., and McCamy, K., 1976, The geology of the Oceanographer Fracture Zone: A model for fracture zones: Journal of Geophysical Research: Solid Earth, v. 81, p. 4117–4128, https://doi.org/10.1029/JB081i023p04117.

Furlong, K.P., Sheaffer, S.D., and Malservisi, R., 2001, Thermal-rheological controls on deformation within oceanic transforms, *in* Holdsworth, R.E., et al., eds., The Nature and Tectonic Significance of Fault Zone Weakening: Geological Society, London, Special Publication 186, p. 65–83, https://doi.org/10.1144/GSL.SP.2001.186.01.05.

Gallo, D.G., Fox, P.J., and Macdonald, K.C., 1986, A Sea Beam investigation of the Clipperton transform fault: The morphotectonic expression of a fast slipping transform boundary: Journal of Geophysical Research: Solid Earth, v. 91, p. 3455–3467, https://doi.org/10.1029/JB091iB03p03455.

Gómez-Ortiz, D., and Bhrigu, N.P.A., 2005, 3DINVER. M: A MATLAB program to invert the gravity anomaly over a 3-D horizontal density interface by Parker–Oldenburg's algorithm: Computers & Geosciences, v. 31, p. 513–520, https://doi.org/10.1016/j.cageo.2004.11.004.

Gregg, P., Behn, M., Lin, J., and Grove, T., 2009, Melt generation, crystallization, and extraction beneath segmented oceanic transform faults: Journal of Geophysical Research: Solid Earth, v. 114, https://doi.org/10.1029/2008JB006100.

Gregg, P.M., Lin, J., Behn, M.D., and Montési, L.G., 2007, Spreading rate dependence of gravity anomalies along oceanic transform faults: Nature, v. 448, p. 183–187, https://doi.org/10.1038/nature05962.

Grevemeyer, I., Rüpke, L.H., Morgan, J.P., Iyer, K., and Devey, C.W., 2021, Extensional tectonics and two-stage crustal accretion at oceanic transform faults: Nature, v. 591, p. 402–407, https://doi.org/10.1038/s41586-021-03278-9.

Growe, K., Grevemeyer, I., Singh, S.C., Marjanović, M., Gregory, E. P., Papenberg, C., Vaddineni, V., Gómez de la Peña, L., and Wang, Z., 2021, Seismic structure of the St. Paul Fracture Zone and Late Cretaceous to Mid Eocene oceanic crust in the equatorial Atlantic Ocean near 18° W: Journal of Geophysical Research: Solid Earth, v. 126, https://doi.org/10.1029/2021JB022456.

Kumar, R.R., and Gordon, R.G., 2009, Horizontal thermal contraction of oceanic lithosphere: The ultimate limit to the rigid plate approximation: Journal of Geophysical Research: Solid Earth, v. 114, https://doi.org/10.1029/2007JB005473.

Lin, J., and Morgan, J.P., 1992, The spreading rate dependence of three-dimensional mid-ocean ridge gravity structure: Geophysical Research Letters, v. 19, p. 13–16, https://doi.org/10.1029/91GL03041.

Marjanović, M., et al., 2020, Seismic crustal structure and morphotectonic features associated with the Chain Fracture Zone and their role in the evolution of the equatorial Atlantic region: Journal of Geophysical Research: Solid Earth, v. 125, https://doi.org/10.1029/2020JB020275.

Mishra, J.K., and Gordon, R.G., 2016, The rigid-plate and shrinking-plate hypotheses: Implications for the azimuths of transform faults: Tectonics, v. 35, p. 1827–1842, https://doi.org/10.1002/2015TC003968.

Morgan, J.P., and Forsyth, D.W., 1988, Three-dimensional flow and temperature perturbations due to a transform offset: Effects on oceanic crustal and upper mantle structure: Journal of Geophysical Research: Solid Earth, v. 93, p. 2955–2966, https://doi.org/10.1029/JB093iB04p02955.

Morgan, W.J., 1968, Rises, trenches, great faults, and crustal blocks: Journal of Geophysical Research: Solid Earth, v. 73, p. 1959–1982, https://doi.org/10.1029/JB073i006p01959.

Muller, M.R., Minshull, T.A., and White, R., 2000, Crustal structure of the Southwest Indian Ridge at the Atlantis II fracture zone: Journal of Geophysical Research: Solid Earth, v. 105, p. 25,809–25,828, https://doi.org/10.1029/2000JB900262.

Nagy, D., 1966, The gravitational attraction of a right rectangular prism: Geophysics, v. 31, p. 362–371, https://doi.org/10.1190/1.1439779.

NOAA National Geophysical Data Center, 2009, ETOPO1 1 Arc-Minute Global Relief Model: NOAA National Centers for Environmental Information, https://doi.org/10.7289/V5C8276M.

Parker, R., 1973, The rapid calculation of potential anomalies: Geophysical Journal International, v. 31, p. 447–455, https://doi.org/10.1111/j.1365-246X.1973.tb06513.x.

Pollard, D.D., and Aydin, A., 1984, Propagation and linkage of oceanic ridge segments: Journal of Geophysical Research: Solid Earth, v. 89, p. 10,017–10,028, https://doi.org/10.1029/JB089iB12p10017.

Prince, R.A., and Forsyth, D.W., 1988, Horizontal extent of anomalously thin crust near the Vema Fracture Zone from the three-dimensional analysis of gravity anomalies: Journal of Geophysical Research: Solid Earth, v. 93, p. 8051–8097, https://doi.org/10.1029/JB093iB07p08051.

Ren, Y., Geersen, J., and Grevemeyer, I., 2022, Impact of spreading rate and age-offset on oceanic transform fault morphology: Geophysical Research Letters, v. 49, p. 1–10, https://doi.org/10.1029/2021GL096170.

Sandwell, D.T., Müller, R.D., Smith, W.H., Garcia, E., and Francis, R., 2014, New global marine gravity model fromCryoSat-2 and Jason-1 reveals buried tectonic structure: Science, v. 346, p. 65–67, https://doi.org/10.1126/science.1258213.

Sasajima, R., and Ito, T., 2017, Anisotropic horizontal thermal contraction of young oceanic lithosphere inferred from stress release due to oceanic intraplate earthquakes: Tectonics, v. 36, p. 1988–2021, https://doi.org/10.1002/2017TC004680.

Severinghaus, J.P., and Macdonald, K.C., 1988, High inside corners at ridge-transform intersections: Marine Geophysical Researches, v. 9, p. 353–367, https://doi.org/10.1007/BF00315005.

Sparks, D.W., and Parmentier, E.M., 1991, Melt extraction from the mantle beneath spreading centers: Earth and Planetary Science Letters, v. 105, p. 368–377, https://doi.org/10.1016/0012-821X(91)90178-K.

Stein, C.A., and Stein, S., 1992, A model for the global variation in oceanic depth and heat flow with lithospheric age: Nature, v. 359, p. 123–129, https://doi.org/10.1038/359123a0.

Turcotte, D.L., 1974, Are transform faults thermal contraction cracks?: Journal of Geophysical Research: Solid Earth, v. 79, p. 2573–2577, https://doi.org/10.1029/JB079i017p02573.

Van Avendonk, H.J., Harding, A.J., Orcutt, J.A., and McClain, J.S., 1998, A two-dimensional tomographic study of the Clipperton transform fault: Journal of Geophysical Research: Solid Earth, v. 103, p. 17,885–17,899, https://doi.org/10.1029/98JB00904.

Van Avendonk, H., Harding, A., Orcutt, J., and McClain, J., 2001, Contrast in crustal structure across the Clipperton transform fault from travel time tomography: Journal of Geophysical Research: Solid Earth, v. 106, p. 10,961–10,981, https://doi.org/10.1029/2000JB900459.

Wilcock, W.S., Purdy, G., and Solomon, S.C., 1990, Microearthquake evidence for extension across the Kane transform fault: Journal of Geophysical Research: Solid Earth, v. 95, p. 15,439–15,462, https://doi.org/10.1029/JB095iB10p15439.

Printed in USA

Guo, Z., et al., 2023, Disparate crustal thicknesses beneath oceanic transform faults and adjacent fracture zones revealed by gravity anomalies: Geology, https://doi.org/10.1130/G50429.1

Disparate crustal thicknesses beneath oceanic transform faults and adjacent fracture zones revealed by gravity anomalies

Zhikui Guo[1,2], Sibiao Liu[2], Lars Rüpke[2,*], Ingo Grevemeyer[2], Jason P. Morgan[3], Dietrich Lange[2], Yu Ren[2], and Chunhui Tao[1,4,*]

[1]*Key Laboratory of Submarine Geosciences, SOA, Second Institute of Oceanography, MNR, Hangzhou 310012, China*

[2]*GEOMAR, Helmholtz Centre for Ocean Research, Wischhofstrasse 1-3, 24148 Kiel*

[3]*Southern University of Science and Technology, Xueyuan Avenue 1088, 518055 Shenzhen*

[4]*School of Oceanography, Shanghai Jiao Tong University, 1954 Huashan Rd., Shanghai 200030, China*

[*]*lruepke@geomar.de, taochunhui@sio.org.cn*

SUPPLEMENTARY MATERIAL

1 Geodynamic simulations

We use the open-source code ASPECT version 2.1.0 (Bangerth et al., 2019) to develop 3-D geodynamic models with nonlinear viscoplastic rheology, following model setups similar to that in Grevemeyer et al. (2021). The steady-state simulations calculate the coupled thermo-mechanical evolution of ridge-transform systems, where the temperature field of the transform-fracture zone evolves dynamically in response to the prescribed surface spreading rate and the internal mantle flow.

In our models, the flow is driven by a kinematic, strike-slip boundary condition at the surface (Figure S1). The front and back sides have free-slip boundary conditions. Other boundary conditions (the left and right sides and the bottom) are set to the lithostatic pressure to allow free flow of material in and out. The temperatures at the top and bottom boundaries are fixed to 0°C and 1300°C, respectively. All other sides are insulated, i.e., no horizontal heat flux. The density varies with temperature: $\rho(T) = \rho_0[1 - \alpha(T - T_0)]$, where ρ_0 is the reference density at temperature T_0 and α is the volumetric thermal expansion coefficient (Table SS1).

The model resolution is 2.5 km/element in the ridge-transform area (0-10 km deep) and 10 km/element elsewhere. The geometry of the ridge-transform system and its spreading rate (Table SS2) are taken from the local bathymetric data (Grevemeyer et al., 2021) and the global topographic dataset of ETOPO1 (Amante and Eakins, 2009). The viscoplastic rheology contains a wet-olivine dislocation-creep viscosity (Hirth and Kohlstedt, 2003) and Drucker Prager plasticity (Table SS1). Further details on the viscoplastic setup and governing equations in ASPECT are provided elsewhere (e.g. Glerum et al., 2018;

Bangerth et al., 2019).

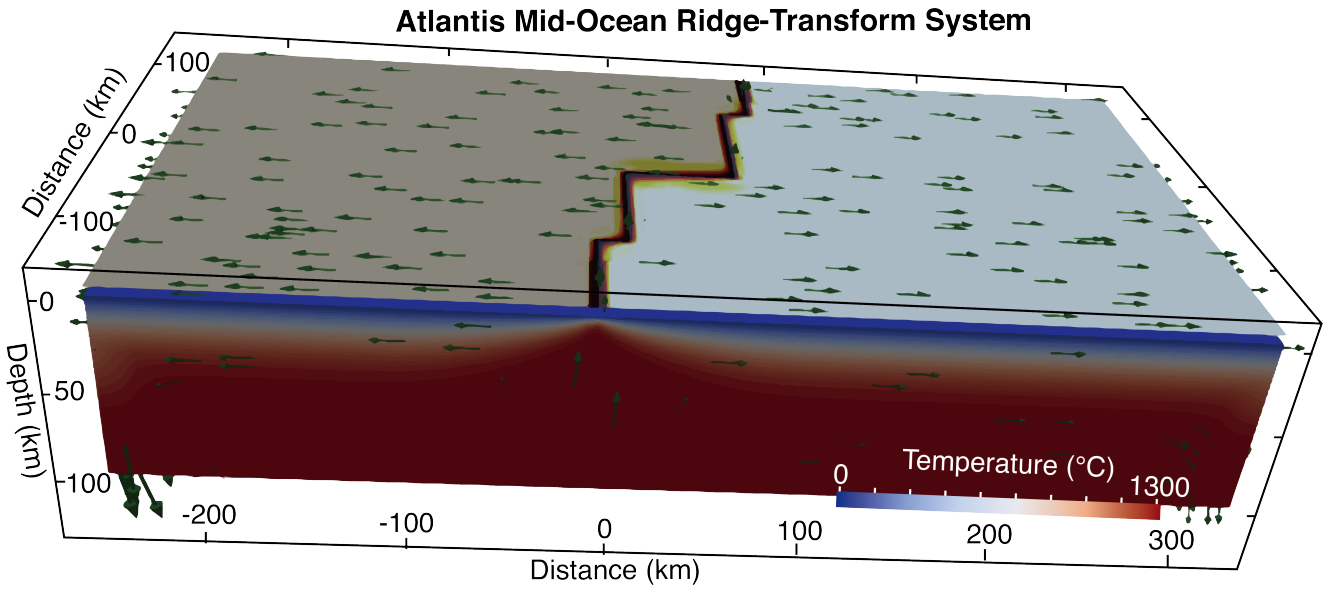

Figure S1. Model setup for the geodynamic simulation of the Atlantis transform example. The geometry of the mid-ocean ridge-transformation system (dark red) is extracted from bathymetric data Figure S3a. A kinematic boundary condition is imposed at the surface to simulate the Atlantis spreading, balanced by mantle upwelling from the open bottom boundary (green arrows).

2 Thermal corrections

The gravity correction (δg_T) of thermal effect is calculated from thermal-induced density anomalies estimated from 3-D geodynamic flow models. The density anomalies are calculated by $\delta\rho = \alpha\rho_0(T - T_0)$ and stored in an unstructured mesh consisting of cubic cells (see Figure S2). The gravity forward computing of such 3D density distribution is implemented in a C++ program named vtk2grav(Guo, 2022). For a specific cell C_i, it has a uniform density anomaly value $\delta\rho_i$ and the analytical solution(Nagy, 1966) of its gravity at point $P(x_j, y_j, z_j)$ can be expressed as follows,

$$\delta g_{T_i}(x_j,y_j,z_j) = G\delta\rho_i \left(x\ln(y+r) + y\ln(x+r) - z\arcsin\frac{z^2+y^2+yr}{(y+r)\sqrt{y^2+z^2}} \right) \Bigg|_{z_1-z_j}^{z_2-z_j} \Bigg|_{y_1-y_j}^{y_2-y_j} \Bigg|_{x_1-x_j}^{x_2-x_j} \tag{1}$$

where $r = \sqrt{x^2+y^2+z^2}$, $G = 6.67408 \times 10^{-11}\ m^3\ kg^{-1}\ s^{-2}$ is the gravitational constant. The notations $(x_1, x_2, y_1, y_2, z_1, z_2)$ of coordinates of cell C_i are shown in Figure S2. Therefore, the thermal correction at point $P(x_j, y_j, z_j)$, which is the same as the data points of the mantle Bouguer anomaly map, can be calculated as,

Table S1. Parameters used in the geodynamic model and RMBA calculation.

Parameter	Value
Sea water density ($kg\ m^{-3}$)	1030
Reference crustal density ($kg\ m^{-3}$)	2700
Reference mantle density, ρ_0 ($kg\ m^{-3}$)	3300
Reference crustal thickness (km)	6
Reference temperature, T_0 (°C)	1300
Thermal expansion, α (1/K)	3.5e-5
Thermal conductivity ($WK^{-1}m^{-1}$)	3.0
Heat capacity ($Jkg^{-1}K^{-1}$)	1250
Activation volume for dislocation creep (cm^3mol^{-1})	22
Activation energy for dislocation creep (kJmol^{-1})	520
Prefactor for dislocation creep ($Pa^{-n}s^{-1}$)	3.6e-14
Stress exponent for dislocation creep	3.5
Frictional angle (°)	30
Cohesions (MPa)	10

$$\delta g_T(x_j,y_j,z_j) = \sum_{i=1}^{N} \delta g_{Ti}(x_j,y_j,z_j) \tag{2}$$

where N is the cell number of the 3D geodynamic model result.

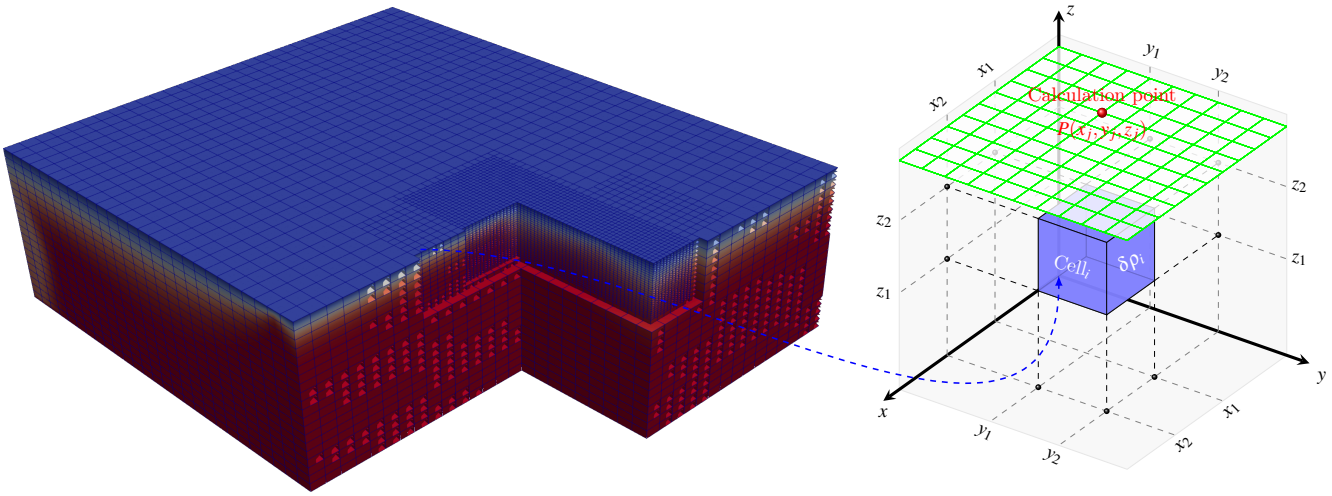

Figure S2. Mesh of the 3D thermal model result (left) and notation used for gravity forward of a cubic body (right). $x_1, x_2, y_1, y_2, z_1, z_2$ are the coordinates of six corner point of the cubic body (transparent blue box with black edges). $P(x_j,y_j,z_j)$ represent the gravity forward calculation point and the greenish grid represents data points of the MBA map (e.g. Figure S3b) which requires thermal correction.

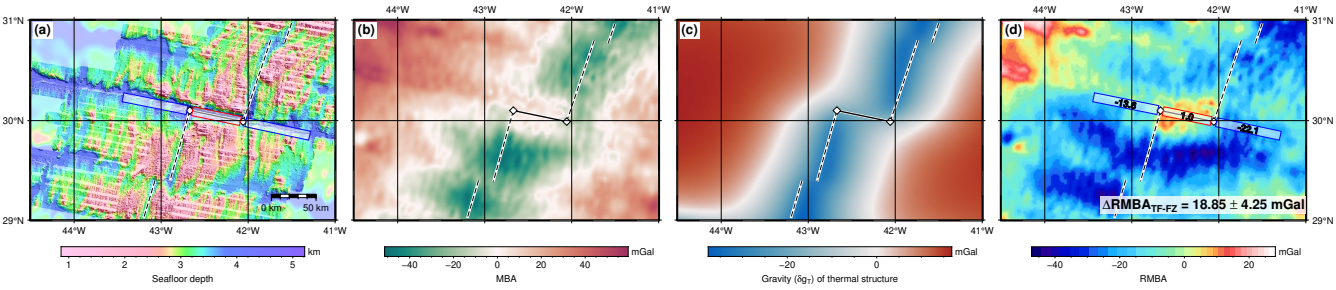

Figure S3. Input data and results of the Atlantis transform fault offsetting the Mid-Atlantic Ridge. (a) Bathymetric map; (b) Mantle Bouguer Anomaly (MBA); (c) gravitational effect of the lithospheric thermal structure; (d) Residual Mantle Bouguer Anomaly (RMBA). Symbols and lines as in Figure 2

.

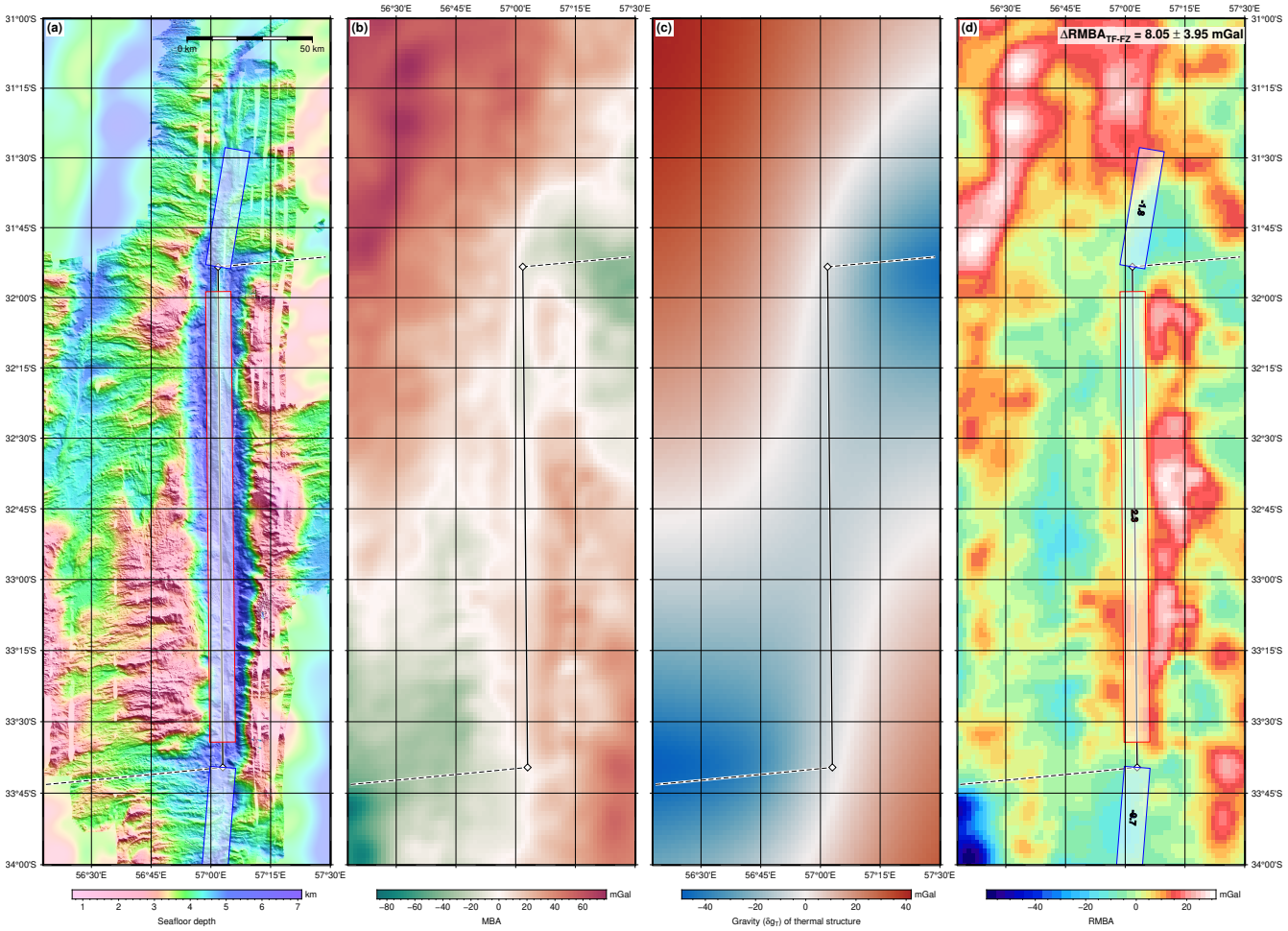

Figure S4. Input data and results of the Atlantis II transform fault offsetting the Southwest Indian Ridge. (a) Bathymetric map; (b) Mantle Bouguer Anomaly (MBA); (c) gravitational effect of the lithospheric thermal structure; (d) Residual Mantle Bouguer Anomaly (RMBA). Symbols and lines as in Figure 2.

.

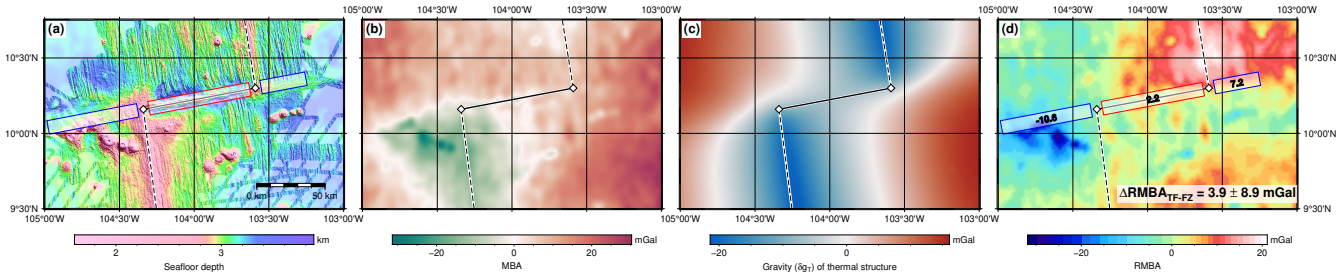

Figure S5. Input data and results of the Clipperton transform fault offsetting the East Pacific Rise. (a) Bathymetric map; (b) Mantle Bouguer Anomaly (MBA); (c) gravitational effect of the lithospheric thermal structure; (d) Residual Mantle Bouguer Anomaly (RMBA). Symbols and lines as in Figure 2.

.

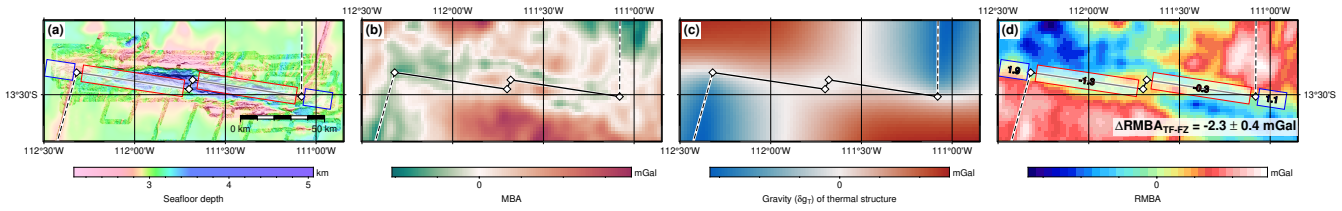

Figure S6. Input data and results of the Garrett transform fault offsetting the East Pacific Rise. (a) Bathymetric map; (b) Mantle Bouguer Anomaly (MBA); (c) gravitational effect of the lithospheric thermal structure; (d) Residual Mantle Bouguer Anomaly (RMBA). Symbols and lines as in Figure 2.

.

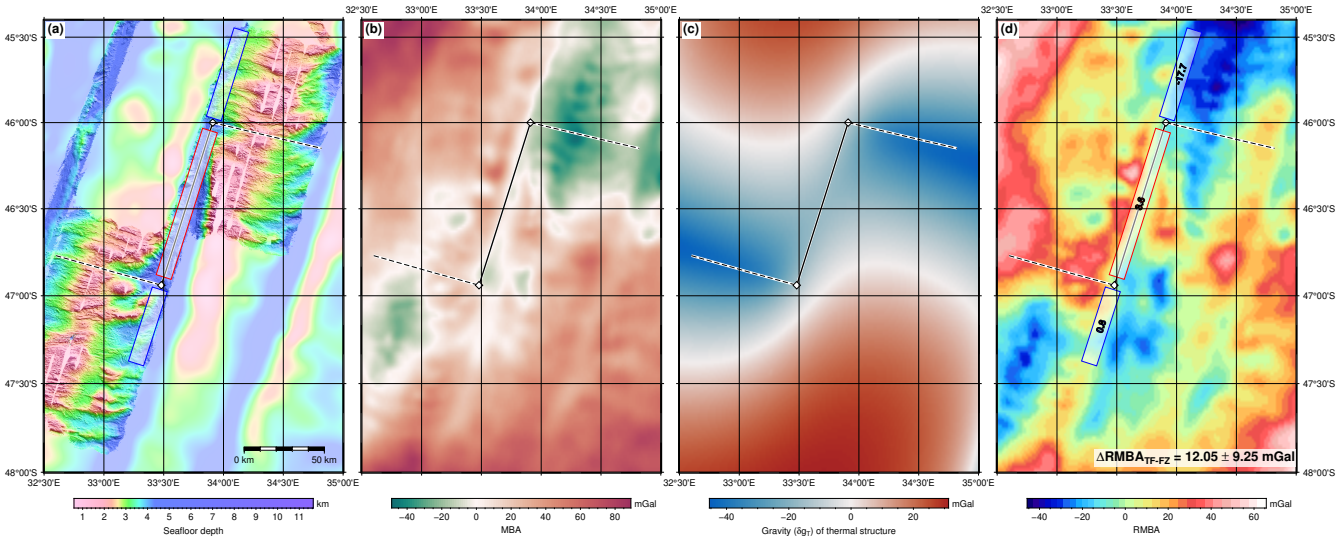

Figure S7. Input data and results of the Marion transform fault offsetting the Southwest Indian Ridge. (a) Bathymetric map; (b) Mantle Bouguer Anomaly (MBA); (c) gravitational effect of the lithospheric thermal structure; (d) Residual Mantle Bouguer Anomaly (RMBA). Symbols and lines as in Figure 2.

.

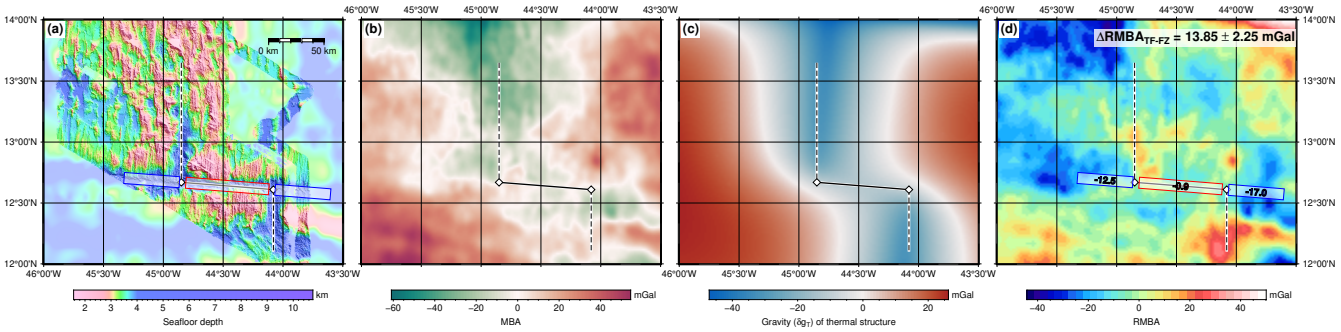

Figure S8. Input data and results of the Marathon transform fault offsetting the Mid-Atlantic Ridge. (a) Bathymetric map; (b) Mantle Bouguer Anomaly (MBA); (c) gravitational effect of the lithospheric thermal structure; (d) Residual Mantle Bouguer Anomaly (RMBA). Symbols and lines as in Figure 2.

.

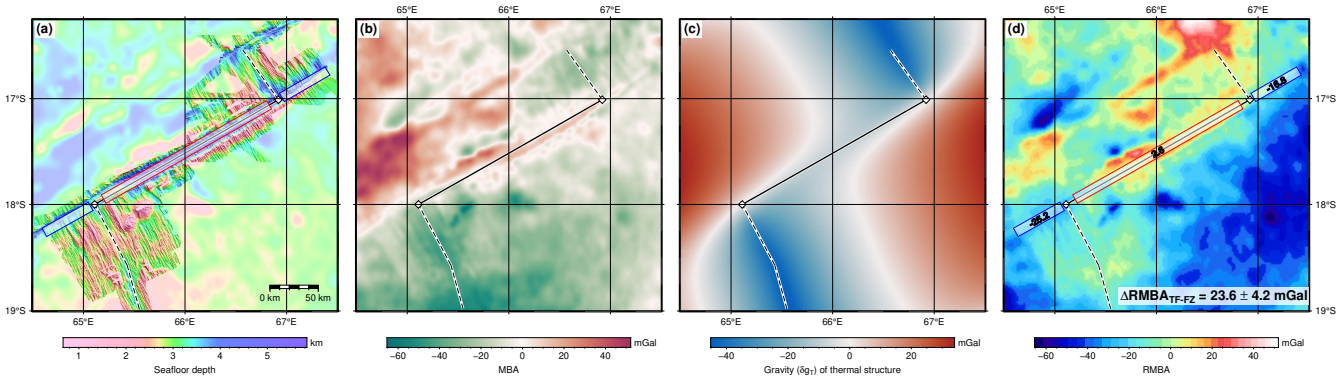

Figure S9. Input data and results of the Marie Celester transform fault offsetting the Central Indian Ridge. (a) Bathymetric map; (b) Mantle Bouguer Anomaly (MBA); (c) gravitational effect of the lithospheric thermal structure; (d) Residual Mantle Bouguer Anomaly (RMBA). Symbols and lines as in Figure 2.

.

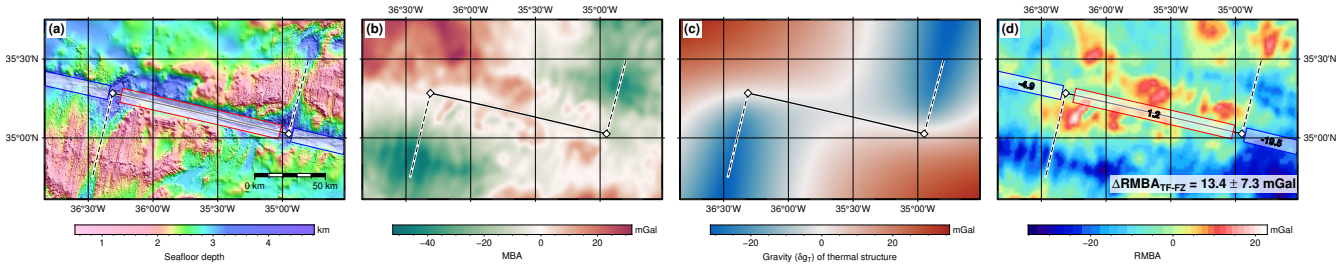

Figure S10. Input data and results of the Oceanographer transform fault offsetting the Mid-Atlantic Ridge. (a) Bathymetric map; (b) Mantle Bouguer Anomaly (MBA); (c) gravitational effect of the lithospheric thermal structure; (d) Residual Mantle Bouguer Anomaly (RMBA). Symbols and lines as in Figure 2.

.

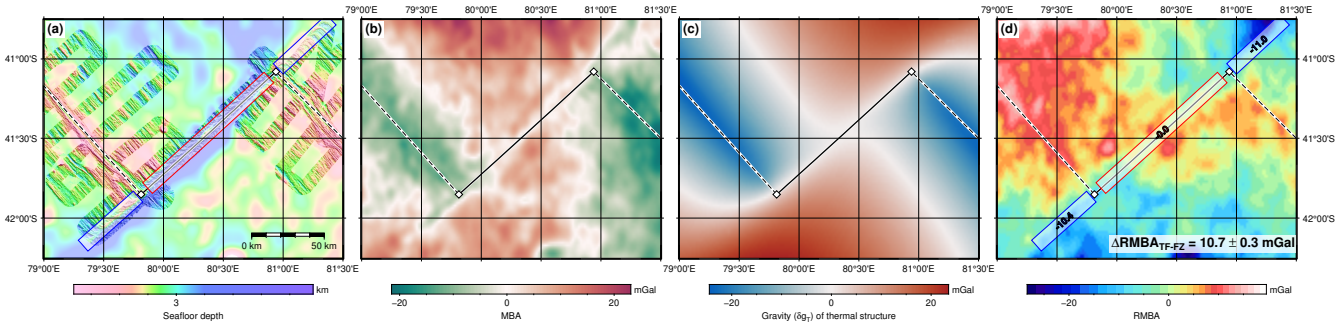

Figure S11. Input data and results of the Vlamingh transform fault offsetting the Southeast Indian Ridge. (a) Bathymetric map; (b) Mantle Bouguer Anomaly (MBA); (c) gravitational effect of the lithospheric thermal structure; (d) Residual Mantle Bouguer Anomaly (RMBA). Symbols and lines as in Figure 2.

.

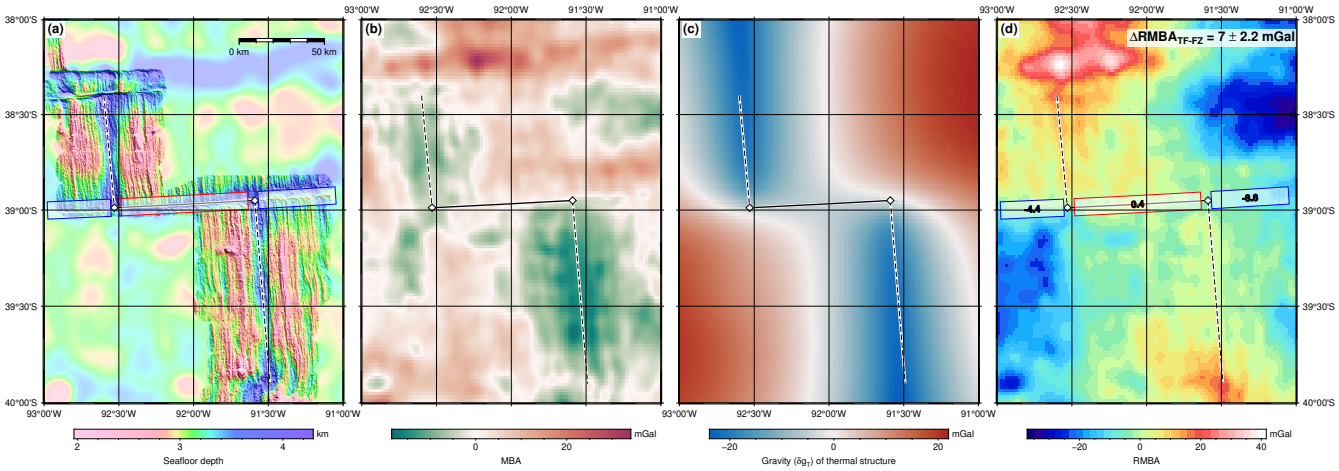

Figure S12. Input data and results of the CR-TF 39°S transform fault offsetting the Chile Ridge. (a) Bathymetric map; (b) Mantle Bouguer Anomaly (MBA); (c) gravitational effect of the lithospheric thermal structure; (d) Residual Mantle Bouguer Anomaly (RMBA). Symbols and lines as in Figure 2.

.

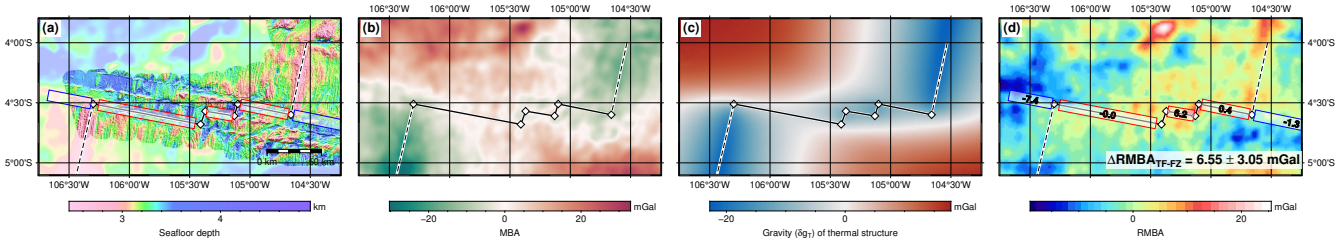

Figure S13. Input data and results of the Gofar transform fault offsetting the East Pacific Rise. (a) Bathymetric map; (b) Mantle Bouguer Anomaly (MBA); (c) gravitational effect of the lithospheric thermal structure; (d) Residual Mantle Bouguer Anomaly (RMBA). Symbols and lines as in Figure 2.

.

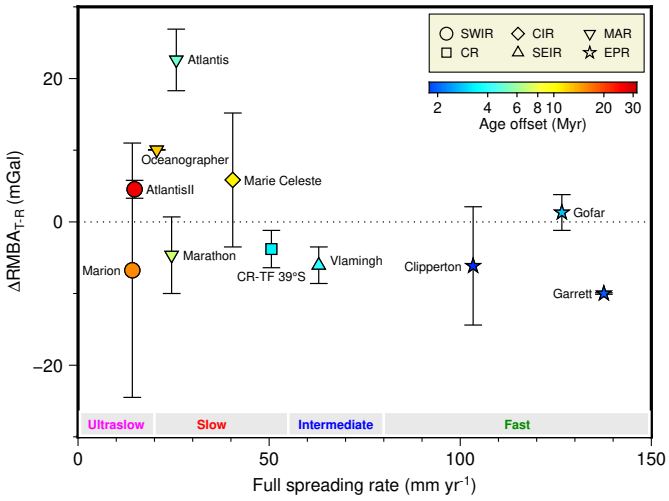

Figure S14. Variation of ΔRMBA$_{T\text{-}R}$ as a function of spreading rate. ΔRMBA$_{T\text{-}R}$—mean difference of RMBA between transform fault and associated ridge segments. Associated spreading ridge of each transform fault is indicated by different symbols. SWIR (circle)—Southwest Indian Ridge; CIR (diamond)—Central Indian Ridge; MAR (inverted triangle)—Mid-Atlantic Ridge; CR-TF 39°S (square)—Transform fault near 39°S offsetting the Chile Ridge; SEIR (triangle)—Southeast Indian Ridge; EPR (star)—East Pacific Rise. The with of average box along ridge segments is 20 km which is consistent with that in Gregg et al. (2007).

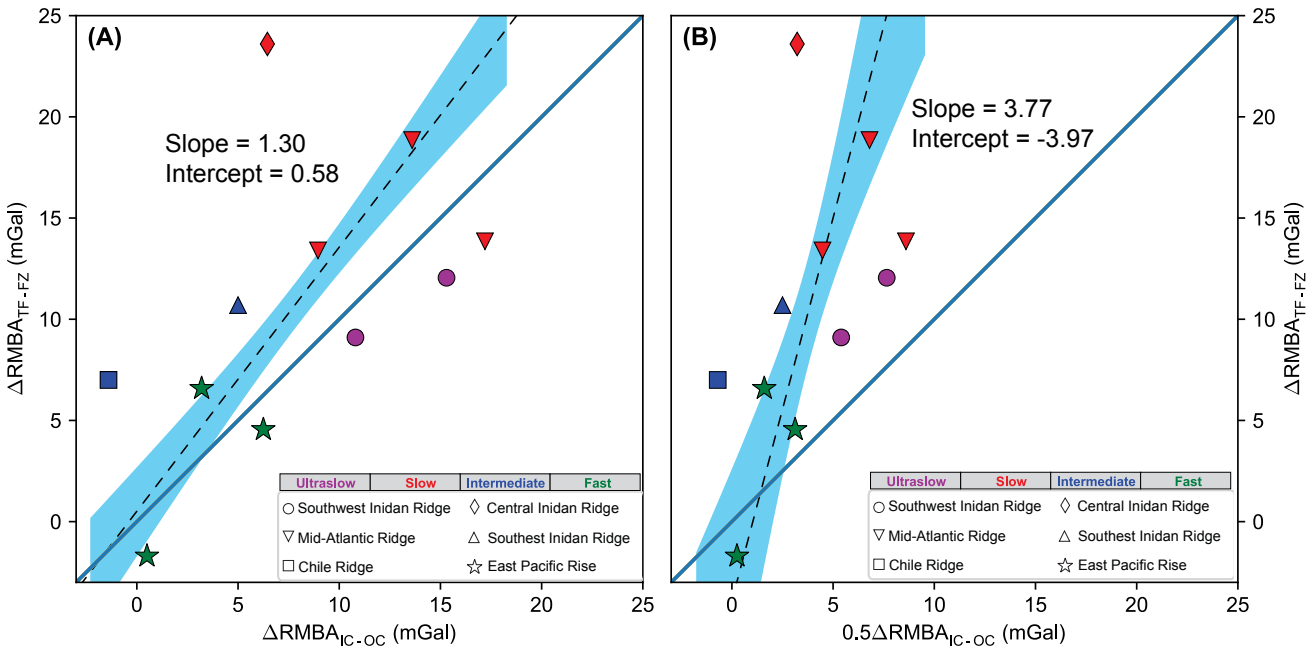

Figure S15. Correlation between $\Delta RMBA_{TF-FZ}$ and $\Delta RMBA_{IC-OC}$. (A) $\Delta RMBA_{TF-FZ}$ versus $\Delta RMBA_{IC-OC}$. (B) $\Delta RMBA_{TF-FZ}$ versus $0.5\Delta RMBA_{IC-OC}$. The blue line indicates equal gravity. Dashed line represents linear regression, and the blue-shaded region denotes the 95% confidence region.

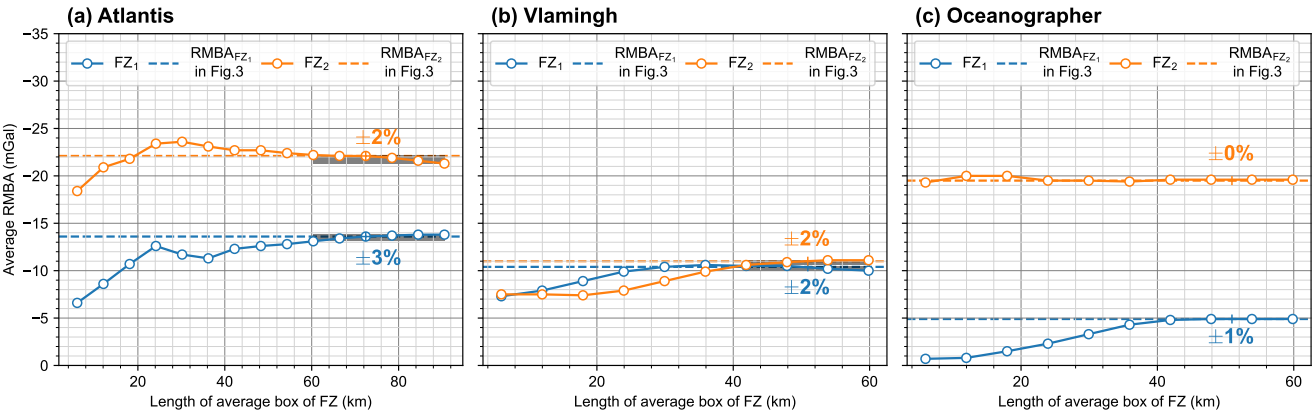

Figure S16. Average RMBA calculation in FZs is started from a small box with length 6 km, then incrementally (interval is 6 km) increase the box length to the maximum length of high-resolution bathymetry coverage. These tests are done for (a) Atlantis, (b) Vlamingh and (c) Oceanographer with significant lateral extents of FZ bathymetry. The solid lines with circle markers represent average RMBA of FZ changes with length of average box. The dashed lines represent the average RMBA value of FZs used in our main result in the main text (e.g. Figure 3)

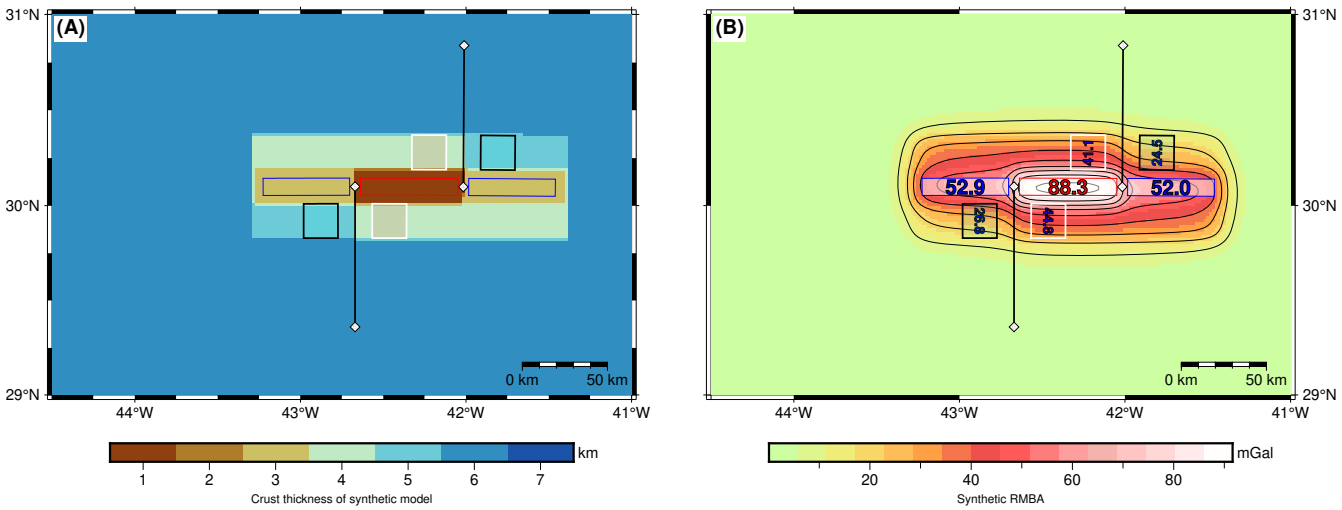

Figure S17. Example of Synthetic model. (A) Synthetic crustal thickness with IC=3 km, OC = 5km, TF = 1 1km, FZ = 3 km, and the normal crust thickness is 6 km. (B) RMBA due to the crustal structure shown in (A). The density of crust and mantle are listed in Table S1. The red box denotes the average region of transform fault. The blue, black and white boxes denote the average region of fracture zones, outside corners and inside corners, respectively. The number in each box in figure (B) shows the average RMBA value. Black lines with diamond marker show the ridges and RTIs.

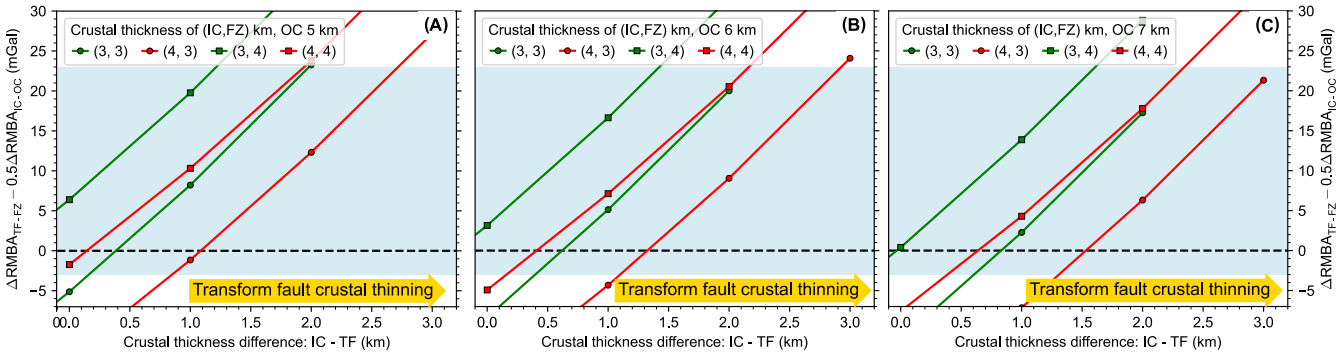

Figure S18. $\Delta RMBA_{TF-FZ} - \Delta RMBA_{IC-OC}$ **of synthetic models with different combinations of crustal thickness of IC, TF, FZ.** (A), (B) and (C) represent synthetic model group with crust thickness of OC 5 km, 6 km and 7 km, respectively. Each data point represent result of a synthetic model (see Figure S17) with specific combination of crustal thickness of IC, FZ, OC (see legend) and FZ. The positive direction of x-axis means transform fault crust thinning relative to inside corner. The light blue area represent $\Delta RMBA_{TF-FZ} - \Delta RMBA_{IC-OC}$ range of observation data (see Figure 3 in the main text).

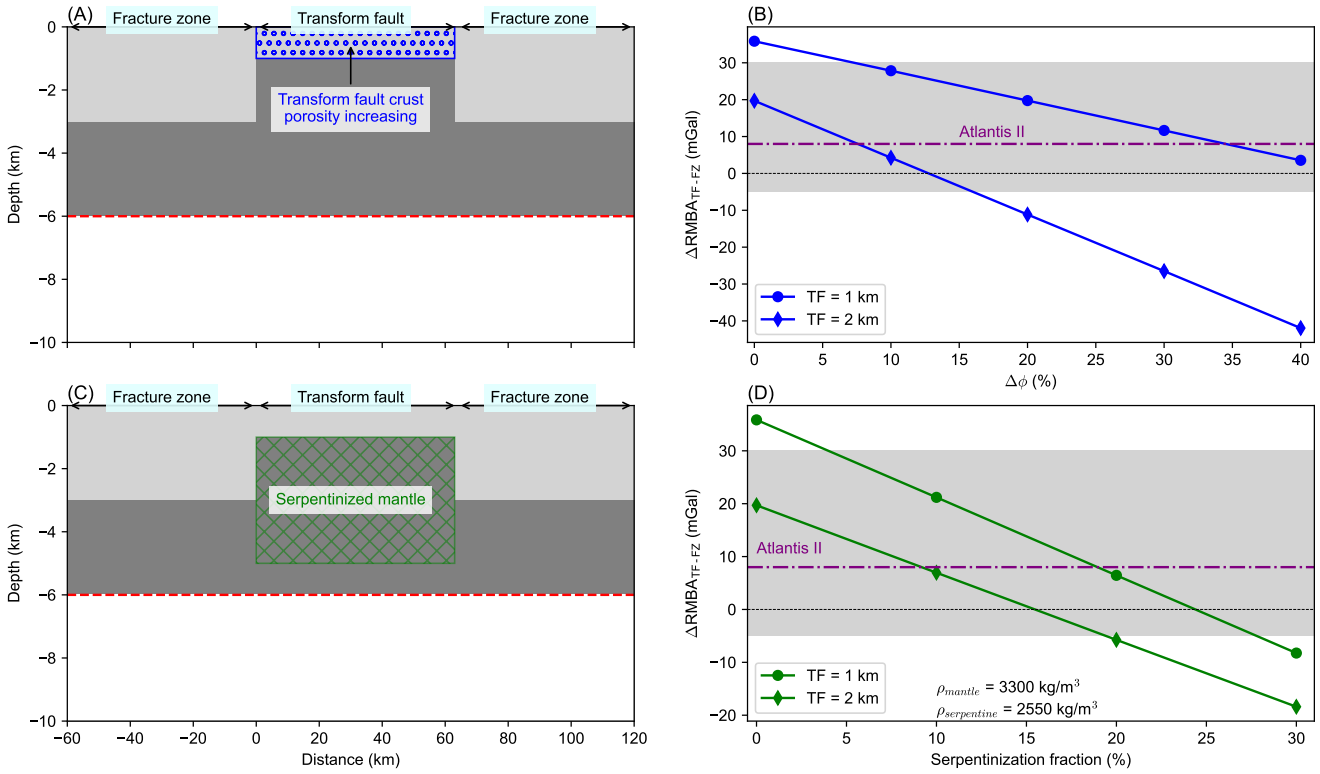

Figure S19. Synthetic model result of the gravity effect of crustal porosity increasing and mantle serpentinization underneath transform fault. (A) shows the geometry of fracture-transform-fracture profile and where is the crustal porosity increasing. (B) $\Delta RMBA_{TF-FZ}$ as a function of porosity increasing in transform fault crust. (C) shows where is the serpentinized mantle. (D) shows $\Delta RMBA_{TF-FZ}$ as a function of serpentinization fraction. Legends in (C) and (D) represent two models with TF crustal thickness 1 km, 2km and 2.5 km, respectively. The map view of the crustal structure of the synthetic model is shown in Figure S17A.

Table S2. Transform fault characteristics used in this study.

Transform fault	Latitude (°N)	Longitude (°E)	Spreading rate (mm yr^{-1})	Age offset (Myr)	$\Delta RMBA_{OTF\text{-}FZ}$ (mGal)	$\Delta RMBA_{IC\text{-}OC}$ (mGal)	Reference
Atlantis	30.05	-42.32	25.7	4.90	18.85	13.60	Figure S3
Atlantis II	-32.78	57.07	14.8	26.45	9.10	10.80	Figure S4
Clipperton	10.22	-103.93	103.4	1.62	4.55	6.25	Figure S5
Garrett	-13.40	-111.50	137.6	1.95	-1.70	0.50	Figure S6
Marion	-46.45	33.72	14.2	15.49	12.05	15.29	Figure S7
Marathon	12.65	-44.50	24.5	6.94	13.85	17.2	Figure S8
Marie Celester	-17.51	66.00	40.5	10.91	23.6	6.45	Figure S9
Oceanographer	35.25	-35.60	20.6	12.33	13.40	8.95	Figure S10
Vlamingh	-41.47	80.36	63	4.03	10.70	5.00	Figure S11
CR-TF 39°S	-38.97	-92.05	50.6	3.24	7.00	-1.40	Figure S12
Gofar	-4.60	-105.85	126.6	2.81	6.58	3.20	Figure S13

SUPPLEMENTARY REFERENCES

Amante, C. and Eakins, B. W.: ETOPO1 arc-minute global relief model: procedures, data sources and analysis, https://doi.org/10.7289/V5C8276M, 2009.

Bangerth, W., Dannberg, J., Gassmoeller, R., and Heister, T.: ASPECT v2.1.0, https://doi.org/10.5281/zenodo.2653531, 2019.

Glerum, A., Thieulot, C., Fraters, M., Blom, C., and Spakman, W., 2018, Nonlinear viscoplasticity in ASPECT: benchmarking and applications to subduction: Solid Earth, 9, 267–294, https://doi.org/10.5194/se-9-267-2018.

Gregg, P. M., Lin, J., Behn, M. D., and Montési, L. G., 2007, Spreading rate dependence of gravity anomalies along oceanic transform faults: Nature, 448, 183–187, https://doi.org/10.1038/nature05962.

Grevemeyer, I., Rüpke, L. H., Morgan, J. P., Iyer, K., and Devey, C. W., 2021, Extensional tectonics and two-stage crustal accretion at oceanic transform faults: Nature, 591, 402–407, https://doi.org/10.1038/s41586-021-03278-9.

Guo, Z.: vtk2grav: A computer program for gravity forward of 3D density distribution in VTK format, https://doi.org/10.5281/zenodo.5831568, URL `https://doi.org/10.5281/zenodo.5831568`, 2022.

Hirth, G. and Kohlstedt, D., 2003, Rheology of the upper mantle and the mantle wedge: A view from the experimentalists: Washington DC American Geophysical Union Geophysical Monograph Series, 138, 83–105, https://doi.org/10.1029/138GM06.

Nagy, D., 1966, The gravitational attraction of a right rectangular prism: Geophysics, 31, 362–371, https://doi.org/10.1190/1.1439779.

CHAPTER 4

MANUSCRIPT #3

Sensitivity of gravity anomalies to mantle rheology at mid-ocean ridge – transform fault systems

Sibiao Liu [(1)], Zhikui Guo [(1,2)], Lars Rüpke [(1)], Jason P. Morgan [(3)], Ingo Grevemeyer [(1)], Yu Ren [(1)], and Chuanzhi Li [(4)]

(1) GEOMAR Helmholtz Centre for Ocean Research Kiel, Kiel, Germany
(2) Second Institute of Oceanography, MNR, Hangzhou, China
(3) Southern University of Science and Technology, Shenzhen, China
(4) Institute for Advanced Ocean Study, Ocean University of China, Qingdao, China

Published in 2023 in *Earth and Planetary Science Letters*, 622, 118420

Earth Planet. Sci. Lett. 622 (2023) 118420

Contents lists available at ScienceDirect

Earth and Planetary Science Letters

journal homepage: www.elsevier.com/locate/epsl

Sensitivity of gravity anomalies to mantle rheology at mid-ocean ridge – transform fault systems

Sibiao Liu [a,*], Zhikui Guo [a,b,*], Lars H. Rüpke [a,*], Jason P. Morgan [c], Ingo Grevemeyer [a], Yu Ren [a], Chuanzhi Li [d]

[a] GEOMAR Helmholtz-Zentrum für Ozeanforschung Kiel, Wischhofstrasse 1-3, Kiel 24148, Germany
[b] Key Laboratory of Submarine Geosciences, MNR, Second Institute of Oceanography, MNR, Hangzhou 310012, China
[c] Southern University of Science and Technology, Xueyuan Avenue 1088, Shenzhen 518055, China
[d] Key Lab of Submarine Geosciences and Prospecting Techniques, Ministry of Education, Institute for Advanced Ocean Study, Ocean University of China, Qingdao 266100, China

ARTICLE INFO

Keywords:
Gravity anomaly
Mantle rheology
Mid-ocean ridge
Oceanic transform fault

ABSTRACT

Marine gravity data can provide information on the distribution of mass anomalies in the oceanic crust and upper mantle. Computing corresponding gravity anomalies, especially so-called 'residual' gravity anomalies that directly reflect variations in the crustal structure, relies on gravity corrections of both seafloor relief and lithospheric thermal structure. The lithospheric thermal gravity correction involves either a plate cooling approximation or a mantle flow model with the latter typically done using simplified assumptions on mantle rheology. However, a detailed study of how differing rheological models affect the computed gravity anomalies is still missing. Here, we systematically examine the differences in residual mantle Bouguer anomalies (RMBA) caused by differing assumptions on mantle rheology for 16 mid-ocean ridge – transform fault systems. Our calculations show that isoviscous models tend to underpredict RMBA values within the transform deformation zone and overpredict them in the far field at older plate ages, when compared to plate cooling and nonlinear viscoplastic models. This discrepancy stems from isoviscous models failing to capture plate-like deformation, as well as their inability to resolve brittle failure and the associated strain localization that leads to warm upwelling beneath the transform fault. By exploring a wide parameter range, we find that the importance of mantle rheology scales with plate tectonic parameters at the mid-ocean ridge – transform fault system such as transform age offset, spreading rate, and transform fault length. These findings suggest that gravity thermal corrections at the intrinsically three-dimensional ridge – transform systems should employ mantle flow models that resolve plate-like deformation and brittle failure.

1. Introduction

The analysis of marine gravity data is one of the classic geophysical methods to infer subsurface density variations from potential field observations and to relate those to seafloor morphology (e.g., Kuo and Forsyth, 1988; Lin et al., 1990; Lin and Morgan, 1992; Escartín and Lin, 1995; Crosby et al., 2006; Gregg et al., 2007; Blackman et al., 2008, 2009; Sandwell et al., 2014). A typical example is the use of gravity measurements to estimate variations in crustal thickness beneath mid-ocean ridges (MOR) and oceanic transform faults (OTF), especially when seismic coverage is sparse (e.g., Prince and Forsyth, 1988; Alvey et al., 2008; Marjanović et al., 2011; Wang et al., 2011).

Marine gravity anomalies have been used to obtain fundamental insights into the crustal architectures of different seafloor tectonic compartments in the mid-ocean ridge – transform fault system including the MOR, inside/outside corner (IC/OC) of the ridge, the OTF, and the adjacent fracture zone (FZ). Escartín and Lin (1995) found that the IC of slow-spreading ridges has a higher residual mantle Bouguer anomaly (RMBA) than the OC, indicating a thinner crust and supporting the model of asymmetric tectonic extension near the ridge – transform intersection (RTI). Gregg et al. (2007) explored differences in the computed RMBA values between the transform deformation zone and the average of the two adjacent ridge segments and reported a spreading-rate dependent difference between the two. At

* Corresponding authors.
E-mail addresses: sliu@geomar.de (S. Liu), guozk@sio.org.cn (Z. Guo), lruepke@geomar.de (L.H. Rüpke).

https://doi.org/10.1016/j.epsl.2023.118420
Received 29 June 2023; Received in revised form 15 September 2023; Accepted 22 September 2023
Available online 2 October 2023

slow-spreading rates, the obtained values are positive pointing to thin crust beneath slow-slipping transform faults. At fast-spreading rates, the obtained values are slightly negative, which could be indicative of thicker crust at segment ends and/or enhanced porosity/fracturing towards segment ends. Guo et al. (2023) used a similar approach to identify a consistent variation in crustal thickness between active transform faults and the adjacent passive fracture zones, suggesting thinner crust beneath the transform deformation zone with respect to fracture zone crust.

A standard processing workflow in the marine domain includes the removal of predictable components from the measured gravity field to create gravity anomalies that can be more easily interpreted in terms of density variations and changes in crustal architecture. These correction steps include the subtraction of a reference value to yield the free-air anomaly and the removal of bathymetric effects to obtain the Bouguer anomaly. At mid-ocean ridges, where gravity variations stem primarily from crustal thickness variations, it is customary to subtract a reference crustal thickness. Since seafloor cooling with age manifests itself as a long wavelength gravity signal, a thermal correction can be done to remove this effect from the Bouguer anomaly or mantle Bouguer anomaly, resulting in the residual Bouguer anomaly (Alvey et al., 2008; Blackman et al., 2008, 2009; Chappell and Kusznir, 2008; Zhang et al., 2020) or RMBA (Prince and Forsyth, 1988; Gregg et al., 2007; Wang et al., 2011; Guo et al., 2023), which is then directly related to crustal thickness variations from the reference value.

A crucial processing step in the aforementioned gravity studies is the thermal correction step, which requires a thermal model in combination with a gravity forward calculation (Prince and Forsyth, 1988; Guo, 2022). At mid-ocean ridge systems, the temperature field can be obtained either from simple analytical solutions such as the half-space or plate cooling models (Stein and Stein, 1992; Turcotte and Schubert, 2014), or by using numerical models that resolve mantle flow and the resulting thermal structure (Morgan and Forsyth, 1988). Geodynamic models that address mid-ocean ridge mantle flow can be complex and are often simplified to make the gravity corrections more tractable (e.g., Kuo and Forsyth, 1988; Escartín and Lin, 1995; Blackman et al., 2008, 2009). A 'classic' model for these corrections at mid-ocean ridge – transform fault systems is one that resolves isoviscous mantle flow passively driven by surface plate motion (Morgan and Forsyth, 1988). It provides the steady-state temperature field resulting from the thermo-mechanical evolution of a stable spreading axis (Morgan and Parmentier, 1987) and accounts for lateral heat conduction across the transform fault and fracture zones.

A shortcoming of isoviscous models is that they cannot resolve feedbacks between plate cooling and tectonic deformation (e.g., Shen and Forsyth, 1992; Kohli et al., 2021). Previous geodynamic studies have established the complex interactions between magmatic accretion, plate cooling, mantle flow, and tectonic faulting at mid-ocean ridge – transform fault systems (e.g., Chen and Morgan, 1990; Furlong et al., 2001; Behn et al., 2007; Gregg et al., 2009; Zhang et al., 2022). For example, Behn et al. (2007) found systematic differences in the predicted mantle flow field and temperature structure beneath OTFs for isoviscous, temperature-dependent viscous, and viscoplastic mantle. A viscoplastic, localizing rheology results in a transform fault plane that is oblique at depth causing extension and mantle upwelling, which results in a warmer thermal structure (Grevemeyer et al., 2021). This rheology-dependent thermal structure has been applied in submarine earthquake investigations, where it has been identified as a key factor controlling the maximum depth of seismicity along OTFs (Roland et al., 2010).

Interestingly, the influence of mantle rheology on the lithospheric temperature field has not fully propagated into processing workflows for marine gravity data and the gravity studies mentioned above all use differing thermal models. The following questions remain therefore unanswered: (1) Which changes would a more complete treatment of mantle rheology cause for the thermal correction in gravity studies? (2) How would these changes be distributed over the different seafloor tectonic compartments of the mid-ocean ridge – transform fault system? (3) What are the relationships between seafloor tectonic characteristics of this system (i.e., spreading rate, transform age offset, and transform offset length) and changes in gravity anomalies induced by the assumptions of different mantle rheologies?

We here address these questions by first calculating the RMBA with differing rheology-dependent thermal corrections for 16 mid-ocean ridge – transform fault systems (Fig. 1). These selected systems cover the full range of spreading rates from ultraslow to fast and are taken from the Mid-Atlantic Ridge, East Pacific Rise, and ridges in the Indian Ocean. Second, we systematically analyze the difference in the RMBA (ΔRMBA) across multiple thermal models and the distribution of these discrepancies, and determine correlations between the rheology-induced ΔRMBA and ridge – transform tectonic characteristics. Lastly, we compare our results with prior gravity studies using half-space cooling and/or the isoviscous flow models.

2. Methods

2.1. Lithospheric thermal correction

To investigate the effects of mantle rheology on the thermal gravity anomaly (g_T), we examine four types of models comprising three passive mantle flow models with progressively more realistic rheology approximations and the half-space plate cooling (HSC) model. The temperature field in the HSC model is calculated using the half-space cooling formula (Turcotte and Schubert, 2014): $T = T_s + (T_m - T_s)(1 - erfc(z/2\sqrt{\kappa x/u_{half}}))$, where T_s and T_m are temperatures of the surface and mantle, respectively, z is the depth from 0 at the seafloor down to 100 km, κ is thermal diffusivity, x is the distance to the ridge axis, and u_{half} is the half-spreading rate.

In the passive mantle flow models, we adopt the approach proposed by Morgan and Forsyth (1988) to simulate the 3D steady-state mantle flow driven passively by seafloor spreading. We use the geodynamic finite element code ASPECT (Advanced Solver for Problems in Earth's ConvecTion; Bangerth et al., 2022) to compute thermal solutions for steady-state flow models using different rheologies including isoviscosity (ISOV), nonlinear strain rate-, temperature-, and pressure-dependent viscosity (NLV), and nonlinear viscosity with frictional plasticity (NLVP).

In geodynamic flow simulations, the following three conservation equations of mass (1), momentum (2), and energy (3) are considered to govern the evolution of thermal structure in the mid-ocean ridge – transform fault system:

$$\nabla \cdot \vec{u} = 0 \tag{1}$$

$$-\nabla \cdot (2\eta\, \dot{\varepsilon}(\vec{u})) + \nabla p = \rho \vec{g} \tag{2}$$

$$\rho C_p \left(\frac{\partial T}{\partial t} + \vec{u} \nabla T \right) = \nabla \cdot k \nabla T \tag{3}$$

with η viscosity, ρ density, $\vec{g}$ the gravity vector. The deviatoric strain rate tensor $\dot{\varepsilon}$ is represented by the symmetric gradient of the velocity $\dot{\varepsilon}(\vec{u}) = \frac{1}{2}(\nabla \vec{u} + \nabla \vec{u}^T)$. Mass and momentum equations represent the incompressible Stokes equations with the velocity field $\vec{u} = \vec{u}(\vec{x}, t)$, and the pressure field $p = p(\vec{x}, t)$, where $\vec{x}$ and t denote space and time, respectively. The energy equation for the temperature field $T = T(\vec{x}, t)$ is coupled to the above Stokes equations and describes heat conduction and advection with the flow velocity. C_p is the specific heat capacity, k is the thermal conductivity.

Mantle material assumes a viscous rheology that follows a wet olivine flow law (Hirth and Kohlstedt, 2003). In the viscous regime, we use the dislocation creep mechanism to calculate the viscosity:

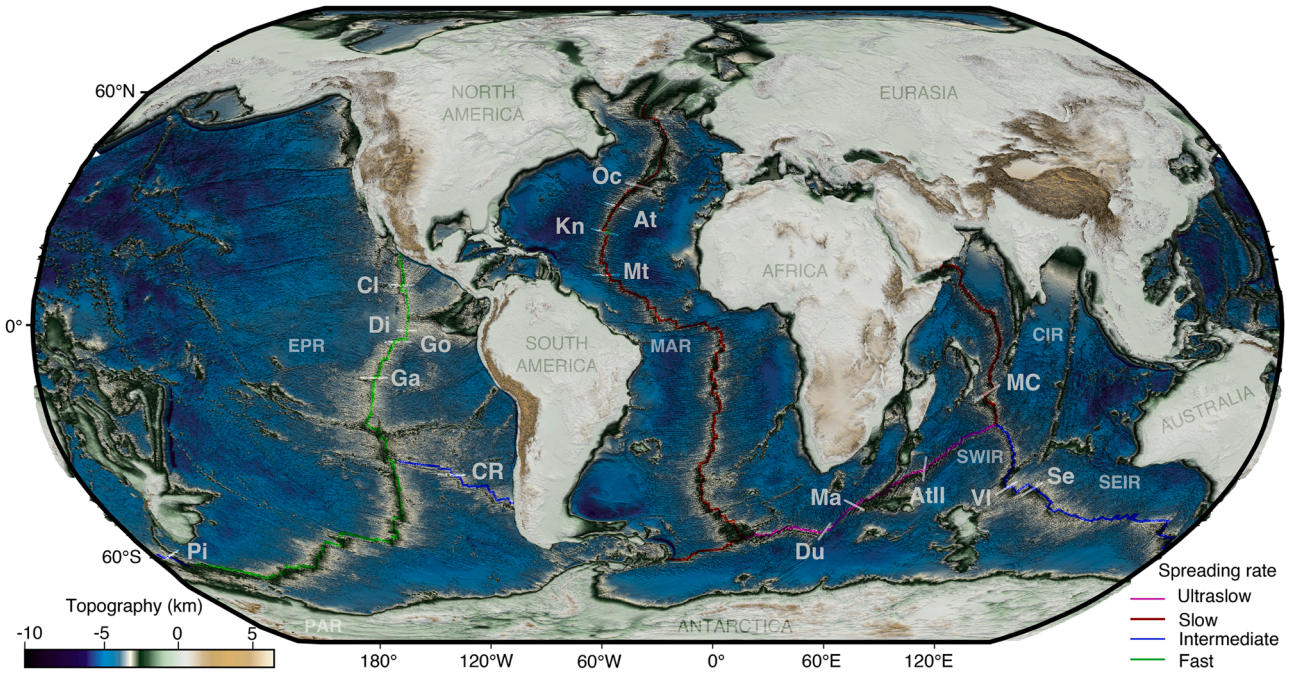

Fig. 1. Global topography map displaying the locations of 16 mid-ocean ridge – transform fault systems examined in this study. They are labeled as Atlantis II (AtII), Du Toit (Du), and Marion (Ma) on the ultraslow-spreading Southwest Indian Ridge (SWIR); Atlantis (At), Kane (Kn), Marathon (Mt), and Oceanographer (Oc) on the slow-spreading Mid-Atlantic Ridge (MAR); Marie Celeste (MC) on the slow-spreading Central Indian Ridge (CIR); Pitman (Pi) on the intermediate-spreading Pacific Antarctic Ridge (PAR); SEIR at 88°E (Se) and Vlamingh (Vl) on the intermediate-spreading Southeast Indian Ridge (SEIR); Transform offsetting at 39 °S on the intermediate-spreading Chile Ridge (CR); Clipperton (Cl), Discovery (Di), Garret (Ga), and Gofar (Go) on the fast-spreading East Pacific Rise (EPR). Bathymetric data used in this study are derived from a combination of recently compiled high-resolution multibeam data (Grevemeyer et al., 2021; Ren et al., 2022) and the ETOPO1 dataset (NOAA, 2009).

$$\eta = \frac{1}{2B^{1/n}\dot{\varepsilon}_{II}^{\frac{(1-n)}{n}}} exp\left(\frac{E+PV}{nRT}\right) \tag{4}$$

where $\dot{\varepsilon}_{II}^2 = \frac{1}{2}\dot{\varepsilon}(\vec{u})\dot{\varepsilon}(\vec{u})$ is the second invariant of the deviatoric strain rate tensor $\dot{\varepsilon}$, R is the gas constant, B, n, E, V are the laboratory viscosity parameters. The plastic rheology is used to characterize brittle weakening of the oceanic lithosphere and uses the Drucker – Prager yield criterion in ASPECT (Glerum et al., 2018), which parametrizes the yield stress σ_{yield} as a function of the cohesion c_0, friction angle φ, and pressure p in 3D:

$$\sigma_{yield} = \frac{6c_0 cos\varphi}{\sqrt{3}(3-sin\varphi)} + \frac{6sin\varphi}{\sqrt{3}(3-sin\varphi)}p \tag{5}$$

The thermo-mechanical and rheological properties used in this study are provided in Table 1. Note that we do not discuss models that include elasticity. Test simulations accounting for visco-elasto-plastic deformation yielded a temperature field almost identical to those of the visco-plastic model (Figure S1), likely as a consequence of the prescribed plate motion without a free surface. The models are incompressible and therefore do not resolve thermal contraction and also do not account for viscous dissipation.

All thermal models are data-oriented, in that the geometries of the 16 mid-ocean ridge – transform fault systems are extracted from bathymetric observations and their spreading rates inferred from plate motion (Table 2). Therefore, the horizontal length and lateral extent are

Table 1
Parameters used in thermal models and gravity anomaly calculations.

Gravity anomaly calculations	
Sea water density, kg m^{-3}	1030
Reference crustal density, kg m^{-3}	2700
Reference crustal thickness, km	6
Reference mantle density, kg m^{-3}	3300
Asthenospheric temperature, °C	1300
Material properties in thermal models	
Thermal conductivity - k, W K^{-1} m^{-1}	3
Thermal expansion - α, K^{-1}	3.5×10^{-5}
Specific heat capacity - C_p, J kg^{-1} K^{-1}	1250
Frictional angle - φ, °	30
Cohesions - c_0, MPa	10
Dislocation creep pre-exponential factor - B, Pa^{-n} s^{-1}	3.77×10^{-14}
Dislocation creep activation energy - E, kJ mol^{-1}	520
Dislocation creep activation volume - V, cm^3 mol^{-1}	22
Power law exponent, n	3.5

Table 2
Seafloor tectonic characteristics of 16 mid-ocean ridge – transform fault systems.

Ridge system	Transform fault	Spreading rate, mm yr^{-1}	Offset length, km	Age offset, Myr	Reference
EPR	Clipperton	103.4	84	1.6	Figure S6a
	Discovery*	125.4	68	1.1	Figure S6b
	Garret*	137.6	134	2.0	Figure S6c
	Gofar (south)*	126.6	178	2.8	Figure S6d
CR	Chile Ridge 39°S	52	81	3.1	Figure S7
PAR	Pitman	55.2	66	2.4	Figure S8
SEIR	SEIR88	65.4	68	2.1	Figure S9a
	Vlamingh	63	127	4.0	Figure S9b
CIR	Marie Celeste	40.5	215	10.6	Figure S10
MAR	Atlantis	24	63	5.3	Figure S11a
	Kane (east)	23.8	150	12.6	Figure S11b
	Marathon	24.5	84	6.9	Figure S11c
	Oceanographer	25.8	127	9.8	Figure S11d
SWIR	Atlantis II	14.8	196	26.5	Figure S12a
	Du Toit	15.9	133	16.7	Figure S12b
	Marion	16.5	110	13.3	Figure S12c

* The transform offset length is the sum of the lengths of transform segments in the Discovery, Garret, and Gofar transforms.

different in each ridge – transform case (Fig. 2). We extend each model domain by 100 km in all lateral directions to make boundary effects small. For example, in the slow-spreading Marie Celeste case, the observed OTF and MOR lengths are roughly 215 km and 120 km, respectively. Accordingly, we configure lengths of the simulated OTF-FZ zone (including the OTF and two FZs) and the MOR (including two ridge segments) to be 600 km and 250 km, respectively. This results in a model domain of 800 km by 450 km after adding 100 km extension to all lateral boundaries. The depth of all thermal models is set at 100 km. The resolution is 2.5 km per element at 0–30 km depth and 10 km per element below.

Mantle flow is driven passively by imposing horizontal plate spreading velocities on the top boundary. For example, as the observed spreading velocity for the Clipperton case is 103.4 mm yr^{-1}, the half-spreading rate on the surface in its thermal model is set to 51.7 mm yr^{-1}. All lateral boundaries and the bottom boundary are open so that materials can freely flow in and out of the model domain to maintain mass balance. The initial temperature is set to 0 °C at the surface and 1300 °C at the bottom (Fig. 2). The thermal gradient at lateral boundaries is zero.

After extracting the temperature field from the thermal model, we use the thermal expansion equation $\Delta\rho = \alpha\rho_{ref}(T_{ref} - T)$ to convert it into a density anomaly field, where α and ρ_{ref} are the thermal expansion coefficient and the reference mantle density at reference temperature $T_{ref} = 1300\,^{\circ}C$. We then compute the thermal gravity correction by converting this field to the g_T field using a gravity forward model (Guo, 2022). More details about the forward calculation can be found in the supplementary materials of Guo et al. (2023).

2.2. Estimation of the residual mantle Bouguer anomaly

We calculate the RMBA in compliance with the classical processing methodology from Prince and Forsyth (1988):

$$RMBA = g_{faa} - g_{wc} - g_{cm} - g_T \tag{6}$$

g_{faa} is the free-air anomaly extracted from global satellite-derived gravity data (Sandwell et al., 2014). g_{wc} and g_{cm} are gravity anomalies from the water – crust and crust – mantle interfaces. g_T is the thermal gravity correction for plate cooling. Note that sediments are not considered here but should be included when computing gravity anomalies for specific ridge – transform fault systems affected by sedimentation such as the Blanco transform fault on the Juan de Fuca Ridge.

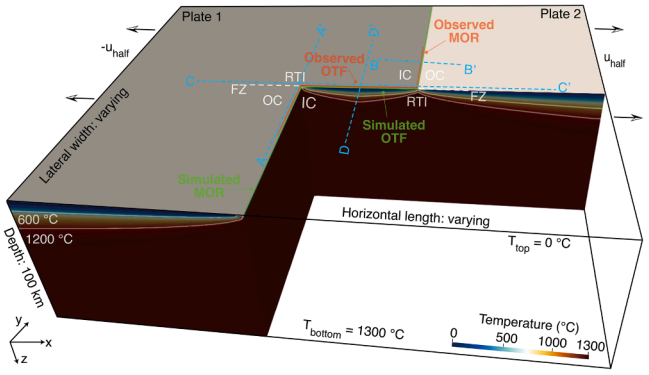

Fig. 2. Thermal model configuration. The simulated OTF length in the model is the same as observed length. The simulated MOR length in the model is 100 km longer than observed length. The model domain (horizontal length and lateral width) is different in each mid-ocean ridge – transform fault system but the vertical depth is fixed at 100 km deep. u_{half}: the half-spreading rate. Ridge – transform tectonic compartments include MOR: mid-ocean ridge, OTF: oceanic transform fault, FZ: fracture zone, RTI: ridge – transform intersection, IC/OC: inside/outside corner of the MOR axis. Dashed blue lines show the locations of transects used in Fig. 4.

Fig. 3 illustrates these processing steps and the magnitude and shape of the three correction terms. The two Bouguer correctionsg_{wc} and g_{cm} are computed from high-resolution multibeam bathymetry data (Fig. 3a) augmented by ETOPO1 data (NOAA, 2009) to fill holes in the multibeam coverage using Parker's method (Parker, 1973) as implemented in GMT's *gravfft* command. We adopt the convention that g_{wc} and g_{cm} exclude the Bouguer slab and only include variations around the mean water and Moho depths, respectively (Figs. 3d-e). Subtracting these two corrections from the free-air anomaly (Fig. 3b) provides the mantle Bouguer anomaly. Removal of the lithospheric thermal contribution g_T (Fig. 3f) from the mantle Bouguer anomaly then yields the RMBA (Fig. 3c). To stay consistent with the aforementioned Bouguer corrections, we shift g_T (Fig. 3f) and the RMBA by a constant amount equivalent to their respective average values. These mean values can be thought of as a zero-level when assessing the relative magnitudes of the anomalies (e.g., Kuo and Forsyth, 1988; Lin et al., 1990; Gregg et al., 2007; Guo et al., 2023).

Figs. 3d-f illustrate the different shapes and magnitudes of the three corrections. The Bouguer correction for variations in water depth dominates in terms of magnitude and contained wavelengths in the pattern (Fig. 3d). The Bouguer correction for variations around a reference crustal thickness (Fig. 3e) is damped and much smaller in magnitude as it is evaluated around the reference Moho level (here 6 km). The thermal correction, here computed from a viscoplastic mantle flow model, treats the long wavelength behavior of plate cooling (Fig. 3f).

Regarding the RMBA calculations for each tectonic compartment (Fig. 3c), we follow the same data approaches as Gregg et al. (2007) for the MOR, Escartín and Lin (1995) for the IC and OC, and Guo et al. (2023) for the OTF and adjacent FZ. Specifically, the RMBA is calculated by averaging the values over a 10-km-wide rectangular box in the OTFs and FZs, a 20-km-wide box in the MOR and adjacent IC/OC regions (i.e., different color boxes in Figs. 3c and S2). The length of the box is varied to ensure that it covers approximately 90% of each tectonic compartment. We use separated boxes for each transform segment when the OTF is internally split as in some fast-spreading cases such as the Discovery transform (Figure S2). The final RMBA value for each compartment is the result of averaging the values of the corresponding two boxes. For example, $RMBA_{MOR} = 0.5 * (\widetilde{RMBA_{MOR1}} + \widetilde{RMBA_{MOR2}})$, where $\widetilde{RMBA_{MOR1}}$ and $\widetilde{RMBA_{MOR2}}$ are the average RMBAs of the MOR1 and MOR2, respectively. Tectonic characteristics of the 16 mid-ocean ridge – transform fault systems are provided in Table 2.

3. Results and discussion

3.1. Effects of mantle rheology on the ridge – transform thermal structure

Mantle rheology controls the steady-state temperature field of the mid-ocean ridge – transform fault system by affecting mantle flow dynamics beneath the oceanic lithosphere. Taking the fast-slipping Clipperton transform fault system on the fast-spreading East Pacific Rise and the Atlantis transform fault system on the slow-spreading Mid-Atlantic ridge as examples, Fig. 4 compares the temperature structures computed with different rheological models along four transects (Fig. 2). We plotted 600 °C and 1200 °C isotherms, which represent approximately the depth of brittle-ductile transition and solidus depth, respectively (Behn et al., 2007). Figure S4 in the supplementary materials shows depth maps of both isotherms in the Clipperton example.

In the A-A' transect (Figs. 4a, e), with respect to the half-space cooling model, all three passive flow models predict a colder mantle under the ridge axis due to vertical heat conduction and a smooth temperature transition into the older plate across the RTI due to the lateral heat conduction. The across ridge-axis profile away from the RTI

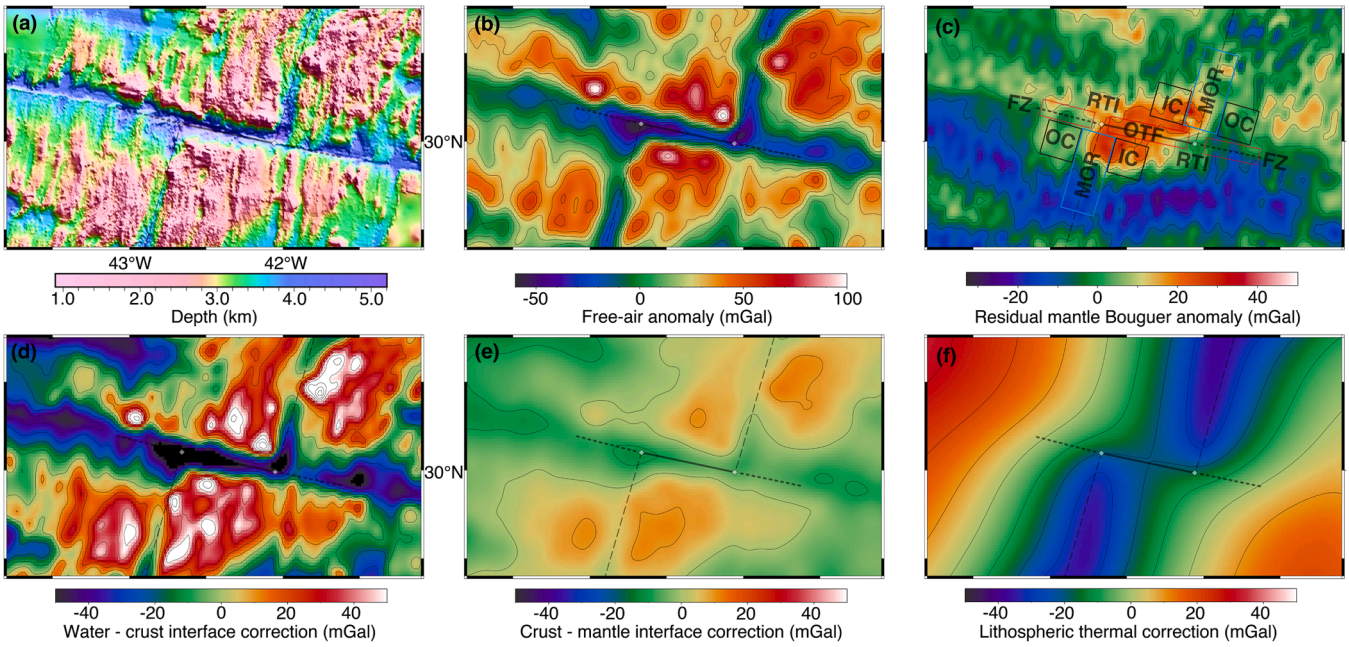

Fig. 3. Gravity anomaly calculation workflow using the Atlantis transform system on the Mid-Atlantic Ridge as an example. (a-c) maps of the bathymetry, the free-air anomaly, and the residual mantle Bouguer anomaly (RMBA), respectively. (d-f) gravity anomaly maps of the water – crust interface, crust – mantle interface, and lithospheric thermal corrections, respectively. Zero levels in the RMBA and the three correction maps are arbitrary when evaluating the relative magnitudes of the anomalies. All gravity anomaly maps are contoured at 10-mGal intervals.

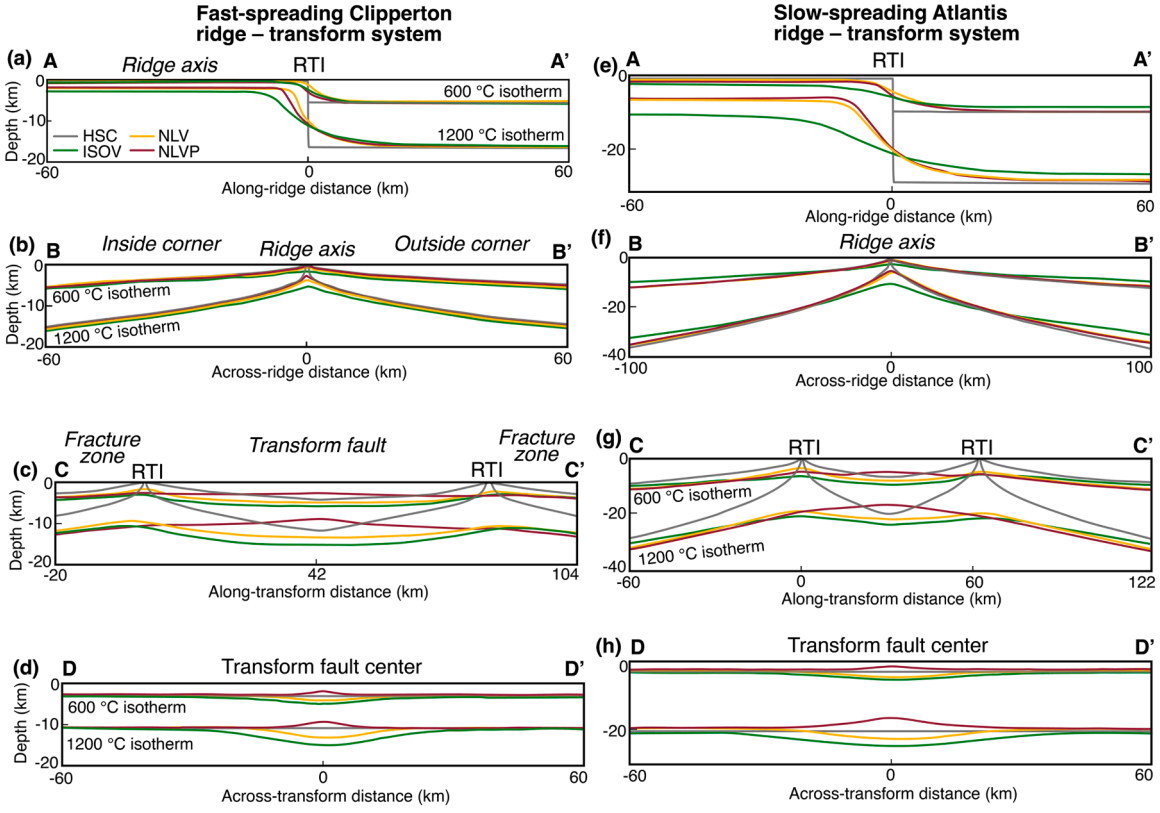

Fig. 4. Thermal structures along four transects containing various tectonic compartments of the Clipperton and Atlantis mid-ocean ridge – transform fault systems. Locations of the transects are shown in Fig. 2. HSC: half-space cooling model, ISOV: isoviscous model, NLV: nonlinear viscous model, NLVP: nonlinear viscoplastic model. RTI: ridge – transform intersection.

(B-B' transect) illustrates that the thermal structures predicted by the passive flow solutions tend towards the half-space cooling solution as the plate ages (Figs. 4b, f). An exception is the isoviscous flow solution. Beneath the ridge axis, it represents the coldest model, due to the lowest (not localized) upwelling velocities. In the far field, at higher plate ages (Fig. 4f), the ISOV solution is warmer than the other passive flow

solutions and the half-space cooling case. This is a consequence of different mantle flow fields with the HSC, NVL, NLVP models all predicting/assuming plate-like behavior, while the ISOV model follows the classic corner flow solution, where the vertical flow extends further off-axis causing a delay in plate cooling. This effect is more noticeable at the older plate ages at ultraslow- and slow-spreading systems (Fig. 4f).

The C-C' transect along the transform fault – fracture zones (Figs. 4c, g) shows that the mantle flow models predict temperatures that are generally between the temperatures predicted by the half-space cooling model for older and younger plate, respectively. An exception is the central part of the transform fault, where the viscoplastic model (NLVP) predicts elevated temperatures. This is also illustrated by the transform-perpendicular profile D-D' (Figs. 4d, h), which shows anomalously high temperature for the NLVP case and low temperatures for the other flow models.

Our modelled thermal structures agree with the findings of earlier ridge – transform thermal models. In particular, the passive flow models accounting for lateral heat exchange result in a colder mantle beneath the transform fault relative to the half-space cooling model (Morgan and Forsyth, 1988). If the assumed mantle rheology changes from isoviscous to nonlinear viscous, upwelling beneath the ridge axis becomes more localized and its temperature increases; also, the sub-transform fault becomes warmer (Shen and Forsyth, 1992; Furlong et al., 2001). This upwelling is further enhanced if brittle failure is considered. In that case, oblique brittle failure, in response to the contrasting plate strengths across the transform fault, results in extensional deformation and thereby mantle upwelling that causes a warmer thermal structure (Figures S3–4; Behn et al., 2007; Grevemeyer et al., 2021).

3.2. Effects of rheology-dependent thermal structure on the RMBA

Here we investigate how much the RMBA differs as a function of the assumed mantle rheology and where these changes are most concentrated using a set of 16 mid-ocean ridge – transform fault systems. We shift g_T in the passive flow models by the mean value of thermal gravity anomalies in the half-space cooling model. This enhances the comparability of gravity anomalies resulting from diverse thermal corrections. We first present the estimated gravity anomaly difference due to different thermal solutions by using the fast-spreading Clipperton transform as an example (Fig. 5) and then analyze how these differences are affected by varying spreading rate (Fig. 6). Model results for all studied mid-ocean ridge – transform fault cases can be found in Figures S6–12.

Fig. 5 illustrates how the RMBA changes as a function of mantle rheology as a correlation plot for the Clipperton transform on the East Pacific Rise; a corresponding figure for the slow-slipping Atlantis transform can be found in Figure S5. Figs. 5a-c, the left-hand panel, shows how the mantle flow models predict colder sub-axial temperatures resulting in a negative ΔRMBA with respect to the HSC model. The sub-transform temperatures are lower than the HSC as well resulting in a negative ΔRMBA in the transform deformation zone. An exception is the NLVP case, which is hotter than the HSC case in the transform center making ΔRMBA positive (Fig. 5c). Figs. 5d-e, middle panel, compares the ISOV solution with the more complex flow solutions. Due to the colder thermal structure in the ISOV case (Figs. 4a-d), the ΔRMBA is positive throughout the mid-ocean ridge – transform fault system when compared to the NLV and NLVP cases. The negative ΔRMBA values in the far field are due to the aforementioned slightly warmer ISOV solution at older plate ages. Interestingly, a comparison between the NLV

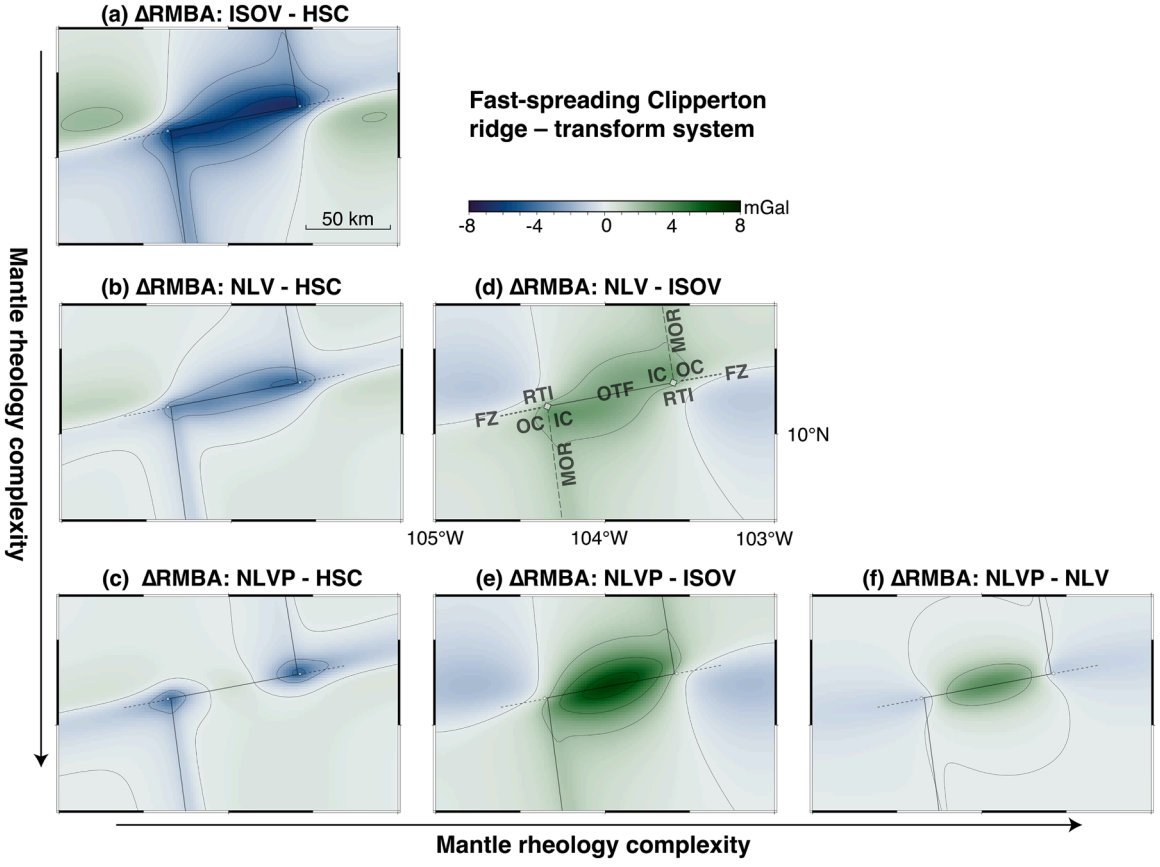

Fig. 5. ΔRMBA between different rheological models for the Clipperton transform system on the fast-spreading East Pacific Ridge. (a-c) ΔRMBA between passive flow models (ISOV isoviscous, NLV nonlinear viscous, and NLVP nonlinear viscoplastic) and the half-space cooling (HSC) model, respectively. (d-f) ΔRMBA between various passive flow models. All gravity anomaly maps are contoured at 2-mGal intervals.

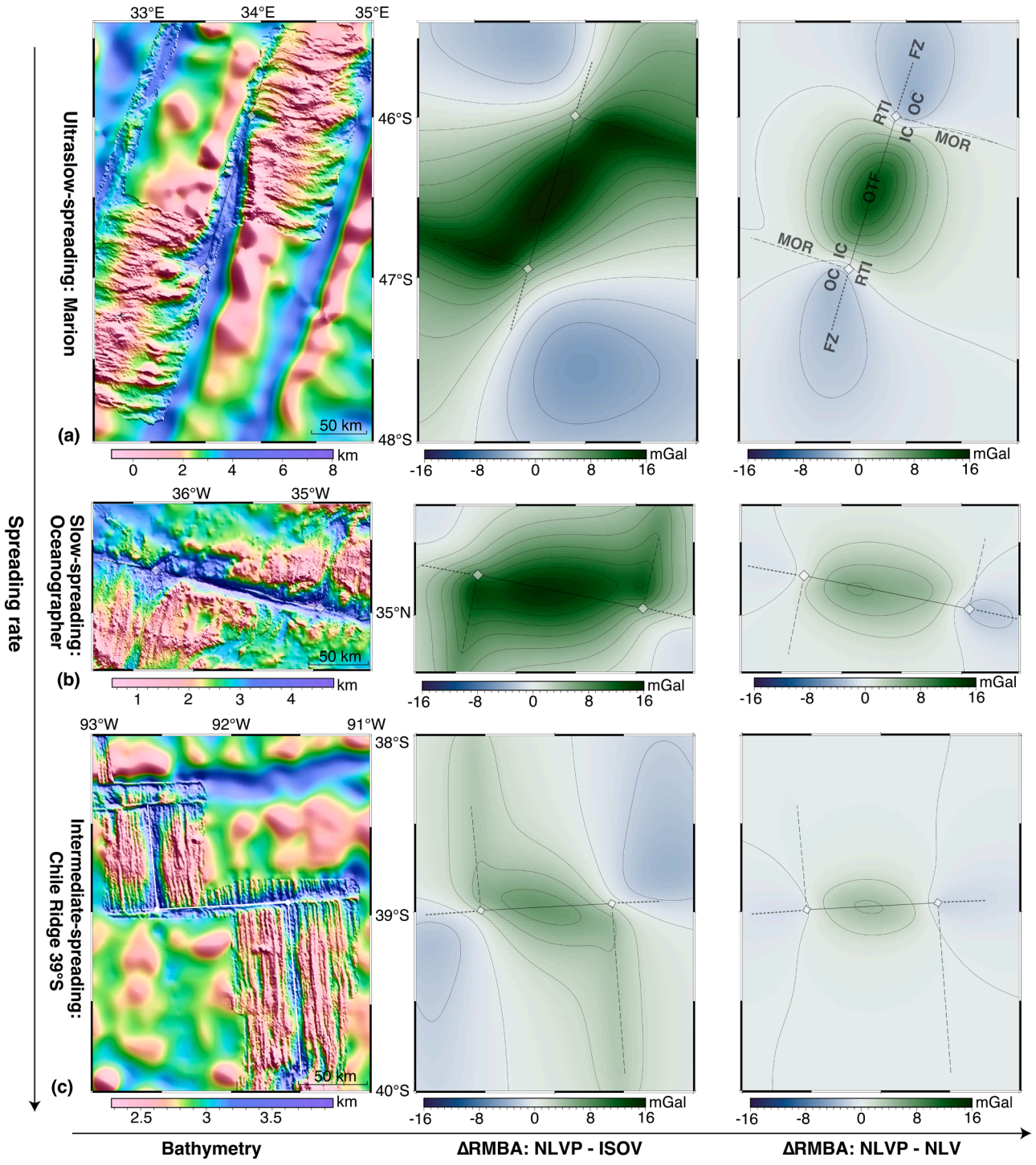

Fig. 6. Bathymetry and ΔRMBA maps for other spreading mid-ocean ridge – transform fault systems, including (a) the ultraslow-spreading Marion case, (b) the slow-spreading Oceanographer case, and (c) the intermediate-spreading Chile Rise at 39°S case. All gravity anomaly maps are contoured at 2-mGal intervals.

and NLVP solutions shows that the ΔRMBA is positive in the transform deformation zone as a consequence of mantle upwelling in response to oblique brittle failure (Fig. 5f).

Fig. 6 summarizes the RMBA differences among the ISOV, NLV, and NVLP solutions as a function of spreading rate by using the three ridge – transform examples Marion, Oceanographer, and Chile Ridge at 39 °S. These systems have increasing spreading rates and decreasing age offsets of approximately 13 Myr, 10 Myr, and 3 Myr (Table 2). Similar to the fast-slipping Clipperton case, the positive ΔRMBA is distributed throughout the ridge – transform system when subtracting the ISOV from the NLVP and its magnitude tends to increase as plate separation slows. Striking is the oblique sub-transform large positive values of the ΔRMBA, which can reach ~28 mGal in the Atlantis II transform (Figure S12a). These oblique positive anomalies are a consequence of the warm mantle upwelling and generally scale with age offset (Grevemeyer et al., 2021). Noticeable are also the gravity anomaly differences in the far field resulting from the differing cooling trends between the NLVP (plate-like) and ISOV (corner flow) models.

The gravity anomaly differences between the NLV and NLVP solutions are less pronounced. The predicted warm mantle upwelling in the

NLVP still results in a positive ΔRMBA when subtracting the NLV from the NLVP, but its value is approximately half of the ΔRMBA value between the NLVP and the ISOV solutions. The oblique plate separation axis in the NLVP case (Grevemeyer et al., 2021) also makes the NLVP solution slightly colder than the NLV solution in the fracture zone region causing a negative ΔRMBA.

3.3. Correlations between ridge – transform tectonic characteristics and rheology-induced changes in the RMBA

Gravity has often been used to identify differences between the various tectonic compartments of ridge-transform systems. For example, Escartín and Lin (1995) compared inside and outside corners of the ridge axis, Gregg et al. (2007) and Guo et al. (2023) quantified differences between transform faults and adjacent ridge segments and between transform faults and fracture zones, respectively. It is therefore of practical relevance to constrain how assumptions about mantle rheology in the thermal correction affect predicted gravity of the different compartments of ridge-transform systems (Fig. 2). Given the extensive range of tectonic parameters (including spreading rates, transform age offsets, and transform fault lengths), we focus here on gravity differences linked to age offset, which is a dominant parameter for transform morphology (Grevemeyer et al., 2021; Guo et al., 2023; Ren et al., 2022).

We follow the same approach as above and compute the four thermal corrections (HSC, ISOV, NLV, NLVP) for the 16 ridge – transform systems listed in Table 2. The predicted differences in ΔRMBA are then analyzed as a function of spreading rate and age offset. This analysis reveals systematic correlations and we define a strong correlation when the value of the coefficient of determination (R^2) is greater than 0.8, a moderate correlation when R^2 is between 0.5 and 0.8, a weak correlation when R^2 is between 0.2 and 0.5, and no correlation when R^2 is smaller than 0.2.

Fig. 7 summarizes the results. The first row shows the differences in ΔRMBA for the ISOV and HSC thermal corrections for major tectonic compartments. As the isoviscous mantle flow solution results in a cooler mantle beneath the mid-ocean ridge (Fig. 4), the RMBA from the ISOV solution is lower than from the HSC solution and their RMBA difference intermediately correlates with spreading rate (Fig. 7a). Similarly, ΔRMBA between these two solutions decreases with increasing age offset for all other tectonic compartments (Figs. 7b-e). There are strong correlations in the IC and OC regions (up to ~21 mGal reduction near ridge areas) whereas the correlations are intermediate and weak in the OTF and adjacent FZ, respectively (up to ~15 mGal reduction).

The second row of Fig. 7 shows the results for NLVP – ISOV, where the rheological approximation becomes more complicated in passive flow models. The MOR results still follow the same systematic as described in Fig. 4 for the thermal structure. NLVP solution is always warmer than the ISOV solution, especially at slow spreading rates. The ΔRMBA between NLVP and ISOV is therefore always positive and we find a strong correlation of ΔRMBA with spreading rate (Fig. 7f). The IC and OC regions are analyzed as a function of age offset. As discussed above, if plastic failure is accounted for (NLVP), transform faulting includes an extensional component that scales with age offset and which causes mantle upwelling. As a consequence, the NLVP solution is always significantly warmer than the ISOV solution in the IC region and the reported values are all positive with a strong correlation with age offset (Fig. 7g). The results of OC are also affected by this process but the absolute values are lower and there is only an intermediate correlation (Fig. 7h). The results for the transform region itself (OTF) also show the effect of warm mantle upwelling as a function of age offset. All values are positive and there is a strong correlation with age offset (Fig. 7i). The gravity signal above the FZ are not heavily affected by the resolved deformation mechanisms within the transform fault region and there is only a weak correlation with age offset (Fig. 7j).

3.4. Comparison with previous gravity studies

In the light of the presented systematics, we have reviewed how differing thermal corrections would impact on previously reported differences between tectonic compartments of ridge – transform systems. Here, we calculate and analyze the ΔRMBA between the oceanic transform fault and adjacent ridge segments, transform fault and fracture zones, and inside and outside corners of the ridge segment for the 16 ridge – transform systems (Fig. 8).

As seen for the ΔRMBA between the ridge and its adjacent transform ($\Delta RMBA_{T\text{-}R}$; Fig. 8a), all ridge – transform systems except the Atlantis case have a negative $\Delta RMBA_{T\text{-}R}$ using the half-space cooling solution. Our findings for the slow-slipping transforms on the Mid-Atlantic Ridge (Kane, Atlantis, Marathon, and Oceanographer) are compatible with previous gravity analyses with a half-space cooling correction (Wang et al., 2011). In contrast, the $\Delta RMBA_{T\text{-}R}$ using the isoviscous solution becomes mostly positive in the ultraslow- and slow-spreading systems but remains negative for the intermediate- and fast-spreading ones, which confirms earlier findings of spreading rate dependence of gravity structures along MORs and OTFs (Gregg et al., 2007; Lin and Morgan, 1992). Interestingly, the $\Delta RMBA_{T\text{-}R}$ becomes negative when switching

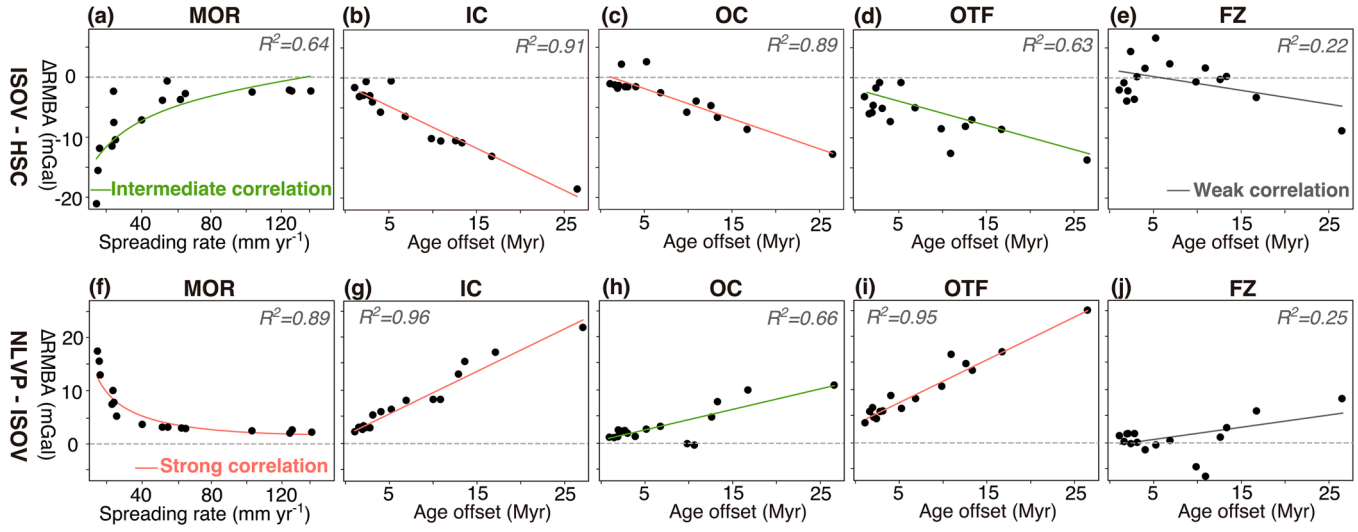

Fig. 7. Best correlations between a particular tectonic feature and the predicted ΔRMBA in 16 mid-ocean ridge – transform fault systems after (a) ISOV vs HSC corrections and (b) NLVP vs ISOV corrections, respectively. The dashed gray line means no RMBA difference.

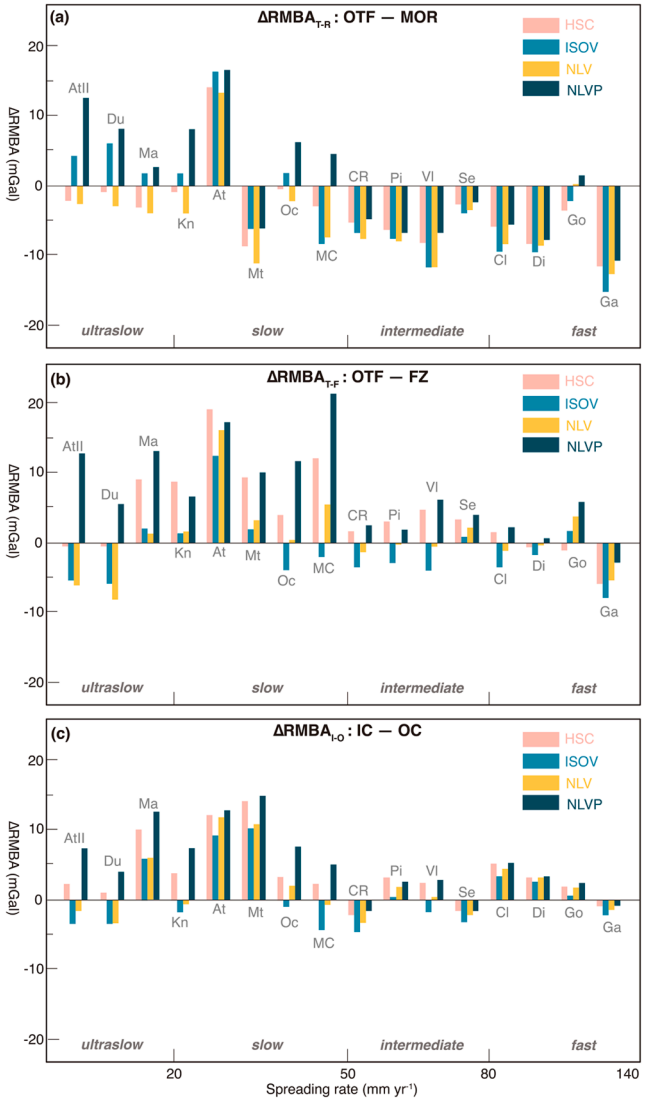

Fig. 8. Variations in ΔRMBA between different seafloor tectonic compartments, such as (a-b) between the OTF and MOR, (c-d) between the OTF and FZ, and (e-f) between the IC and OC, using rheology-dependent thermal corrections.

the ISOV solution to the NLV solution in the ultraslow- and slow-spreading systems but becomes positive again when using the NLVP solution. This can be attributed to a substantial increase in the RMBA below the ultraslow- and slow-slipping OTFs due to its warm mantle upwelling, but the degree of increase is not sufficient to change the turning of the $\Delta RMBA_{T\text{-}R}$ in intermediate- and fast-spreading systems (e.g., Fig. 6c).

Figs. 8b illustrates the maps of the ΔRMBA between oceanic transform faults and adjacent fracture zones ($\Delta RMBA_{T\text{-}F}$) obtained from different thermal models. The OTF basically has a higher RMBA than the FZ in the HSC thermal model, but a lower RMBA in more than half of the ridge – transform cases with the ISOV solution due to its cold subtransform thermal correction (e.g., Fig. 5a). As previously noted, integrating viscoplastic rheology into the flow model will enhance the subtransform RMBA, resulting in a positive $\Delta RMBA_{T\text{-}F}$. The gravity analysis along a viscoplastic transform fault is consistent with earlier gravity work (Guo et al., 2023), arguing that the positive $\Delta RMBA_{T\text{-}F}$ appears to be a result of relatively thin crust beneath the oceanic transform fault.

On the subject of the difference in RMBA between the IC and OC ($\Delta RMBA_{I\text{-}O}$; Fig. 8c), it has both positive and negative values in the ISOV and NLV models, but predominantly remains positive in the HSC and NLVP models. The small difference between the latter two models is because the effect of viscoplastic rheology on gravity signal are much lower in the ridge flanks than in the transform deformation zone. The presence of the positive $\Delta RMBA_{I\text{-}O}$ implies an asymmetrical crustal structure on both sides of the mid-ocean ridge, which appears to be independent of spreading rate.

3.5. Model limitations and potential future directions

There are still several potential areas of improvement for an even more rigorous 3D thermal correction to estimate the gravity anomaly over spreading/rifting systems. First of all, the initial temperature field in our half-space cooling model is calculated based on an observed constant spreading rate within each individual mid-ocean ridge – transform fault system instead of the natural seafloor age field which is more heterogeneous (Müller et al., 2008). Second, to simplify interpretation, we omitted a correction for sediment thickness in the typical ridge – transform setting due to its variability across different ridge – transform systems. If accurate regional sediment thickness data are available, gravity anomalies due to changes in sediment thickness should be included in the calculation of the residual gravity field.

Third, changes in assumed rheological parameters can slightly influence the simulated temperature field. However, previous sensitivity tests of these parameters suggest that it is primarily the processes of nonlinear viscosity and brittle weakening, not the specific model parameterizations, that leads to the distinct thermal structure along the ridge axis and adjacent transform deformation zone (Behn et al., 2007; Shen and Forsyth, 1992). Fourth, our thermal model ignores the process of hydrothermal circulation which contributes to the thermal evolution of the shallow oceanic crust. This is because we focus more on the effect of rheological approximation changes in the deep mantle thermal structure.

Residual gravity anomalies are not only calculated in the ridge – transform scenario but also in other geological settings like rifted margins (e.g., Breivik et al., 1999; Chappell and Kusznir, 2008), subduction zones (e.g., Bassett and Watts, 2015), and regions of plume-ridge interaction (e.g., Maia et al., 2000; Georgen et al., 2001). Especially at rifted margins, the thermal field and the margin structures are strong functions of mantle rheology and it appears plausible that gravity corrections are also highly sensitive to the chosen mechanical model - but that is beyond the scope of this study that is specific to mid-ocean ridge – transform fault systems.

Nevertheless, more observational constraints such as high-resolution bathymetry, seafloor age data, regional sediment thickness map and rock types, and a proper treatment of the large-scale effects of hydrothermal circulation are desirable to consider in the geodynamic flow model to obtain a more accurate gravity field. Last but not least, it is worthwhile to evaluate gravity-derived crustal thickness maps of mid-ocean ridge – transform fault systems based on 3D thermal corrections with the assumption of more realistic mantle rheology in future marine gravity models.

Conclusions

We have investigated the sensitivity of gravity anomalies to the rheology-dependent thermal structures in mid-ocean ridge – transform fault systems. In summary, disregarding the effects of 3D passive mantle flow results in an overestimated thermal gravity contribution and thereby an underestimation of the residual gravity anomaly field. A more realistic nonlinear viscoplastic mantle rheology should therefore be included when computing 3D thermal gravity corrections. Our main findings include:

1 The predicted RMBA can vary significantly depending on the mantle rheology used in the step of thermal correction. It is lower in the

passive flow models than in the half-space plate cooling model due to lateral heat conduction and advection. Differences in gravity anomalies are greatest between the isoviscous flow and half-space cooling solutions.

2 The use of more physically complete rheological approximations, such as a non-Newtonian temperature-, pressure-, and strain rate-dependent viscosity with a plastic approximation for brittle weakening, increases substantially the RMBA field throughout the spreading system. This is due to the deep mantle flow becoming more vigorous, especially underneath the viscoplastic transform deformation zone with massive warm mantle upwelling.

3 The importance of mantle rheology scales with seafloor tectonic characteristics at the mid-ocean ridge – transform fault system such as transform age offset, spreading rate and transform fault length. Statistics on the correlations between these characteristics and RMBA differences among tectonic compartments reveal that the ΔRMBAs due to different rheology-dependent thermal solutions correlate with spreading rate under mid-ocean ridges and vary systematically with age offset in other tectonic compartments. The differences in rheology-dependent gravity anomalies can be up to the order of tens of mGal.

Data availability

All bathymetric data are obtained from Grevemeyer et al. (2021), available at https://doi.pangaea.de/10.1594/PANGAEA.924451. We use open-source code ASPECT version 2.3.0 (https://aspect.geodynamics.org). All parameters for the model inputs are shown in Tables 1 and 2. You can find our gravity forward approach for determining thermal corrections using 3D temperature or density data in VTK format at https://doi.org/10.5281/zenodo.5831568.

CRediT authorship contribution statement

Sibiao Liu: Conceptualization, Data curation, Formal analysis, Investigation, Methodology, Software, Validation, Visualization, Writing – original draft, Writing – review & editing. **Zhikui Guo:** Data curation, Methodology, Software, Visualization, Writing – review & editing. **Lars H. Rüpke:** Conceptualization, Methodology, Validation, Visualization, Writing – review & editing. **Jason P. Morgan:** Formal analysis, Methodology, Writing – review & editing. **Ingo Grevemeyer:** Resources, Writing – review & editing. **Yu Ren:** Resources, Writing – review & editing. **Chuanzhi Li:** Resources, Writing – review & editing.

Declaration of Competing Interest

The authors declare that they have no known competing financial interests or personal relationships that could have appeared to influence the work reported in this paper.

Acknowledgments

We thank A. Beniest, R. Bousquet, C. Devey, A. Hagen, T. H. Hansteen, and D. Lange for discussions that helped motivate this work. We are very grateful to the editor and two anonymous reviewers for their constructive comments. We also thank the Beacon Program under Zhihu Inc. for its support of the Deep Sea Light project. We acknowledge the computing resources granted by the Resource Allocation Board, Germany. The calculations for this study were conducted on the supercomputer at NHR@ZIB under the project shk00051.

Supplementary materials

Supplementary material associated with this article can be found, in the online version, at doi:10.1016/j.epsl.2023.118420.

References

Alvey, A., Gaina, C., Kusznir, N.J., Torsvik, T.H., 2008. Integrated crustal thickness mapping and plate reconstructions for the high Arctic. Earth Planet. Sci. Lett. 274, 310–321. https://doi.org/10.1016/j.epsl.2008.07.036.

Bangerth, W., Dannberg, J., Fraters, M., Gassmoeller, R., Glerum, A., Heister, T., Myhill, R., Naliboff, J., 2022. ASPECT: advanced solver for problems in earth's convection, user manual. figshare. doi:10.6084/m9.figshare.4865333.v9.

Bassett, D., Watts, A.B., 2015. Gravity anomalies, crustal structure, and seismicity at subduction zones: 1. Seafloor roughness and subducting relief. Geochem. Geophys. Geosyst. 16, 1508–1540. https://doi.org/10.1002/2014GC005684.

Behn, M.D., Boettcher, M.S., Hirth, G., 2007. Thermal structure of oceanic transform faults. Geology 35, 307. https://doi.org/10.1130/G23112A.1.

Blackman, D.K., Canales, J.P., Harding, A., 2009. Geophysical signatures of oceanic core complexes. Geophys. J. Int. 178, 593–613. https://doi.org/10.1111/j.1365-246X.2009.04184.x.

Blackman, D.K., Karner, G.D., Searle, R.C., 2008. Three-dimensional structure of oceanic core complexes: effects on gravity signature and ridge flank morphology, Mid-Atlantic Ridge, 30°N: structure of oceanic core complexes. Geochem. Geophys. Geosyst. 9 https://doi.org/10.1029/2008GC001951 n/a-n/a.

Breivik, A.J., Verhoef, J., Faleide, J.I., 1999. Effect of thermal contrasts on gravity modeling at passive margins: results from the western Barents Sea. J. Geophys. Res. Solid Earth 104, 15293–15311. https://doi.org/10.1029/1998JB900022.

Chappell, A.R., Kusznir, N.J., 2008. Three-dimensional gravity inversion for Moho depth at rifted continental margins incorporating a lithosphere thermal gravity anomaly correction. Geophys. J. Int. 174, 1–13. https://doi.org/10.1111/j.1365-246X.2008.03803.x.

Chen, Y., Morgan, W.J., 1990. A nonlinear rheology model for mid-ocean ridge axis topography. J. Geophys. Res. Solid Earth 95, 17583–17604. https://doi.org/10.1029/JB095iB11p17583.

Crosby, A.G., McKenzie, D., Sclater, J.G., 2006. The relationship between depth, age and gravity in the oceans. Geophys. J. Int. 166, 553–573. https://doi.org/10.1111/j.1365-246X.2006.03015.x.

Escartín, J., Lin, J., 1995. Ridge offsets, normal faulting, and gravity anomalies of slow spreading ridges. J. Geophys. Res. Solid Earth 100, 6163–6177. https://doi.org/10.1029/94JB03267.

Furlong, K., Sheaffer, S., Malservisi, R., 2001. Thermal-rheologic controls on deformation within oceanic transforms. Geol. Soc. 186, 65–84. https://doi.org/10.1144/GSL.SP.2001.186.01.05.

Georgen, J.E., Lin, J., Dick, H.J.B., 2001. Evidence from gravity anomalies for interactions of the Marion and Bouvet hotspots with the Southwest Indian Ridge: effects of transform offsets. Earth Planet. Sci. Lett. 187, 283–300. https://doi.org/10.1016/S0012-821X(01)00293-X.

Glerum, A., Thieulot, C., Fraters, M., Blom, C., Spakman, W., 2018. Nonlinear viscoplasticity in ASPECT: benchmarking and applications to subduction. Solid Earth 9, 267–294. https://doi.org/10.5194/se-9-267-2018.

Gregg, P.M., Behn, M.D., Lin, J., Grove, T.L., 2009. Melt generation, crystallization, and extraction beneath segmented oceanic transform faults. J. Geophys. Res. Solid Earth 114. https://doi.org/10.1029/2008JB006100.

Gregg, P.M., Lin, J., Behn, M.D., Montési, L.G.J., 2007. Spreading rate dependence of gravity anomalies along oceanic transform faults. Nature 448, 183–187. https://doi.org/10.1038/nature05962.

Grevemeyer, I., Rüpke, L.H., Morgan, J.P., Iyer, K., Devey, C.W., 2021. Extensional tectonics and two-stage crustal accretion at oceanic transform faults. Nature 591, 402–407. https://doi.org/10.1038/s41586-021-03278-9.

Guo, Z., 2022. vtk2grav: a computer program for gravity forward of 3D density distribution in VTK format. doi:10.5281/zenodo.5831568.

Guo, Z., Liu, S., Rüpke, L.H., Grevemeyer, I., Morgan, J.P., Lange, D., Ren, Y., Tao, C., 2023. Disparate crustal thicknesses beneath oceanic transform faults and adjacent fracture zones revealed by gravity anomalies. Geology 51, 300–304. https://doi.org/10.1130/G50429.1.

Hirth, G., Kohlstedt, D., 2003. Rheology of the upper mantle and the mantle wedge: a view from the experimentalists. Wash. DC Am. Geophys. Union Geophys. Monogr. Ser. 138, 83–105. https://doi.org/10.1029/138GM06.

Kohli, A., Wolfson-Schwehr, M., Prigent, C., Warren, J.M., 2021. Oceanic transform fault seismicity and slip mode influenced by seawater infiltration. Nat. Geosci. 14, 606–611. https://doi.org/10.1038/s41561-021-00778-1.

Kuo, B.-Y., Forsyth, D.W., 1988. Gravity anomalies of the ridge-transform system in the South Atlantic between 31 and 34.5 °S: upwelling centers and variations in crustal thickness. Mar. Geophys. Res. 10, 205–232. https://doi.org/10.1007/BF00310065.

Lin, J., Morgan, J.P., 1992. The spreading rate dependence of three-dimensional mid-ocean ridge gravity structure. Geophys. Res. Lett. 19, 13–16. https://doi.org/10.1029/91GL03041.

Lin, J., Purdy, G.M., Schouten, H., Sempere, J.-C., Zervas, C., 1990. Evidence from gravity data for focusedmagmatic accretionalong the Mid-Atlantic Ridge. Nature 344, 627–632. https://doi.org/10.1038/344627a0.

Maia, M., Ackermand, D., Dehghani, G.A., Gente, P., Hékinian, R., Naar, D., O'Connor, J., Perrot, K., Phipps Morgan, J., Ramillien, G., Révillon, S., Sabetian, A., Sandwell, D., Stoffers, P., 2000. The Pacific-Antarctic Ridge–Foundation hotspot interaction: a case study of a ridge approaching a hotspot. Mar. Geol. 167, 61–84. https://doi.org/10.1016/S0025-3227(00)00023-2.

Marjanović, M., Carbotte, S.M., Nedimović, M.R., Canales, J.P., 2011. Gravity and seismic study of crustal structure along the Juan de Fuca Ridge axis and across pseudofaults on the ridge flanks. Geochem. Geophys. Geosyst. 12 https://doi.org/10.1029/2010GC003439.

Morgan, J.P., Forsyth, D.W., 1988. Three-dimensional flow and temperature perturbations due to a transform offset: effects on oceanic crustal and upper mantle structure. J. Geophys. Res. 93, 2955. https://doi.org/10.1029/JB093iB04p02955.

Morgan, J.P., Parmentier, E.M., 1987. A three-dimensional gravity study of the 95.5°W propagating rift in the Galapagos spreading center. Earth Planet. Sci. Lett. 81, 289–298. https://doi.org/10.1016/0012-821X(87)90165-8.

Müller, R.D., Sdrolias, M., Gaina, C., Roest, W.R., 2008. Age, spreading rates, and spreading asymmetry of the world's ocean crust. Geochem. Geophys. Geosyst. 9 https://doi.org/10.1029/2007GC001743.

NOAA National Geophysical Data Center, 2009. ETOPO1 1 Arc-Minute Global Relief Model. NOAA National Centers for Environmental Information. https://doi.org/10.7289/V5C8276M.

Parker, R.L., 1973. The Rapid Calculation of Potential Anomalies. Geophysical Journal of the Royal Astronomical Society 31, 447–455. https://doi.org/10.1111/j.1365-246X.1973.tb06513.x.

Prince, R.A., Forsyth, D.W., 1988. Horizontal extent of anomalously thin crust near the Vema Fracture Zone from the three-dimensional analysis of gravity anomalies. J. Geophys. Res. 93, 8051. https://doi.org/10.1029/JB093iB07p08051.

Ren, Y., Geersen, J., Grevemeyer, I., 2022. Impact of spreading rate and age-offset on oceanic transform fault morphology. Geophys. Res. Lett. 49 https://doi.org/10.1029/2021GL096170.

Roland, E., Behn, M.D., Hirth, G., 2010. Thermal-mechanical behavior of oceanic transform faults: implications for the spatial distribution of seismicity. Geochem. Geophys. Geosystems 11. https://doi.org/10.1029/2010GC003034.

Sandwell, D.T., Müller, R.D., Smith, W.H.F., Garcia, E., Francis, R., 2014. New global marine gravity model from CryoSat-2 and Jason-1 reveals buried tectonic structure. Science 346, 65–67. https://doi.org/10.1126/science.1258213.

Shen, Y., Forsyth, D.W., 1992. The effects of temperature- and pressure-dependent viscosity on three-dimensional passive flow of the mantle beneath a ridge-transform System. J. Geophys. Res. 97, 19717. https://doi.org/10.1029/92JB01467.

Stein, C.A., Stein, S., 1992. A model for the global variation in oceanic depth and heat flow with lithospheric age. Nature 359, 123–129. https://doi.org/10.1038/359123a0.

Turcotte, D.L., Schubert, G., 2014. Geodynamics, 3rd edition. Cambridge University Press, Cambridge, United Kingdom.

Wang, T., Lin, J., Tucholke, B., Chen, Y.J., 2011. Crustal thickness anomalies in the North Atlantic Ocean basin from gravity analysis. Geochem. Geophys. Geosyst. 12 https://doi.org/10.1029/2010GC003402.

Zhang, F., Lin, J., Zhang, X.B., Ding, W.W., Wang, T.T., Zhu, J., 2020. Asymmetry in oceanic crustal structure of the South China Sea basin and its implications on mantle geodynamics. Int. Geol. Rev. 62, 840–858. https://doi.org/10.1080/00206814.2018.1425922.

Zhang, F., Lin, J., Zhou, Z., Yang, H., Morgan, J.P., 2022. Mechanism of progressive broad deformation from oceanic transform valley to off-transform faulting and rifting. Innovation 3, 100193. https://doi.org/10.1016/j.xinn.2021.100193.

Earth and Planetary Science Letters

Supporting Information for

Sensitivity of gravity anomalies to mantle rheology at mid-ocean ridge – transform fault systems

Sibiao Liu [(1)], Zhikui Guo [(1,2)], Lars H. Rüpke [(1)], Jason P. Morgan [(3)], Ingo Grevemeyer [(1)], Yu Ren [(1)], and Chuanzhi Li [(4)]

(1) GEOMAR Helmholtz Centre for Ocean Research Kiel, Kiel, Germany
(2) Second Institute of Oceanography, MNR, Hangzhou, China
(3) Southern University of Science and Technology, Shenzhen, China
(4) Institute for Advanced Ocean Study, Ocean University of China, Qingdao, China

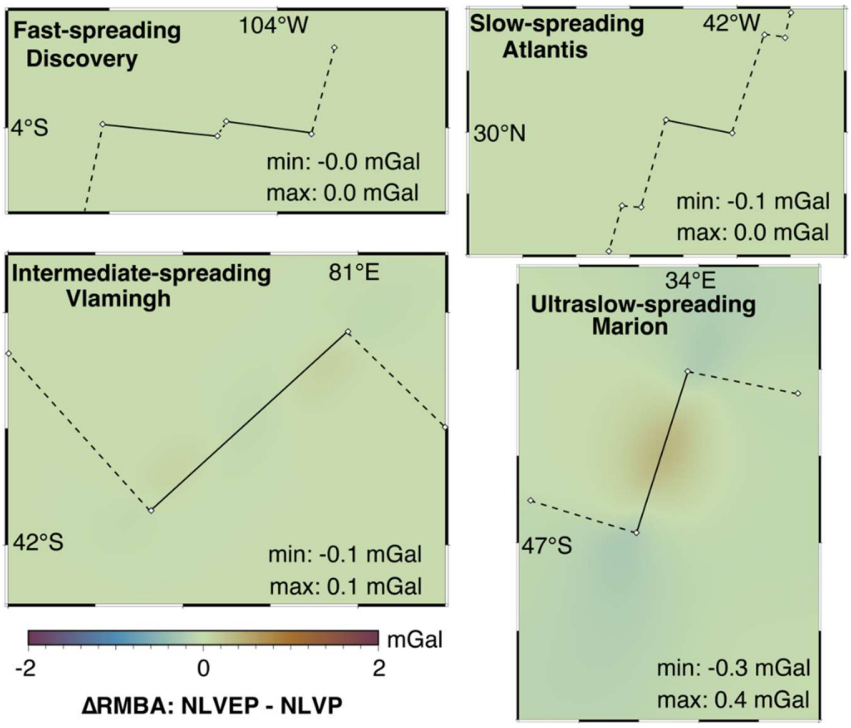

Figure S1. (**a-d**) Maps of the predicted residual mantle Bouguer anomaly difference (ΔRMBA) between the nonlinear visco-elasto-plastic (NLVEP) thermal model and the nonlinear viscoplastic (NLVP) thermal model in different mid-ocean ridge – transform fault systems. The solid (dashed) black lines mark oceanic transform faults (ridge segments) and the diamonds connecting them represent the ridge-transform intersections.

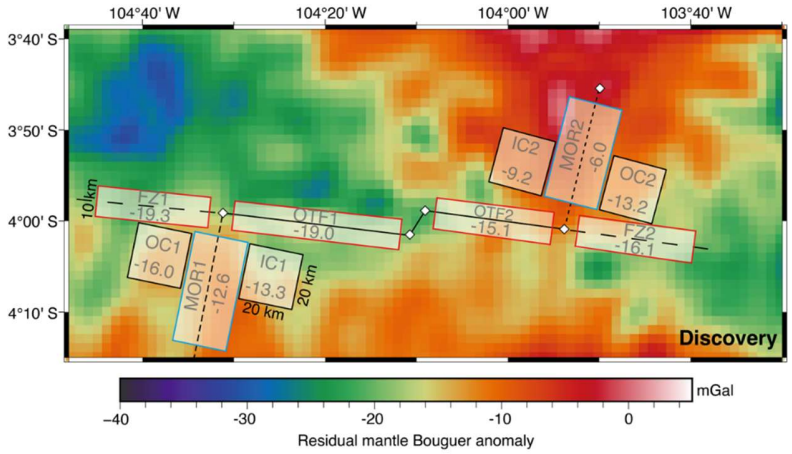

Figure S2. A diagram of the average residual mantle Bouguer anomaly calculation for each tectonic compartment. Here we use the RMBA map of the Discovery transform system as an example. Zero level is arbitrary when evaluating the relative magnitudes of the anomalies.

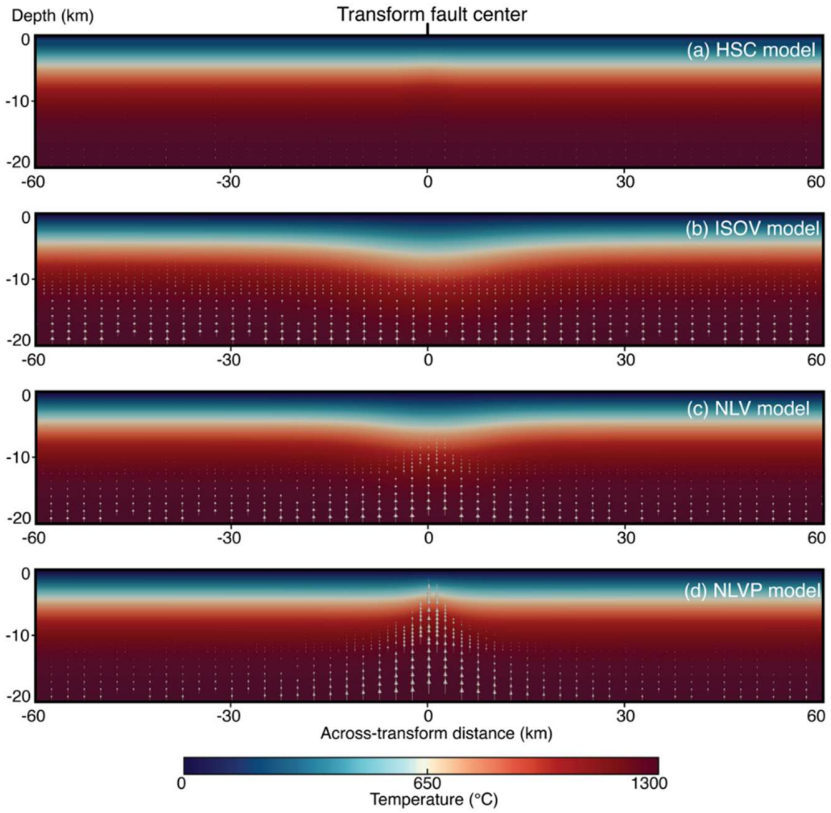

Figure S3. Steady-state thermal structures along the across-transform transect D-D', showing the mantle flow patterns (arrows) below the oceanic lithosphere for different thermal models. HSC: half-space cooling model, ISOV: isoviscous model, NLV: nonlinear viscous model, NLVP: nonlinear viscoplastic model.

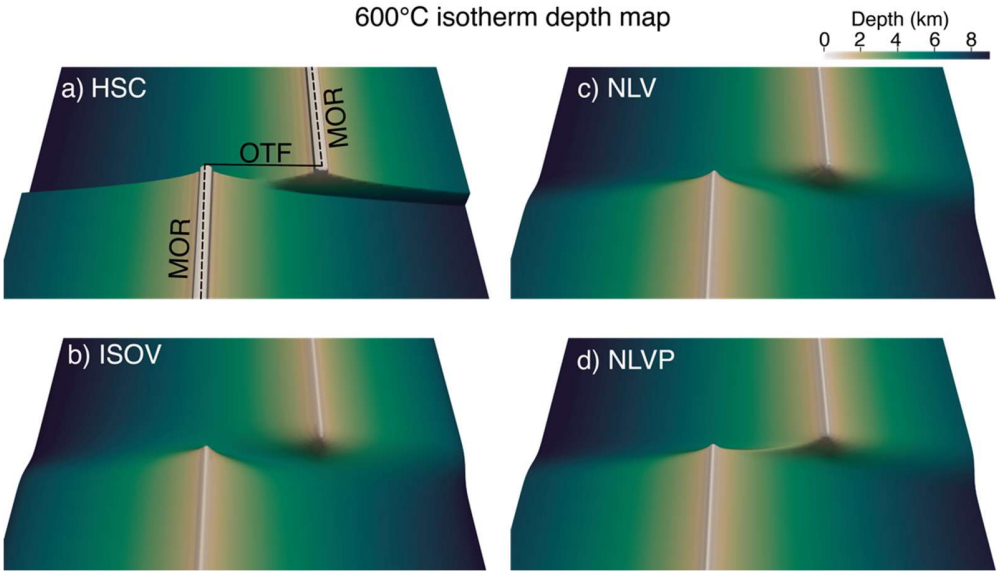

Figure S4a. Depth map of the 600°C isotherm for different thermal correction models of the Clipperton ridge – transform system. HSC: half-space cooling model, ISOV: isoviscous model, NLV: nonlinear viscous model, NLVP: nonlinear viscoplastic model.

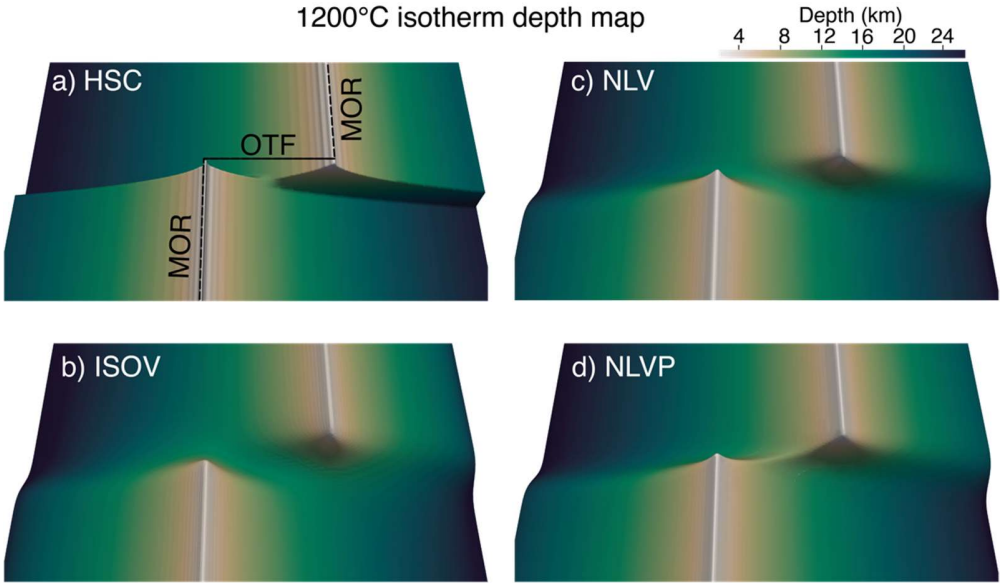

Figure S4b. Depth map of the 1200°C isotherm for different thermal correction models of the Clipperton ridge – transform system. HSC: half-space cooling model, ISOV: isoviscous model, NLV: nonlinear viscous model, NLVP: nonlinear viscoplastic model.

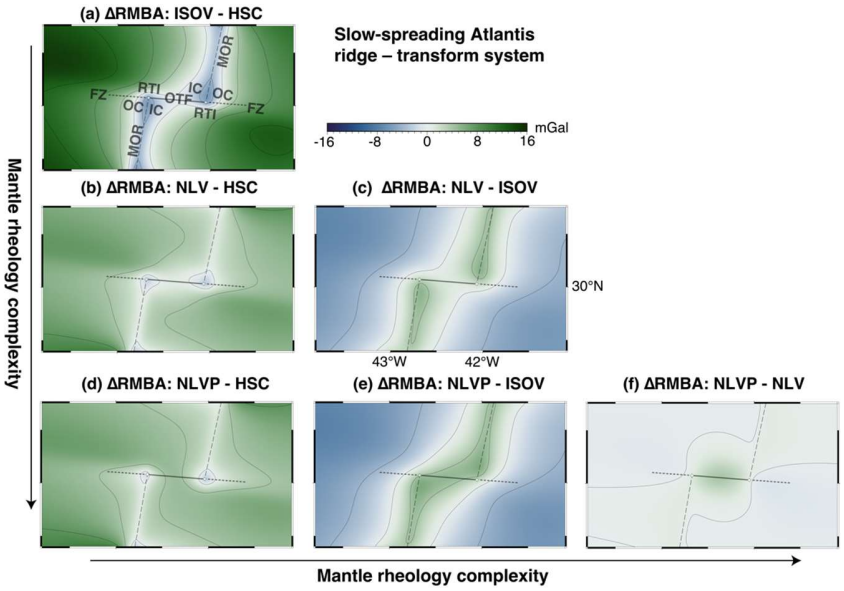

Figure S5. ΔRMBA between different rheological models for the Atlantis transform system on the slow-spreading Mid-Atlantic Ridge. **(a-c)** ΔRMBA between passive flow models (ISOV isoviscous, NLV nonlinear viscous, and NLVP nonlinear viscoplastic) and the half-space cooling (HSC) model, respectively. **(d-f)** ΔRMBA between various passive flow models. All gravity anomaly maps are contoured at 4-mGal intervals.

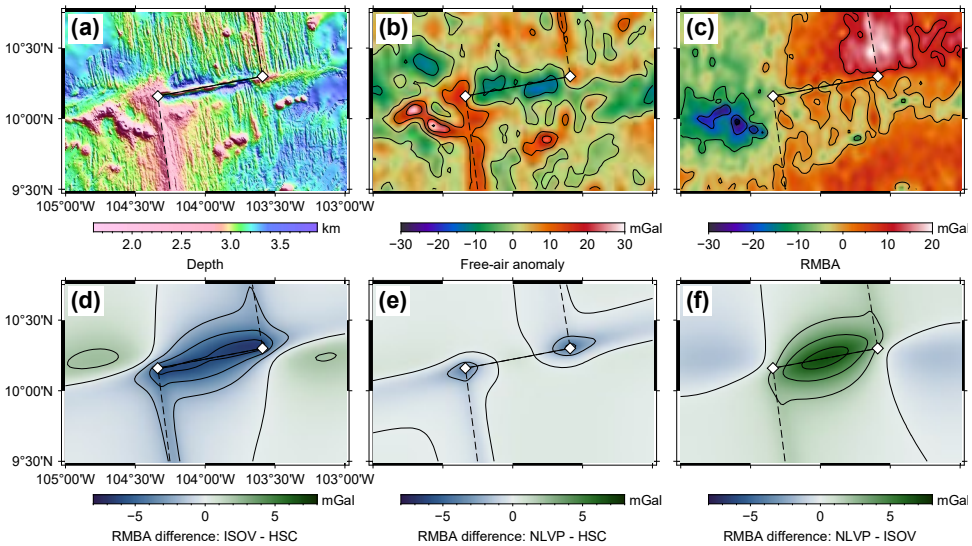

Figure S6a. Estimated gravity anomalies for the Clipperton ridge – transform system. Note that the RMBA map is calculated using the nonlinear viscoplastic thermal solution. The solid (dashed) black lines mark oceanic transform faults (ridge segments). Maps of the free-air anomaly and the RMBA are contoured at 10-mGal intervals. The three correction maps are contoured at 2-mGal intervals. Zero level in the RMBA map is arbitrary when evaluating the relative magnitudes of the anomalies.

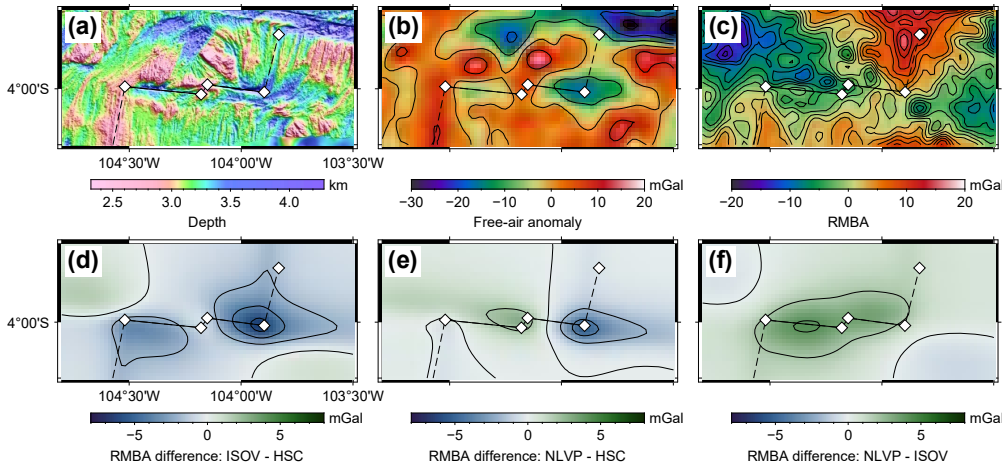

Figure S6b. Gravity predictions for the Discovery ridge – transform system. Note that the RMBA map is calculated using the nonlinear viscoplastic thermal solution. The solid (dashed) black lines mark oceanic transform faults (ridge segments). Maps of the free-air anomaly and the RMBA are contoured at 10-mGal intervals. The three correction maps are contoured at 2-mGal intervals. Zero level in the RMBA map is arbitrary when evaluating the relative magnitudes of the anomalies.

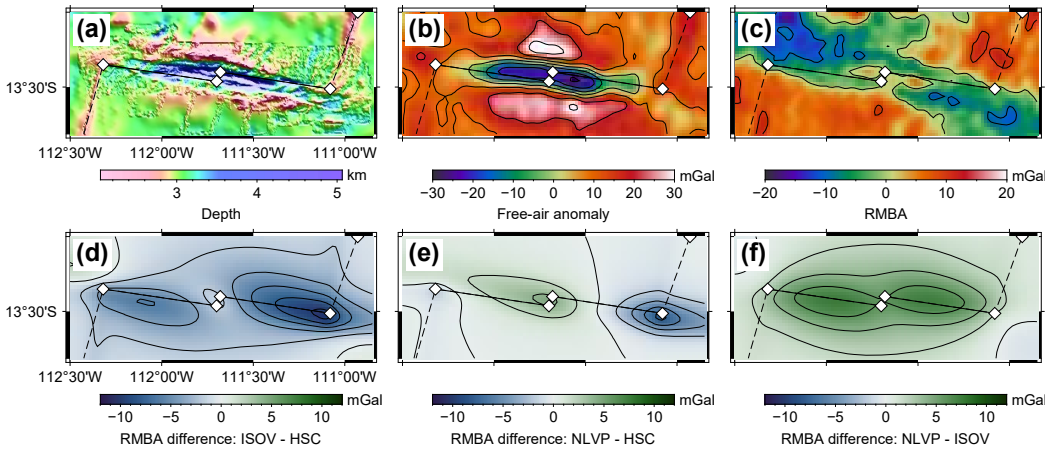

Figure S6c. Gravity predictions for the Garret ridge – transform system. Note that the RMBA map is calculated using the nonlinear viscoplastic thermal solution. The solid (dashed) black lines mark oceanic transform faults (ridge segments). Maps of the free-air anomaly and the RMBA are contoured at 10-mGal intervals. The three correction maps are contoured at 2-mGal intervals. Zero level in the RMBA map is arbitrary when evaluating the relative magnitudes of the anomalies.

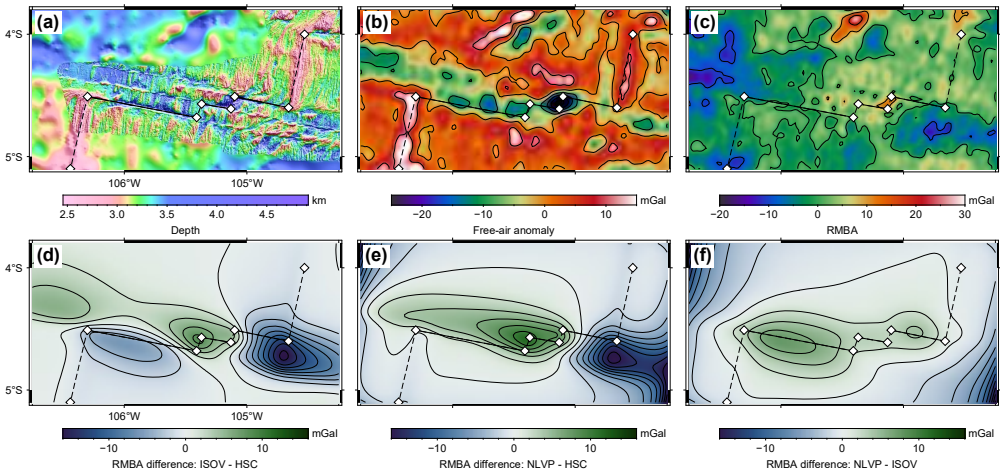

Figure S6d. Gravity predictions for the Gofar (south) ridge – transform system. Note that the RMBA map is calculated using the nonlinear viscoplastic thermal solution. The solid (dashed) black lines mark oceanic transform faults (ridge segments). Maps of the free-air anomaly and the RMBA are contoured at 10-mGal intervals. The three correction maps are contoured at 2-mGal intervals. Zero level in the RMBA map is arbitrary when evaluating the relative magnitudes of the anomalies.

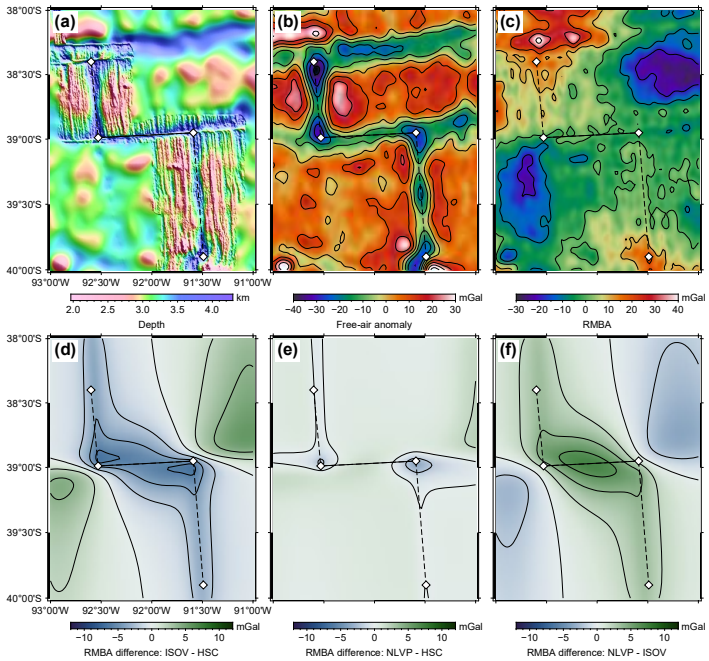

Figure S7. Gravity predictions for the Chile Ridge 39°S ridge – transform system. Note that the RMBA map is calculated using the nonlinear viscoplastic thermal solution. The solid (dashed) black lines mark oceanic transform faults (ridge segments). Maps of the free-air anomaly and the RMBA are contoured at 10-mGal intervals. The three correction maps are contoured at 2-mGal intervals. Zero level in the RMBA map is arbitrary when evaluating the relative magnitudes of the anomalies.

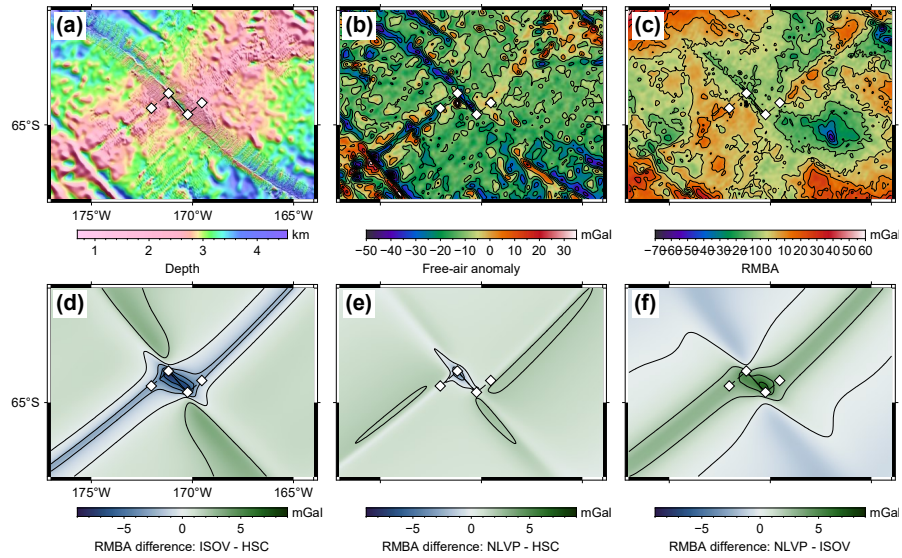

Figure S8. Gravity predictions for the Pitman ridge – transform system. Note that the RMBA map is calculated using the nonlinear viscoplastic thermal solution. The solid (dashed) black lines mark oceanic transform faults (ridge segments). Maps of the free-air anomaly and the RMBA are contoured at 10-mGal intervals. The three correction maps are contoured at 2-mGal intervals. Zero level in the RMBA map is arbitrary when evaluating the relative magnitudes of the anomalies.

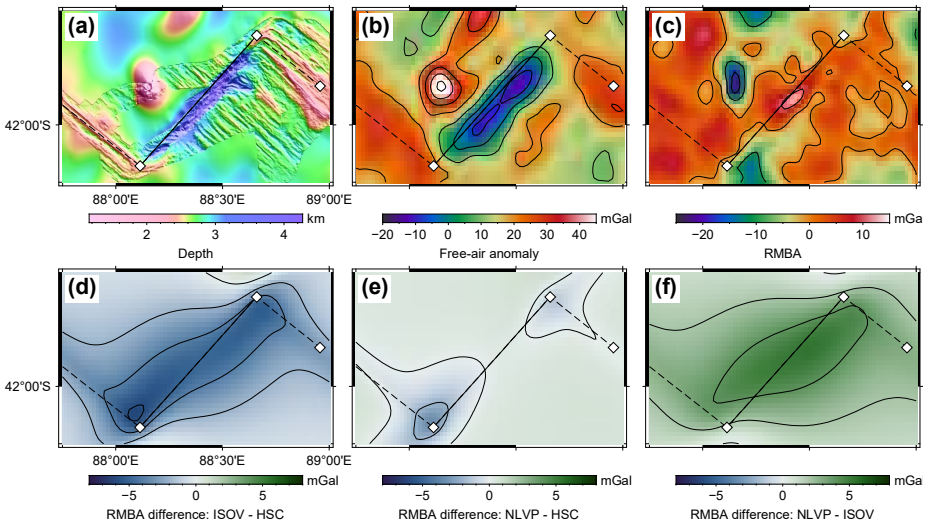

Figure S9a. Gravity predictions for the SEIR88 ridge – transform system. Note that the RMBA map is calculated using the nonlinear viscoplastic thermal solution. The solid (dashed) black lines mark oceanic transform faults (ridge segments). Maps of the free-air anomaly and the RMBA are contoured at 10-mGal intervals. The three correction maps are contoured at 2-mGal intervals. Zero level in the RMBA map is arbitrary when evaluating the relative magnitudes of the anomalies.

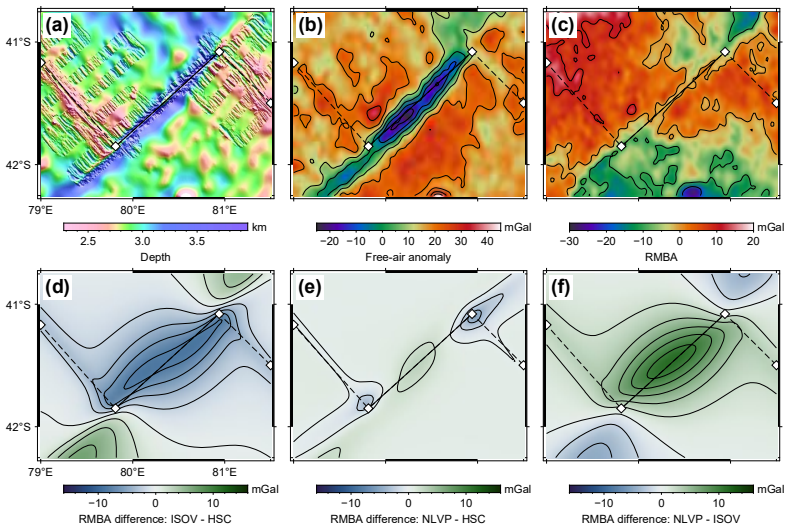

Figure S9b. Gravity predictions for the Vlamingh ridge – transform system. Note that the RMBA map is calculated using the nonlinear viscoplastic thermal solution. The solid (dashed) black lines mark oceanic transform faults (ridge segments). Maps of the free-air anomaly and the RMBA are contoured at 10-mGal intervals. The three correction maps are contoured at 2-mGal intervals. Zero level in the RMBA map is arbitrary when evaluating the relative magnitudes of the anomalies.

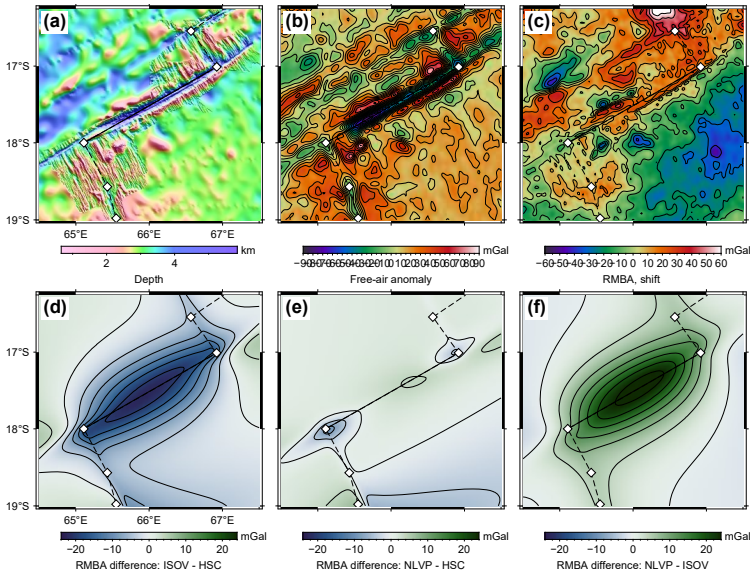

Figure S10. Gravity predictions for the Marie Celeste ridge – transform system. Note that the RMBA map without shift is calculated using the nonlinear viscoplastic thermal solution. The solid (dashed) black lines mark oceanic transform faults (ridge segments). Maps of the free-air anomaly and the RMBA are contoured at 10-mGal intervals. The three correction maps are contoured at 4-mGal intervals. Zero level in the RMBA map is arbitrary when evaluating the relative magnitudes of the anomalies.

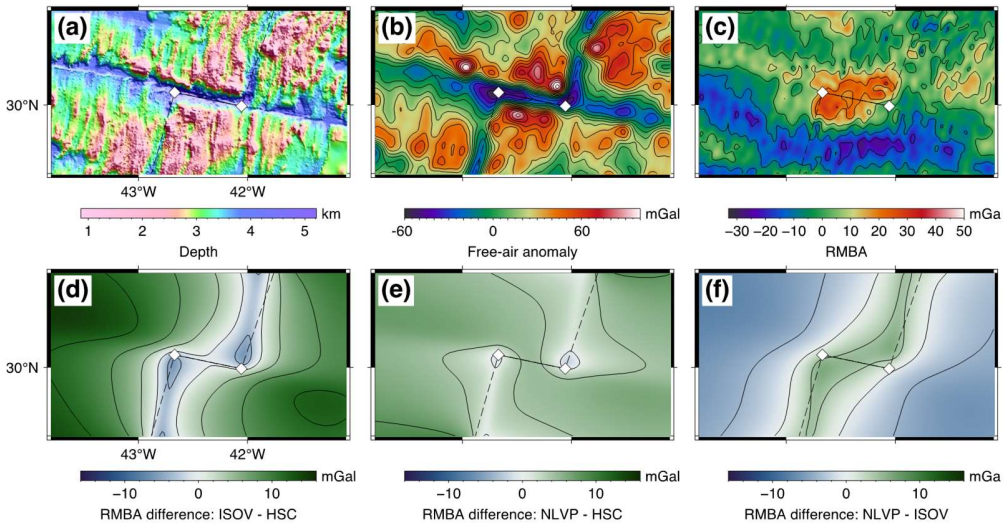

Figure S11a. Gravity predictions for the Atlantis ridge – transform system. Note that the RMBA map is calculated using the nonlinear viscoplastic thermal solution. The solid (dashed) black lines mark oceanic transform faults (ridge segments). Maps of the free-air anomaly and the RMBA are contoured at 10-mGal intervals. The three correction maps are contoured at 4-mGal intervals. Zero level in the RMBA map is arbitrary when evaluating the relative magnitudes of the anomalies.

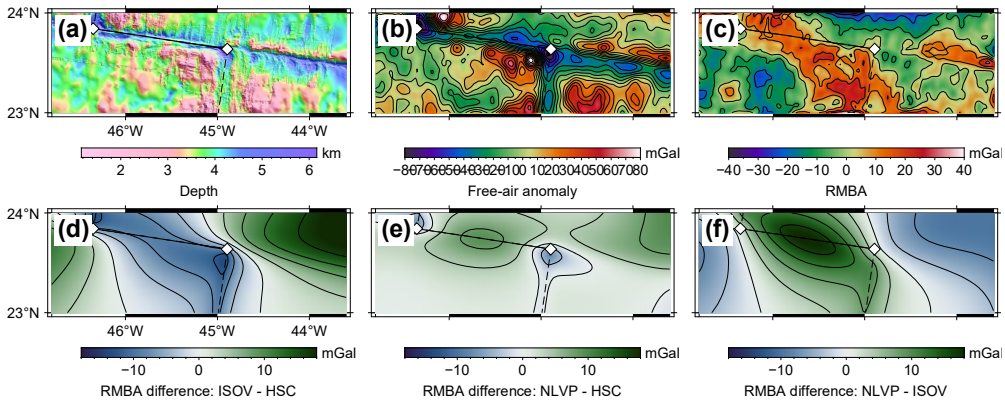

Figure S11b. Gravity predictions for the Kane (east) ridge – transform system. Note that the RMBA map is calculated using the nonlinear viscoplastic thermal solution. The solid (dashed) black lines mark oceanic transform faults (ridge segments). Maps of the free-air anomaly and the RMBA are contoured at 10-mGal intervals. The three correction maps are contoured at 4-mGal intervals. Zero level in the RMBA map is arbitrary when evaluating the relative magnitudes of the anomalies.

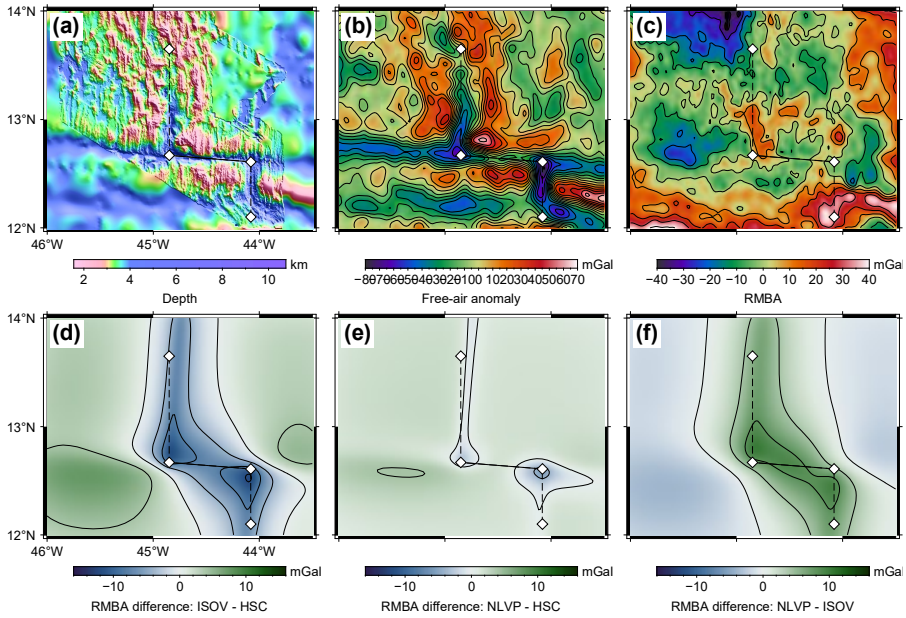

Figure S11c. Gravity predictions for the Marathon ridge – transform system. Note that the RMBA map is calculated using the nonlinear viscoplastic thermal solution. The solid (dashed) black lines mark oceanic transform faults (ridge segments). Maps of the free-air anomaly and the RMBA are contoured at 10-mGal intervals. The three correction maps are contoured at 4-mGal intervals. Zero level in the RMBA map is arbitrary when evaluating the relative magnitudes of the anomalies.

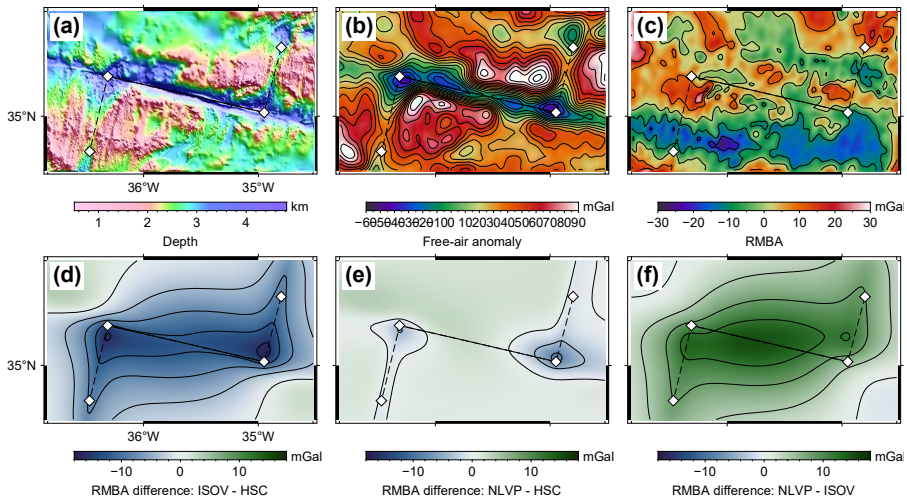

Figure S11d. Gravity predictions for the Oceanographer ridge – transform system. Note that the RMBA map is calculated using the nonlinear viscoplastic thermal solution. The solid (dashed) black lines mark oceanic transform faults (ridge segments). Maps of the free-air anomaly and the RMBA are contoured at 10-mGal intervals. The three correction maps are contoured at 4-mGal intervals. Zero level in the RMBA map is arbitrary when evaluating the relative magnitudes of the anomalies.

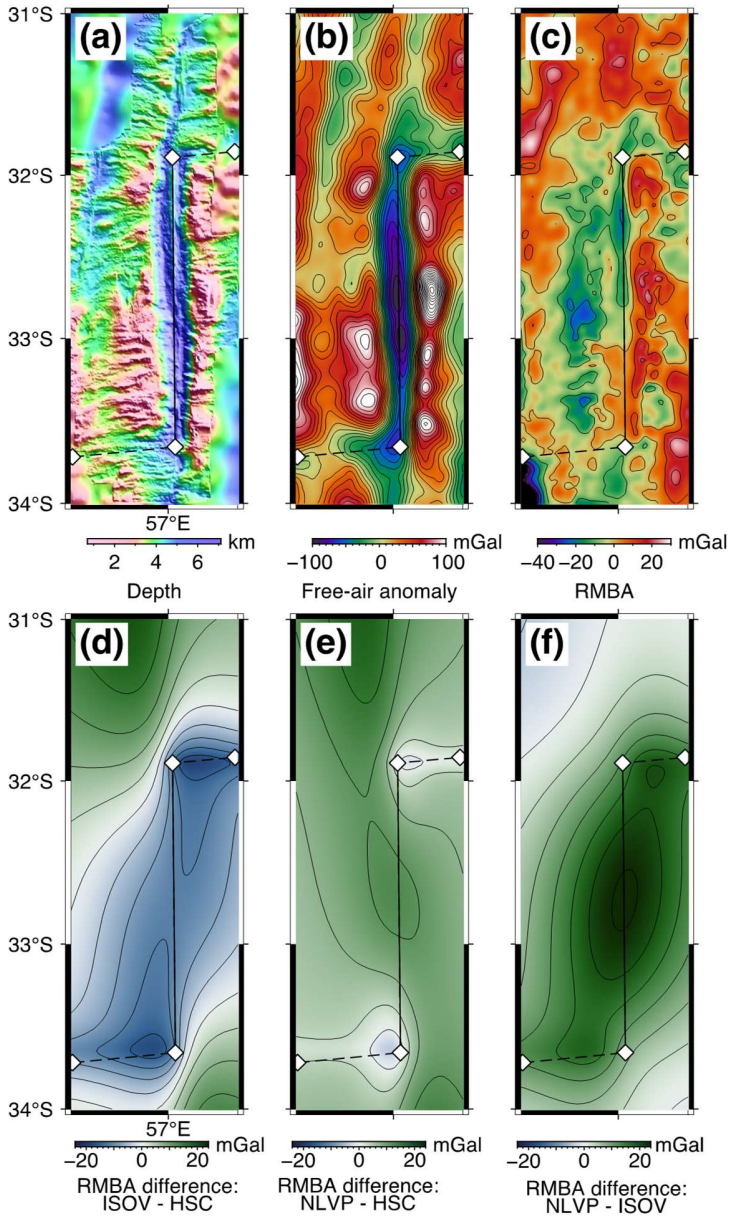

Figure S12a. Gravity predictions for the Atlantis II ridge – transform system. Note that the RMBA map is calculated using the nonlinear viscoplastic thermal solution. The solid (dashed) black lines mark oceanic transform faults (ridge segments). Maps of the free-air anomaly and the RMBA are contoured at 10-mGal intervals. The three correction maps are contoured at 4-mGal intervals. Zero level in the RMBA map is arbitrary when evaluating the relative magnitudes of the anomalies.

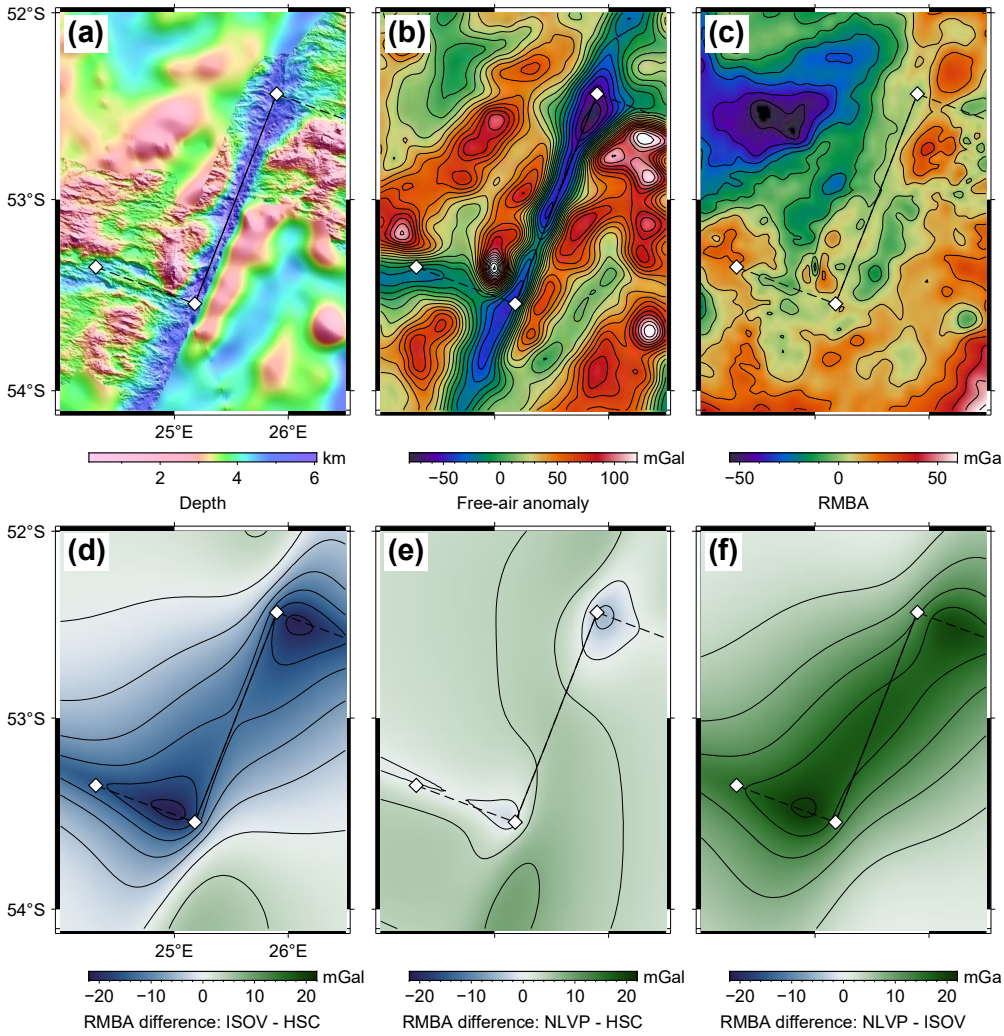

Figure S12b. Gravity predictions for the Du Toit ridge – transform system. Note that the RMBA map is calculated using the nonlinear viscoplastic thermal solution. The solid (dashed) black lines mark oceanic transform faults (ridge segments). Maps of the free-air anomaly and the RMBA are contoured at 10-mGal intervals. The three correction maps are contoured at 4-mGal intervals. Zero level in the RMBA map is arbitrary when evaluating the relative magnitudes of the anomalies.

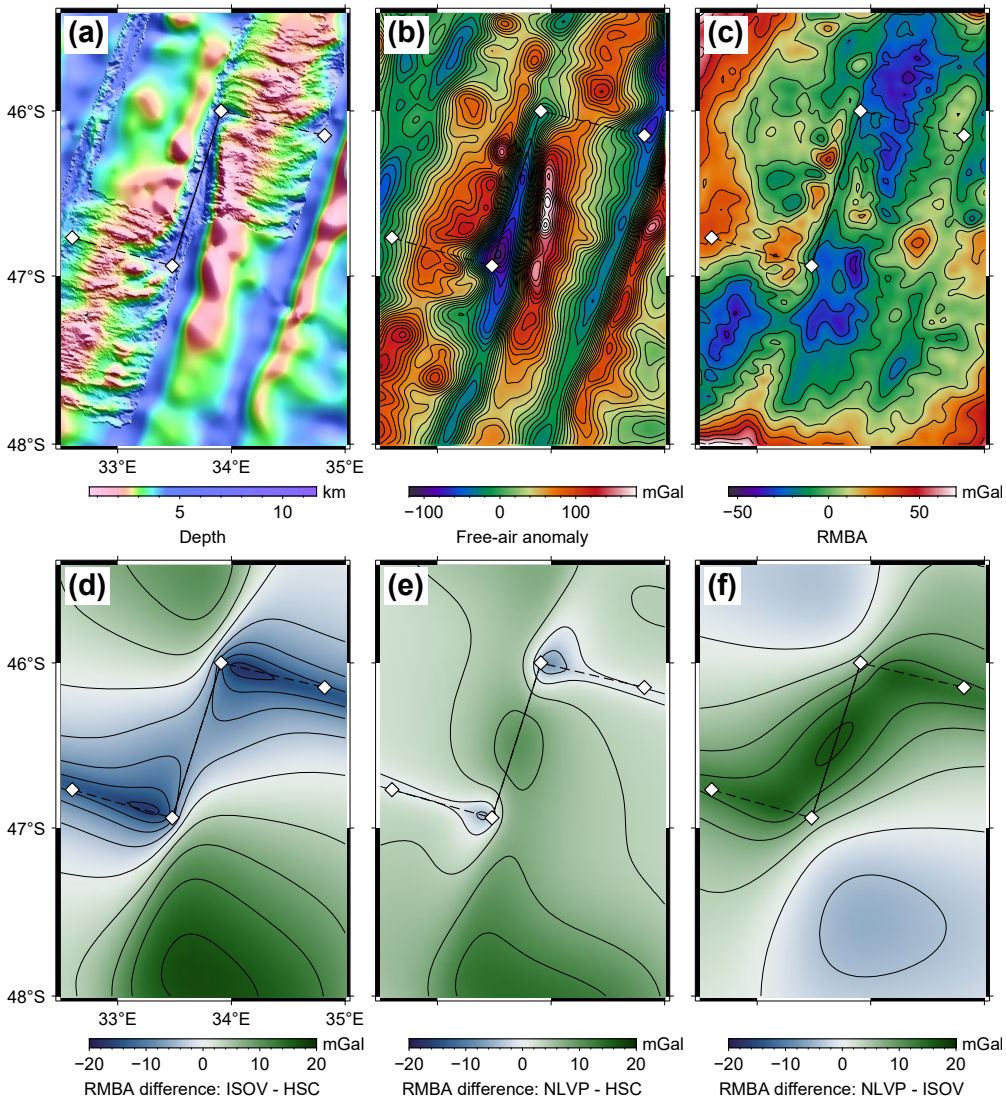

Figure S12c. Gravity predictions for the Marion ridge – transform system. Note that the RMBA map is calculated using the nonlinear viscoplastic thermal solution. The solid (dashed) black lines mark oceanic transform faults (ridge segments). Maps of the free-air anomaly and the RMBA are contoured at 10-mGal intervals. The three correction maps are contoured at 4-mGal intervals. Zero level in the RMBA map is arbitrary when evaluating the relative magnitudes of the anomalies.

CHAPTER 5

MANUSCRIPT #4

Strike-slip versus extensional tectonics at the Oceanographer transform fault, Mid-Atlantic Ridge at 35°N

Ingo Grevemeyer [(1)], Dietrich Lange [(1)], Ingo Klaucke [(1)], Lars Rüpke [(1)], Anouk Beniest [(1,2)], Laura Gómez de la Peña [(1,3)], Yu Ren [(1)], Christian Filbrandt [(1)], Helene-Sophie Hilbert [(1)], Yuhan Li [(1)], Louisa Murray-Bergquist [(1,2)], Katharina Unger Moreno [(1)], Thor Hansteen [(1)], and Colin W. Devey [(1)]

(1) GEOMAR Helmholtz Centre for Ocean Research Kiel, Kiel, Germany
(2) now at Department of Geology and Geochemistry, Vrije Universiteit Amsterdam, Amsterdam, Netherlands
(3) now at Instituto de Ciencias del Mar, CSIC, Barcelona, Spain

Submitted to *Journal of Geophysical Research: Solid Earth*

This chapter contains a manuscript which has been submitted to *Journal of Geophysical Research: Solid Earth*. Please note that the manuscript contains its own reference list and refers to its own figure and page numbers.

Strike-slip versus extensional tectonics at the Oceanographer transform fault, Mid-Atlantic Ridge at 35°N

Ingo Grevemeyer[1], Dietrich Lange[1], Ingo Klaucke[1], Lars H. Ruepke[1], Anouk Beniest[1,2], Laura Gómez de la Peña[1, 3], Yu Ren[1], Christian Filbrandt[1], Helene-Sophie Hilbert[1], Yuhan Li[1], Louisa Murray-Bergquist[1, 2], Katharina Unger Moreno[1], Thor Hansteen[1], and Colin W. Devey[1]

[1] GEOMAR Helmholtz Centre for Ocean Research Kiel, Wischhofstraße 1-3, 24148 Kiel, Germany

[2] *now at* Department of Geology and Geochemistry, Vrije Universiteit Amsterdam, Netherlands

[3] *now at* Instituto de Ciencias del Mar, CSIC, Barcelona, Spain

Key points:

The Oceanographer transform is morphologically and seismically segmented, outlining systematic changes of stress patterns

At >15 km from the ridge-transform intersections, the active transform fault is a narrow zone of deformation, showing strike-slip faulting

Near ridge-transform intersections, deformation is distributed and cross-cuts the inside corner, issuing normal faulting and a wide valley

Abstract

Oceanic transform faults and their fracture zones are among the most striking features of ocean basins. Plate tectonics describes them as strike-slip zones connecting mid-ocean ridge segments. Still, no generally accepted theory exists for the lateral strain partitioning resulting in deep and wide transform valleys and extensively tectonized inside corners. Here, we present results from multibeam bathymetry and a micro-seismicity survey from the slow-slipping Oceanographer transform on the Mid-Atlantic Ridge near 35°N. Swath-mapping echosounder data reveal a segmented transform fault. Away from the ridge-transform intersections (RTI) and in the eastern half of the transform valley, micro-earthquakes recorded on ocean-bottom-seismometers focus along the observed fault strands. Approaching the RTI, however, many micro-earthquakes cut across the inside corner, while the active faults step towards the inside corner, paralleling the trend of the transform valley. Focal mechanisms

point to transform-normal extension in the inside corner region, while strike-slip deformation is only recorded at distances larger than 15 km and away from the RTIs. These observations support a scenario in which deformation beneath a right-angular ridge-transform boundary at the seafloor develops into an oblique shear zone at depth, causing crustal thinning and consequently forming transform valleys. Away from RTIs, seismicity is focused on a narrow and segmented strike-slip fault as predicted by plate tectonics. Oceanic transform faults are consequently not only strike-slip but are also shaped by extensional processes, arguing for a revision of the concept of conservative plate boundaries to account for their morphology, segmentation, and significant lateral differences in seismic behaviour.

Plain language summary

Plate tectonics introduces three types of plate boundaries, including conservative plate margins or transform faults showing strike-slip tectonism. Oceanic transform faults offset mid-ocean ridges and generally run within wide and deep valleys. However, the processes forming these valleys remain enigmatic. Here, we present new data from high-resolution bathymetry and micro-earthquakes detected on ocean-bottom-seismometers. Seafloor morphology and the distribution of earthquakes reveal a segmented plate boundary and seismicity indicates diffuse activity over a broad area, cutting across the inside corner domain between the spreading centre and the transform fault with focal mechanisms showing transform-normal extensional tectonics instead of showing transcurrent motion. In contrast, strike-slip tectonics occurs only >15 km away from adjacent spreading segments. These observations support a scenario in-line with numerical simulations, showing that at ridge-transform intersections the right-angular plate boundary at the seafloor develops into an oblique shear zone at depth, causing crustal thinning and consequently forming transform valleys.

1. Introduction

Oceanic transform faults (OTF) laterally offset mid-ocean ridge spreading segments by 20-850 km (e.g., Sandwell, 1986; Ren et al., 2022) every 70-200 km (Macdonald et al., 1988). Along with their inactive traces, the fracture zones, OTFs strongly shape the morphology of ocean basins. Plate tectonics defines transforms as conservative strike-slip plate boundaries, where one plate moves past another and crust is neither formed nor consumed (Wilson, 1965).

Large earthquakes rupturing along OTFs show strike-slip motion, when recorded far away on stations of the global seismic network (e.g., Sykes, 1967; Abercrombie and Ekström, 2000). Yet, transform faults generally develop prominent valleys (1 km to 18 km wide) around the trace of the primary fault zone (e.g., Ren et al., 2022). Wolfsohn-Schwer & Boettcher (2019) reviewed the bathymetry for 199 transform-fault-ridge offsets and found that basically, all OTFs show a prominent valley, except seven revealing crest-like features within a valley, and only another five lacking a trough-like morphology and hence indicating that transform valleys are a global feature. The depth of those valleys increases with increasing age-offset across OTFs, which may support extension across transform faults (e.g., Grevemeyer et al., 2021; Ren et al., 2022). If correct, this behaviour would indicate that OTFs are not simple strike-slip boundaries but highly complex and structured fault zones.

Numerical simulations of the deformation patterns beneath OTFs (e.g., Behn et al., 2007) imply that the right-angular strike-slip fault at the seafloor becomes increasingly oblique with depth (Furlong et al., 2001; Grevemeyer et al., 2021) and may develop into a shear zone with a component of extension. If these predicted mantle flow patterns are indeed related to the observed morphological features of transform faults, ridge-transform intersections (RTI) should show a broad deformation zone extending from the spreading axis, across the inside corner domain into the transform fault and focal mechanisms should indicate partly extensional movement in the vicinity of RTIs. Yet, little systematic evidence has been found to support this theory, although some studies conducted roughly four decades ago provided some evidence for transform-normal extensional tectonics (Cessaro & Hussong, 1986; Wilcock et al., 1990). However, these patterns were interpreted as a result of regional mantle flow or thermal contraction (Wilcock et al., 1990) and were not considered to be an intrinsic characteristic feature of OTFs.

Detailed field evidence of the behaviour of OTFs is still rare. Consequently, we conducted a seismological study at the Oceanographer transform offsetting the Mid-Atlantic Ridge (MAR) south of the Azores to fill this knowledge gap partly (Figure 1). A seismic network of ocean bottom seismometers (OBS) and hydrophones (OBH) was deployed to record the local seismic activity over a period of up to five months. Our results indicate extensional tectonics in the inside corner region. Micro-seismicity with extensional focal mechanisms occurs over a diffuse zone of deformation and transitions over a short distance of just fifteen kilometres away from the RTI into the strike-slip motion as predicted by plate tectonics.

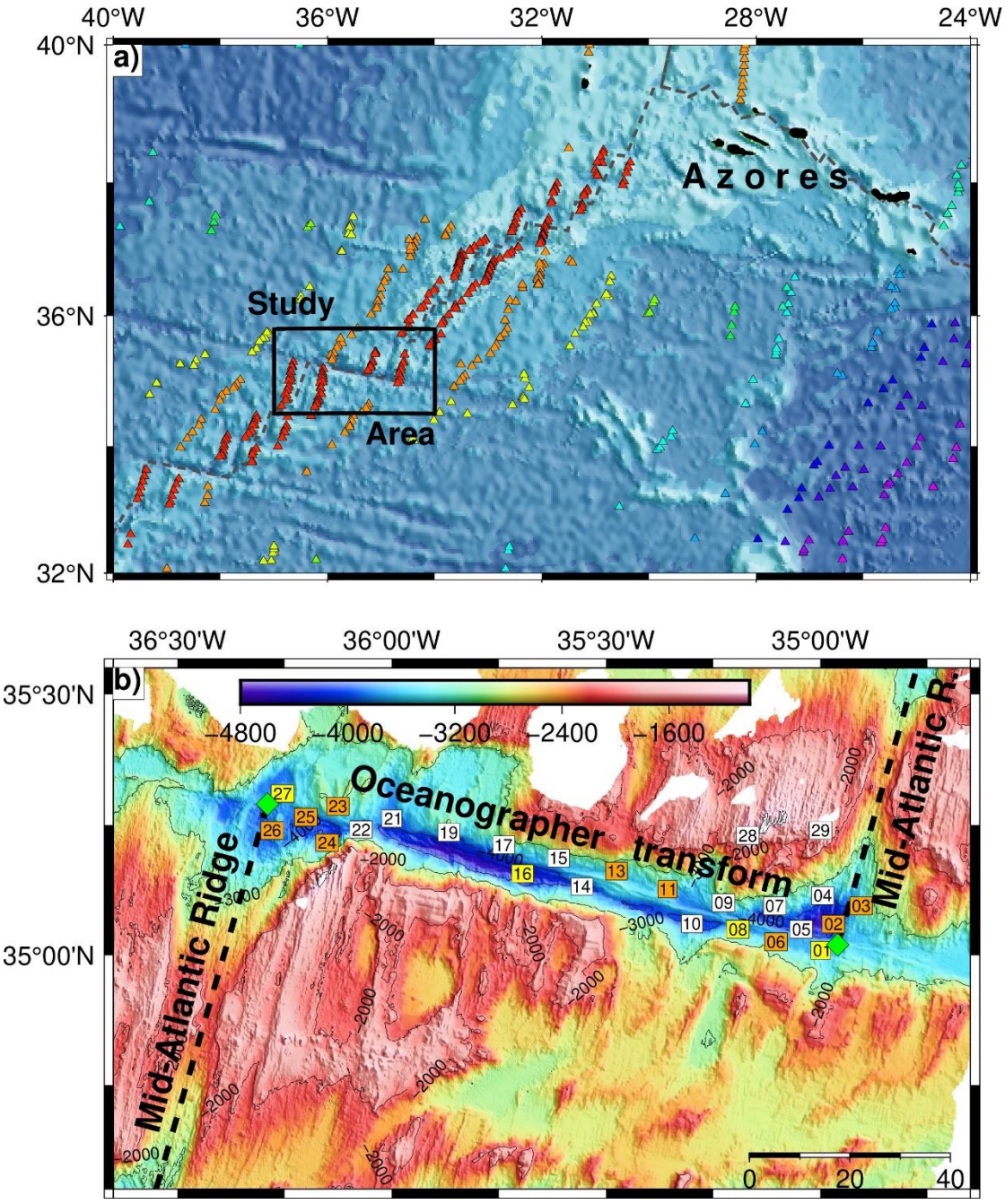

Figure 1. a) Bathymetric location map (Tozer et al., 2019) and spreading isochrones (Seaton et al., 2014) to the south of Azores; b) Swath-echosounder bathymetric map of the Oceanographer OTF and available OBS stations (numbered squares); RTIs are marked by green diamonds.

2. Geological setting

The Mid-Atlantic Ridge is highly segmented and offset by a large number of transform faults. Those with the largest offsets occur in the equatorial Atlantic (e.g., Chain, Romanche and St.

Paul) and, together with their fracture zones, span the ocean from continent to continent (e.g., Wilson, 1965). These large equatorial OTFs have relatively complicated structures (e.g., Searle et al., 1994; Ligi et al., 2002). In contrast, the 120 km long Oceanographer transform fault near 35°N can be considered a type-example of an OTF at the slow spreading MAR. Swath-bathymetric data collected in the early 2000s (Rabain et al., 2001) showed that the transform fault runs within a ~10 km wide valley and has two well-defined segments which are linked by a small pressure ridge roughly at the centre of the OTF system near 35°30'W (Figure 1). A number of *Alvin* submersible dives showed that the tectonic deformation zone along the transform valley, i.e., the plate boundary was defined by a narrow swath centred along the axis of maximum depth (Fox et al. 1985). Based on identified magnetic spreading anomalies to the north and south of the OFT, its age-offset is about 14 million years at the western and 10 million years at the eastern RTI, respectively (DeMets et al., 2015), and hence fault slip is on the order of 22 mm/yr.

Seismic refraction data obtained along the Oceanographer transform (Ambos & Hussong, 1986) suggests that the crust along the transform valley is slightly thinner (4-5 km) than normal (6-7 km) oceanic crust (e.g., Grevemeyer et al., 2018). However, its velocity structure seems to be different, providing several percent slower values in the lower crust, which may suggest that magmatic crust has been overprinted by faulting and fracturing and hence may support higher porosities than normal crust as deduced for the Gofar transform in the Pacific Ocean (Roland et al., 2012).

At the Oceanographer transform fault, the global Centroid-Moment-Tensor (GCMT) catalogue (Dziewonski et al., 1981; Ekström et al., 2012) reported six strike-slip earthquakes with moment magnitudes Mw≥6 occurring in 1982, 1990, 2003, 2010, 2019, and 2022 (i.e., roughly one event every 10 years), but does not report any normal faulting or trans-tensional earthquake. All five earthquakes with Mw>6 occurred on the western segment of the oceanic transform fault (OTF) to the west of 35°32'W, which is characterized by a deep transform valley (Figure 2a)

3. Data acquisition

3.1 Bathymetry and backscatter

Bathymetric and backscatter data for this study were collected during RV METEOR cruise M170 in 2021 and RV MARIA S. MERIAN cruise MSM122 in 2023 using a hull-mounted

Kongsberg Simrad EM122 multi echosounder (Figure 2). Both systems use a 1°x1° configuration and operate at 12 kHz producing 432 beams. Swath width was slightly reduced to 130°, and the system operated in equidistant, dual-ping and frequency-modulated mode. Raw data were filtered using a triangulation method, subsequently manually cleaned and gridded at 50 m grid size and displayed using the Generic Mapping Tool (GMT) of Wessel et al. (2019). The Simrad EM122 system also registers backscatter intensity data that have been processed using MB-system (https://www.mbari.org/products/research-software/mb-system) and GMT.

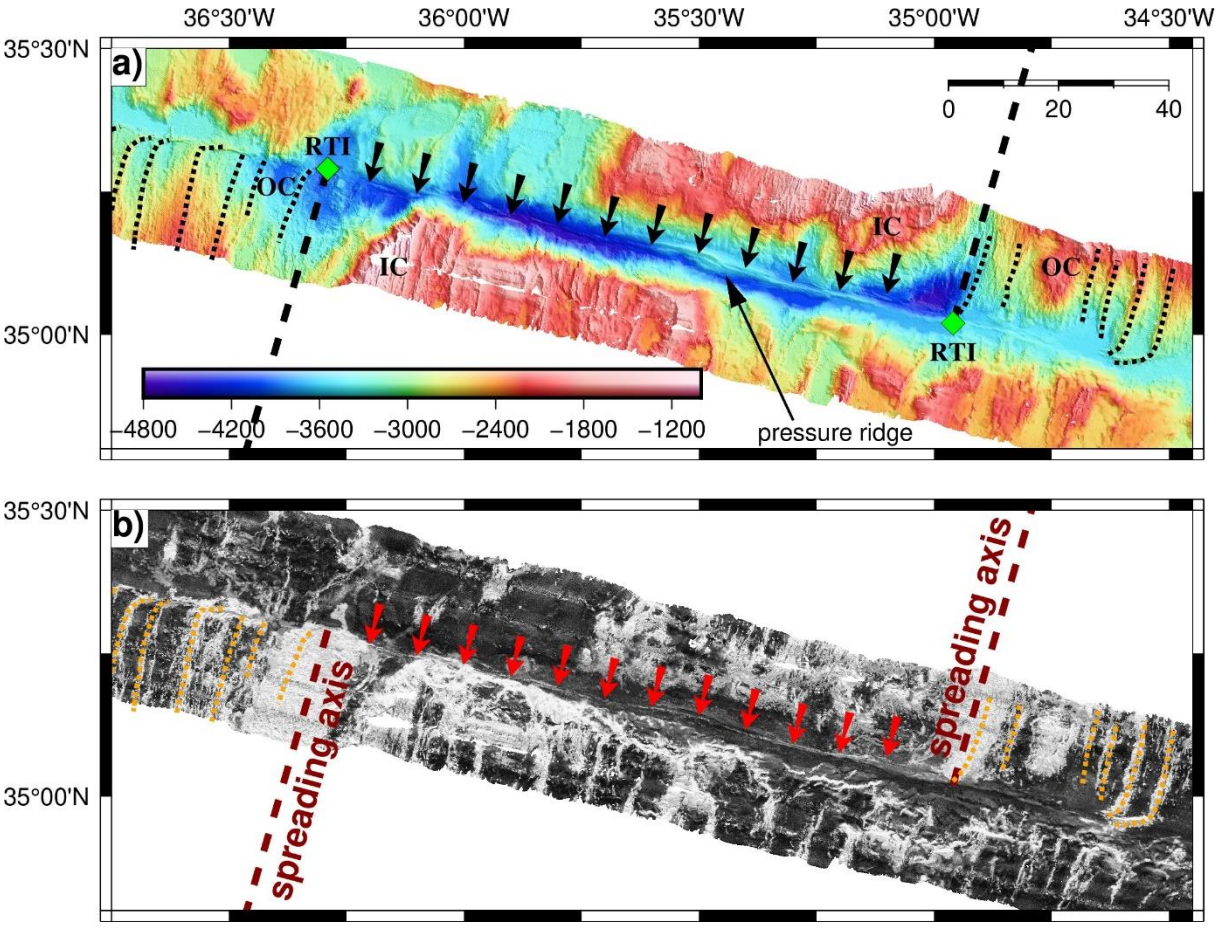

Figure 2. a) Bathymetry and b) backscatter (high intensity in white, low intensity in black) from the Kongsberg EM122 echosounder survey of the Oceanographer transform fault (bathymetric data are combined from cruise M170 and MSM122; backscatter: only MS122); RTI: ridge-transform intersection predicated from right-angular geometry; IC: inside corner; OC: outside corner; dashed lines: ridges indicating robust magmatic activity; arrows: transform plate boundary identified using both bathymetry and backscatter.

3.2 Seismological data

During RV METEOR cruise M170 a seismological network was planned to be operated between 21 January to 2 February 2021, monitoring seismicity along the Oceanographer Transform Fault using ocean-bottom-seismometers (OBS) and hydrophones (OBH). The network consisted of 6 Trillium Compact OBS, 12 short-period (4.5 Hz geophone) OBS and 11 OBH from GEOMAR's OBS pool. Unfortunately, two short-period OBS only recorded on the hydrophone channel, leaving effectively 10 short-period OBS and 13 OBH. An unforeseen medical incident during instrument recovery forced us to leave the study area on the 2 February after recovering only the 11 OBH. The remaining OBS stayed on the seabed until RV METEOR cruise M175 in early June 2021 (Figure 3). Four OBS stopped recording in March 2021 but luckily were equipped with an absolute clock allowing timing without corrections. For the other OBS/H, clocks were synchronized before and after recovery, and the time drift was corrected assuming a linear drift.

The detection threshold dropped after the degradation of the network from ~11 events per day to less than one event per day after only 11 OBS were available (Figure S1) and will be outlined below. This also resulted in a change in the magnitude of completeness, increasing from Mw=2.2 to Mw=2.8 after the network degraded (Figure S2).

4. Seismic events and methodology

At the Oceanographer transform fault, seabed-moored seismic stations were deployed at intervals of 10-15 km within the transform valley, covering the active transform fault and the adjacent inside corner highs (Figure 1b). Our dataset was composed of 13 single channel (hydrophone only) and 13 four component recordings. Unfortunately, this heterogeneous layout of instruments made it difficult to rely on machine-learning detection of earthquakes in continuous seismic time series as those tools require either three-component data when trained using onshore seismic stations (e.g., Münchmeyer et al., 2022) or four component data for marine seismic networks (Bornstein et al., 2024). We therefore searched for larger earthquakes (i.e., about magnitude 2 or larger) in the continuous time series using a traditional short-term-average to long-term-average ratio (STA/LTA) trigger algorithm. In addition, for the first 12-days with 26 working OBS, we also checked daily records visually for additional small magnitude earthquakes, as we were interested in identifying as many earthquakes as possible. However, we only included earthquakes detected on four OBS/H with at least one S-

onset time. Later, after the network was degraded, we only considered events that were recorded at 6 or more stations with two S-wave onsets to provide reliable event locations. This approach allowed for appropriate coverage after the number of recording stations was reduced. Events were registered into a SEISAN database (Havskov & Ottemöller, 2000) and P- and S-wave onset times were determined by a human operator. Each onset has been classified into one of four categories, having picking errors of ±0.05 s, ±0.1 s, ±0.15 s and ±0.2 s, respectively. In general, the P-wave phase-pick error is of the order of ±0.05-0.1 s, while most S-wave phase-pick errors were larger at between ±0.1-0.2 s.

The quality of focal parameters of local earthquakes is inherently associated with a number of features, including the total number of phase readings, the number of P- and S-wave arrivals, the distance of each station from the epicentre, and the azimuthal distribution of stations. In addition, a correct earthquake location requires a correct velocity structure, which is never exactly known and results in a trade-off between velocity model and earthquake parameters. Theoretical arrival times were calculated using a 1D velocity-depth function derived from a seismic refraction survey across the transform fault (Ambos & Hussong, 1986), showing P-wave velocity (Vp) increasing from 2.8 km/s near the seafloor to 6.1 km/s at 2 km depth and to 6.8 km/s at 5 km. The underlying upper mantle has velocities of 8 km/s. Shear-wave velocity (Vs) was constrained from a constant ratio between P- and S-wave velocity (Vp/Vs) of 1.8 as revealed by a modified Wadati plot (Figure S3). For hypocentre determination, we used the non-linear oct-tree search algorithm of the NonLinLoc program package (Lomax et al., 2000). Travel times in the model were calculated using the finite-difference solution to the Eikonal equation (Podvin & Lecomte, 1991). The oct-tree algorithm provides more reliable information on location uncertainties than linearized inversions by exploring the probability density functions (PDF) of each individual event over the search area. The maximum likelihood location is chosen as the preferred location and for each event NonLinLoc estimates a 3D error ellipsoid (68% confidence) from the PDF.

To minimize the effects of 3D wave-propagation, station corrections were calculated and iteratively updated until the average RMS (root-mean-squares) misfit yields a minimum. For this procedure, we used earthquakes observed by five or more stations that were sampled during the first 12 days and showing an epicentral gap of <180°. Station corrections reduced the initial RMS value from ~0.12 s to ~0.07 s, and the Gaussian distribution of residuals (Figure S4) show that the resulting station terms are appropriate.

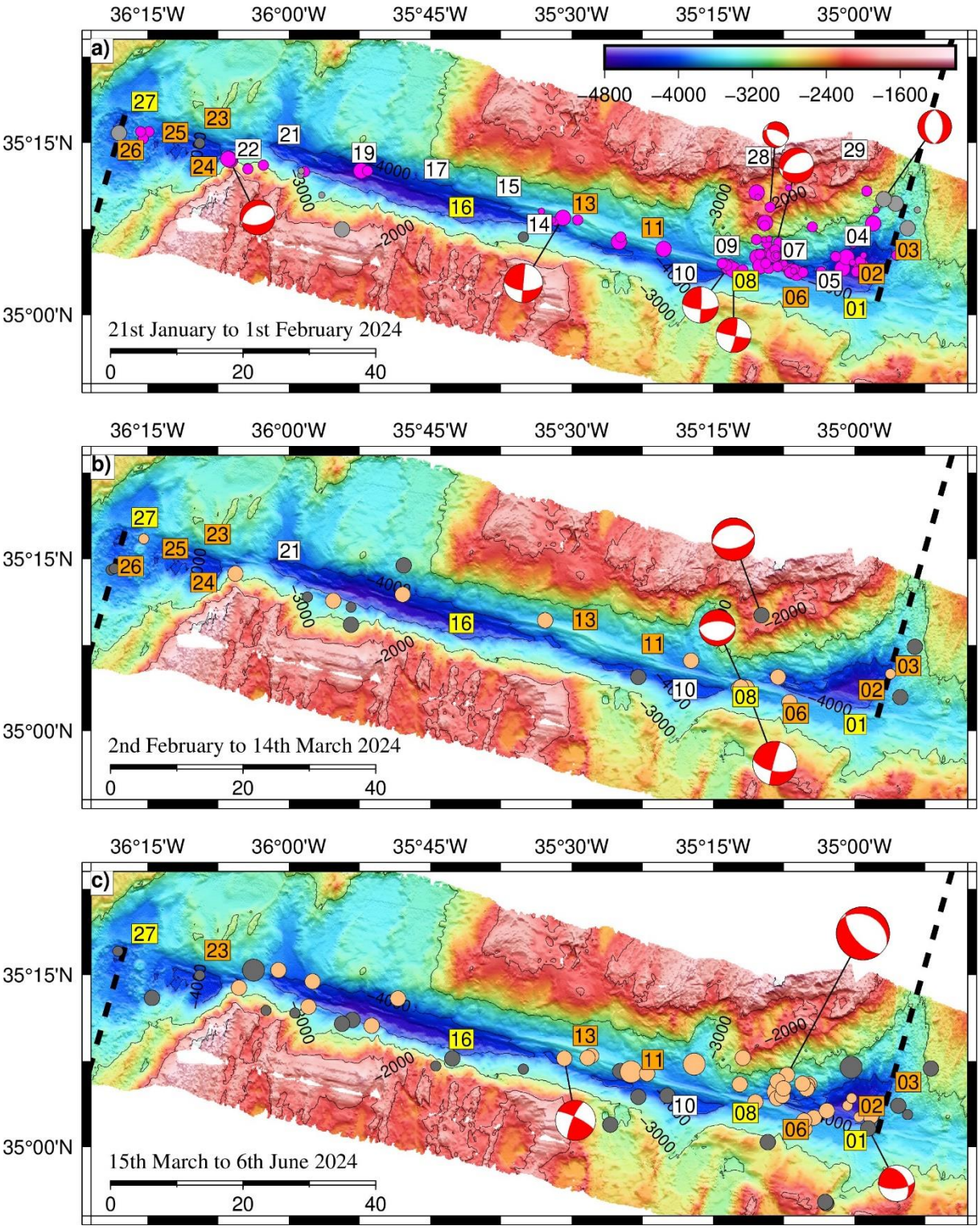

Figure 3. Distribution of local seismicity superimposed to the new multibeam bathymetry: circles show epicentres (0.4 < Mw ≤ 3.9); size of circles scales with magnitude. Magenta (first 12-days of deployment, highest quality) and orange (degraded network) circles indicate events recorded within the network (gap of ≤180°). Grey circles indicate events with a gap>180°. Seismicity plotted as a function of OBS availability: a) 26 OBS 22-day in January, b) 15 OBS until mid-March, c) 11 OBS from mid-March to early July.

Moment magnitudes were obtained using the method and code of Ottemöller & Havskov (2003), which searches for the combination of seismic moment (M_0) and corner frequency (f_0) that fits the observed spectra. During the deployment, the strongest local earthquake (www.isc.ac.uk/cgi-bin/web-db-run?event_id=620226238) was also reported in the global seismic catalogue of the International Seismological Centre (ISC). We estimated its moment magnitude with 3.9 and ISC its magnitude with 3.5, but ISC reported the surface wave magnitude Ms instead of Mw. A several percent lower Ms than Mw is expected for magnitudes below Ms=5-6 (Johnston, 1996; Sawires et al., 2019) and therefore, our magnitude estimates seem to be reliable, especially as OBS sometimes suffer from poor coupling and unknown effects can contribute to the transfer functions.

To provide hypocenters with high precision, we follow the approach of Harderbeck & Husen (2010); thus, ideally, eight or more travel time arrivals, including one S-onset and one arrival time within the focal depth's distance from the epicenter are required (Chatelain et al., 1980). Additionally, a correctly timed S-wave arrival recorded within 1.4 focal depth's distance from the epicenter is also required to improve focal depth (Gomberg et al., 1990). We relaxed these rules to increase the number of events recorded at our temporary network and use as an initial criterion that at least six OBSs should have recorded any earthquake to be processed, including one observed S-wave arrival at a nearby OBS. Further, events should occur within the network and hence have a station gap of <180°. In the case of our network, we have ~1,440 P-wave phase readings and ~740 S-wave readings; thus, the criteria for S-wave arrivals were always met. With an instrument spacing of 10-15 km for a network of 26 OBSs (Fig. 1b), we have a dense station separation and coverage of the median valley, allowing us to locate events at high precision and revealing that most events occur at crustal level or within the uppermost mantle at focal depths of <15 km below seafloor. Similar features were found at other mid-ocean ridge settings (e.g., Parnell-Turner et al., 2017; Grevemeyer et al., 2013; 2019). After the network degraded, only events of Mw~2.6 or larger fulfilled the criteria.

In order to evaluate focal parameters, we used an iterative location procedure. Initially, only Vp structure and P-onset times were used. In a second step, we included S-waves, assessing S-wave velocity from Vp/Vs ratio. Both approaches provide matching epicentral locations and focal depths. Gaussian distribution of residuum's suggests that appropriate station terms have been applied (Figure S4).

Focal mechanisms (Table 1) were derived from P-wave first motions using FOCMEC (Snoke et al., 1984) and FPFIT (Reasenberg & Oppenheimer, 2019) and we chose only those where both procedures provide a common solution (Figure 4).

5. Results and Interpretation

5.1 Bathymetry and backscatter intensity

The new multibeam data cover a roughly 10,000 km² large area around the Oceanographer Transform and the beginning of the adjacent fracture zones in both the east and the west, including the intersections with the MAR. The Oceanographer OTF is shown as a 120 km long, up to 15 km wide and over 4000 m deep depression (Figure 2a). The valley is flanked by steep mountains or walls, which, at the inside corner highs, culminate in less than ~1500 m water depth. The greatest water depths of over 4500 m are reached in the nodal basins at the eastern RTI as well as the western half of the transform valley.

Based on a right-angular geometry at the intersection between the spreading axis and the transform fault, RTIs would occur at the centre and terminus of the median valley of the adjoining segments of the MAR (Figure 2). In the vicinity of both RTIs of the Oceanographer, the median valley shows a triangular shape. At the inside corners and most prominent in the vicinity of the eastern RTI (Figure 5a), a number of terraces and escarpments occur, showing evidence for down-slope land sliding and mass wasting. They do not parallel the trend of the spreading axis, but strike SW-NE. Near the summit, the morphology of SW-NE striking lineations indicates normal faulting and it is reasonable to suggest also the escarpments on the middle slope represent hanging walls of large normal faults. At the lower slope of the inside corner, some terraces strike parallel to the strike of the transform, showing a stairway-like morphology.

The active transform fault runs within the deep transform valley. The shallowest setting within the valley is a pressure ridge-like feature near 35°20’W roughly halfway between the ridge transform intersections (Figure 2a). It marks a segment boundary of shallower seafloor to the east and deeper seafloor to the west. On either side of the pressure ridge, the fault stretches out to the RTIs. Westward between 35°40’W and 36°W, the fault trace is composed of subparallel lineations or small subdued ridges. From the pressure ridge eastward, the fault strand is marked by an up to 500 m high (with respect to the surrounding valley floor) and up to 4 km wide ridge-like feature. This ridge is itself cut by up to 12 km long and up to 100 m

deep grooves. The transform fault shows characteristic kinks where the inside corners impinge on the transform valley and hence the trace of the transform steps or curves towards the inside corners, forming secondary segment boundaries. Facing the MAR valleys, the fault strands show small subdued ridge-like morphology paralleling the strike of the transform. However, clear fault strands disappear approaching the RTIs.

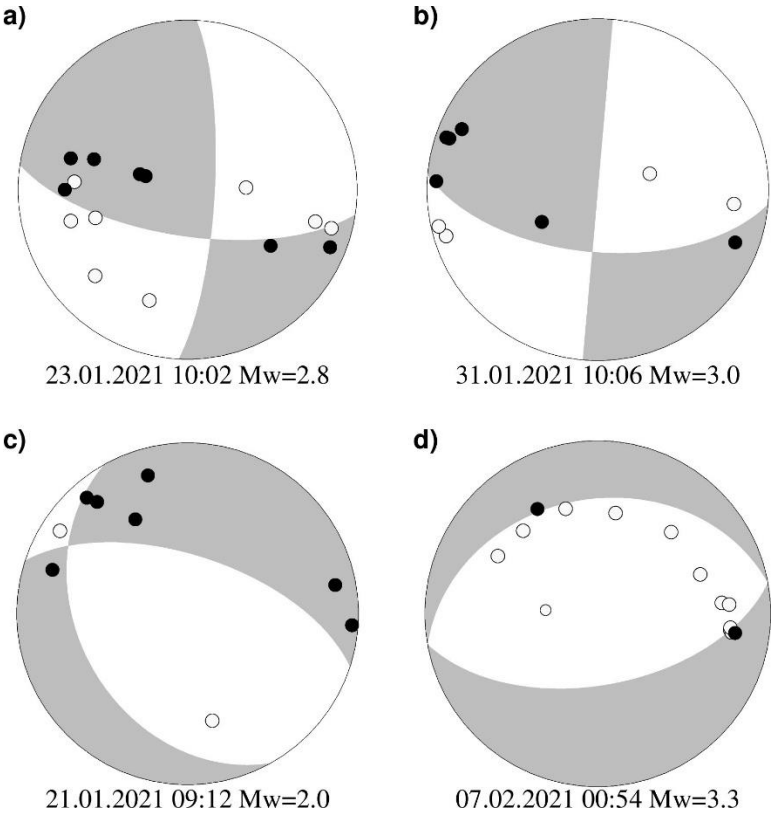

Figure 4. Examples of focal mechanisms from first motion polarities: a) and b) strike-slip events away from RTIs; c) and d): normal faulting near RTI/inside corner high.

Backscatter intensity of the EM122 echosounder is a measure of the strength of the energy being returned from the seabed. The returned signal is strong from either steep morphology facing the vessel or rough and young volcanic seabed, but gets weak over thickly sedimented seafloor. Considering the effects of the bathymetry, backscatter is strongest where the mid-ocean ridge joins the transform valley (Figure 2b), indicating ongoing or recent magmatic activity, lacking a thick sedimentary blanket. At the western intersection of the MAR with the transform, strong backscatter extends rather symmetrically along the centre of the spreading axis and is even slightly overshooting onto the adjoining older plate. At the eastern

intersection, backscatter intensity along the spreading axis is asymmetric, being strong in the outside corner and weak where the median valley of the MAR approaches the nodal basin.

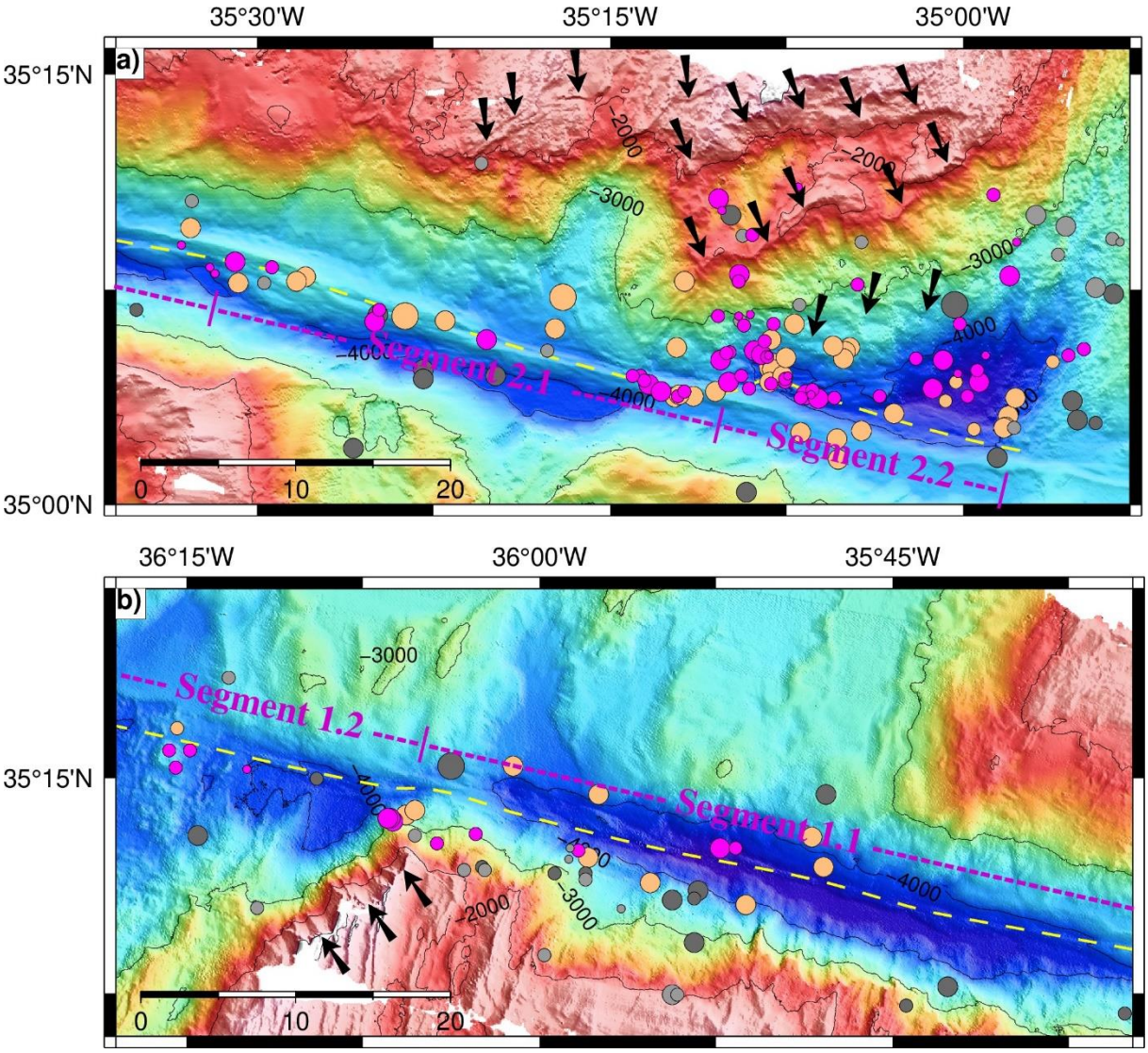

Figure 5. Zoom into seismic segments showing seismicity on bathymetry gridded at 50 m; a) eastern segment 2 of the Oceanographer OTF, b) western segment 1. Arrows indicate normal faults, escarpments and terraces revealed in seafloor morphology; yellow dashed line: plate boundary from bathymetry and backscatter intensity (see Fig. 2).

Within the transform valley, the fault trace shows up with intermediate backscatter intensities in multibeam backscatter data, while the surrounding transform valley basin shows low backscatter intensities, suggesting that the seabed is covered by sediments. This interpretation is supported by areas of rather flat seafloor, indicating sediment ponds. Sediments are

probably derived from mass wasting and sediment transport from the steep slopes of the transform shoulders into the valley. In general, the active fault is a continuous feature clearly detectable within the transform valley. However, especially in the eastern nodal basin, the fault is poorly defined, but its backscatter intensity increases as the fault curves westwards out of the basin, running along the small bathymetric ridge before approaching the pressure ridge (Figure 2). At the pressure ridge, the fault curves slightly southward following a small ridge of rather subdued morphology. Before the fault approaches the western intersection with the MAR, the transform valley gets rugged and neither backscatter nor any well-defined bathymetric features clearly outline the fault trace. One interpretation might be that recent mass wasting products cover the active fault. Thereafter, higher backscatter outlining the fault strand moves towards the median valley of the adjoining western MAR segment. Here, a small bathymetric ridge defines the transform. Approaching the RTI, the fault trace disappears in the strong backscatter signal of recent volcanic activity.

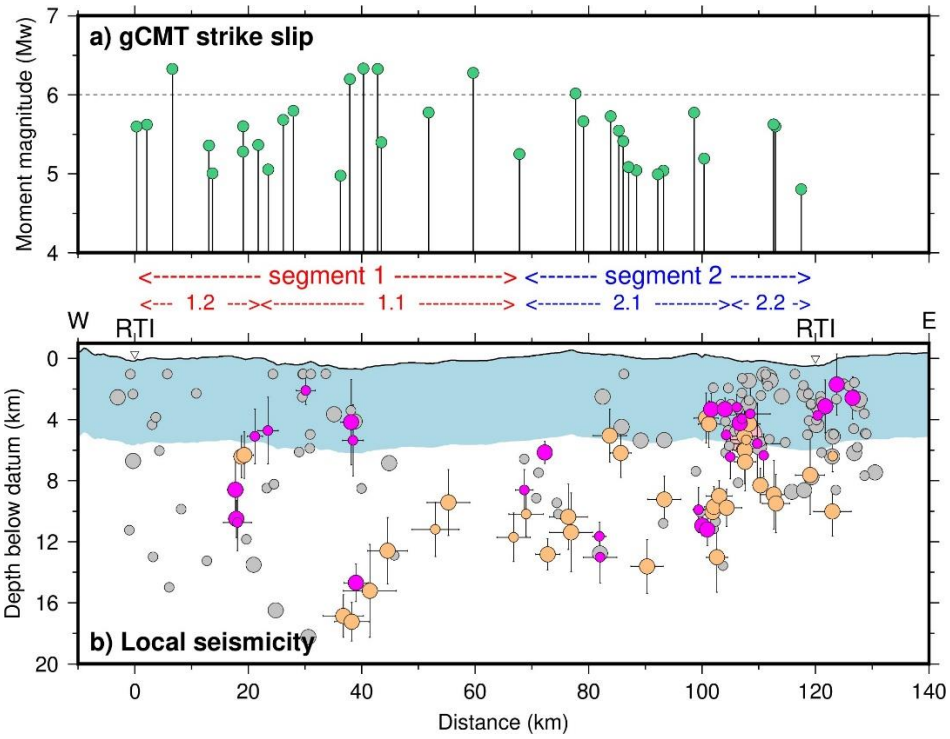

Figure 6. a) Profile showing strike-slip earthquakes along the Oceanographer transform from the global GCMT catalogue (Dziewonski et al., 1981; Ekström et al., 2012). b) Vertical profile of local Micro-seismicity along the transform. Coloured circles as in Fig. 3. The blue shaded area indicates a 5 km thick of oceanic crust derived from seismic refraction data (Ambos & Hussong, 1986).

Based on the bathymetric and backscatter data, we can define a segmented transform fault. Thus, west of the pressure ridge, we have two segments named 1.1 and 1.2, where 1.1 is the main segment just west of the pressure ridge (Figures. 5 and 6a). The two segments east of the pressure ridge are 2.1 and 2.2 with the latter being near the inside corner.

In the vicinity of the RTIs, the seafloor is generally deepest where the MAR joins the transform valley, but towards the adjoining fracture zones the seafloor shallows rapidly. Near the western RTI, the transition is more gradual, but rather abrupt at the eastern RTI rising from ~4400 m to ~3500 m approaching the outside corner and the adjacent fracture zone valley. On either side of the active transform, we see a number of volcanic ridges approaching and sometimes intruding into the fracture zone (Figure 2a). At the western fracture zone, they are well preserved, J-shaped and a common feature in the outside corner. These ridges basically extend across the entire fracture zone and terminate at the toe of the northern shoulder of the valley. In the east, a 25-30 km wide domain shows little evidence for such ridges in the vicinity of the RTI, but east of 34°30'W two ridges cut into the fracture zone, including a volcanic feature running obliquely across the entire fracture zone valley. Backscatter corroborates the interpretation of seafloor morphology. Thus, volcanic or J-shaped ridges show high backscatter and terminate on the older plate (Figure 2b), suggesting that some volcanic rocks erupted across the plate boundary onto the older plate. Near the eastern RTI, high backscatter generally terminates roughly midway of the fracture zone (Figure 2b) valley and hence ~5-8 km from the toe of the shoulder of the older plate, instead of terminating at the toe as observed at the western RTI. In general, J-shaped ridges cutting into the fracture zone show gaps between them suggesting they form episodic.

5.2 Micro-seismicity

During the 12 days when the full network operated, we located 115 earthquakes, resulting in an average of ~11 events per day (Fig. 3a). Thereafter, we sampled additional 87 events (Figure 3b and 3c) over 128 days, resulting in a total number of 202 local earthquakes. Focal depths of well-recorded earthquakes are between ~1 km to 10 km at both RTIs and reach 4 to 16 km in the transform valley (Figure 6b).

Figure 3 shows the availability of OBS as a function of time and seismicity recovered during the matching period. In addition, thirteen robust focal mechanisms (Table 1, Figures 3 and 4) could be estimated to evaluate the local stress field. During the operation of the full network

before 2 February 2021, only 9 events had a gap >180° and hence may have suffered from a trade-off between geographical location and depth, while 106 local earthquakes had well-resolved focal parameters. Thereafter, network degradation and hence fewer stations may result into a decreased azimuthal coverage of some local earthquakes, but most events, eastward of the pressure ridge and segment boundary near 35°25'W have generally well resolved hypocentres, especially those with a gap <180°. Moment magnitudes of the observed seismicity range from 0.4 < Mw ≤3.9, but the magnitude of completeness dropped from 2.2 to 2.8 after the number of available OBS decreased from 26 to 11 (Figure S2).

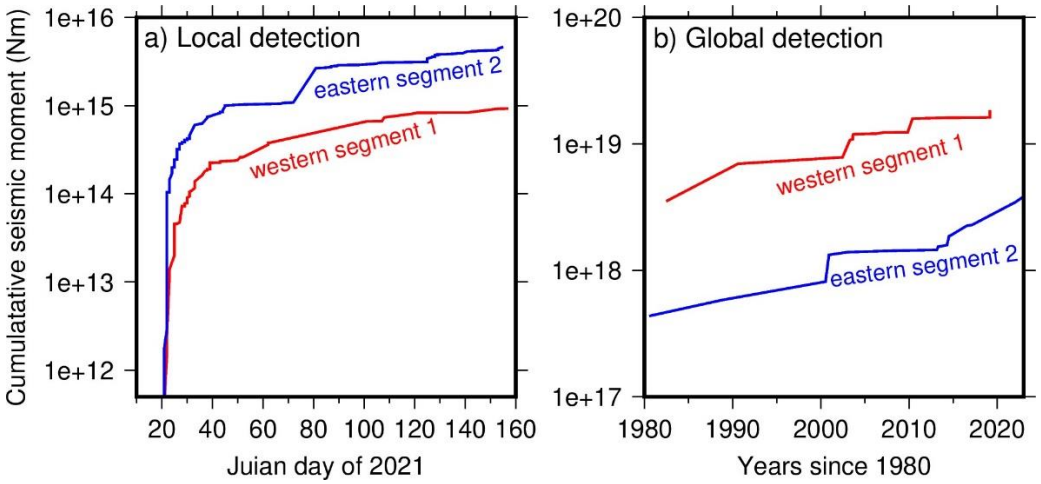

Figure 7. a) Cumulative seismic moment release from the GCMT catalogue (Dziewonski et al., 1981; Ekström et al., 2012) of large strike-slip earthquakes along the Oceanographer transform fault; b) Cumulative moment release from micro-earthquakes. Colour coding for events as defined in Fig. 3a.

Micro-earthquakes away from both RTIs were primarily focused in the transform valley (Figures 3 and 5) and the best located events with a gap <180° cluster along the trace of the fault as revealed by bathymetric data and hence along the segments 1.1 and 2.1. Focal mechanisms show strike-slip faulting consistent with mechanisms reported for Mw>5.5 earthquakes in the global Centroid Moment Tensor catalogue (Dziewonski et al., 1981; Ekström et al., 2012). Only a few events occur away from the fault and below the valley walls. However, those generally have gaps >180° and due to their larger trade-off between focal depth and location, these epicentres might be slightly biased away from the fault trace.

Approaching both RTIs, micro-earthquake epicentres are no longer confined to the simple right-angular geometry of the plate boundary and move away from the trend of the segment 2.1. Instead, the seismicity follows the geological surface expression of the fault (segment 2.2) and hence steps toward the inside corner, forming a second strand of seismic activity and merging at its terminus with the scattered seismic activity associated with the adjoining spreading segment (Figure 5a). In addition, a large number of events occur at the inside corners of both RTIs. In contrast, the westernmost transform segment 1.2 remains seismically rather quiet (Figure 5b), showing little correlation between the geologically defined fault zone and the occurrence of seismic activity.

Focal mechanisms of earthquakes at the inside corner show normal faulting on fault planes subparallel to the trend of the transform valley and include the largest recorded event of Mw~3.9 on the 22 March 2021, which was also reported with Ms~3.5 by the International Seismological Centre (see chapter above). About 70% of the recorded earthquakes occur at the eastern segment of the Oceanographer OTF east of the small pressure ridge near 35°30'W, dominating the seismic moment release along the Oceanographer (Figure 7a). Interestingly, the majority of seismicity is occurring in the vicinity of the eastern RTI. Thus, the estimated b-values of 1.4 are probably dominated by tectonic processes acting on the RTI rather than characterizing the strike-slip faulting.

6. Discussion

6.1 Strike-slip versus extensional tectonics

6.1.1 Seismological constraints

Plate tectonics defines OTF as simple strike-slip plate boundaries. In the Pacific Ocean, local OBS networks yield ample evidence for strike slip faulting at transform faults (e.g., Tréhu and Solomon, 1983; Ren et al., 2023). Large (M>5) earthquakes at Atlantic OTFs have long been known to show simple strike-slip motion (e.g., Sykes, 1967; Bergman and Solomon, 1988; Abercrombie and Ekström, 2000; Grevemeyer, 2020). On the other hand, local micro-earthquake surveys often failed to detect strike-slip tectonics, but rather showed extensional or dip-slip tectonics (e.g., Cessaro and Hussong, 1986; Wilcock et al., 1990; Yu et al., 2021). This discrepancy in the seismogenic behaviour may indicate that OTFs show temporal extensional tectonics between two larger strike-slip events. A number of potential sources of extension across the transform have been proposed, including thermal stress in the young

oceanic lithosphere, topographic loading, or motion of the asthenosphere relative to the surface plate (Wilcock et al., 1990). Yet, OTFs may show a vertical zonation with shallow strike-slip tectonics and deeper-seated extensional tectonics. The latter is supported by observations of Yu et al. (2021), suggesting that the M=7.1 2016 Romanche supersonic strike-slip earthquake (Hicks et al., 2020) ruptured the brittle domain above the 600°C isotherm, while a substantial amount of deformation is accommodated in the semibrittle mylonitic mantle that resides at greater depths. However, contrasting observations were not used to derive a new conceptual model, providing a unifying interpretation.

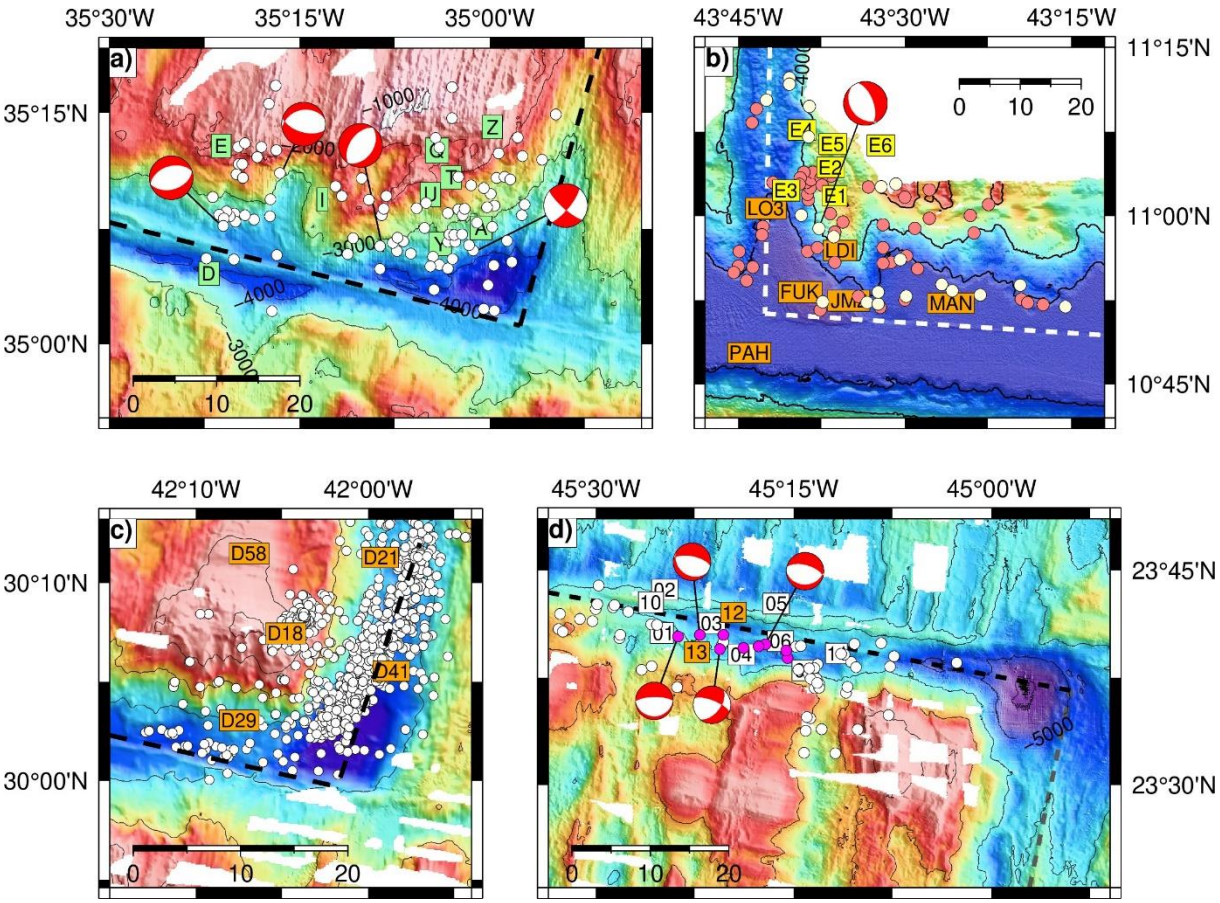

Figure 8. Review of micro-seismicity over Atlantic OTFs and RTIs recorded on networks of ocean-bottom-seismometers; Oceanographer (Cessaro & Hussong, 1986), and Vema (Rowlett and Forsyth, 1984; Louden et al., 1986), Atlantis (Collins et al., 2012), Kane (Wilcock et al., 1990). Multibeam bathymetry plotted with the micro-earthquakes is from the compilations of Grevemeyer et al. (2021) and Ren et al. (2022), except for the Atlantis OTF where data are from Escartin et al. (2022).

Our micro-seismicity survey supports both strike-slip and extensional faulting at the Oceanographer OTF. A key observation is that seismic activity at the eastern RTI occurs over

a broad area across the inside corner, with little seismicity occurring near the RTI along the trace of the transform itself. Similar features were previously found in a number of micro-seismicity studies in the 1970s and 1980s, for example at St. Paul (Francis et al., 1978), Oceanographer (Cessaro & Hussong, 1986; Figure 8a), and Vema (Rowlett and Forsyth, 1984; Louden et al., 1986; Figure 8b). Cessaro & Hussong (1986) studied micro-seismicity and stress patterns at the Oceanographer in the 1980s. Combined, our data and their observations suggest that the Oceanographer transform is persistently showing similar stress pattern over at least 50 years, supporting extensional tectonics near the eastern RTI.

The observation that much of the seismicity at RTIs does not follow the expected right-angular plate boundary, but is cutting across the inside corner domain is not only evidenced by data collected before 1990 but is also a common feature observed in other modern surveys, especially at the Atlantis transform (Figure 8c). Collins et al. (2012) found that most of the detected seismic activity occurred at the western part of the valley at the toe of the Atlantis massif, an oceanic core complex towering over the valley of the MAR and the OTF at the inside corner. Furthermore, a large number of earthquakes occurred away from the ridge axis at the inside corner and the western walls of the median valley. The spatial patterns of the seismic activity suggest that the observed features could be explained by changes in the stress field at the inside corner associated with weak coupling on the adjacent transform (Collins et al., 2012). Rowlett (1981) interpreted such patterns as evidence for internal deformation of the inside corner by secondary faults off from the plate boundary. We instead prefer the interpretation that the observed features are controlled by a plate boundary which is gradually changing its geometry with depth, as indicated by numerical modelling (Furlong et al., 2001; Grevemeyer et al., 2021; Tian et al., 2024), turning the surface strike-slip fault into an oblique shear zone at depth. Fault plane solutions derived from our deployment support this scenario, showing extensional mechanisms near the RTIs where the obliquity of the plate boundary in numerical simulations is strongest. Most importantly, the strike of normal faulting focal mechanisms roughly parallels the strike of normal faults detected in the morphology of the southern slope of the eastern inside corner.

Away from the spreading segments and RTIs, seismicity at the Oceanographer OTF is focused along the morphologically defined transform trace and strike-slip faulting dominates the stress field. Interestingly, observations from the Kane transform (Wilcock et al., 1990) show a different pattern suggesting that extensional tectonics may occur serval tens of kilometres away from the inside corner domain (Figure 8d). Wilcock et al. (1990) suggested

that the observed behaviour at Kane may support temporal extensional tectonics between two larger strike-slip events.

6.1.2 Geomorphological constraints

Bathymetric data from the eastern RTI and inside corner of the Oceanographer OTF show escarpments and lineations running oblique to both the transform fault and the Mid-Atlantic Ridge (Figures 2 and 5), indicating tectonic stresses acting on the inside corner high. They most likely represent fault traces but most are located rather high on the inside corner high (Figure 5a). Continuous escarpments on the middle and lower slope are not visible in the high-resolution bathymetric data. However, observations with the submersible *Alvin* further corroborate evidence as suggested by extensional focal mechanisms, revealing a variety of vertical cliffs that Karson et al. (1984) interpreted as fault planes. These faults exhibit a wide range of fault orientations and even transform-parallel faults show no evidence for strike-slip displacements but show that normal (dip-slip) displacement is ubiquitous (Karson et al., 1984). The locations of the dives correspond in our bathymetric data to small concave escarpments that could be interpreted as marking the location of a fault trace (Figure 5a). We believe that these faults are the surface expression of normal or dip-slip faults that are indicated by our observed micro-seismicity and extensional focal mechanism. The seafloor observations by Karson et al. (1984) also indicate that outside convex terraces at the foot of the inside corner most likely represent talus debris from the exposed faults further upslope (Figure 5a).

Similar observations were made at the eastern RTI of the Vema OTF. *Nautile* dives (Mamaloukas-Frangoulis et al., 1991) also found evidence for normal faulting at the inside corner, striking parallel to the trend of the transform fault. Mamaloukas-Frangoulis et al. (1991) interpreted the geological evidence in terms of stresses supporting “the reactivation of large normal faults on the adjacent flanks of the southern wall and the median ridge”. Such features are also described at the Atlantis massif, a core complex and oceanic detachment fault at the Atlantis transform, where the southern flank of the core complex is cut by a fault and seafloor morphology indicates southward facing normal faults and some degree of southward facing slumping and mass wasting (Escartín et al., 2022). Collins et al. (2012) found that micro-earthquakes are abundant at the inside corner (Figure 8c), but the orientation of stresses is poorly resolved.

All these observations, especially extensional focal mechanisms near RTIs, agree well with the predictions from 3-dimensional geodynamic numerical modelling (Grevemeyer et al., 2021; Tian et al., 2024), which reveal that the mantle flow at depth, driven by a lithospheric kinematic strike-slip boundary condition at an orthogonal surface transform fault, does not exactly mimic the rectilinear plate boundary, but instead, organizes itself into an oblique shear zone with respect to the surface expression of the transform. Simulations suggest that the difference in age and hence strength of the two plates moving in opposite directions causes drag within the younger plate, which in turn, stretches the crust and lithosphere near the RTIs, causing extension and finally nurturing transform valleys. Extensional tectonics at RTIs and below inside corners may also explain the occurrence of the Lost City hydrothermal vent field on the inside corner high of the Atlantis transform (Kelly et al., 2001), a setting generally thought to be an anomalously cold environment. However, extension will preferentially fracture this region and pull up warmer mantle beneath it.

Away from the junction between the MAR and the OTF, seismicity is centred along the topographic trace of the fault and focal mechanisms support strike-slip motion as envisioned in plate tectonics models. This observation is supported by *Alvin* dives and photographic imaging (Fox et al., 1985) as well as backscatter intensity (Figure 2b), showing ongoing tectonism to be focused along a narrow fault system, while the valley walls away from the RTIs exhibit little evidence for recent faulting (Fox et al., 1985).

6.2 Focal depths

Micro-earthquakes along mid-ocean ridges generally do not occur right below the seabed, but 2-3 km deeper. In most cases, earthquakes occurred at depth ranges of 2 to 10 km below seafloor and hence the majority of earthquakes ruptured within the lower crust or uppermost mantle (Wolfe et al., 1995; Collins et al., 2012; Grevemeyer et al., 2013). Focal depth seems to increase with decreasing spreading rate (Grevemeyer et al., 2019), probably reflecting cooler lithospheric temperature. The Kane transform is one of the few examples where local seismicity was studied at a slowly slipping transform fault, indicating that seismic activity was focused at 3-10 km (Wilcock et al., 1990). At the large offset Romanche OTF in the equatorial Atlantic, most micro-earthquakes occurred much deeper at 10-30 km (Yu et al., 2021) and hence within the upper mantle, supporting estimates for the rupture of large strike-slip earthquakes of M>6 with centroids at 8-20 km (Abercrombie and Ekström, 2001; Grevemeyer, 2020). Our study revealed focal depths of well-recorded earthquakes of ~1-10

km at both RTIs, reaching 4-16 km in the transform valley and thus may suggest systematic deepening of earthquake rupture away from the spreading axis (Figure 6b), probably indicating temperatures decreasing with increasing distance to the RTIs. A deepening of micro-earthquakes away from the RTI was also found at the eastern RTI of the Romanche OTF (Yu et al., 2021), but focal depth there reached deeper into the upper mantle.

A seismic refraction study of the Oceanographer OTF (Ambos and Hussong, 1986) found that crust along the transform is in the order of 5 km thick. Roughly 50% of our source depth estimates exceed 5-6 km below the seafloor and hence occur below the seismically derived crust-mantle boundary, suggesting that much of the seismic activity occurs in the uppermost lithospheric mantle, especially along the transform and away from the RTIs. Near both RTIs, however, basically all micro-earthquakes occurred at <5 km and hence above the seismically derived crust-mantle boundary and therefore in the crust.

6.3 Segmentation and transform fault heterogeneity

Bathymetric features in transform valleys, like median ridges, flower structures or pressure ridges, may form in the course of plate boundary reconfiguration and transpression (e.g., Pockalny et al., 1997; Harmon et al., 2018) and might be characterized by variations in crustal thickness or properties (Harmon et al., 2018; Leptokaropoulos et al., 2023). At the Chain OTF, they either mark segments or segment boundaries where seismic characteristics change, perhaps indicating fault damage zones facilitating fluid transport (Leptokaropoulos et al., 2023). At the Oceanographer OTF, a prominent bathymetric feature occurs near 35°20’W to the east of the geometric centre of the transform, which we interpret as pressure ridge (Figures 2a and 5a). Its geographic location is coincident with a seismic segment boundary, revealing that all globally detected large strike-slip earthquakes of Mw >6-6.5 occur solely to the west of the pressure ridge (Figure 6), where the seafloor is characterized by subdued relief. In contrast, only a single globally detected earthquake in the eastern segment reached Mw=6, while all other events were of smaller magnitudes suggesting that the total seismic moment release of the OTF is dominated by the western segment (Figure 7). This kind of transform fault segmentation is inherently related to most large offset OTFs and is a characteristic feature in the global earthquake record (Shi et al., 2022), but it is also documented in local seismicity surveys (e.g., McGuire et al., 2012; Ren et al., 2023).

Interestingly, the micro-seismic record did not support the moment release observed in the global earthquake record. Instead, the eastern segment of the Oceanographer shows much more activity and a higher moment release than the western segment. Thus, when compared to the globally derived seismic moment release, we observe a disparity between the moment release of large versus small earthquakes (Figure 7). One explanation might be that both segments show different frictional properties with the western segment being stronger and the eastern segment being weaker. This interpretation is supported by Shi et al. (2022), defining the eastern segment of the Oceanographer as creeping. Fault creep has been suggested to be controlled by fluid transport and hydrothermal alteration at the Chain OTF (Leptokaropoulos et al., 2023). On the other hand, the seismic moment release of the eastern segment is dominated by seismic activity at the inside corner and thus might not be characteristic for the active strike-slip fault, indicating a poorly understood relationship between segmentation, fault locking, fault creep, and seismic activity.

The new high-resolution bathymetric data indicate that the transform valley of the Oceanographer is much deeper than both adjacent fracture zones of an older age, supporting observation from a global study of 44 OTFs (Grevemeyer et al., 2021) showing that transform valleys are buried at RTIs, with seafloor depth quickly decreasing over a relatively short distance when approaching the fracture zones. This feature has recently been reproduced by numerical simulations (Tian et al., 2024). Yet, depth changes at RTIs disagree with plate tectonics that stipulate crustal aging and hence cooling of the lithosphere causes older seafloor to subside with increasing age (e.g., Parson and Scatter, 1977). Observations near RTIs, however, indicate uplift or shallowing. Burial of transform faults is now suggested to be driven by magmatic activity of the adjacent spreading segment affecting and overprinting the transform valley (Grevemeyer et al., 2021; Tian et al., 2024).

At fast-spreading ridges, it has been concluded that dykes propagating along the ridge axis penetrate into the transform fault (Fornari et al., 1989; Barth et al., 1994; Gregg et al., 2007), rotating in the direction of the transform and increasing the crustal thickness locally (Barth, 1994), sometimes causing intense magmatism on the adjacent older plate (e.g., Gallo et al., 1986; Fornari et al., 1989; Barth et al., 1994). Both ridges overshooting from the adjacent spreading segment into the transform (Marjanovic et al., 2020) and J-shaped ridges cutting across fracture zones are also found at slow- and ultraslow spreading ridges (Grevemeyer et al., 2021). Interestingly, dyke propagation seems to occur exclusively on the outside corner of an RTI (e.g., Gallo et al., 1986; Barth et al., 1994; Grevemeyer et al., 2021). Such features are

well-preserved in the outside corner of the western RTI of the Oceanographer, but occur also at the eastern fracture zone (Figure 2). Gaps between some of these ridges suggest that the emplacement of J-ridges is episodic. However, the overall depth trend of the fracture zones reveals that morphological features mapped on the seafloor are only of minor importance for the burial of transform zones, suggesting that much of the magmatic activity may occur in the form of intrusions. Guo et al. (2023) studied gravity field anomalies over transform-fracture-zone systems, including the Oceanographer OTF, and found evidence for a second phase of magmatic accretion at RTIs, adding roughly 1-2 km of crust to OTFs while crust and lithosphere are transported into the fracture zone.

7. Conclusions

We investigated the morphology, seismicity and deformation of the Oceanographer transform fault using swath-mapping bathymetric data and constraints from ocean-bottom seismology. Prominent changes in seafloor depth between the transform and its fracture zones and the seismicity of the Oceanographer transform reveals systematic changes in stress patterns along the fault, supporting more complex dynamics than expected. Thus, the idea that ridge-transform intersections are defined by a simple right-angular geometry connecting two adjacent spreading segments is inconsistent with our observations. Instead, we found that the transform fault is segmented both morphologically and seismically. As observed at other transforms, major segment boundaries within the transform valley might be characterized by prominent bathymetric features. At the Oceanographer, a pressure ridge near 35°20’W separates two segments of distinctive moment release. In addition, smaller secondary segment boundaries occur near both inside corners where the transform approaches the median valley of the adjoining spreading segments, stepping into the median valleys.

The ridge-transform intersections of the Oceanographer are characterized by widespread seismicity cutting across the inside corner and normal faulting roughly parallel to the trend of the transform fault. We hypothesize that the wide transform valley is formed in the vicinity of RTIs by extensional tectonics over a roughly ~15 km wide domain, challenging the definition of OTFs as inherently conservative plate boundaries. However, away from the RTIs, the transform valley crust is passively moved along the transform boundary with deformation and seismic activity occurring along a narrow strike-slip fault and crust is neither formed nor consumed.

Acknowledgements

We thank Captains Detlef Korte and Rainer Hammacher and their crews for the excellent sea-going operation aboard R/V METEOR during cruises M170 and M175. Both cruises were funded by the German Science Foundation (DFG / GPF20-3/090). Additional bathymetric and backscatter data used in this study were collected aboard the R/V MARIA S: MERIAN cruise MSM122. We acknowledge the support of Captain Ralf Schmidt and his crew and appreciate funding from the DFG (GPF22-1/039). Data analysis was co-funded by the European Research Council (ERC) under the framework programme Horizon Europe of the European Union (ERC-TRANSFORMERS-101096190).

Data Availability Statement

Raw multibeam bathymetric data can are from Grevemeyer & Unger-Moreno, 2022; https://doi.org/10.1594/PANGAEA.942780) and Grevemeyer et al. (2024; https://doi.org/10.1594/PANGAEA.965974). The open source software MB-System (Caress, D. W., and D. N. Chayes, MB-System: Mapping the Seafloor, available at https://www.mbari.org/technology/mb-system/) was used to process the multibeam bathymetric data. Waveform event data from the ocean-bottom-seismometers are from Grevemeyer & Lange (2024; https://doi.pangaea.de/10.1594/PANGAEA.973137) and were processed using the SEISAN software package (Havskov & Ottemöller, 2000) version 12, available at https://www.geo.uib.no/seismo/SOFTWARE/SEISAN/). The Global Centroid-Moment-Tensor (CMT) data were extracted from the Global CMT Catalogue (Dziewonski et al., 1981; Ekström et al., 2012). The data are available at https://www.globalcmt.org/. Maps and figures were created through Generic Mapping Tools (GMT) version 6 (Wessel et al., 2019) licensed under LGPL version 3 or later, available at https://www.generic-mapping-tools.org/.

References

Abercrombie, R. E., & G. Ekström (2001). Earthquake slip on oceanic transform faults. *Nature*, 410, 74–77, doi:10.1038/35065064.

Ambos E.L., & Hussong, D. M. (1986). Oceanographer transform fault structure compared to that of surrounding oceanic crust: results from seismic refraction analysis. *Journal Geodynamics*, 5, 79-102, doi:10.1016/0264-3707(86)90024-4.

Barth, G. A., Kastens, K. A., & Klein, E. M. (1994). The origin of bathymetric highs at ridge-transform intersections: A multidisciplinary case study at the Clipperton Fracture Zone. *Marine Geophysical Researches*, 16(1), 1–50. https://doi.org/10.1007/BF01812444

Barth, G. A. (1994). Oceanic crust thickens approaching the Clipperton Fracture Zone, *Marine Geophysical Researches*, 16, 51-64, doi:10.1007/BF01812445

Behn, M.D., Boettcher, M. S. & Hirth G. (2007). Thermal structure of oceanic transform faults. *Geology*, 35, 307-310, doi:10.1130/G23112A.1.

Bergman, E.A. & Solomon S. C. (1988). Transform fault earthquakes in the North Atlantic: Source mechanisms and depth of faulting. *Journal of Geophysical Research*, 93(B8), 9027-9057, doi:10.1029/JB093iB08p09027.

Bornstein, T., Lange, D., Münchmeyer, J., Woollam, J., Rietbrock, A., Barcheck, G., Grevemeyer, I., Tilmann, F. (2024). PickBlue: Seismic phase picking for ocean bottom seismometers with deep learning. *Earth and Space Science*, 11, e2023EA003332. https://doi.org/10.1029/2023EA003332

Cessaro, R. K., & D.M. Hussong (1986), Transform seismicity at the intersection of the Oceanographer fracture zone and the Mid-Atlantic Ridge. *Journal of Geophysical Research*, 91(B5), 4839– 4853, doi:10.1029/JB091iB05p04839.

Chatelain, J.L., Roecker, S.W., Hatzfeld, D., & Molnar, P. (1980). Microearthquake seismicity and fault plane solutions in the Hindu Kush region and their tectonic implications. *Journal of Geophysical Research*, 85(B3), 1365-1387, doi:10.1029/JB085iB03p01365.

Collins, J. A., Smith, D. K. & McGuire J. J. (2012), Seismicity of the Atlantis Massif detachment fault, 30°N at the Mid-Atlantic Ridge, *Geochemistry, Geophysics, Geosystems*, 13, Q0AG11, doi:10.1029/2012GC004210.

DeMets, C., Iaffaldano, G., & Merkouriev, S. (2015). High-resolution Neogene and Quaternary estimates of Nubia-Eurasia-North America Plate motion. *Geophysical Journal International*, 203, 416–427, doi:10.1093/gji/ggv277.

Dziewonski, A. M., Chou, T.-A., & Woodhouse, J. H. (1981). Determination of earthquake source parameters from waveform data for studies of global and regional seismicity. Journal of Geophysical Research, 86(B4), 2825–2852. https://doi.org/10.1029/JB086iB04p02825

Ekström, G., Nettles, M., & Dziewoński, A. M. (2012). The global CMT project 2004–2010: Centroid-moment tensors for 13,017 earthquakes. Physics of the Earth and Planetary Interiors, 200–201, 1–9. https://doi.org/10.1016/j.pepi.2012.04.002

Escartín, J., John, B., Cannat, M., Olive, J.-A., Cheadle, M. Früh-Green, G., & Cotterill, C. (2022). Tectonic termination of oceanic detachment faults, with constraints on tectonic uplift and mass wasting related erosion rates. *Earth and Planetary Science Letters*, 2022, 554, doi:10.1016/j.epsl.2022.117449.

Fornari, D. J., Gallo, D. G., Edwards, M. H., Madsen, J. A., Perfit, M. R., & Shor, A. N. (1989). Structure and topography of the Siqueiros transform fault system: Evidence for the development of intra-transform spreading centers. *Marine Geophysical Researches*, 11(4), 263–299. https://doi.org/10.1007/BF00282579

Fox, P. J., Moody, R. H., Karson, J. A., Bonatti, E., Kidd, W. S. F., Crane, K., Gallo, D. G., Stroup, J. B., Fornari, D. J., Elthon, D., Hamlyn, P. Casey, J. F., Needham D., & Sartori R. (1985). The geology of the oceanographer transform: the transform domain. *Marine Geophysical Researches*, 7, 329-358, doi:10.1007/BF00316773.

Francis, T. J. G., Porter, I. T. and Lilwall, R. C. (1978). Microearthquakes near the eastern end of St. Paul's Fracture Zone. *Geophysical Journal Royal Astronomical Society*, 53, 201-217, doi:10.1111/j.1365-246X.1978.tb03738.x.

Furlong, K. P., Sheaffer, S. D., & Malservisi, R. (2001). Thermal-rheological controls on deformation within oceanic transforms. *Geological Society of London Special Publications*, 186, 65–83. doi:10.1144/GSL.SP.2001.186.01.05.

Gallo, D. G., Fox, P. J., & Macdonald, K. C. (1986). A Sea Beam investigation of the Clipperton Transform Fault: The morphotectonic expression of a fast slipping transform boundary. *Journal of Geophysical Research*, 91(B3), 3455–3467. https://doi.org/10.1029/JB091iB03p03455.

Gomberg, J.S., Shedlock,K.M., and Roecker, S.W., 1990, The effect of S-Wave arrival times on the accuracy of hypocenter estimation. *Bulletin Seismological Society America*, 80, 1605-1628, doi: 10.1785/BSSA08006A1605.

Gregg, P. M., Lin, J., Behn, M. D., & Montési, L. G. J. (2007). Spreading rate dependence of gravity anomalies along oceanic transform faults. *Nature*, 448(7150), 183–187, https://doi.org/10.1038/nature05962

Grevemeyer, I., Reston, T.J., & Moeller, S. (2013). Microseismcity of the Mid-Atlantic Ridge at 7°–8°15′S and at the Logatchev Massif oceanic core complex at 14°40′N–14°50′N. *Geochemistry, Geophysics, Geosystems*, 14, 3532–3554, doi:10.1002/ggge.20197.

Grevemeyer, I., Ranero, C.R., & Ivandic, M. (2018). Structure of oceanic crust and serpentinization at subduction trenches: *Geosphere*, 14(2), 395–418, doi:10.1130/GES01537.1.

Grevemeyer, I., Hayman, N.W., Lange, D., Peirce, C., Papenberg, C., Van Avendonk, H.J.A., Schmid, F., Gómez de La Peña, L., & Dannowski, A. (2019). Constraining the maximum depth of brittle deformation at slow- and ultraslow-spreading ridges using microseismicity: *Geology*, 47, 1069–1073, doi:10.1130/G46577.1.

Grevemeyer, I. (2020). Upper mantle structure beneath the Mid-Atlantic Ridge from regional waveform modelling. *Bulletin Seismological Society America.* 110, 18–25, doi:10.1785/0120190080117.

Grevemeyer, I., Ruepke, L., Morgan, J. P., Iyer, K. and Devey, C. W. (2021) Extensional tectonics and two-stage crustal accretion at oceanic transform faults. *Nature*, 591, 402-407, doi:10.1038/s41586-021-03278-9.

Grevemeyer, I. & Unger-Moreno, K. (2022) Multibeam bathymetry raw data (Kongsberg EM 122 working area dataset) of RV METEOR during cruise M170 (dataset), *PANGAEA*, https://doi.org/10.1594/PANGAEA.942780

Grevemeyer, I., Ruepke, L. H; Zhang, Y. & Schumacher, M. (2024) Multibeam bathymetry raw data (Kongsberg EM 122 entire dataset) of RV MARIA S. MERIAN during cruise MSM122, *PANGAEA*, https://doi.org/10.1594/PANGAEA.965974

Grevemeyer, I. & Lange, D. (2024) Microseismicity in the period 01/2021-06/2021 at the Oceanographer transform fault, Mid-Atlantic Ridge, 36°N, SEISAN/MSEED waveform files, *PANGAEA*, https://doi.pangaea.de/10.1594/PANGAEA.973137

Guo, Z., Liu, S., Ruepke, L., Grevemeyer, I., Morgan, J. P., Lange, D., Ren, Y. & Tao, C. (2023). Disparate crustal thicknesses beneath oceanic transform faults and adjacent fracture zones revealed by gravity anomalies. *Geology*, 51, 300–304. doi:10.1130/G50429.1.

Harmon, N., Rychert, C., Agius, M., Tharimena, S., Le Bas, T., Kendall, J. M., & Constable, S. (2018). Marine geophysical investigation of the Chain Fracture Zone in the equatorial Atlantic from the PI-LAB experiment. *Journal of Geophysical Research: Solid Earth*, 123, 11,016–11,030. https://doi.org/10.1029/2018JB015982

Havskov, J., & Ottemöller,L. (2000). SEISAN earthquake analysis software. *Seismological Research Letters*, 70, 532–534, doi:10.1785/gssrl.70.5.532.

Hicks, S. P., Okuwaki, R., Steinberg, A., Rychert, C. A., Harmon, N., Abercrombie, R. E., Bogiatzis, P., Schlaphorst, D., Zahradnik, J., Kendall, J. M., Yagi, Y., Shimizu, K., & Sudhaus, H. (2020). Back-propagating supershear rupture in the 2016 Mw 7.1 Romanche transform fault earthquake. *Nature Geoscience*, 13, 647–653, doi:10.1038/s41561-020-0619-9.

Husen, S., & Hardebeck, J. L. (2010). Earthquake location accuracy, *Community Online Resource for Statistical Seismicity Analysis*, doi:10.5078/corssa-55815573.

Johnston, A. C. (1996). Seismic moment aseessment of earthquakes in stable continental regions - I. Instrumental seismicity. *Geophysical Journal International*, 124, 381–414, doi:10.1111/j.1365-246X.1996.tb07028.x.

Karson, J. A., Fox, P. J., Sloan, H., Crane, K., Kidd, W. S. F., Bonatti, E., Stroup, J. B., Fornari, D. J., Elthon, D., Hamlyn, P., Casey, J. F., Gallo, D. G., Needham, D., and Sartori, R. (1984). The geology of the Oceanographer Transform: The ridge-transform intersection. *Marine Geophysical Researches*, 6, 109–141, doi:10.1007/BF00285956.

Kelly, D. S. et al., 2001. An off-axis hydrothermal-vent field near the Mid-Atlantic Ridge at 30°N, *Nature*, 412, 145–149, doi: 10.1038/35084000.

Leptokaropoulos, K., Rychert, C. A., Harmon, N., Schlaphorst, D., Grevemeyer, I., Kendall, J.-M. & Singh, S. C., 2023, Broad fault zones enable deep fluid transport and limit earthquake magnitudes. *Nature Communications*, 4, 5748, doi:10.1038/s41467-023-41403-6

Ligi, M., Bonatti, E., Gasperini, L., & Poliakov, A. N. B. (2002). Oceanic broad multifault transform plate boundaries. *Geology*, 30, 11–14, doi:10.1130/0091-7613(2002)030<0011:OBMTPB>2.0.CO;2.

Louden, K. E., White, R. S., Potts, C. G., & Forsyth, D. W. (1986). Structure and seismotectonics of the Vema fracture zone, Atlantic Ocean, *Journal Geological Society London*, 143, 795–805, doi: doi:10.1144/gsjgs.143.5.0795.

Lomax, A., Virieux, A. J., Volant, P., and Berge, C. (2000). Probabilistic earthquake location in 3D and layered models: Introduction of a Metropolis-Gibbs method and comparison with linear locations. in Advances in Seismic Event Location, Thurber, C. H. and Rabinowitz, eds., N., Kluwer, Amsterdam, p. 101-134, doi:10.1007/978-94-015-9536-0_5.

Macdonald, K., Fox, P. J., Perram, L. J., Eisen, M. F., Haymon, R. M., Miller, S. P., Carbotte, S. M., Cormier, M.-H., & Shor, A. N. (1988). A new view of the mid-ocean ridge from the behaviour of ridge-axis discontinuities. *Nature*, 335, 217–225, doi:10.1038/335217a0.

Mamaloukas-Frangoulis, V., Auzende, J.-M., Bideau, D., Bonatti, E., Cannat, M., Honnorez, J., Lagabrielle, Y., Malavieille, J., Mével, C., & Needham, H. D. (1992). In-situ study of the eastern ridge-transform intersection of the Vema Fracture Zone, *Tectonophysics*, 190(1), 55-71, https://doi.org/10.1016/0040-1951(91)90354-U.

Marjanović, M., Singh, S. C., Gregory, E. P. M., Grevemeyer, I., Growe, K., Wang, Z., et al. (2020). Seismic crustal structure and morphotectonic features associated with the Chain Fracture Zone and their role in the evolution of the equatorial Atlantic region. *Journal of Geophysical Research: Solid Earth*, 125, e2020JB020275. https://doi.org/10.1029/2020JB020275

Münchmeyer, J., Woollam, J., Rietbrock, A., Tilmann, F., Lange, D., Bornstein, T., et al. (2022). Which picker fits my data? A quantitative evaluation of deep learning based seismic pickers. *Journal of Geophysical Research: Solid Earth*, 127, e2021JB023499, doi:10.1029/2021JB023499.

Ottemöller, L., & Havskov, J. (2003). Moment magnitude determination for local and regional earthquakes based on source spectra. *Bulletin Seismological Society America*, 93, 203–214, doi:10.1785/0120010220.

Parnell-Turner, R., Sohn, R.A., Peirce, C., Reston, T.J., Macleod, C.J., Searle, R.C., & Simão, N.M. (2017). Oceanic detachment faults generate compression in extension. *Geology*, 45, 923-926, doi:10.1130/G39232.1.

Podvin, P., & Lecomte, L. (1991). Finite difference computation of traveltimes in very contrasted velocity models: a massively parallel approach and its associated tools. *Geophysical Journal International*, 105, 271–284. doi:10.1111/j.1365-246X.1991.tb03461.x.

Pockalny, R. A., P. J. Fox, D. J. Fornari, K. C. Macdonald, & M. R. Perfit (1997). Tectonic reconstruction of the Clipperton and Siqueiros Fracture Zones: Evidence and consequences of plate motion change for the last 3 Myr, *Journal of Geophysical Research,* 102(B2), 3167–3181, doi:10.1029/96JB03391.

Parsons, B., & J. G. Sclater (1977). An analysis of the variation of ocean floor bathymetry and heat flow with age, *Journal of Geophysical Research*, 82(5), 803–827, doi:10.1029/JB082i005p00803.

Rabain, A., Cannat, M., Escartín, J., Pouliquen, G., Deplus, C., & Rommevaux-Jestin, C. (2001). Focused volcanism and growth of a slow spreading segment (Mid-Atlantic Ridge, 35°N). *Earth Planetary Science Lette*rs, 185, 211–224, doi:10.1016/S0012-821X(00)00371-X.

Reasenberg, P.A. & Oppenheimer, D. (1985) FPFIT, FPPLOT and FPPAGE: FORTRAN Computer Programs for Calculating and Displaying Earthquake Fault-Plane Solutions. US *Geological Survey Open-File Report*, 85-739, 109 p.

Ren, Y., Geersen, J., & Grevemeyer, I. (2022). Impact of spreading rate and age-offset on oceanic transform fault morphology. *Geophysical Research Letters*, 49, e2021GL096170, doi:10.1029/2021GL096170.

Ren, Y., Lange, D., & Grevemeyer, I. (2023). Seismotectonics of the Blanco transform fault system, northeast Pacific: Evidence for an immature plate boundary. *Journal of Geophysical Research: Solid Earth*, 128, e2022JB026045. doi:10.1029/2022JB026045.

Rowlett, H. (1981). Seismicity at intersection of spreading centers and transform faults: ecent faulting and microearthquakes at the intersection of the Vema Fracture zone and the Mid-Atlantic Ridge. *Journal of Geophysical Research*, 86(B5), 3815-3820, doi:10.1029/JB086iB05p03815.

Rowlett, H., & Forsyth, D. W. (1984). Recent faulting and microearthquakes at the intersection of the Vema Fracture zone and the Mid-Atlantic Ridge. *Journal of Geophysical Research*, 89(B7), 6079-6094, doi:10.1029/JB089iB07p06079.

Sandwell, D. T. (1986). Thermal stress and the spacings of transform faults. *Journal of Geophysical Research*, 91(B6), 6405–6417, doi:10.1029/JB091iB06p06405

Searle, R.C., Thomas, M. V., & Jones, E. J. W. (1994). Morphology and tectonics of the Romanche transform and its environs. *Marine Geophysical Researches*, 16, 427-453, doi:10.1007/BF01270518.

Seton, M., Whittaker, J., Wessel, P., Müller, R. D., DeMets, C., Merkouriev, S., Cande, S., Gaina, C., Eagles, G., Granot, R., Stock, J., Wright, N., & Williams, S. (2014). Community infrastructure and repository for marine magnetic identifications. *Geochemistry, Geophysics, Geosystems*, 5(4), 1629-1641, doi:10.1002/2013GC005176.

Shi, P., Wei, M., & Pockalny, R. A. (2022). The ubiquitous creeping segments on oceanic transform faults. *Geology*, 50, 199–204, doi:10.1130/G49562.1.

Sawires, R., Santoyo, M.A., Peláez, J.A. & Corona Fernández, R. D. (2019). An updated and unified earthquake catalog from 1787 to 2018 for seismic hazard assessment studies in Mexico. *Scientific Data*, 6, 241, doi:10.1038/s41597-019-0234-z.

Sykes, L. R. (1967). Mechanism of earthquakes and nature of faulting on the mid-oceanic ridges. *Journal of Geophysical Research*, 72(8), 2131– 2153, doi:10.1029/JZ072i008p02131.

Tian, X., Behn, M. D., Ito, G., Schierjott, J. C., Kaus, B. J. P. & Popov, A. A. (2024). Magmatism controls global oceanic transform fault topography. *Nature Communications*, 15, 1914, doi:10.1038/s41467-024-46197-9.

Tozer, B., Sandwell, D. T., Smith, W. H. F., Olson, C., Beale, J. R., & Wessel, P. (2019). Global Bathymetry and Topography at 15 Arc Sec: SRTM15+. *Earth and Space Science*, 6, 1847–1864. https://doi.org/10.1029/2019EA000658

Tréhu, A. M., & Solomon, S. C. (1983). Earthquakes in the Orozco Transform Zone: Seismicity, source mechanisms, and tectonics. *Journal of Geophysical Research*, 88(B10), 8203–8225, doi:10.1029/JB088iB10p08203.

Wilcock, W. S. D., Purdy, G. M., & Solomon, S. C., (1990). Microearthquake evidence for extension across the Kane Transform Fault. *Journal of Geophysical Research*, 95(B10), 15439–15462, doi:10.1029/JB095iB10p15439.

Wilson, J. T. (1965). A New Class of Faults and their Bearing on Continental Drift. *Nature*, 207, 343–347, doi:10.1038/207343a0.

Wessel, P., Luis, J. F., Uieda, L., Scharroo, R., Wobbe, F., Smith, W. H. F., & Tian, D. (2019). The Generic Mapping Tools version 6. *Geochemistry, Geophysics, Geosystems*, 20, 5556–5564, doi:10.1029/2019GC008515.

Wolfe, C. J., Purdy, G. M., Toomey, D. R. & Solomon, S. C. (1995). Microearthquake characteristics and crustal velocity structure at 29°N on the Mid-Atlantic Ridge: The architecture of a slow spreading segment. *Journal of Geophysical Research*, 100(B12), 24449–24472, doi:10.1029/95JB02399.

Wolfson-Schwehr, M., & Boettcher, M. S., 2019, Global characteristics of oceanic transform fault structure and seismicity. in Duarte, J. C. (Ed.), Transform plate boundaries and fracture zones (pp. 21–59), Elsevier, doi:10.1016/B978-0-12-812064-4.00002-5.

Yu, Z., Singh, S. C., Gregory, E. P. M., Maia, M., Wang, Z., and Brunelli, D., 2021, Semibrittle seismic deformation in high-temperature mantle mylonite shear zone along the Romanche transform fault. *Science Advances*, 7, doi:10.1126/sciadv.abf3388.

Table. 1: Focal mechanisms

Year	Date	Time	Latitude	Longitude	Depth	Mag.	Focal mechanism
2021	0122	0912	35.156708	-35.149384	5.0	2.0	308/60/-90
2021	0123	1002	35.069733	-35.222626	10.9	2.8	093/70/04
2021	0123	1946	35.065613	-35.213928	11.0	2.7	102/87/09
2021	0125	0912	35.226746	-36.105652	10.5	2.7	080/56/-78
2021	0126	2054	35.168152	-34.948425	3.1	2.6	180/40/-90
2021	0127	1749	35.087128	-35.142975	4.2	2.7	086/53/-65
2021	0131	1006	35.141144	-35.515594	6.1	3.0	095/60/00
2021	0202	0901	35.062866	-35.191040	8.9	3.4	102/01/-06
2021	0207	0054	35.168152	-35.164490	13.0	3.3	260/34/-90
2021	0304	1417	35.039978	-35.182800	10.1	2.8	269/60/-90
2021	0322	1956	35.080261	-35.135193	8.0	3.9	140/61/-78
2021	0509	1803	35.128784	-35.513306	12.8	3.1	297/78/14
2021	0512	0331	35.027161	-34.975891	10.0	2.8	085/66/51

(Depth is in km; Mag. is moment magnitude Mw; focal mechanism: strike, dip, and rake)

Journal of Geophysical Research: Solid Earth

Supporting Information for

Strike-slip versus extensional tectonics at the Oceanographer transform fault, Mid-Atlantic Ridge at 35°N

Ingo Grevemeyer [(1)], Dietrich Lange [(1)], Ingo Klaucke [(1)], Lars H. Ruepke [(1)], Anouk Beniest [(1,2)], Laura Gómez de la Peña [(1, 3)], Yu Ren [(1)], Christian Filbrandt [(1)], Helene-Sophie Hilbert [(1)], Yuhan Li [(1)], Louisa Murray-Bergquist [(1, 2)], Katharina Unger Moreno [(1)],Thor Hansteen [(1)], and Colin W. Devey [(1)]

(1) GEOMAR Helmholtz Centre for Ocean Research Kiel, Kiel, Germany

(2) now at Department of Geology and Geochemistry, Vrije Universiteit Amsterdam, Amsrerdam, Netherlands

(3) now at Instituto de Ciencias del Mar, CSIC, Barcelona, Spain

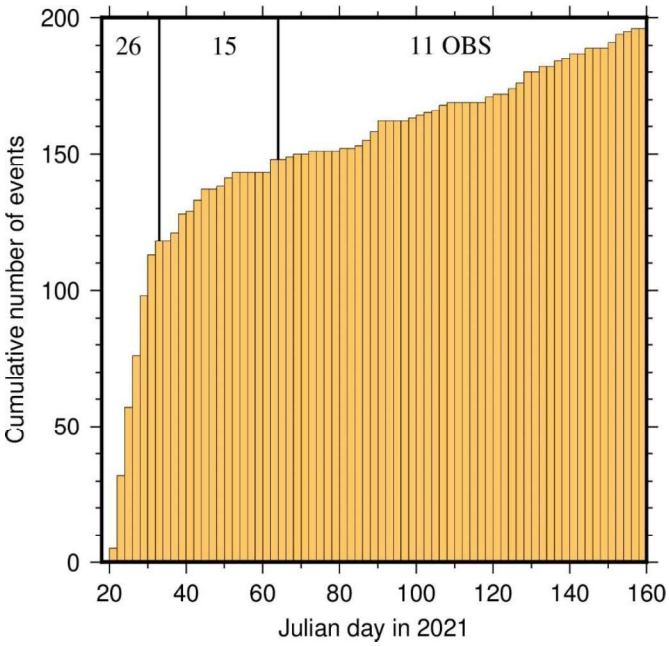

Figure S1: Cumulative number of events

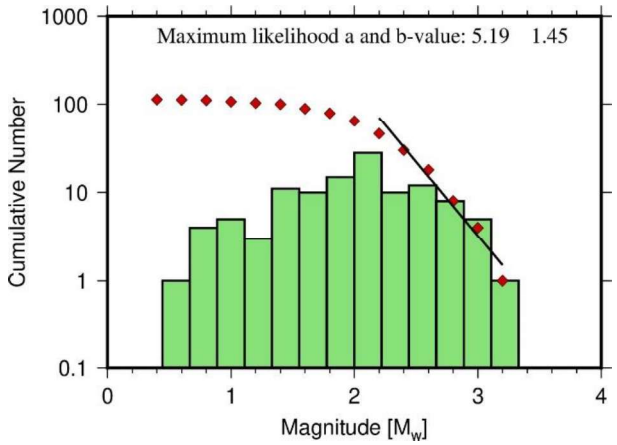

Figure S2a: b-value for first 12-days deployment

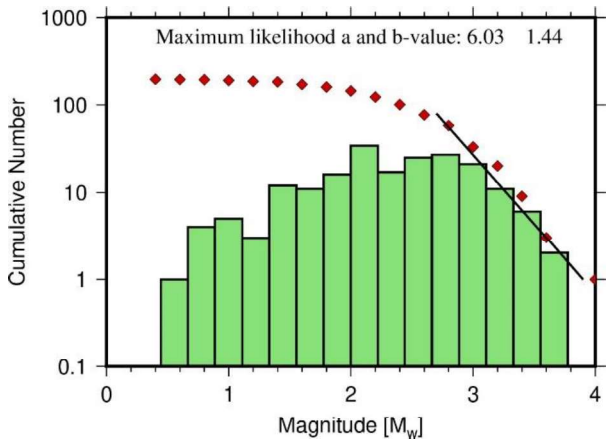

Figure S2b: b-value for entire deployment

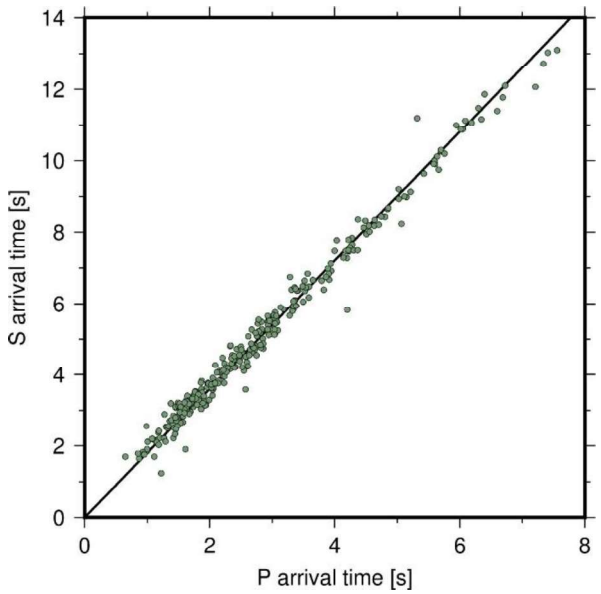

Figure S3: Modified Wadati-Diagram; straight line indicates Vp/Vs ratio of 1.8

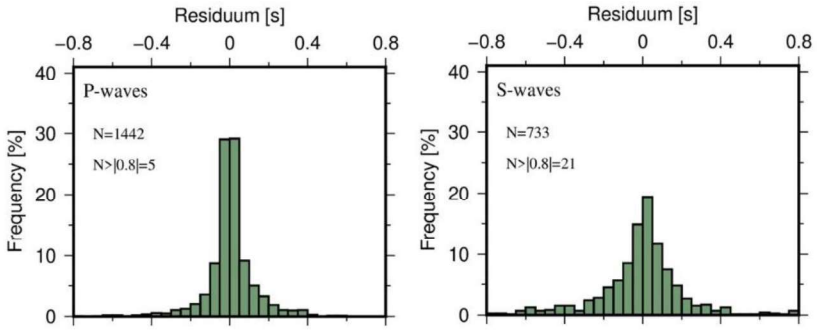

Figure S4: Travel time residuals of calculated versus observed arrival times.

CHAPTER 6

MANUSCRIPT #5

Seismotectonics of the Blanco transform fault system, northeast Pacific: Evidence for an immature plate boundary

Yu Ren [(1)], Dietrich Lange [(1)], and Ingo Grevemeyer [(1)]

(1) GEOMAR Helmholtz Centre for Ocean Research Kiel, Kiel, Germany

Published in 2023 in *Journal of Geophysical Research: Solid Earth*, 128, e2022JB026045

JGR Solid Earth

RESEARCH ARTICLE
10.1029/2022JB026045

Seismotectonics of the Blanco Transform Fault System, Northeast Pacific: Evidence for an Immature Plate Boundary

Yu Ren[1], **Dietrich Lange**[1], **and Ingo Grevemeyer**[1]

[1]GEOMAR Helmholtz Centre for Ocean Research Kiel, Kiel, Germany

Key Points:

- Local seismicity of the Blanco transform fault system (BTFS) reveals along-strike variations dominated by strike-slip and oblique dip-slip
- The BTFS developed from non-transform offsets rather than discrete transform faults in response to plate rotation and ridge propagation
- The BTFS consists of a mature plate boundary in the east and an immature system in the west, separated by a central spreading center

Supporting Information:

Supporting Information may be found in the online version of this article.

Correspondence to:

Y. Ren,
yren@geomar.de

Citation:

Ren, Y., Lange, D., & Grevemeyer, I. (2023). Seismotectonics of the Blanco transform fault system, northeast Pacific: Evidence for an immature plate boundary. *Journal of Geophysical Research: Solid Earth*, *128*, e2022JB026045. https://doi.org/10.1029/2022JB026045

Received 14 NOV 2022
Accepted 27 FEB 2023

Author Contributions:

Conceptualization: Ingo Grevemeyer
Formal analysis: Yu Ren, Ingo Grevemeyer
Investigation: Yu Ren
Methodology: Dietrich Lange
Resources: Ingo Grevemeyer
Supervision: Dietrich Lange, Ingo Grevemeyer
Visualization: Yu Ren
Writing – original draft: Yu Ren
Writing – review & editing: Dietrich Lange, Ingo Grevemeyer

Abstract At the Blanco transform fault system (BTFS) off Oregon, 138 local earthquakes and 84 double-couple focal mechanisms from ocean-bottom-seismometer recordings jointly discussed with bathymetric features reveal a highly segmented transform system without any prominent fracture zone traces longer than 100 km. In the west, seismicity is focused at deep troughs (i.e., the West and East Blanco, and Surveyor Depressions). In the east, the BTFS lacks a characteristic transform valley and instead developed the Blanco Ridge, which is the most seismically active feature, showing strike-slip and dip-slip faulting. Sandwiched between the two main segments of the BTFS is the Cascadia Depression, representing a short intra-transform spreading segment. Seismic slip vectors reveal that stresses at the eastern BTFS are roughly in line with plate motion. In contrast, stresses to the west are clockwise skewed, indicating ongoing reorganization of the OTF system. As we observed no prominent fracture zones at the BTFS, plate tectonic reconstructions suggest that the BTFS developed from non-transform offsets rather than pre-existing transform faults during a series of ridge propagation events. Our observations suggest that the BTFS can be divided into two oceanic transform systems. The eastern BTFS is suggested to be a mature transform plate boundary since ∼0.6 Ma. In contrast, the western BTFS is an immature transform system, which is still evolving to accommodate far-field stress change. The BTFS acts as a natural laboratory to yield processes governing the development of oceanic transform faults.

Plain Language Summary The Blanco transform fault system (BTFS) northwest off the coast of Oregon is seismically very active. We used 1 year of ocean bottom seismometer data collected between September 2012 and October 2013 to locate 138 local earthquakes. The events align perfectly with the morphologic features of the BTFS, dividing the BTFS into five transform segments and two short intra-transform spreading centers. Furthermore, we observe different seismotectonic behaviors of the western and eastern BTFS based on the along-strike variation in morphology, magnetization, focal depth distribution, and strain partitioning. Although many segmented oceanic transform systems were formed from a single transform fault in response to rotations in plate motion, the BTFS turns out to be originated from non-transform offsets between ridge segments, as we observed no prominent fracture zone traces neither in morphology nor gravity field data. A clockwise shift in the Juan de Fuca/Pacific pole of rotation at ∼5 Ma followed by a series of ridge propagation events initiated the formation of the BTFS, integrated each segment of the BTFS by shortening the ridge segments in between. Our observations suggest that the Blanco Ridge and the Gorda transform segment in the eastern BTFS were formed at ∼1.6 and 0.6 Ma, respectively, and ever since, the eastern BTFS became a mature transform boundary. In contrast, seismic slip vectors comparing to plate motion directions reveal that stresses in the western BTFS are systematically skewed, suggesting the immature transform plate boundary is still adjusting to the new stress regime.

1. Introduction

Oceanic transform faults (OTFs) offset the spreading axis by tens to hundreds of kilometers and hence are some of the most noticeable tectonic features in deep ocean basins. Plate tectonics defined OTFs as first-order tectonic discontinuities of mid-ocean ridges and long-lived tectonic features (Carbotte et al., 2015; Macdonald et al., 1988; J. T. Wilson, 1965). In the Atlantic Ocean, most large OTFs were introduced during rifting; thus, their fracture zones cut through the entire ocean basin (Matthews et al., 2011; J. T. Wilson, 1965). In the Pacific Ocean, some fracture zones represent the longest linear features on our planet, like the over 10,000 km long Clipperton fracture zone (Menard, 1967). However, north of ∼41°N, none of the long and prominent fracture zone traces of the Pacific is directly linked to any OTF offsetting the modern spreading ridges in the eastern Pacific (Matthews et al., 2011). The collision of the Farallon spreading center with North America at ∼28 Ma caused a major

reorientation of the tectonic plate boundaries (Atwater & Stock, 1998), giving birth to the Juan de Fuca and the Cocos plates and causing a number of abandoned spreading ridges in the eastern Pacific Ocean (Lonsdale, 2005).

In the northeast Pacific, the northward migration of the Mendocino triple junction (Atwater & Stock, 1998) and the Cobb hotspot (Karsten & Delaney, 1989) controlled the recent plate reorganization. Between 20 and 2 Ma, spreading at the Juan de Fuca Ridge (JdFR) and Gorda Ridge (GR) occurred without developing any OTF as the area lacks evidence of any prominent fracture zone longer than 100 km (Matthews et al., 2011). Instead, magnetic anomalies and bathymetric features suggest that the geometry of both ridges was controlled by ridge propagation (Carbotte et al., 2008; Marjanović et al., 2011; D. S. Wilson, 1993; Wilson et al., 1984), probably governed by the Cobb hotspot, which is today located under the JdFR (Karsten & Delaney, 1989). The Blanco transform fault system (BTFS) is located northwest off the coast of Oregon and has a total length of ∼350 km (Figure 1 and Figure S1 in Supporting Information S1). The evolution and formation of the BTFS are inherently related to plate boundary reconfiguration by propagating ridges (Embley & Wilson, 1992).

The formation of the BTFS resulted from a clockwise rotation of plate motion, occurring at ∼5 Ma (D. S. Wilson, 1993; Wilson et al., 1984). Between ∼5 and ∼1.8 Ma, three ridge propagation events set the stage for the main features characterizing the BTFS today. Embley and Wilson (1992) suggested that the propagating rift tip would be linked to the adjacent spreading segment by an OTF. However, this would imply that new OTFs develop continuously and instantaneously during propagation. Instead, it might be more realistic to consider the broad transform zone model (McKenzie, 1986; D. S. Wilson, 1988, 1990) that the propagating ridge extends at a constant rate as it takes over the spreading role from the doomed rift. Propagation is going to leave behind a characteristic V-shaped pseudofault. Such pseudofaults were observed on either side of the JdFR (e.g., Marjanović et al., 2011), at the Mid-Atlantic Ridge (Dannowski et al., 2018; Kahle et al., 2016) or in Iceland (Karson, 2017; Morgan & Kleinrock, 1991). During propagation, the spreading responsibility is transferred from one ridge segment to the other. Active deformation occurs in a broad transform zone as material shears in the process of being transferred from one plate to the other. This results in a sheared zone between the failed ridge and its inner pseudofault instead of creating a simple OTF (McKenzie, 1986). The complex tectonic features of a transform zone can perhaps best be seen in northern Iceland, where propagation generated the Tjörnes transfer zone with deformation in three different strands (Karson, 2017) with the basins of the Grimsey Fault Zone in the north roughly mimicking the depressions of the western BTFS. However, while propagation in Iceland is continuing, it has stopped ∼1.8 Ma at the BTFS (D. S. Wilson, 1993).

Therefore, the BTFS represents a natural laboratory to study the development of an OTF system after ridge propagation and shortening of spreading segments terminated. Karson (2017) noted that ridge parallel strike-slip faults in south Iceland transform zone are reactivated spreading related normal faults. It might be reasonable to hypothesize that features formed within the shear zone between the propagating ridge and the doomed ridge favored the nucleation of new strike-slip segments of an immature OTF.

Here, we study the seismotectonic of the BTFS using constraints from 1 year of ocean-bottom-seismometer (OBS) data obtained in 2013 (Figure S2 in Supporting Information S1) during the Blanco Transform OBS Experiment (Kuna, 2020; Nábělek & Braunmiller, 2012). Local seismicity and focal mechanisms along the entire BTFS reveal recent faulting and deformation. Bathymetry (Ryan et al., 2009) and aeromagnetic (Bankey et al., 2002) data sets are also used to corroborate our seismicity study findings. We further discuss results in terms of stresses acting at a mature fault system or a still evolving OTF.

2. Tectonic Setting

The BTFS represents a major left-lateral ridge-crest discontinuity and connects the intermediate-spreading GR in the southeast with the JdFR in the northwest (Figure 1a). The BTFS is a highly segmented OTF system marked by topographic highs (the Parks Plateau [PP] and the Blanco Ridge [BR]) and deep troughs (the West and East Blanco Depressions [WBD and EBD], Surveyor Depression [SUR], Cascadia Depression [CAS], and Gorda Depression [GD]) (Dauteuil, 1995; Embley & Wilson, 1992), as well as the Cascadia Channel cutting into the intersection between the CAS and the BR. An interesting feature is that the plate boundary along the BTFS is characterized by a positive magnetic anomaly (Figure 1b).

Teleseismic analysis (e.g., Dziak et al., 1991) inferred the seismic coupling strength is different along the west and east segments of BTFS, although the routine event locations along the BTFS are scattered and systematically

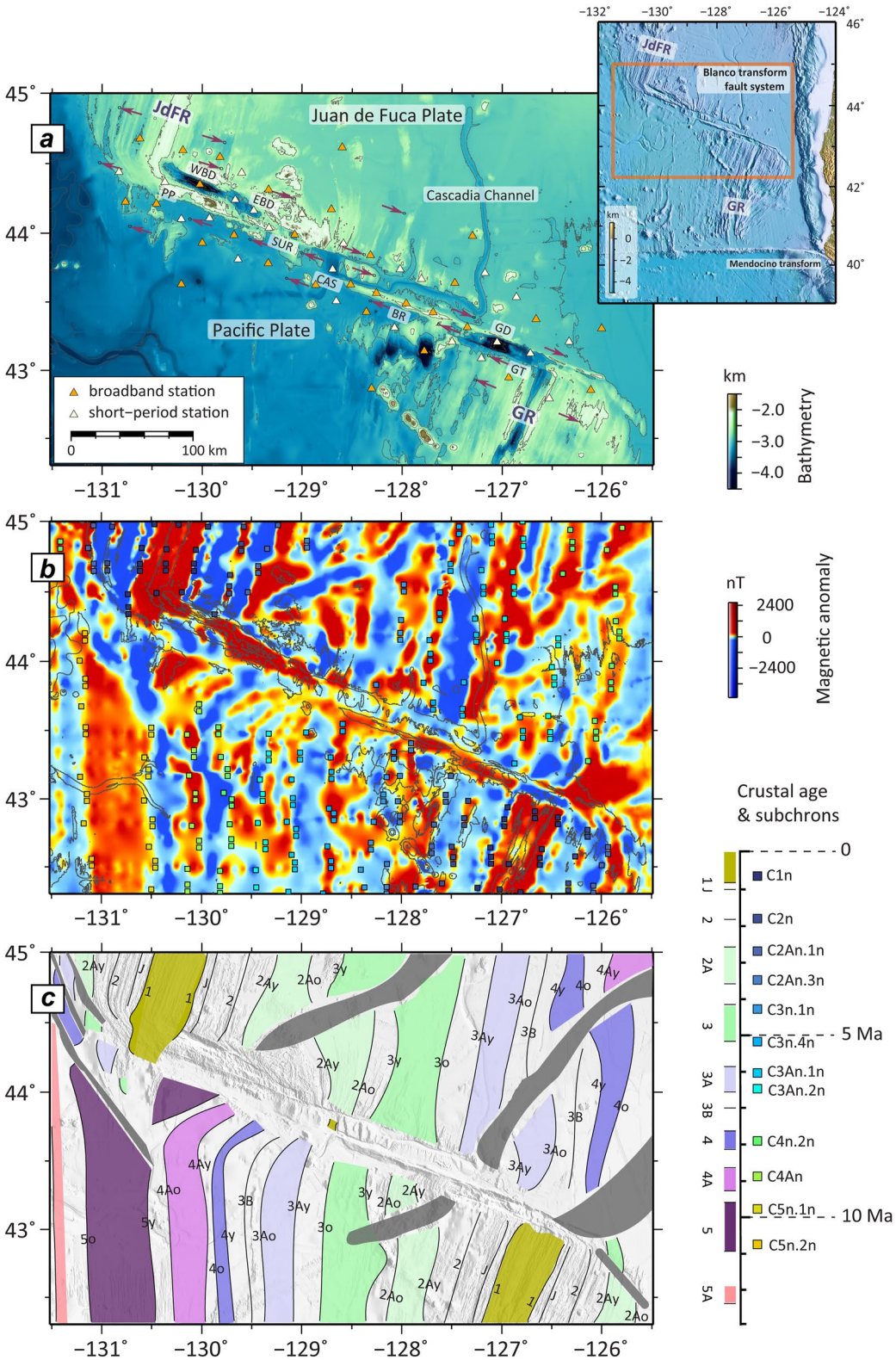
a
b
c
JdFR
Juan de Fuca Plate
Pacific Plate
Cascadia Channel
WBD
PP
EBD
SUR
CAS
BR
GD
GT
GR
broadband station
short−period station
0
100 km
Blanco transform fault system
Mendocino transform
km
−2.0
−3.0
−4.0
Bathymetry
nT
2400
0
−2400
Magnetic anomaly
Crustal age & subchrons
C1n
C2n
C2An.1n
C2An.3n
C3n.1n
C3n.4n
C3An.1n
C3An.2n
C4n.2n
C4An
C5n.1n
C5n.2n
0
5 Ma
10 Ma
−131°
−130°
−129°
−128°
−127°
−126°
45°
44°
43°

Figure 1.

shifted from the bathymetric features (e.g., Williams et al., 2019). The U.S. Navy's Sound Surveillance System (SOSUS) enabled earthquake detection using hydro-acoustic tertiary (T-) waves (e.g., Dziak et al., 2000, 2003; Géli et al., 2014), which significantly improved the precision of event locations. However, using the joint epicenter determination (JED) technique, Braunmiller and Nábělek (2008) suggested that the bathymetric features might bias the hydro-acoustic SOSUS locations along the BTFS, and that the lack of precise and accurate event locations put a limit on the identification of active faults, especially in the western BTFS.

The easternmost Gorda transform (GT) segment was identified from the bathymetric map (Embley & Wilson, 1992). Morphologically, from the intersection between the GR and GT, the linear fault trace extends northwestward ~20 km beyond the GD (Figure 1a). The GD is a ~20-km-long (trending NW-SE) and ~10-km-wide (trending NE-SW) basin with a central depth of ~4.4 km (Embley & Wilson, 1992). Troughs extend primarily to the southeast to the eastern ridge-transform intersection (RTI), into a region of negative magnetization (Figure 1b). The GD is bounded by the western GT and eastern BR transform segments. The 130-km-long BR connects the GD in the east and the CD in the west (Figure 1a), and it is the best-studied segment of BTFS to date. Braunmiller & Nábělek (2008) proposed that the eastern BR (east of 128°W) is fully coupled, due to the high seismicity combined with abundant relatively large events. Kuna et al. (2019) detected and located micro-earthquakes of the BR, and proposed a mode of slip at the BR where the fault zone in the crust is brittle and fully seismically coupled while in the mantle it creeps partially and episodically.

Located in the central BTFS, the CAS is an extensional basin bounded by the BR and SUR on the southern and northern sides (Figure 1a). A kinematic model by Embley and Wilson (1992) suggested that the CAS might be a remnant of a rift segment shortened due to a southward propagation event at ~5 Ma. Seismic reflection data revealed the presence of igneous intrusions within the sediments, suggesting the CAS is an intra-transform spreading center (Embley & Wilson, 1992). Furthermore, the CAS is seismically active (Johnson & Jones, 1978) and marked by normal faulting (Braunmiller & Nábělek, 2008).

From the northern boundary of the CAS, the fault trace extends to the southeast for around 120 km (Figure 1a), forming the southern scarp of the PP. To the northeast of the PP are three troughs (SUR, WBD, and EBD), marking the possible active tectonic features of the western BTFS. The SUR seems like a small pull-apart basin, as the northern and southern walls are discernible from seafloor morphology (Figure 1a). However, the master faults of EBD and WBD are difficult to interpret (Embley & Wilson, 1992), as many scarps are observed. The kinematic model of Embley and Wilson (1992) suggested that the western segment of BTFS was recently formed to accommodate far-field stress change.

Kuna et al. (2019) used micro-earthquake data collected during the Blanco Transform OBS Experiment in 2012, revealing depth-dependent seismic features of the BR. Yet, their study focused only on a regional subset sandwiched between the CD, which is an intra-transform spreading center, and the GD, interpreted as a pull-apart basin in the vicinity of the eastern RTI of BTFS. In addition, the whole seismic data set offers an excellent opportunity to improve our understanding of seismotectonic behaviors of the entire highly segmented oceanic transform system where most tectonic processes remain enigmatic.

3. Data and Methods

3.1. OBS Data

We use OBS data from the Blanco Transform OBS Experiment (Nábělek & Braunmiller, 2012). Fifty-five OBS were deployed between September 2012 and October 2013 (Figure 1a and Figure S2 in Supporting Information S1). Station BB270 did not record data, but all the other 54 OBS continuously recorded 100 samples per second. The average station spacing was approximately 25 km. Thirty-one stations were outfitted with broadband Güralp CMG3T seismometers, and the other 24 stations were equipped with short-period Mark Products L-28LB seismometers co-located with differential pressure gauges.

Figure 1. Tectonic map of the Blanco transform fault system (BTFS). (a) Bathymetry (Ryan et al., 2009) and ocean-bottom-seismometer (OBS) station distribution. Arrows show relative plate motion (DeMets et al., 2010) between the Pacific and Juan de Fuca Plates. The inset map shows prominent transform faults and fracture zones in the northeast Pacific. The colored box indicates the location of our study area. (b) Airborne magnetic anomaly (Bankey et al., 2002). Gray lines indicate the bathymetric contours with 600 m intervals. Color-coded squares show the magnetic picks from Elvers et al. (1973). (c) Crustal ages (modified from D. S. Wilson, 1993). Gray shading outlines propagator wakes (Nedimović et al., 2009). BR, Blanco Ridge; CAS, Cascadia Depression; EBD, East Blanco Depression; GD, Gorda Depression; GR, Gorda Ridge; GT, Gorda transform segment; JdFR, Juan de Fuca Ridge; PP, Parks Plateau; SUR, Surveyor Depression; WBD, West Blanco Depression.

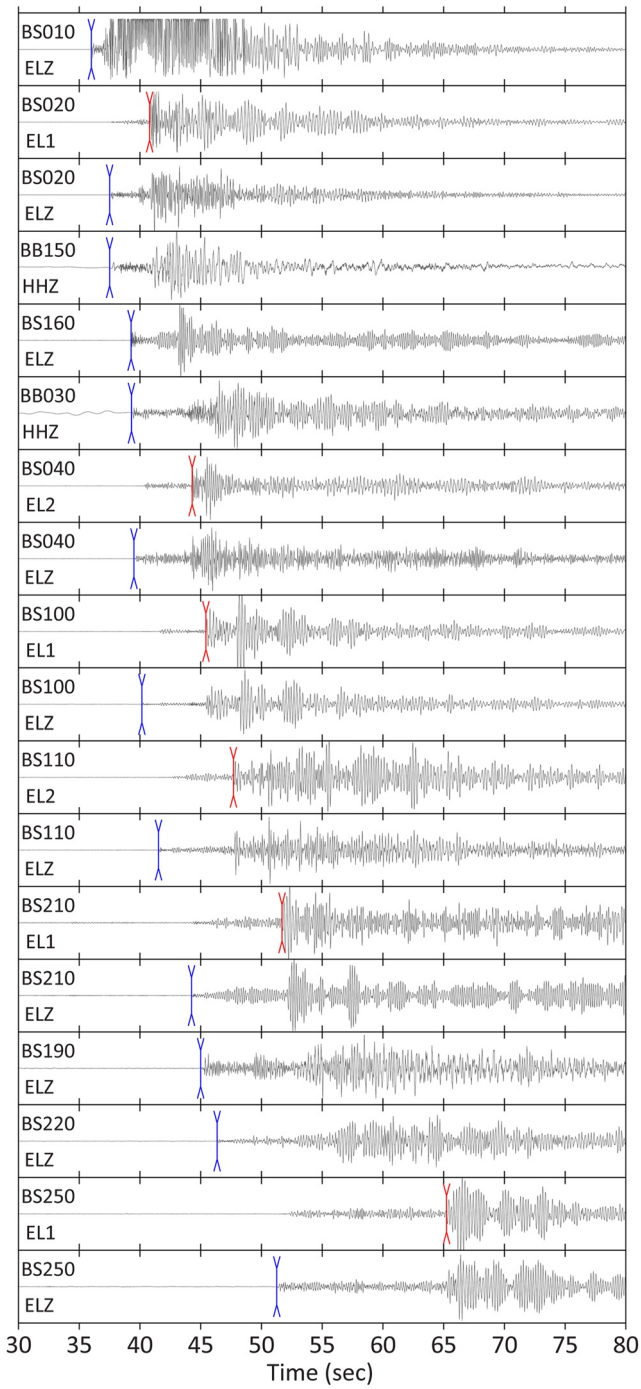

Figure 2. Seismograms of a local event recorded by the ocean-bottom-seismometer (OBS) array. The onsets of P-phase and S-phase arrivals are marked in blue and red, respectively. OBS labeled with "BS" and "BB" indicate short-period and broadband stations, respectively. The EL1 and EL2 represent horizontal channels; HHZ and ELZ stand for vertical channels.

3.2. Earthquake Catalog and Phase Picking

We constructed our seismicity catalog by combining the NEIC (National Earthquake Information Center) and an auto-detected catalog (Figure S3 in Supporting Information S1). The NEIC catalog listed 55 earthquakes between September 2012 and October 2013 along the BTFS. To enlarge our data set, we further applied automated event detection using the *scanloc* module of SeisComP3 (GFZ & Gempa GmbH, 2008). We selected 95 events with phase picks identified at more than 15 OBS stations to ensure the quality of earthquake locations. Interestingly, we found only six events from the auto-detected catalog are in common with the NEIC, supporting a recent observation that the auto-pickers might miss large magnitude events due to very emergent P-arrivals on OBS stations (Gong et al., 2022). Based on both catalogs, we constructed a new catalog with 144 events for earthquake relocation.

Furthermore, we revised the auto-picked phases and picked the NEIC events manually, as most NEIC events were not picked by the automated picker. Figure 2 depicts waveforms of a local event recorded by the OBS array. The onsets of P-phase and S-phase arrivals were manually picked on unfiltered waveforms. We picked P-phase onsets on the vertical channel and S-phase onsets on either one of the horizontal channels, where they are clearest. In total, 2,850 P-phases and 961 S-phases were picked for the determination of earthquake parameters.

3.3. Velocity Model, Event Location, and Magnitudes

Using VELEST (Kissling et al., 1994), we derived a minimum one-dimensional velocity model for the BTFS. We constructed 4,344 initial P-wave velocity models, which were inverted to find the model with the smallest RMS. This minimum 1D P-wave velocity model, with minimum RMS residuals among all output models, is shown in Figure 3. Then, we calculated the 1D minimum S wave velocity model by an additional iteration of inversions using different initial *Vp*/*Vs* ratios (e.g., Husen et al., 1999; Lange et al., 2007). Our minimum 1D velocity model is similar to the one Braunmiller and Nábělek (2008) used in their regional seismicity study utilizing coastal seismic stations (Figure 3), except for the slower P-wave velocity at 4–7 km depth. In the topmost layer within 1.5 km below the seafloor, P-wave velocity is estimated as ~4.6 km/s. P-wave velocities steadily increase from 5.7 to 6.3 km/s at depth between 1.5 and 7 km. At 7 km depth, the P-wave velocities increase from 6.3 to 7.6 km/s, which we interpret as the seismological Moho.

We used the non-linear oct-tree grid-search algorithm (NonLinLoc; Lomax et al., 2000) with the minimum 1D velocity models for *Vp* and *Vp*/*Vs* for event location. By the computation of probability density functions (PDFs) for each event, NonLinLoc allows estimations of location uncertainties. The maximum likelihood point of the complete non-linear location PDF was chosen as the preferred location. From the PDF scatter samples, uncertainties were estimated from 3D error ellipsoids fitted to each cloud of possible event locations. Uncertainties (68% confidence) in latitude, longitude, and depth are 0.5, 0.4, and 1.4 km, respectively. Furthermore, station correction terms (Husen et al., 1999) from NonLinLoc were calculated and iteratively updated to account for local velocity structures below the OBS network (Figure S4 in Supporting Information S1) (Grevemeyer et al., 2019). Finally, we located 138 local events (GAP<180°) with onsets from more than eight OBS stations, including at least one S-phase.

We further calculated local magnitudes (M_l) following Hutton and Boore (1987). The moment magnitudes (M_w) were manually estimated by the procedure described in Ottemöller and Havskov (2003). The M_l of

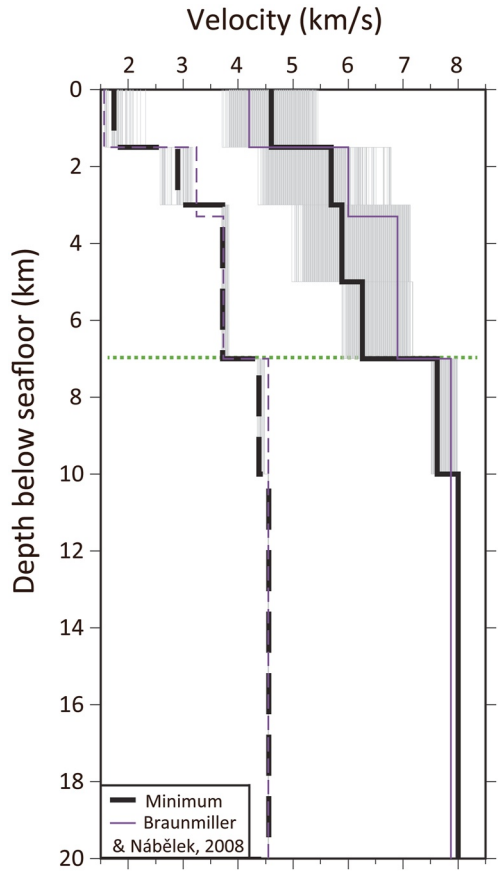

Figure 3. Minimum 1D velocity models of the Blanco transform fault system (BTFS). The P (black solid line) and S (black dashed line) wave velocity models were derived from 4,344 initial P-wave velocity models (gray lines). Solid and dashed purple lines show P-wave and S-wave velocity models used in previous regional seismicity study (Braunmiller & Nábělek, 2008), respectively. Dotted green line indicates the seismological Moho inferred from the minimum 1D velocity models.

nine events and the M_w of three events in our catalog are also listed in the NEIC (Figure S5 in Supporting Information S1). Our magnitudes deviate by −0.46 and 0.73 units from the NEIC values for the M_w and M_l, respectively.

3.4. Focal Mechanisms

We determined focal mechanisms for the events using their first motion polarities of P-phase onsets (Reasenberg & Oppenheimer, 1985). We retrieved focal mechanisms of 84 events with a GAP below 180° and first-motion polarities of P-phase onsets at more than 10 stations.

We also calculated the location bias of the seven events that are included in both gCMT (Ekström et al., 2012) and our catalogs (Figure S6 in Supporting Information S1). We obtain a bias of gCMT in latitude, longitude, and depth of 2.2, 1.1, and 7.9 km, respectively.

4. Results

The 1-year OBS deployment enabled us to depict the local seismicity (Figure 4 and Data Set S1) and focal mechanisms (Figure S7 in Supporting Information S1) along the entire BTFS with trustable location estimates (Figures S8 and S9 in Supporting Information S1). Our local seismicity catalog spans 12 months and includes 138 well-constrained events along the entire BTFS of local magnitudes (M_l) 1.7–4.9 and moment magnitudes (M_w) 1.9–5.2 (Figure S10 in Supporting Information S1). Our catalog is complete for all $M_l \geq 3.5$ events.

The seismicity distribution reveals a greatly improved correlation between the local earthquakes and the morphologic features along the BTFS (Figure 4). From the eastern intersection between the GR and the GT (Figure 5), earthquakes occurred following the fault trace (Figure 5), which formed the southern border of the GD. We show that the GD is seismically active, and normal faulting is observed within this deep basin, supporting that it is formed by extension or transtension (Braunmiller & Nábělek, 2008; Embley & Wilson, 1992). From the northern boundary of the GD to the CAS, local seismicity is also in-line with the structural lineament of the BR. The GD and BR are the most prominent tectonic features east of the CAS, sharing a similar focal depth range between 4 and 10 km depth, despite some deep events under BR and near the ridge-transform-intersection. The CAS is located at the mid-point of BTFS, connecting the eastern and western transform segments. Focal depth below CAS ranges from 4 to 10 km (Figure 6), similar to the eastern BTFS. To the west of CAS, three earthquake clusters occur at SUR, EBD, and WBD, respectively. The focal depth of the three earthquake clusters ranges consistently from 0 to 8 km (Figure 7). Most of the local events at the EBD occur in swarms (Figure S11 in Supporting Information S1).

Focal mechanisms derived in this study benefited significantly from the OBS deployment. Our local catalog includes 84 focal mechanisms with well-resolved event locations (Figures S7, S12, and S13 in Supporting Information S1), revealing the deformation styles of the highly segmented BTFS. The long-term near-field passive seismic observation enabled us to find that the major faulting style of the BTFS is strike-slip to transtensional rather than pure strike-slip (Figures S12 and S14 in Supporting Information S1). Moreover, seismic deformation varies locally along the entire segmented transform fault system. Dominantly strike-slip faulting is observed at the easternmost GT segment between the GD and the GR, including the vicinity of the RTI (Figure 5). The GD is dominated by normal faulting and extensional strike-slip motion. Along the BR, the primary faulting style is strike-slip to transtensional, except for one local event identified as reverse faulting (Figure 5). The CAS in the mid-point of the BTFS favors normal faulting in the central basin and transtensional strike-slip faulting near the BR and the SUR (Figure 6). However, faulting styles of the western BTFS are also quite similar, dominated by transtensional and strike-slip tectonics (Figure 7).

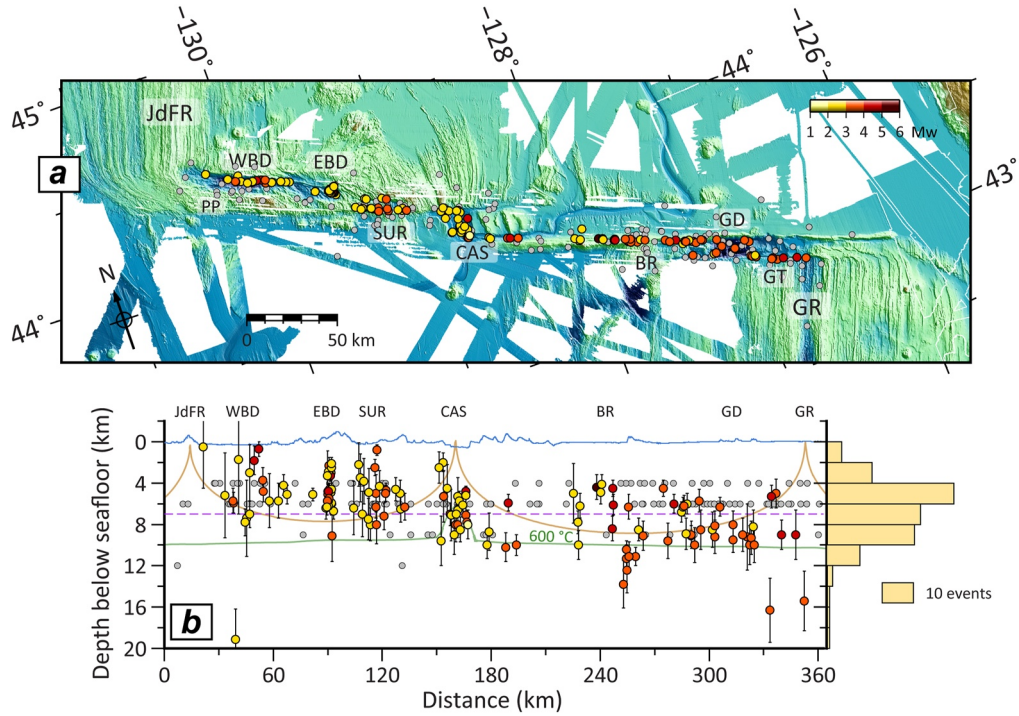

Figure 4. Distribution of local events (color-coded circles) along the entire Blanco transform fault system (BTFS). (a) Local seismicity of the BTFS. The gray circles show the hypocenters from Braunmiller and Nábělek (2008). (b) Along-strike vertical profile showing the focal depth distribution. Error bars indicate focal depth uncertainties (68% confidence). The light blue line shows the complexity of seafloor bathymetry. Dashed purple line shows the Moho discontinuity inferred from our minimum 1D velocity model. Brown and green lines indicate the 600°C isotherms calculated from a half-space cooling model and a numerical model incorporating hydrothermal cooling (Roland et al., 2010), respectively. Histogram on the right shows the focal depth distribution of local events derived in this study.

5. Discussion

The BTFS is a highly segmented OTF system. Morphologically, it is marked by deep troughs and bathymetry highs running along the fault traces (Embley & Wilson, 1992). According to the variation in regional seismicity (gray dots in Figure 4; Figure S12c in Supporting Information S1), Braunmiller and Nábělek (2008) categorized the complex fault system into four segments, namely GD, BR, Cascadia and Surveyor, and West Blanco segments. Three extensional basins (GD and Cascadia and Surveyor segments) and two transform segments (BR and West Blanco segments) were identified in their previous work. However, our local seismicity catalog suggests dividing the BTFS into five strike-slip or transfer segments (i.e., WBD, EBD, SUR, BR, and GT). We define transform segments as features dominated by strike-slip faulting, although some might also show minor dip-slip movement. In addition, three extensional basins (SUR, CAS, and GD) showing features resembling continental pull-apart basins (e.g., Aydin & Nur, 1982; Mann et al., 1983) might represent short intra-transform spreading centers (e.g., Fornari et al., 1989; Grevemeyer et al., 2013; Pickle et al., 2009), as long-lived extensional tectonics should favor the formation of new oceanic crust (van Wijk et al., 2017).

The eastern BTFS (Figure 5) consists of the BR and the GT as transform segments and the extensional basin GD. The CAS, located in the middle of the BTFS, is generally defined as a short spreading segment (Braunmiller & Nábělek, 2008; Embley & Wilson, 1992), but it also shows some characteristic features of a pull-apart basin (Figure 6). The western BTFS (Figure 7) includes three transform segments running along the SUR, EBD, and WBD (Figure 4). The SUR also shows pull-apart-basin-like features, bounded by two transform segments on its northern and southern sides. Detailed local seismicity, bathymetric, and aeromagnetic surveys reveal profound variations in seismotectonic behaviors along the entire BTFS, which will be discussed in detail below.

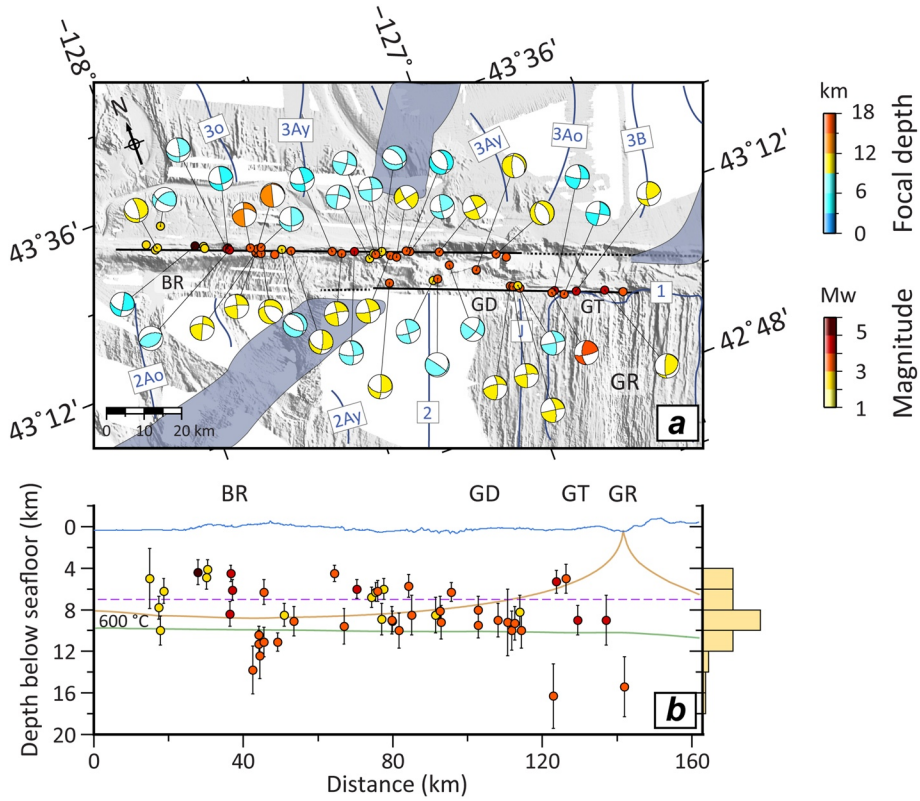

Figure 5. Close-up view of the eastern Blanco transform fault system (BTFS). (a) Local seismicity and focal mechanisms. Dark blue lines indicate the magnetic isochrons as in Figure 1c. Shaded polygons outline propagator wakes. Solid black lines show the interpreted transform fault traces. Dotted lines represent fracture zone traces identified from seafloor bathymetry. (b) Along-strike vertical profile showing the focal depth distribution. All other lines are as in Figure 4.

5.1. Local Seismicity and Tectonic Segments

5.1.1. Eastern Transform Segments

A number of multidisciplinary surveys were conducted to investigate the active tectonics of the eastern BTFS. The easternmost GT was identified from the bathymetry (Embley & Wilson, 1992). However, neither the hydro-acoustic T-wave events (Dziak et al., 2000) nor the JED locations (Braunmiller & Nábělek, 2008) could provide detailed seismological evidence for this active transform segment. However, we find that the local seismicity along the GT fits nicely with its fault trace observed morphologically, supporting the GT is an active transform fault segment bounding the southern side of GD (Figure 5). Near the RTI, earthquakes occurred close to the chron 1 (Brunhes magnetic chron) (Figure 5), indicating the seismotectonic behavior of the GT is related to recent magmatic activity since ~780 kyrs.

We observed seismic activity along both sides of the fault scarps of GT and BR (Figure 5). Previous seismicity studies (Braunmiller & Nábělek, 2008; Dziak et al., 2000) suggested that the fracture zone east of the GD might be seismically active, as a few events were identified (gray dots in Figure 4; Figure S12c in Supporting Information S1) using teleseismic analysis and/or JED technique. However, our local catalog shows that the seismicity didn't extend beyond the GD (Figure 5), indicating that the extending troughs and fracture zone east of the GD are aseismic. Furthermore, extensional strike-slip and normal faulting dominate this region, which is consistent with previous indications that the GD shows features of a pull-apart basin (Embley & Wilson, 1992). Alternatively, it may represent a rather magmatically starved short-spreading segment as found at the Mid-Atlantic Ridge at the Ascension (Grevemeyer et al., 2013) or in the southern segment of the Charlie Gibbs transform system (Skolotnev et al., 2021).

The occurrence of the BR as a prominent ridge-like structure represents a rare case as over 90% of OTFs revealed transform valleys instead of ridge-like morphology (Wolfson-Schwehr & Boettcher, 2019). Consistent

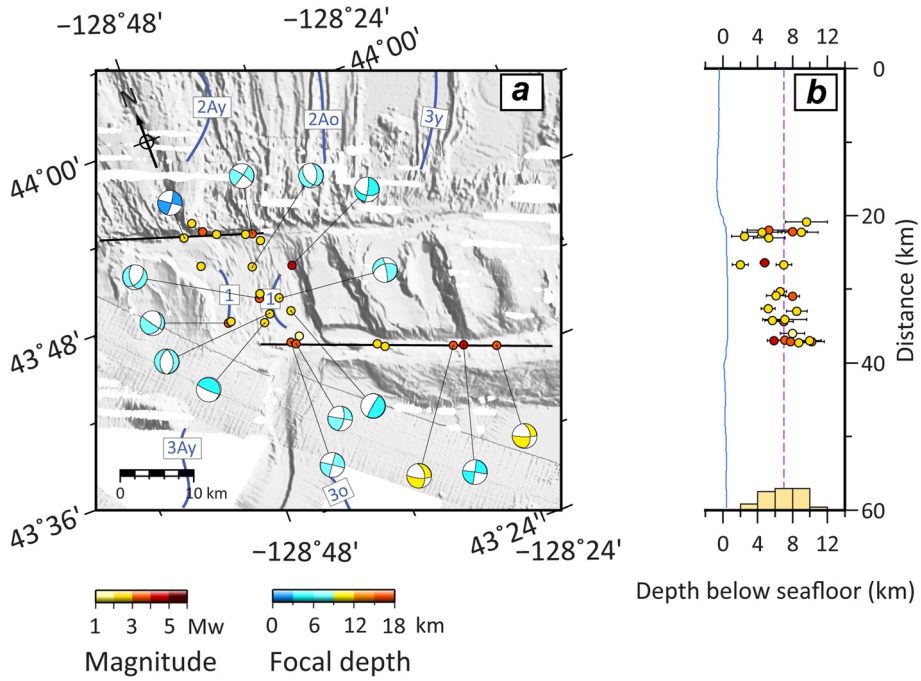

Figure 6. Close-up view of the Cascadia Depression (central Blanco transform fault system [BTFS]). (a) Local seismicity and focal mechanisms. (b) Vertical profile perpendicular to the strike of the BTFS showing the focal depth distribution. Symbols, lines, and labels are as in Figure 5.

with previous seismicity studies (Braunmiller & Nábělek, 2008; Dziak et al., 2000; Kuna et al., 2019), our results indicate that the seismic activity occurs along the BR (Figure 5), and that the seismicity of eastern BR is significantly higher than the western BR (west of 128°W) (Figures 5 and 6). Pockalny et al. (1997) suggested that such ridge-like features may form by compression caused by changes in plate motion. However, our seismic record provides little evidence to support such a scenario. As observed in our study (Figure 5), strike-slip and dip-slip faulting dominate the BR, supporting the proposed formation mechanism that simple shear motion with a small component of extension, which may have nurtured uplift along the fault (Dziak et al., 2000). Furthermore, a negative Bouguer anomaly over the BR (Dziak et al., 2000) may suggest that a low-density body, probably related to serpentine intrusions, caused further uplift of the BR. The occurrence of serpentinization in the mantle below the BR has also been inferred by Kuna et al. (2019) from the character of earthquakes and seismic swarms. The deviation from the characteristic valley-like morphology of OTFs (Grevemeyer et al., 2021; Wolfson-Schwehr & Boettcher, 2019) may suggest that the BR has not yet established its final structure.

5.1.2. Cascadia Depression

The CAS is seismically active (Johnson & Jones, 1978), and marked by normal faulting (Braunmiller & Nábělek, 2008). Consistently, we also observe normal faulting dominating the axis of the CAS (Figure 6), supporting it is a spreading segment (Braunmiller & Nábělek, 2008; Embley & Wilson, 1992). Strike-slip events close to the spreading axis might be related to magma movement. The transtensional strike-slip faulting observed near both ends of the short spreading segment indicates the transition from transform shear stress to tensile ridge axis stress. The focal depth ranges primarily from 4 to 10 km below seafloor, fitting into the focal depth ranges of mid-ocean ridge seismicity (Grevemeyer et al., 2019), suggesting that the magma source is deep. A positive magnetization (Figure 1b) supports the occurrence of the chron 1 (Brunhes magnetic chron) along the short spreading axis (Figure 6a), supporting magma-poor spreading at the CAS.

5.1.3. Western Transform Segments

The western segments reveal the most complex tectonic structures within the BTFS (Embley & Wilson, 1992). Active faults are hard to interpret (Embley & Wilson, 1992) as too many scarps are observed near the bathymetric

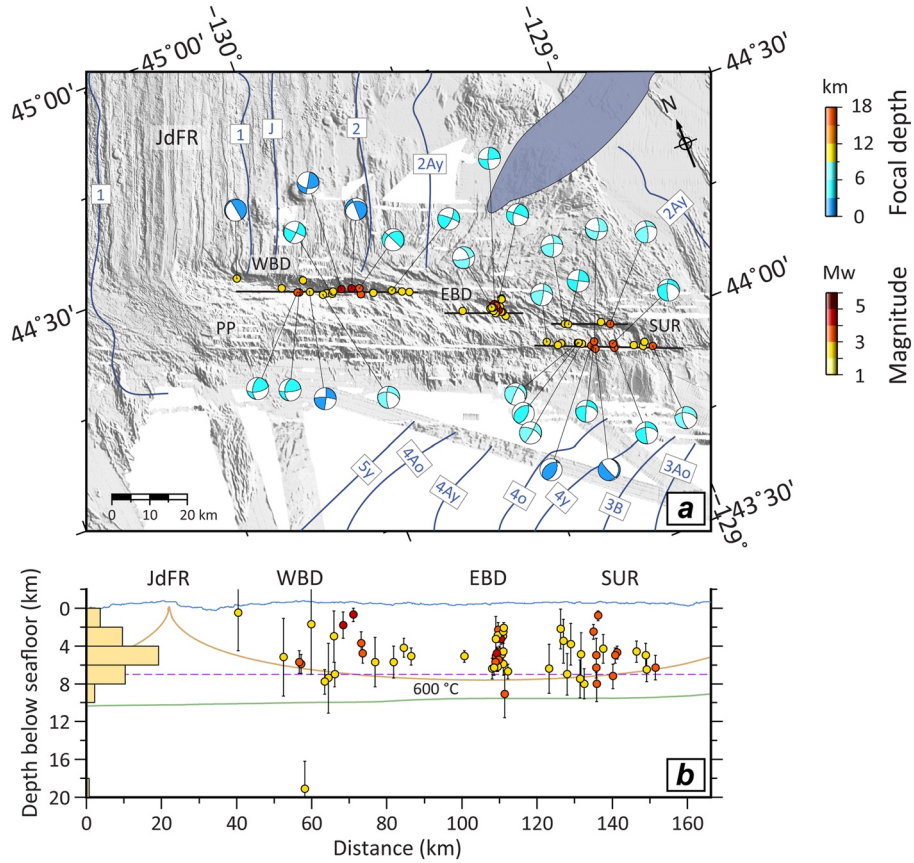

Figure 7. Close-up view of the western Blanco transform fault system (BTFS). (a) Local seismicity and focal mechanisms. (b) Along-strike vertical profile showing the focal depth distribution. Symbols, lines, and labels are as in Figure 5.

features (i.e., PP, WBD, EBD, and SUR). The kinematic model of Embley and Wilson (1992) suggested that the western BTFS was recently formed to accommodate far-field stress change. They speculated the main transform motion had been shifted from the PP to its northeastern troughs and each lineation on the seafloor might be an active fault. Dauteuil (1995) performed a more detailed bathymetric analysis, supporting the existence of a recent jump of the western transform plate boundary and a 15° rotation of the active direction. However, most OTFs generally run along prominent valleys (Ren et al., 2022; Wolfson-Schwehr & Boettcher, 2019), and therefore, it is difficult to understand which processes should have caused a prominent volcano-like feature.

Unfortunately, routine teleseismic event locations along the BTFS are scattered and systematically shifted from the bathymetric features (e.g., Dziak et al., 1991). With significantly improved precision, hydro-acoustic T-wave locations (Dziak et al., 2003; Géli et al., 2014) observed seismic activity near the northern boundary of PP and the southern wall of WBD. However, Braunmiller and Nábělek (2008) doubted the location uncertainties of the hydro-acoustic locations, which might involve systematic biases. In addition, they claimed that their relocated events are too scattered to identify the active faults of the western BTFS (Braunmiller & Nábělek, 2008).

Our results reveal for the first time the stress patterns of local seismic activity along the western BTFS, coinciding with bathymetric features (Figure 7). Between the WBD, EBD, and SUR, seismicity is sparse. At the SUR, two strands of earthquakes align well with the northern and southern walls identified from seafloor morphology, providing robust evidence for the exact location of active faults (Figure 7) and hence can be interpreted as pull-apart tectonics dominated. At the EBD, seismic activity was sparse during the OBS deployment, except for an earthquake swarm from October 2 to 3, 2012 (Figure 7 and Figure S11 in Supporting Information S1). Seismicity along the adjacent WBD occurs in the deepest parts of the central valley, with one extensional event on the northern wall, indicating tectonic extension near the RTI. Therefore, the WBD shows characteristic features on OTFs (Grevemeyer et al., 2021; Ren et al., 2022), while the SUR and EBD are short segments and comparable

to non-transform offsets (e.g., Macdonald et al., 1988). Although the SUR shows similar pull-apart features in seafloor morphology, like the CAS and GD, it is worth noting that the SUR does not show typic seismological pull-apart features as no extensional faulting occurred within the central basin and instead reverse faulting is notable (Figure 7a). Furthermore, the PP is an aseismic tectonic feature, suggesting that the active transform plate boundary runs northward of PP.

5.2. Focal Depth and Thermal Structure of the Eastern and Western Transform Segments

Most previous seismicity studies of the BTFS (e.g., Dziak et al., 2003; Géli et al., 2014) did not provide focal depth determination except for the JED event locations procedure of Braunmiller and Nábělek (2008) and the microseismicity survey along the BR (Kuna et al., 2019). Braunmiller and Nábělek (2008) suggested that focal depths near RTIs are slightly shallower (4–6 km) than in the central transform system (4–9 km) (Figure 4). In contrast, our local seismicity distribution does not support their observation. We observed deep events near the RTIs exceeding 14 km (Figure 4), which were also noticed by a recent microseismicity study of the eastern RTI of the Romanche transform fault (Yu et al., 2021). More interestingly, focal depths of the eastern BTFS are systematically deeper (4–10 km) than those of the western BTFS (0–8 km) (Figures 5 and 7), suggesting different modes of slip at the eastern and western segments of the BTFS. To constrain the maximum depth of faulting, we further extracted the 600°C isotherms (Figures 4, 5, and 7) from a half-space cooling model and a geodynamic model incorporating hydrothermal cooling (Roland et al., 2010).

At the eastern BTFS (Figure 5), more than half of the earthquakes occurred in the uppermost oceanic mantle below 8 km. The other crustal events peak between 4 and 7 km, indicating an aseismic upper oceanic crust. Between 7 and 8 km in depth, it seems to be a 1-km-wide aseismic band around at Moho depth, which was first observed by Kuna et al. (2019). Hydrothermally altered gabbros, diabases, and basalts were dredged from the site between the GD and the BR, supporting active hydrothermal fluid activity at the eastern BTFS (Hart et al., 1990). Therefore, hydrothermal cooling is a critical process affecting the thermal structure of this region (Roland et al., 2010). The local events are mostly constrained by the 600°C isotherm from the hydrothermal cooling model (green lines in Figures 4 and 5), except for a cluster of deep events at the central BR and two events below 14 km near the GR. Braunmiller and Nábělek (2008) suggested the eastern BTFS seems fully coupled; thus, the relative plate motion accounted for brittle deformation in the lower crust and uppermost mantle of the eastern BTFS. The existence of serpentinite peridotite in the uppermost mantle (Dziak et al., 2000; Embley & Wilson, 1992; Kuna et al., 2019) might result in the velocity-strengthening mode that inhibits earthquake nucleation of the upper crust (0–4 km) (Boettcher & Jordan, 2004). Furthermore, deep earthquakes (higher than 600°C) up to ∼16 km were observed at central BR and near GR, supporting the semi-brittle deformation in the mantle (Prigent et al., 2020; Yu et al., 2021).

In contrast, at the western BTFS (Figure 7), most events occurred in the oceanic crust (0–8 km). Like the eastern segment, the 600°C isotherm from the hydrothermal cooling model limits the depth of seismicity and brittle faulting, as Roland et al. (2010) predicted. Compared to the fully coupled eastern BTFS, we suggest a different seismotectonic behavior of the western BTFS; thus, relative plate motion is accommodated mainly via brittle deformation shallower than the 600°C isotherm, while creep dominates in the uppermost mantle.

5.3. Two End-Members of Ridge-Transform Interaction

RTIs endure the most prominent interaction between transform faults and the truncated spreading segments, representing the transition from transform shear stress to tensile stress (Distortions, 1989; Morgan & Parmentier, 1984). Furthermore, RTIs show prominent features, including J-shaped ridges, hummocks, and small volcanic cones extending across the RTI, often covering the outside corner-fracture zone region terminating in the older plate (Grevemeyer et al., 2021). These J-shaped ridges appear to be formed by the progressively oblique prolongation of the adjacent spreading axis across the transform fault.

Here, we observe different types of morphologic features at the western and eastern RTIs as well as along the transform domains. J-shaped ridges occur at both RTIs but are much more prominent at the western RTI where the JdFR surpasses the WBD and curves into the PP (Figures 1a and 7a), indicating that the PP may represent a “rooster comb” as observed at a number of fast spreading OTF. Thus, at the East Pacific Rise, J-shaped ridges are often associated with shallower bathymetry (rooster combs) where the older lith-

osphere and the opposing ridge tip are juxtaposed (Barth, 1994; Fornari et al., 1989; Gallo et al., 1986). As a result, the adjacent WBD shows typical OTF features, running along a deep valley with tectonic extension (Grevemeyer et al., 2021; Ren et al., 2022). However, at the eastern RTI, the northern GR is truncated by the GT, and the J-shaped ridges occur, but do not run across the deep GD (Figures 1 and 5a). Furthermore, the negative magnetic anomaly north to the truncated GR suggests that its seabed was formed before the chron 1 (Brunhes magnetic chron) at least 780 kyrs ago (Figures 1 and 5a), which supports a lack of recent magmatic activity near this region and a weak interaction between the GR and the eastern BTFS. Although both RTIs show characteristic features of OTFs, it is reasonable to suggest that the impact of spreading episodes of the adjacent spreading ridges on the transform faults is weaker in the east than in the west, resulting in a different mode of slip at the western and eastern BTFS.

5.4. Evolution of the BTFS Revisited

Structurally, the BTFS shows strong similarities with other segmented OTFs in the Pacific, like the Siqueiros transform system on the East Pacific Rise (Fornari et al., 1989). At the Siqueiros transform, a documented change in spreading direction caused a single transform fault to be subjected to a series of extensional events that led to the formation of an intra-transform spreading segment (Pockalny et al., 1997). The configuration of the BTFS also resulted from plate reorientation at ∼5 Ma (Embley & Wilson, 1992). However, the BTFS developed from at least two transform faults (Embley & Wilson, 1992) or non-transform ridge offsets (Cowan et al., 1986; McKenzie, 1986; D. S. Wilson, 1990) rather than from a single transform fault. The CAS in the central BTFS, an intra-transform spreading center observed today, is a remnant of a rift segment shortened due to a series of rift propagation events (Embley & Wilson, 1992) instead of extensional events as described at the Siqueiros transform (Pockalny et al., 1997).

However, we have little evidence for stable transform faults at ∼5 Ma as envisioned by Embley and Wilson (1992). In plate tectonics, fracture zones mark the inactive trace of a transform fault (Grevemeyer et al., 2021; Morgan, 1968); hence, any mature transform fault should leave an adjacent fracture zone. However, seafloor morphology (Figure 8) does not provide evidence for fracture zone traces issuing from the westernmost BTFS, indicating that the western segment represents an immature transform system. In contrast, at the eastern BTFS fracture zone, traces of the BR and the GT extends 80 and 30 km to the east and the west of the GD, respectively (dotted lines in Figure 8), suggesting the BR and GT are reasonably mature features. Furthermore, if we idealize that the slip rate is constant (49 mm/yr; DeMets et al., 2010), the initial formation of the BR and GT could be traced at ∼1.6 and ∼0.6 Ma, respectively. Bathymetric and gravity data (Figure 8 and Figure S1 in Supporting Information S1; Matthews et al., 2011) provide no regional evidence of any transform fault or fracture zone between the JdFR and GR before 2 Ma. Therefore, we support the interpretation that the evolution of the BTFS was primarily controlled by ridge propagation (D. S. Wilson, 1993; Wilson et al., 1984) and hence the reorientation of non-transform offsets rather than discrete transform faults as depicted by Embley and Wilson (1992).

Ridge propagation is a temporary phenomenon and inconsistent with simple strike deformation (McKenzie, 1986). The migrating ridge tip may cause a large domain of bookshelf faulting between the propagator and the opposing "doomed" ridge (McKenzie, 1986; Morgan & Kleinrock, 1991), which has also been observed at the Sovanco transform deformation zone linking the northern JdFR and the southern Explorer Ridge (Cowan et al., 1986). We therefore revised the kinematic model of the BTFS (Figure 9), by replacing the simplified discrete transform model (Embley & Wilson, 1992; D. S. Wilson, 1988) with the broad transform zone model (McKenzie, 1986; Morgan & Kleinrock, 1991; D. S. Wilson, 1990) for rift propagation. We suggest that broad transform zones (i.e., bookshelf faulting domains) linked the propagating JdFR and GR before ∼5 Ma (Figure 9a). In response to the clockwise shift in the Juan de Fuca/Pacific pole of rotation at ∼5 Ma (D. S. Wilson, 1993), the bookshelf faulting domain and the ridge segments rotated clockwise, except that the eastern rift segment roughly remained geographically anchored (Embley & Wilson, 1992; Figure 9b). As a result, the ridge segment in the middle was shortened (Figure 9b). Furthermore, a series of ridge propagation events (Embley & Wilson, 1992; D. S. Wilson, 1993) contributed to the complexity of the entire BTFS. The southward propagation of the JdFR integrated two transform deformation zone by eliminating the ridge segments in between, while the northward propagation of the GR attached a small transform deformation zone in the easternmost and shortened the

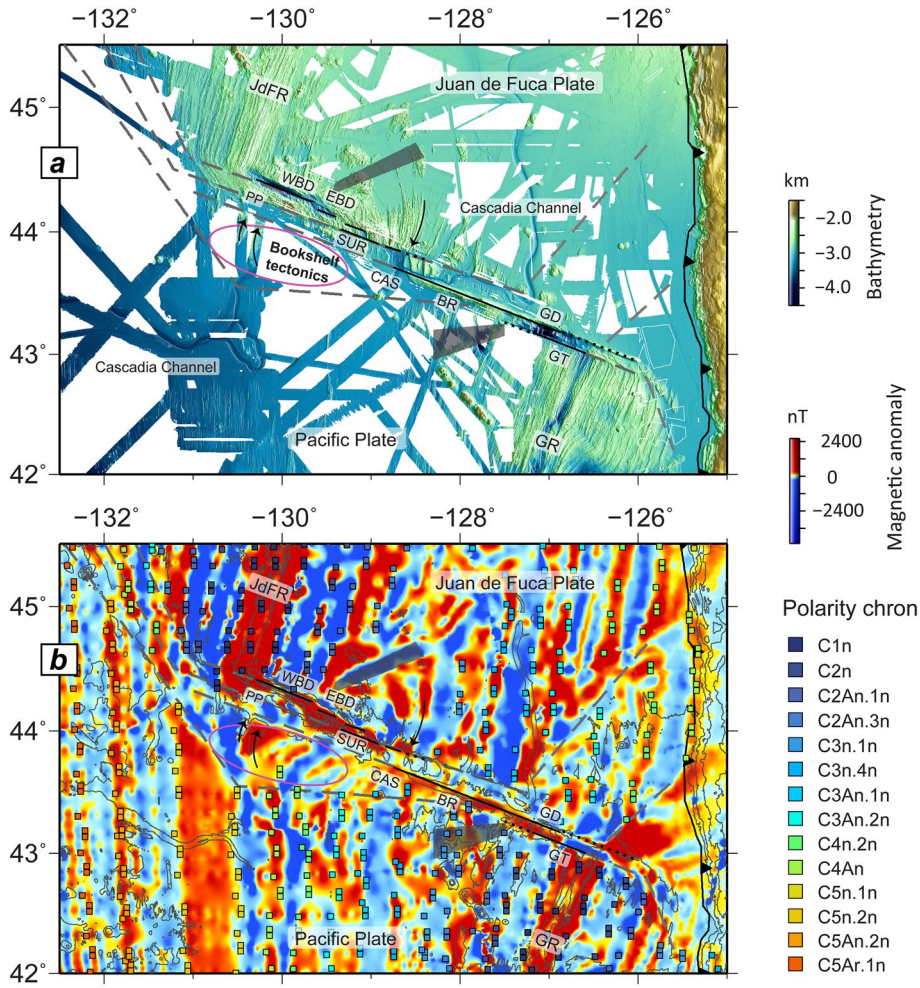

Figure 8. Tectonic interpretation of the Blanco transform fault system (BTFS). Solid black lines show active transform plate boundaries of the BTFS. Dotted lines show fracture zone traces. Dashed lines indicate the pseudofault traces in response to rift propagation and plate rotation. Shaded polygons outlined the narrow zone of the inner-pseudofault and failed rift suggested by D. S. Wilson (1990). Magnetic polarity time scale is as in Figures 1b and 1c.

doomed segment in the north (Figure 9c). At small offsets, the inward jumps of the failed rift cut across the inner-pseudofault into the material formed at the propagator (D. S. Wilson, 1990), which has been marked in the inside corners of the BTFS (Figure 8). Both propagation events of the JdFR and the GR stopped before ∼1.8 Ma (Figure 8; D. S. Wilson, 1993), and thereafter the relative plate motion between the Juan de Fuca and Gorda Plates became reasonably stable. After the propagation events, ridge-transform interaction accounted primarily for the nucleation of active transform faults (e.g., Gerya, 2012). In the eastern BTFS, the northward propagation of GR stopped ∼10 km before reaching the BR deformation zone (Embley & Wilson, 1992), hence the formation of the GD and its extending troughs north to the GR (Figure 9d). The BR and the GT became mature transform faults with the growth of fracture zones since ∼1.6 and ∼0.6 Ma, respectively (Figure 9d). South to the PP, rotated crustal features are notable (highlighted in Figure 8), supporting the rotated bookshelf faulting domain of the BR in response to plate rotation has been transported to the northwest due to seafloor spreading (Figure 9). However, unlike the intra-transform spreading centers CAS and GD, the SUR in the west BTFS does not show typical pull-apart feature, as no extensional faulting was observed within the deep basin (Figure 7a). We suggest that the EBD and SUR are remnant features developed from doomed ridge segments (Embley & Wilson, 1992) that already died during propagation (Figure 9e), leading to ongoing reorganization to accommodate relative plate motion.

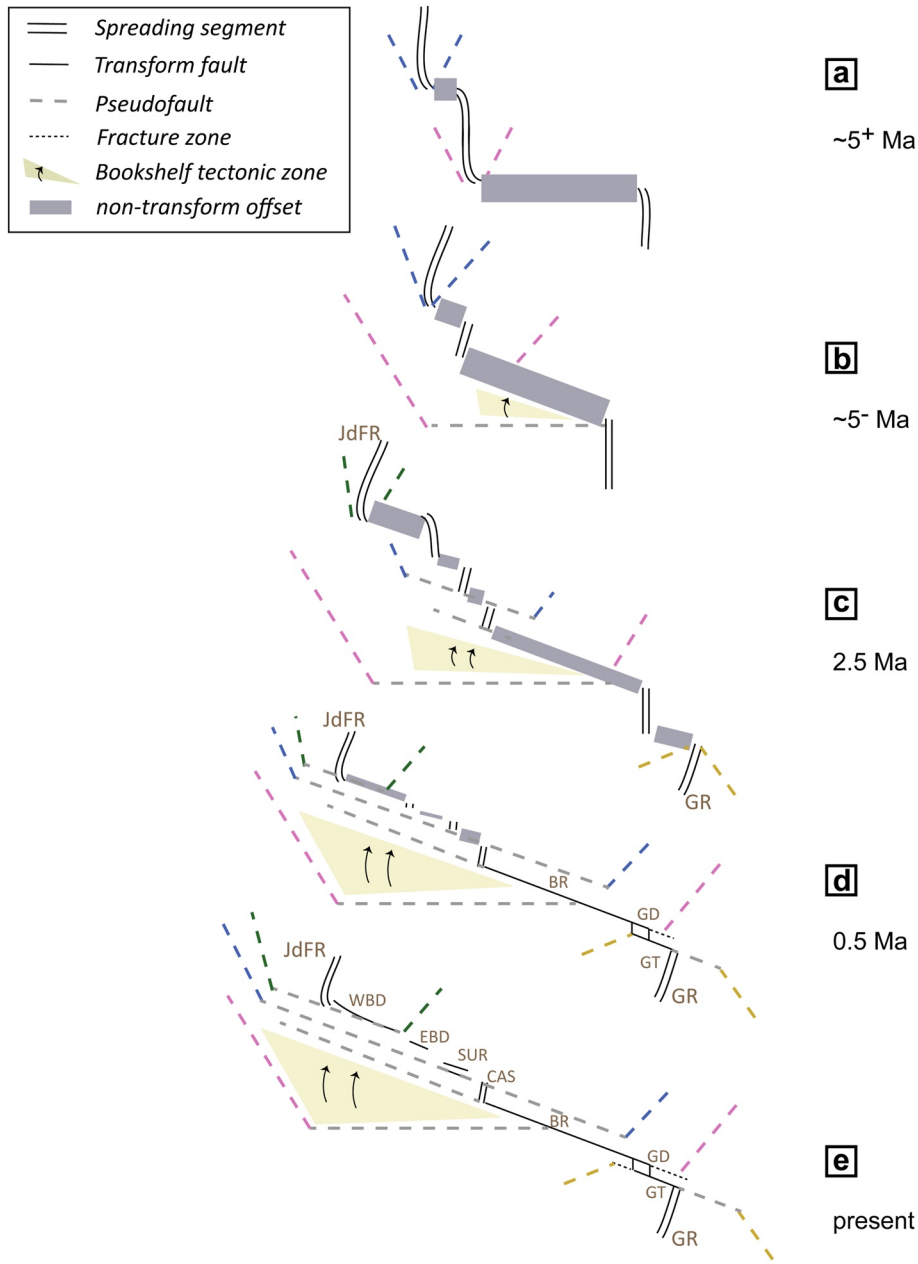

Figure 9. Development of transform faults and ridge segments since the formation of the Blanco transform fault system at around 5 Ma due to the clockwise shift in the Juan de Fuca/Pacific pole of rotation. Modified from Embley and Wilson (1992).

Relative azimuths between slip vector azimuths from focal mechanisms constrained by the OBS network and plate motion azimuths from MORVEL (DeMets et al., 2010) (Figure 10) support the scenario outlined above. As discussed, the pseudofault traces of the most recently active propagating rifts are identifiable at the inside corners from the airborne magnetic anomaly map (Figure 1), reaching the BTFS before chron 2 (~1.86 Ma) (D. S. Wilson, 1993). Therefore, it is indicated that no significant plate rotation has occurred around the BTFS over the past 1.8 Ma, allowing a meaningful comparison between slip vector azimuths from local events and the plate motion azimuths that are averaged over the past 780 kyrs (DeMets et al., 2010). We observed systematic variations in the relative azimuths, which seem to decrease from west to east along the entire BTFS (Figure 10c). The transform segments in the west and the CAS show mostly positive values (i.e., clockwise skewed). At the same time, the relative azimuths are scattered about the trend of plate motion in the east

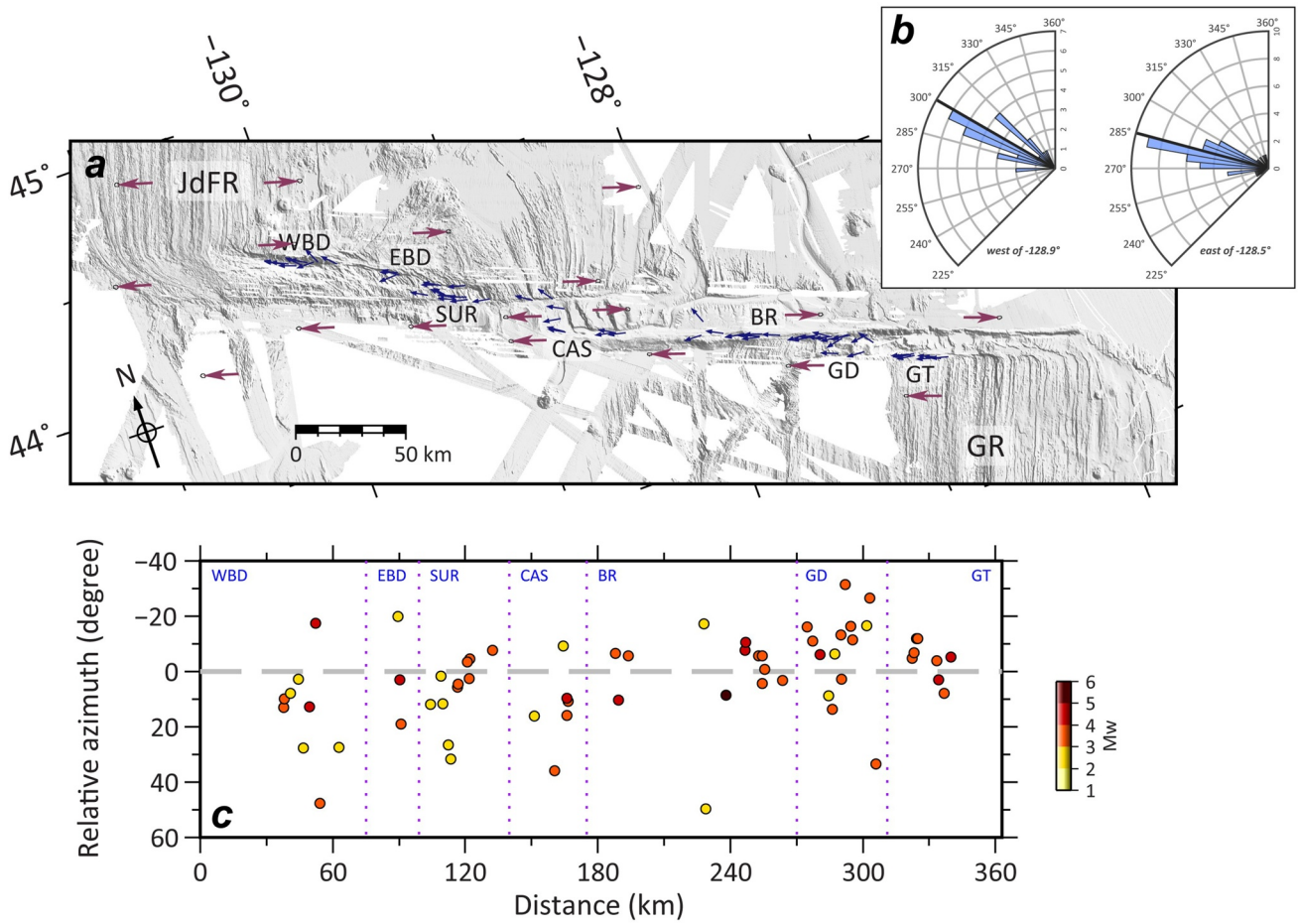

Figure 10. Strain partitioning at the Blanco transform fault system (BTFS). (a) Slip vector derived from 84 focal mechanisms. The blue and brown arrows indicate slip vectors from focal mechanisms and relative plate motion azimuths (DeMets et al., 2010) between the Pacific and Juan de Fuca Plates, respectively. (b) Rose diagrams of slip vector azimuths. The observed azimuths are binned in 5° intervals, and the solid black lines indicate the median azimuths of the western and eastern segments of the BTFS. (c) Variations of slip vector azimuths plotted relative to the plate motion azimuths from DeMets et al. (2010).

segment, though slightly negative values dominate. Therefore, stresses at the eastern segments, which established at ~0.6 Ma, roughly mimic plate motion, while the younger western segment may still adjust to the new stress regime.

Distributions of local events, strain partitioning, bathymetric features, magnetic data, and the tectonic evolution of the BTFS can be better interpreted in terms of two OTF systems instead of a single transform fault system. The CAS would represent the tectonic boundary separating both OTFs. The eastern BTFS is a relatively mature OTF system which was established at ~0.6 Ma, suggested to be highly coupled (Braunmiller & Nábělek, 2008; Kuna et al., 2019), and plate motion is mainly accommodated by brittle deformation in the lower crust and uppermost mantle (4–10 km). In contrast, the western BTFS emerged after a series of ridge propagation events stopped at ~2 Ma. However, in the recent geological past, it has been affected by typical tectonic extension at OTFs (Furlong et al., 2001; Grevemeyer et al., 2021), causing the formation of deep troughs along the active WBD, which is in line with the observation that OTFs commonly run along deep valleys (Ren et al., 2022). Plate motions at the western BTFS are accommodated mainly by brittle deformation at temperatures below 600°C (0–8 km) and creep in the mantle. The clockwise skewed stresses of the western BTFS (Figure 10) suggest that the recent reorganization of the west segments (Braunmiller & Nábělek, 2008; Embley & Wilson, 1992) might still be active in the near future.

6. Conclusions

One year of local seismic activity recorded along the entire BTFS enabled us to reveal the local seismicity and focal mechanisms within a 350-km long and strongly segmented OTF system. Based on high-quality hypocenters of local seismicity together with bathymetric, magnetic, and gravity data sets, we revised the kinematic model of the BTFS for the last ~5 Ma. Our results suggest that:

1. Local events align perfectly with morphologic features of the BTFS, indicating the active transform plate boundaries consist of the GT segment, BR, two strike-slip fault strands of the SUR, EBD, and WBD.
2. In the eastern BTFS, stresses are mainly accommodated by brittle deformation in the lower crust and uppermost mantle (4–10 km below the seafloor). In contrast, plate motions at the western BTFS are accommodated primarily by brittle deformation at temperatures below 600°C (0–8 km) and creep in the mantle. Deep earthquakes were also observed near the RTIs and the BR, inferring semi-brittle deformation.
3. Seafloor bathymetry reveals magma-robust features and J-shaped ridges surpassing the transform valley at the western RTI. However, at the eastern RTI, magma-poor features as well as truncated J-shaped ridges which stopped at the GD are observed. These different behaviors corresponding to strong and weak ridge-transform interaction, respectively, might account for the along-strike variation of the BTFS.
4. Consistent with gravity field data, there is no clear trace of fracture zone of the BTFS, except for the newly developed fracture zones adjacent to BR and GT. We therefore exclude the existence of fracture zones or established transform faults of the BTFS before 2 Ma. Accordingly, our modified kinematic model suggests the BTFS developed from a number of broad transform deformation zones (Cowan et al., 1986; D. S. Wilson, 1990) linking ridge segments during rift propagation events before ~2 Ma, rather than discrete transform faults suggested by Embley and Wilson (1992);
5. The BR and GT of the eastern BTFS were formed at ~1.6 and ~0.6 Ma, respectively. Although the EBD, SUR, CAS, and GD developed from ridge segments during the propagation events of the JdFR and GR, different seismotectonics of each segment suggest the CAS and GD are intra-transform spreading centers, while neither EBD nor SUR is corresponding to the formation of oceanic crust, representing remnant features of doomed rifts that already died during propagation.
6. Seismic slip vectors reveal that stresses in the eastern BTFS roughly coincide with the direction of plate motion, suggesting a mature transform fault system accommodating the plate motion. However, stresses to the west are clockwise skewed, indicating the re-organization of the western BTFS is still active now.
7. Multidisciplinary observations support different seismotectonic behaviors of the western and the eastern BTFS, suggesting that the BTFS could be divided into two oceanic transform systems impacted by two end-members of ridge-transform interaction. The eastern BTFS became a mature transform plate boundary since ~0.6 Ma. Although the westernmost WBD near the RTI shows the typical oceanic transform feature that active faults run along deep valleys, the other segments further away from the RTI may still develop over time. We therefore suggest the western BTFS is an immature transform system, which has been continually evolving to accommodate far-field stress change.

Acknowledgments
Our study benefitted from GEOMAR's OCEANS program. Yu Ren was supported by the China Scholarship Council (Grant 201904910466) and the 2022 Beacon Prize sponsored by Zhihu Incorporation. The authors thank all persons who contributed to data collection in the Blanco Transform OBS experiment (Nábělek & Braunmiller, 2012). Seismic data used in this study, which are archived at the IRIS Data Management Center (http://www.iris.edu), were provided by instruments from the Ocean Bottom Seismic Instrument Center (https://obsic.whoi.edu/). This manuscript benefitted from conversations with Jason P. Morgan, Colin Devey, Lars Rüpke, Sibiao Liu, and Zhikui Guo. The authors thank editor Isabelle Manighetti, associate editor, Milena Marjanović, and an anonymous reviewer for their thoughtful comments and efforts toward improving this manuscript. Open Access funding enabled and organized by Projekt DEAL.

Data Availability Statement

The continuous seismological data are accessible from the IRIS under the network code X9 (2012–2013; https://doi.org/10.7914/SN/X9_2012). Bathymetric data are available via https://www.gmrt.org/GMRTMapTool/. Airborne magnetic anomaly data are available from the USGS Mineral Resources Program (https://mrdata.usgs.gov/magnetic/).

References

Atwater, T., & Stock, J. (1998). Pacific-North America plate tectonics of the Neogene Southwestern United States – An update. *International Geological Review*, *40*(5), 375–402. https://doi.org/10.1080/00206819809465216

Aydin, A., & Nur, A. (1982). Evolution of pull-apart basins and their scale independence. *Tectonics*, *1*(1), 91–105. https://doi.org/10.1029/TC001i001p00091

Bankey, V., Cuevas, A., Daniels, D., Finn, C., Hernandez, I., Hill, P., et al. (2002). Digital data grids for the magnetic anomaly map of North America. USGS Open File Report 2002-414. https://doi.org/10.3133/ofr02414

Barth, G. A. (1994). Oceanic crust thickens approaching the Clipperton Fracture Zone. *Marine Geophysical Researches*, *16*(1), 51–64. https://doi.org/10.1007/BF01812445

Boettcher, M. S., & Jordan, T. H. (2004). Earthquake scaling relations for mid-ocean ridge transform faults. *Journal of Geophysical Research*, *109*(B12), B12302. https://doi.org/10.1029/2004JB003110

Braunmiller, J., & Nábělek, J. (2008). Segmentation of the Blanco Transform Fault Zone from earthquake analysis: Complex tectonics of an oceanic transform fault. *Journal of Geophysical Research*, *113*(B7), B07108. https://doi.org/10.1029/2007JB005213

Carbotte, S. M., Nedimović, M. R., Canales, J. P., Kent, G., Harding, A., & Marjanović, M. (2008). Variable crustal structure along the Juan de Fuca Ridge: Influence of on-axis hot spots and absolute plate motions. *Geochemistry, Geophysics, Geosystems*, *9*(8), Q08001. https://doi.org/10.1029/2007GC001922

Carbotte, S. M., Smith, D. K., Cannat, M., & Klein, E. M. (2015). Tectonic and magmatic segmentation of the Global Ocean Ridge System: A synthesis of observations. In T. J. Wright, A. Ayele, D. J. Ferguson, T. Kidane, & C. Vye-Brown (Eds.), *Magmatic rifting and active volcanism* (Vol. 420, pp. 249–295). Geological Society. https://doi.org/10.1144/SP420.5

Cowan, D. S., Botros, M., & Johnson, H. P. (1986). Bookshelf tectonics: Rotated crustal blocks within the Sovanco Fracture Zone. *Geophysical Research Letters*, *13*(10), 995–998. https://doi.org/10.1029/GL013i010p00995

Dannowski, A., Morgan, J. P., Grevemeyer, I., & Ranero, C. R. (2018). Enhanced mantle upwelling/melting caused segment propagation, oceanic core complex die off, and the death of a transform fault: The Mid-Atlantic Ridge at 21.5°N. *Journal of Geophysical Research: Solid Earth*, *123*(2), 941–956. https://doi.org/10.1002/2017JB014273

Dauteuil, O. (1995). Fault pattern from seabeam processing: The western part of the Blanco Fracture Zone (NE Pacific). *Marine Geophysical Researches*, *17*(1), 17–35. https://doi.org/10.1007/BF01268049

DeMets, C., Gordon, R. G., & Argus, D. F. (2010). Geologically current plate motions. *Geophysical Journal International*, *181*(1), 1–80. https://doi.org/10.1111/j.1365-246X.2009.04491.x

Distortions, A. S. (1989). Rotations and crustal thinning at ridge–transform intersections. *Nature*, *340*(6235), 626–628. https://doi.org/10.1038/340626a0

Dziak, R., Chadwick, W., Fox, C., & Embley, R. (2003). Hydrothermal temperature changes at the southern Juan de Fuca Ridge associated with MW 6.2 Blanco Transform earthquake. *Geology*, *31*(2), 119–122. https://doi.org/10.1130/0091-7613(2003)031<0119:HTCATS>2.0.CO;2

Dziak, R., Fox, C., & Embley, R. (1991). Relationship between the seismicity and geologic structure of the Blanco Transform Fault Zone. *Marine Geophysical Researches*, *13*(3), 203–208. https://doi.org/10.1007/BF00369149

Dziak, R., Fox, C., Embley, R., Nábělek, J., Braunmiller, J., & Koski, R. (2000). Recent tectonics of the Blanco Ridge, eastern Blanco transform fault zone. *Marine Geophysical Researches*, *21*(5), 423–450. https://doi.org/10.1023/A:1026545910893

Ekström, G., Nettles, M., & Dziewoński, A. M. (2012). The global CMT project 2004–2010: Centroid-moment tensors for 13,017 earthquakes. *Physics of the Earth and Planetary Interiors*, *200–201*, 1–9. https://doi.org/10.1016/j.pepi.2012.04.002

Elvers, D., Srivastava, S., Potter, K., Morley, J., & Sdidel, D. (1973). Asymmetric spreading across the Juan de Fuca and Gorda rises as obtained from a detailed magnetic survey. *Earth and Planetary Science Letters*, *20*(2), 211–219. https://doi.org/10.1016/0012-821X(73)90160-X

Embley, R. W., & Wilson, D. S. (1992). Morphology of the Blanco Transform Fault Zone-NE Pacific: Implications for its Tectonic Evolution. *Marine Geophysical Researches*, *14*(1), 25–45. https://doi.org/10.1007/BF01674064

Fornari, D. J., Gallo, D. G., Edwards, M. H., Madsen, J. A., Perfit, M. R., & Shor, A. N. (1989). Structure and topography of the Siqueiros transform fault system: Evidence for the development of intra-transform spreading centers. *Marine Geophysical Researches*, *11*(4), 263–299. https://doi.org/10.1007/BF00282579

Furlong, K. P., Sheaffer, S. D., & Malservisi, R. (2001). Thermal-rheological controls on deformation within oceanic transforms. *Geological Society, London, Special Publications*, *186*(1), 65–83. https://doi.org/10.1144/GSL.SP.2001.186.01.05

Gallo, D. G., Fox, P. J., & Macdonald, K. C. (1986). A Sea Beam investigation of the Clipperton transform fault: The morphotectonic expression of a fast-slipping transform boundary. *Journal of Geophysical Research*, *91*(B3), 3455–3467. https://doi.org/10.1029/JB091iB03p03455

Géli, L., Piau, J., Dziak, R., Maury, V., Fitzenz, D., Coutellier, Q., et al. (2014). Seismic precursors linked to highly compressible fluids at oceanic transform faults. *Nature Geoscience*, *7*(10), 757–761. https://doi.org/10.1038/ngeo2244

Gerya, T. V. (2012). Origin and models of oceanic transform faults. *Tectonophysics*, *522–533*, 34–54. https://doi.org/10.1016/j.tecto.2011.07.006

GFZ & Gempa GmbH. (2008). *The SeisComP seismological software package*. GFZ Data Services. https://doi.org/10.5880/GFZ.2.4.2020.003

Gong, J., Fan, W., & Parnell-Turner, R. (2022). Microseismicity indicates atypical small-scale plate rotation at the Quebrada transform fault system, East Pacific Rise. *Geophysical Research Letters*, *49*(3), e2021GL097000. https://doi.org/10.1029/2021GL097000

Grevemeyer, I., Hayman, N. W., Lange, D., Peirce, C., Papenberg, C., Van Avendonk, H. J. A., et al. (2019). Constraining the maximum depth of brittle deformation at slow- and ultraslow-spreading ridges using microseismicity. *Geology*, *47*(11), 1069–1073. https://doi.org/10.1130/G46577.1

Grevemeyer, I., Reston, T. J., & Moeller, S. (2013). Microseismicity of the Mid-Atlantic Ridge at 7°S–8°15′S and at the Logatchev Massif oceanic core complex at 14°40′N–14°50′N. *Geochemistry, Geophysics, Geosystems*, *14*(9), 3532–3554. https://doi.org/10.1002/ggge.20197

Grevemeyer, I., Rüpke, L. H., Morgan, J. P., Iyer, K., & Devey, C. W. (2021). Extensional tectonics and two-stage crustal accretion at oceanic transform faults. *Nature*, *591*(7850), 402–407. https://doi.org/10.1038/s41586-021-03278-9

Hart, R., Hoefs, J., & Pyle, D. (1990). Multistage hydrothermal systems in the Blanco Fracture Zone. In G. R. McMurray (Ed.), *Gorda Ridge* (pp. 51–75). Springer. https://doi.org/10.1007/978-1-4612-3258-2_4

Husen, S., Kissling, E., Flueh, E., & Asch, G. (1999). Accurate hypocentre determination in the seismogenic zone of the subducting Nazca Plate in northern Chile using a combined on-/offshore network. *Geophysical Journal International*, *138*(3), 687–701. https://doi.org/10.1046/j.1365-246x.1999.00893.x

Hutton, L. K., & Boore, D. M. (1987). The ML scale in Southern California. *Bulletin of the Seismological Society of America*, *77*(6), 2074–2094. https://doi.org/10.1785/BSSA0770062074

Johnson, S. H., & Jones, P. R. (1978). Microearthquakes located on the Blanco Fracture Zone with sonobuoy arrays. *Journal of Geophysical Research*, *83*(B1), 255–261. https://doi.org/10.1029/JB083iB01p00255

Kahle, R., Tilmann, F., & Grevemeyer, I. (2016). Crustal structure and kinematics of the TAMMAR propagating rift system on the Mid-Atlantic Ridge from seismic refraction and satellite altimetry gravity. *Geophysical Journal International*, *206*(2), 1382–1397. https://doi.org/10.1093/gji/ggw219

Karson, J. A. (2017). The Iceland plate boundary zone: Propagating rifts, migrating transforms, and rift-parallel strike-slip faults. *Geochemistry, Geophysics, Geosystems*, *18*(11), 4043–4054. https://doi.org/10.1002/2017GC007045

Karsten, J. L., & Delaney, J. R. (1989). Hot spot-ridge crest convergence in the northeast Pacific. *Journal of Geophysical Research*, *94*(B1), 700–712. https://doi.org/10.1029/JB094iB01p00700

Kissling, E., Ellsworth, W. L., Eberhart-Phillips, D., & Kradolfer, U. (1994). Initial reference models in local earthquake tomography. *Journal of Geophysical Research*, *99*(B10), 19635–19646. https://doi.org/10.1029/93JB03138

Kuna, V. M. (2020). Investigation of slip and tectonics of the Blanco Transform Fault using high-resolution ocean bottom seismic data. Ph.D. thesis. Oregon State University.
Kuna, V. M., Nábělek, J. L., & Braunmiller, J. (2019). Mode of slip and crust–mantle interaction at oceanic transform faults. *Nature Geoscience*, *12*(2), 138–142. https://doi.org/10.1038/s41561-018-0287-1
Lange, D., Rietbrock, A., Haberland, C., Bataille, K., Dahm, T., Tilmann, F., & Flüh, E. R. (2007). Seismicity and geometry of the south Chilean subduction zone (41.5°S–43.5°S): Implications for controlling parameters. *Geophysical Research Letters*, *34*(6), L06311. https://doi.org/10.1029/2006GL029190
Lomax, A., Virieux, J., Volant, P., & Berge-Thierry, C. (2000). Probabilistic earthquake location in 3D and layered models. In C. H. Thurber, & N. Rabinowitz (Eds.), *Advances in seismic event location* (Vol. 18, pp. 101–134). Springer. https://doi.org/10.1007/978-94-015-9536-0_5
Lonsdale, P. (2005). Creation of the Cocos and Nazca plates by fission of the Farallon plate. *Tectonophysics*, *404*(3–4), 237–264. https://doi.org/10.1016/j.tecto.2005.05.011
Macdonald, K., Fox, P., Perram, L., Eisen, M., Haymon, R., Miller, S., et al. (1988). A new view of the mid-ocean ridge from the behavior of ridge-axis discontinuities. *Nature*, *335*(6187), 217–225. https://doi.org/10.1038/335217a0
Mann, P., Hempton, M. R., Bradley, D. C., & Burke, K. (1983). Development of Pull-Apart Basins. *The Journal of Geology*, *91*(5), 529–554. https://doi.org/10.1086/628803
Marjanović, M., Carbotte, S. M., Nedimović, M. R., & Canales, J. P. (2011). Gravity and seismic study of crustal structure along the Juan de Fuca Ridge axis and across pseudofaults on the ridge flanks. *Geochemistry, Geophysics, Geosystems*, *12*(5), Q05008. https://doi.org/10.1029/2010GC003439
Matthews, K. J., Müller, R. D., Wessel, P., & Whittaker, J. M. (2011). The tectonic fabric of the ocean basins. *Journal of Geophysical Research*, *116*(B12), B12109. https://doi.org/10.1029/2011JB008413
McKenzie, D. (1986). The geometry of propagating rifts. *Earth and Planetary Science Letters*, *77*(2), 176–186. https://doi.org/10.1016/0012-821X(86)90159-7
Menard, H. W. (1967). Extension of Northeastern-Pacific Fracture Zones. *Science*, *155*(3758), 72–74. https://doi.org/10.1126/science.155.3758.72
Morgan, W. J. (1968). Rises, trenches, great faults, and crustal blocks. *Journal of Geophysical Research*, *73*(6), 1959–1982. https://doi.org/10.1029/JB073i006p01959
Morgan, J. P., & Kleinrock, M. C. (1991). Transform zone migration: Implications of bookshelf faulting at oceanic and Icelandic propagating ridges. *Tectonics*, *10*(5), 920–935. https://doi.org/10.1029/90TC02481
Morgan, J. P., & Parmentier, E. M. (1984). Lithospheric stress near a ridge-transform intersection. *Geophysical Research Letters*, *11*(2), 113–116. https://doi.org/10.1029/GL011i002p00113
Nábělek, J., & Braunmiller, J. (2012). Plate Boundary Evolution and Physics at an Oceanic Transform Fault System [Dataset]. International Federation of Digital Seismograph Networks. https://doi.org/10.7914/SN/X9_2012
Nedimović, M. R., Bohnenstiehl, D. R., Carbotte, S. M., Canales, J. P., & Dziak, R. P. (2009). Faulting and hydration of the Juan de Fuca plate system. *Earth and Planetary Science Letters*, *284*(1–2), 94–102. https://doi.org/10.1016/j.epsl.2009.04.013
Ottemöller, L., & Havskov, J. (2003). Moment magnitude determination for local and regional earthquakes based on source spectra. *Bulletin of the Seismological Society of America*, *93*(1), 203–214. https://doi.org/10.1785/0120010220
Pickle, R. C., Forsyth, D. W., Harmon, N., Nagle, A. N., & Saal, A. (2009). Thermo-mechanical control of axial topography of intra-transform spreading centers. *Earth and Planetary Science Letters*, *284*(3–4), 343–351. https://doi.org/10.1016/j.epsl.2009.05.004
Pockalny, R. A., Fox, P. J., Fornari, D. J., Macdonald, K. C., & Perfit, M. R. (1997). Tectonic reconstruction of the Clipperton and Siqueiros Fracture Zones: Evidence and consequences of plate motion change for the last 3 Myr. *Journal of Geophysical Research*, *102*(B2), 3167–3181. https://doi.org/10.1029/96JB03391
Prigent, C., Warren, J. M., Kohli, A. H., & Teyssier, C. (2020). Fracture-mediated deep seawater flow and mantle hydration on oceanic transform faults. *Earth and Planetary Science Letters*, *532*, 115988. https://doi.org/10.1016/j.epsl.2019.115988
Reasenberg, P., & Oppenheimer, D. (1985). FPFIT, FPPLOT, and FPPAGE: Fortran computer programs for calculating and displaying earthquake fault-plane solutions. USGS Open File Report, 85-739. https://doi.org/10.3133/ofr85739
Ren, Y., Geersen, J., & Grevemeyer, I. (2022). Impact of spreading rate and age-offset on oceanic transform fault morphology. *Geophysical Research Letters*, *49*(2), e2021GL096170. https://doi.org/10.1029/2021GL096170
Roland, E., Behn, M. D., & Hirth, G. (2010). Thermal-mechanical behavior of oceanic transform faults: Implications for the spatial distribution of seismicity. *Geochemistry, Geophysics, Geosystems*, *11*(7), Q07001. https://doi.org/10.1029/2010GC003034
Ryan, W. B. F., Carbotte, S. M., Coplan, J. O., O'Hara, S., Melkonian, A., Arko, R., et al. (2009). Global multi-resolution topography synthesis. *Geochemistry, Geophysics, Geosystems*, *10*(3), Q03014. https://doi.org/10.1029/2008GC002332
Skolotnev, S., Sanfilippo, A., Peyve, A., Nestola, Y., Sokolov, S., Petracchini, L., et al. (2021). Seafloor spreading and tectonics at the Charlie Gibbs transform system (52-53°N, mid Atlantic ridge): Preliminary results from R/V AN Strakhov expedition S50. *Ofioliti*, *46*(1), 83–101. https://doi.org/10.4454/ofioliti.v46i1.539
van Wijk, J., Axen, G., & Abera, R. (2017). Initiation, evolution and extinction of pull-apart basins: Implications for opening of the Gulf of California. *Tectonophysics*, *719–720*, 37–50. https://doi.org/10.1016/j.tecto.2017.04.019
Williams, J., Hawthorne, J., Rost, S., & Wright, T. (2019). Stress drops on the Blanco oceanic transform fault from interstation phase coherence. *Bulletin of the Seismological Society of America*, *109*(3), 929–943. https://doi.org/10.1785/0120180319
Wilson, D. S. (1990). Kinematics of overlapping rift propagation with cyclic rift failure. *Earth and Planetary Science Letters*, *96*(3–4), 384–392. https://doi.org/10.1016/0012-821X(90)90014-O
Wilson, D. S. (1988). Tectonic history of the Juan de Fuca Ridge over the last 40 million years. *Journal of Geophysical Research*, *93*(B10), 11863–11876. https://doi.org/10.1029/JB093iB10p11863
Wilson, D. S. (1993). Confidence intervals for motion and deformation of the Juan de Fuca Plate. *Journal of Geophysical Research*, *98*(B9), 16053–16071. https://doi.org/10.1029/93JB01227
Wilson, D. S., Hey, R. N., & Nishimura, C. (1984). Propagation as a mechanism of reorientation of the Juan de Fuca Ridge. *Journal of Geophysical Research*, *89*(B11), 9215–9225. https://doi.org/10.1029/JB089iB11p09215
Wilson, J. T. (1965). A new class of faults and their bearing on continental drift. *Nature*, *207*(4995), 343–347. https://doi.org/10.1038/207343a0
Wolfson-Schwehr, M., & Boettcher, M. S. (2019). Global characteristics of oceanic transform fault structure and seismicity. In J. C. Duarte (Ed.), *Transform plate boundaries and fracture zones* (pp. 21–59). Elsevier. https://doi.org/10.1016/B978-0-12-812064-4.00002-5
Yu, Z., Singh, S. C., Gregory, E. P. M., Maia, M., Wang, Z., & Brunelli, D. (2021). Semi-brittle seismic deformation in high-temperature mantle mylonite shear zone along the Romanche transform fault. *Science Advances*, *7*(15), eabf3388. https://doi.org/10.1126/sciadv.abf3388

References From the Supporting Information

Álvarez-Gómez, J. A. (2019). FMC—Earthquake focal mechanisms data management, cluster and classification. *SoftwareX*, *9*, 299–307. https://doi.org/10.1016/j.softx.2019.03.008

Engdahl, E. R. (2006). Application of an improved algorithm to high precision relocation of ISC test events. *Physics of the Earth and Planetary Interiors*, *158*(1), 14–18. https://doi.org/10.1016/j.pepi.2006.03.007

Sandwell, D. T., Müller, R. D., Smith, W. H. F., Garcia, E., & Francis, R. (2014). New global marine gravity model from CryoSat-2 and Jason-1 reveals buried tectonic structure. *Science*, *346*(6205), 65–67. https://doi.org/10.1126/science.1258213

Journal of Geophysical Research: Solid Earth

Supporting Information for

Seismotectonics of the Blanco Transform Fault System, Northeast Pacific: Evidence for an immature plate boundary

Yu Ren [(1)], Dietrich Lange [(1)], and Ingo Grevemeyer [(1)]

(1) GEOMAR Helmholtz Centre for Ocean Research Kiel, Kiel, Germany

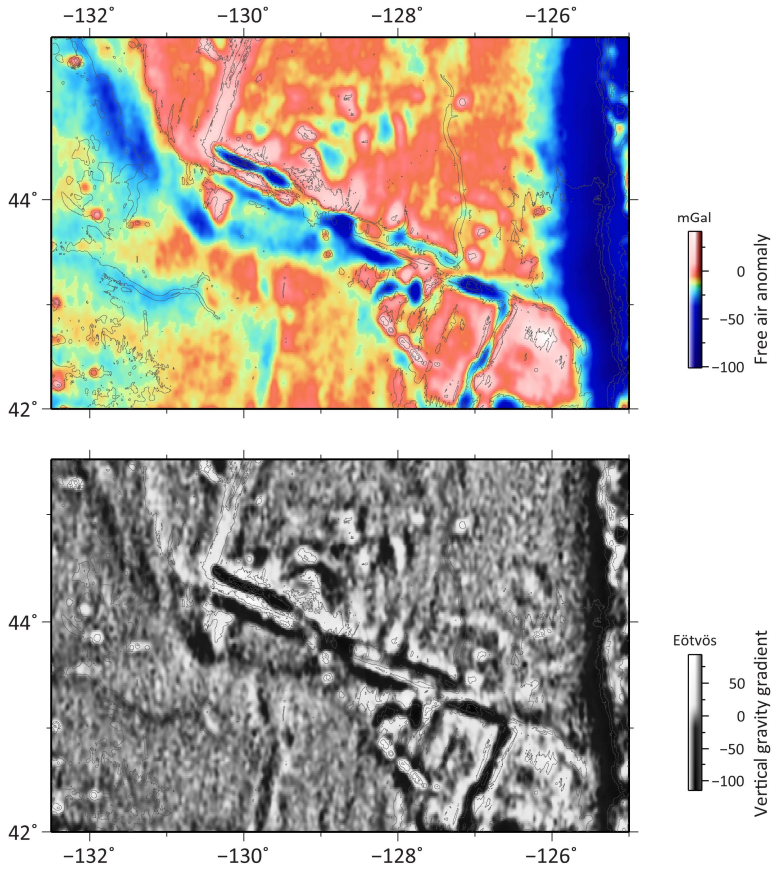

Figure S1. Gravity map (Sandwell et al., 2014) of the 350-km-long Blanco transform fault system (BTFS) in the Northeast Pacific, indicating no fracture zone in the west and a short fracture zone trace developed recently in the east (around 126° W).

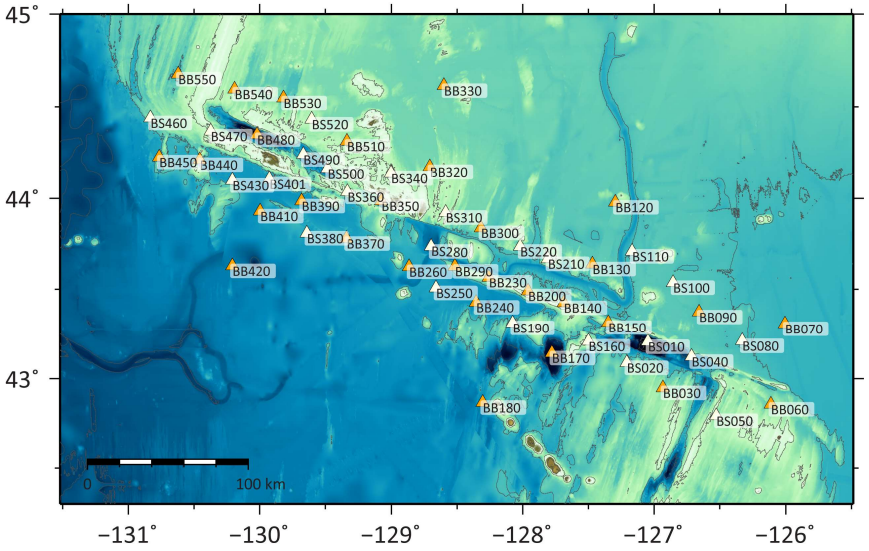

Figure S2. Distribution of the OBS stations (labeled with station names) used in this study.

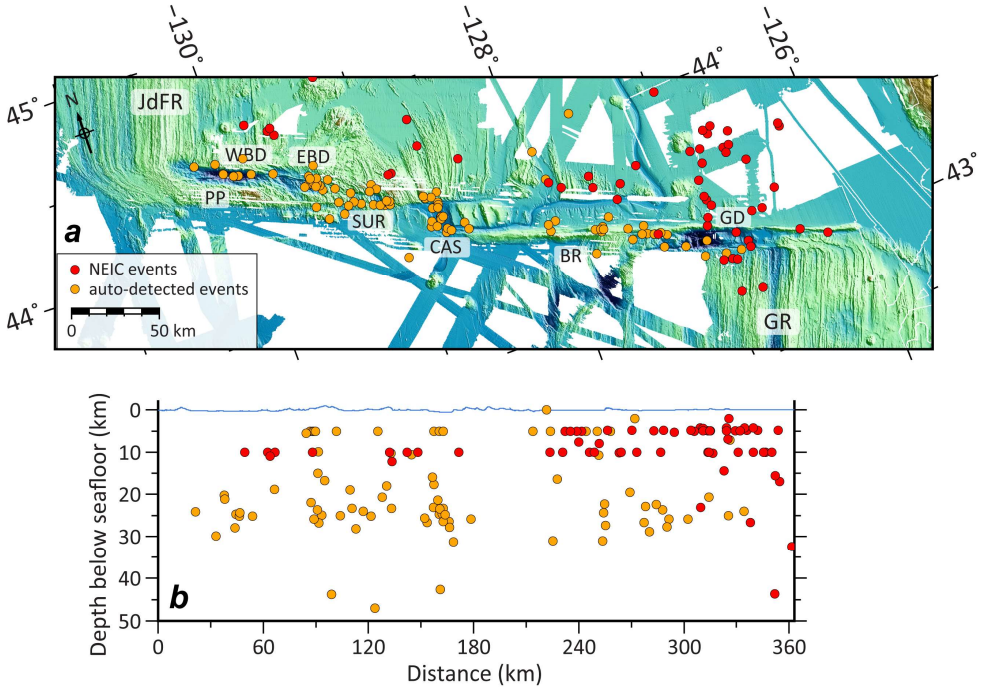

Figure S3. Seismicity catalog constructed in this study for precise relocation. (**a**) Distribution of local events from the NEIC and the auto-detected catalogs along the entire BTFS. (**b**) Along-strike vertical profile showing the focal depth distribution. Red and yellow dots show the location of NEIC and auto-detected events, respectively.

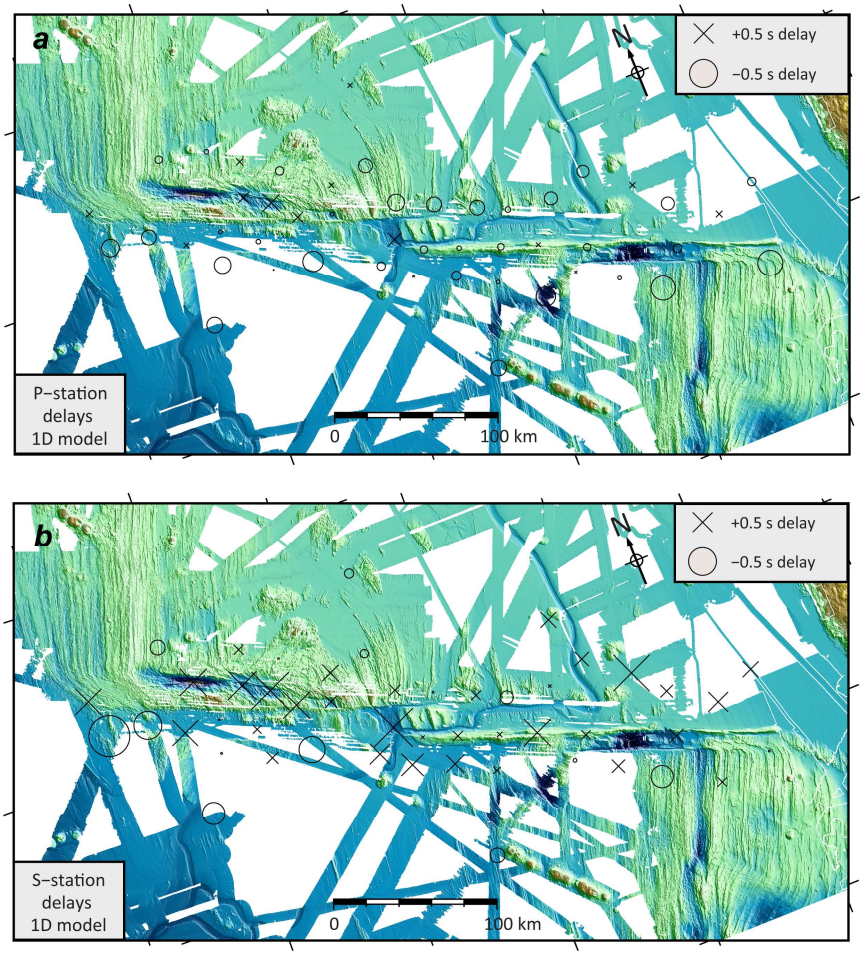

Figure S4. Station corrections for P- (panel **a**) and S- (panel **b**) phase onsets. The size of the symbol scales with the delay of each station.

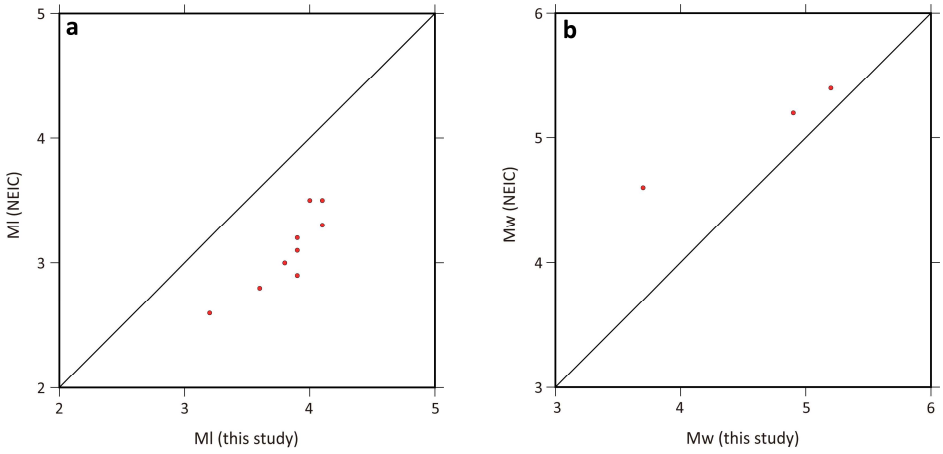

Figure S5. Comparison of the local (panel **a**) and moment magnitudes (panel **b**) for the events that are included in both NEIC and our local catalogs.

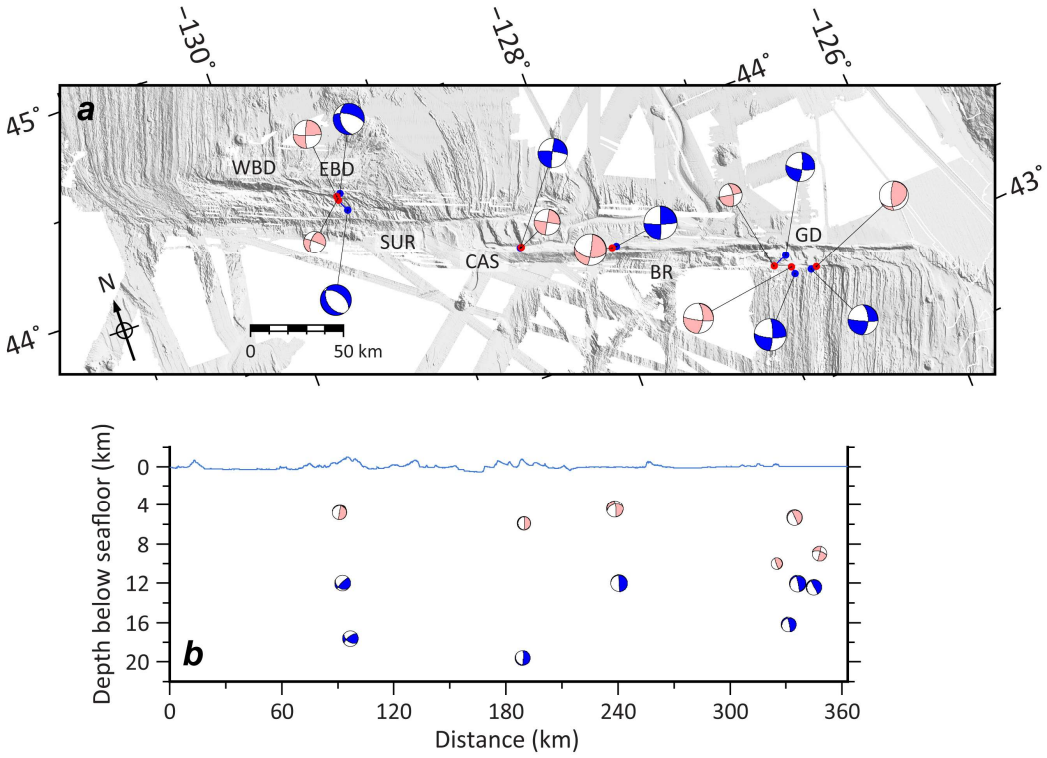

Figure S6. Comparison of the focal mechanisms for the 7 events that are included in both GCMT and our local catalogs. (**a**) Location bias of the GCMT catalog. The locations of GCMT events are in blue, while our local event locations are shown in red. (**b**) Depth bias of the GCMT catalog.

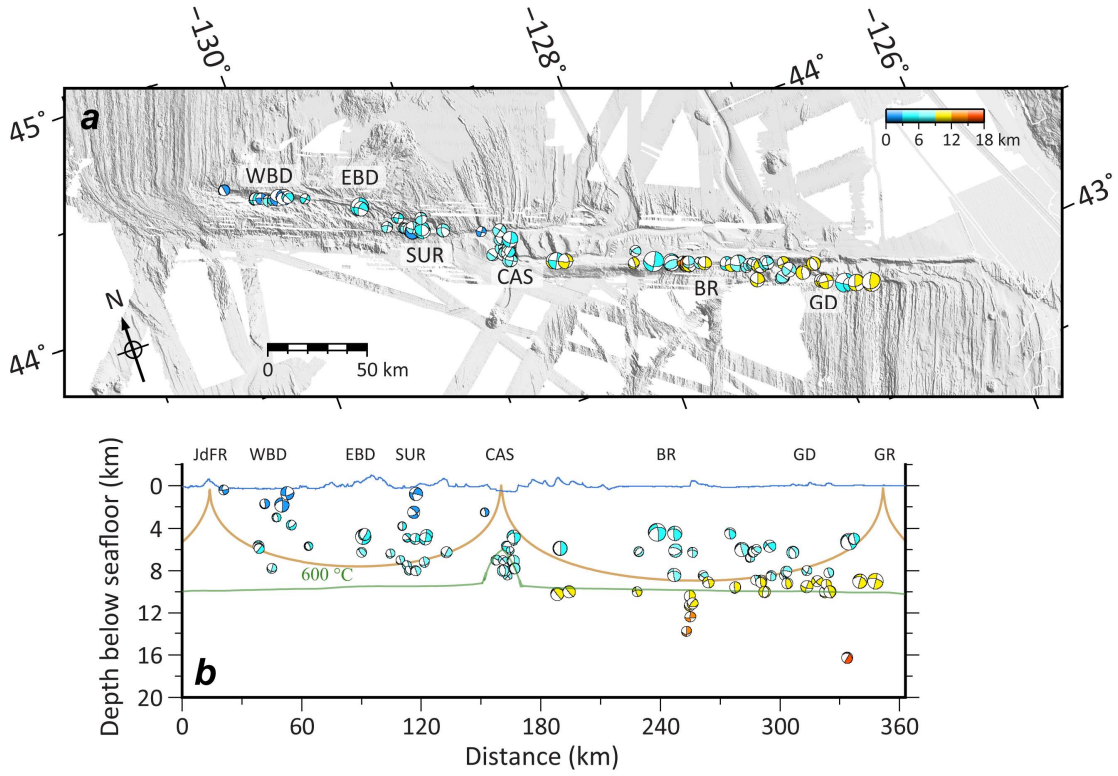

Figure S7. Focal mechanisms of 84 local events recorded by the OBS array. (**a**) Distribution of the focal mechanisms along the BTFS. (**b**) Along-strike vertical profile showing depth distribution of the focal mechanisms. Brown and green lines indicate the 600°C isotherms calculated from a half-space cooling model and a numerical model incorporating hydrothermal cooling (Roland et al., 2010), respectively.

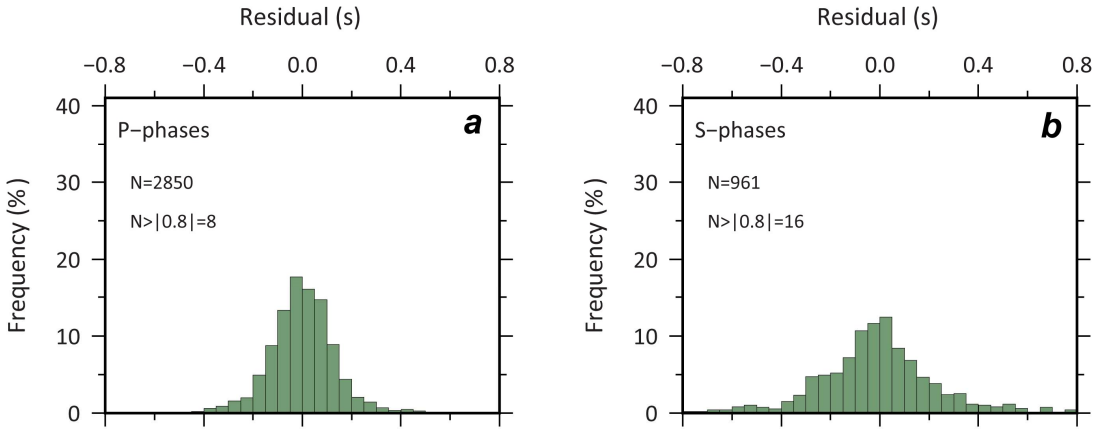

Figure S8. P- (panel **a**) and S-phase (panel **b**) residuals of the location procedures. N: number of phases.

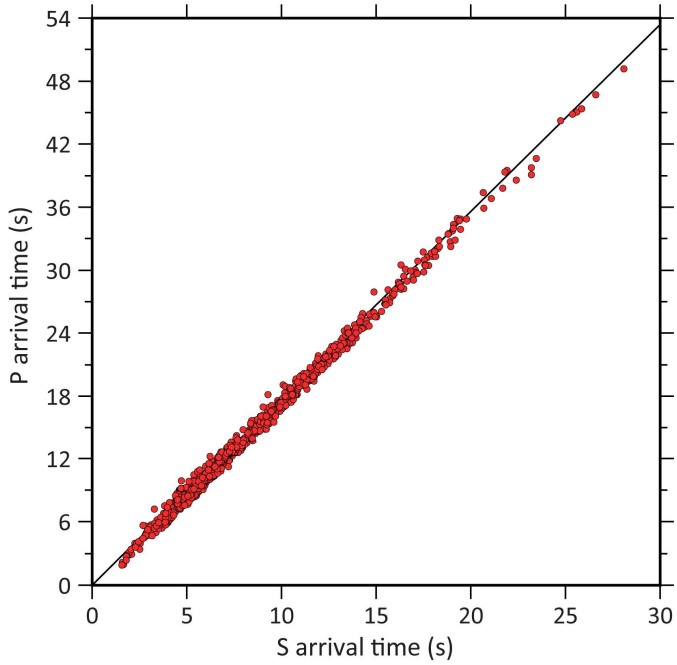

Figure S9. Wadati diagram of P-phase onsets versus S-phase onsets, yielding Vp/Vs ratio for the BTFS.

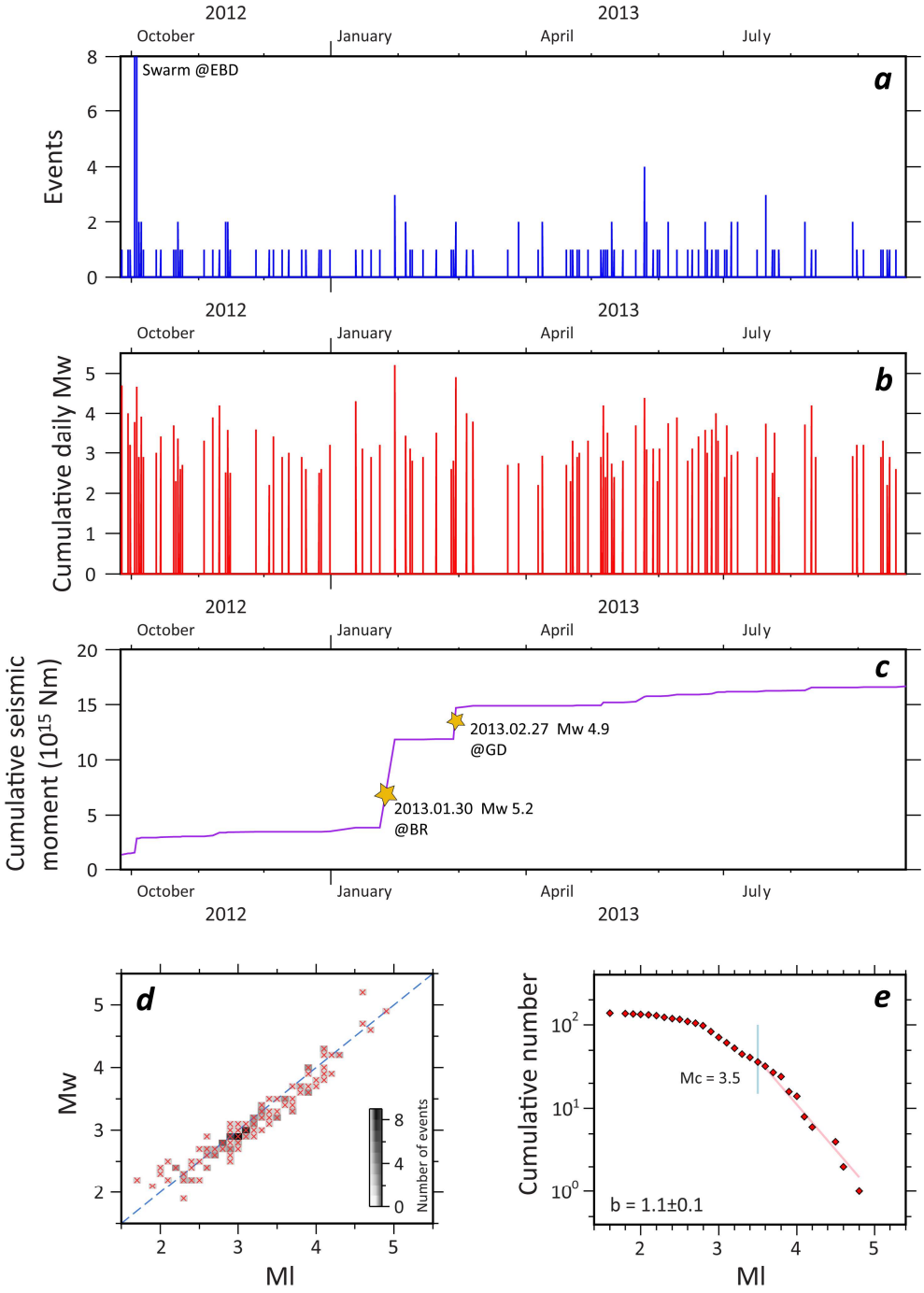

Figure S10. Temporal evolution of the recorded local seismicity of the BTFS. (**a**) The number of events per day. (**b**) Temporal distribution of moment magnitudes. (**c**) Cumulative seismic moment release. (**d**) Relationship between moment magnitude (Mw) and local magnitudes (Ml). (**e**) The frequency-local magnitude distribution of local events along the BTFS in this study.

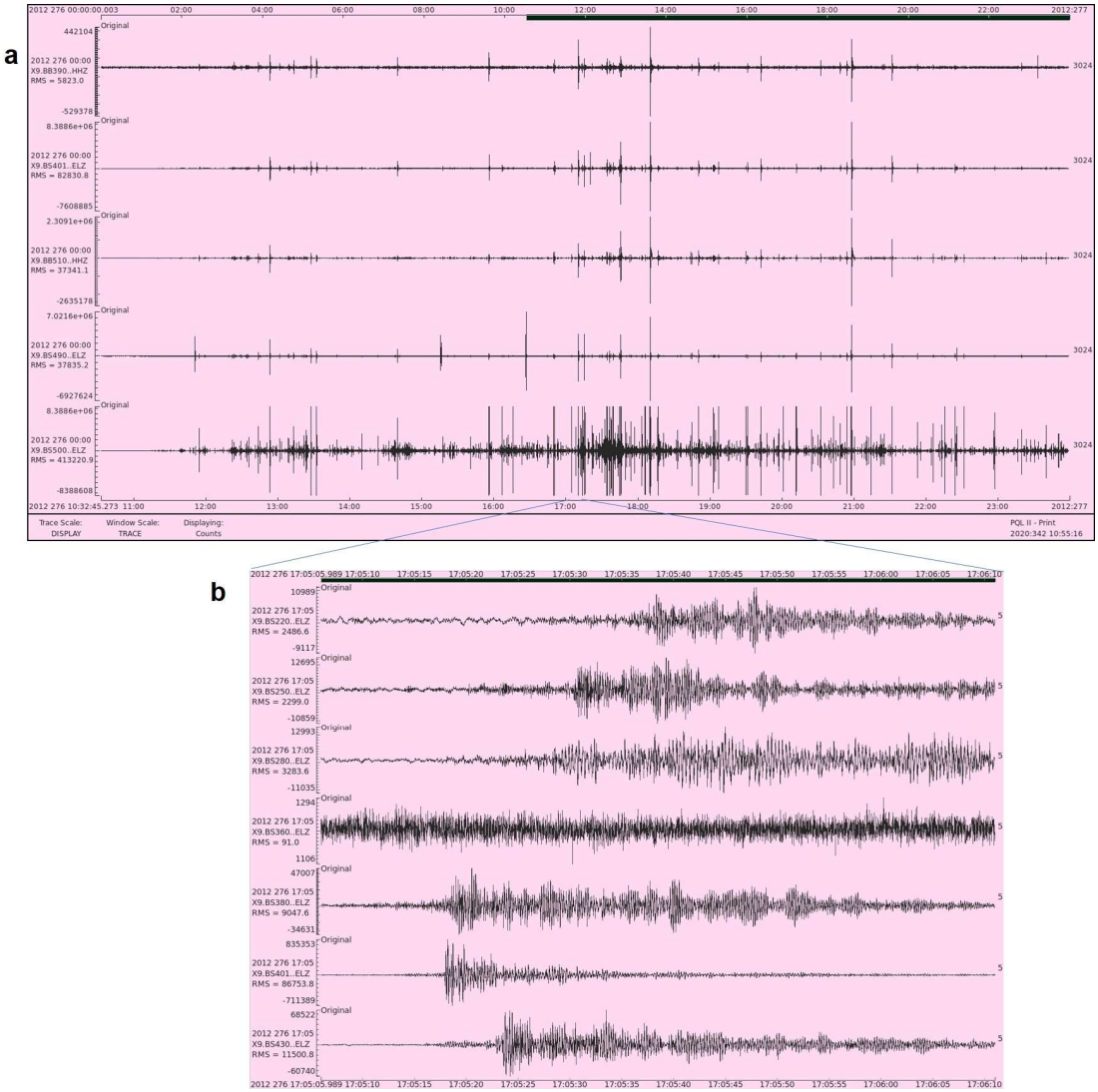

Figure S11. (**a**) Waveform recordings of the Earthquake swarm at EBD recorded by the OBS network. Figure shows 12 hours of Z-components from 5 different OBS stations. (**b**) Elevated noise level of one weak event of the EBD swarm. The locations of the OBS are as in Figure **S2**.

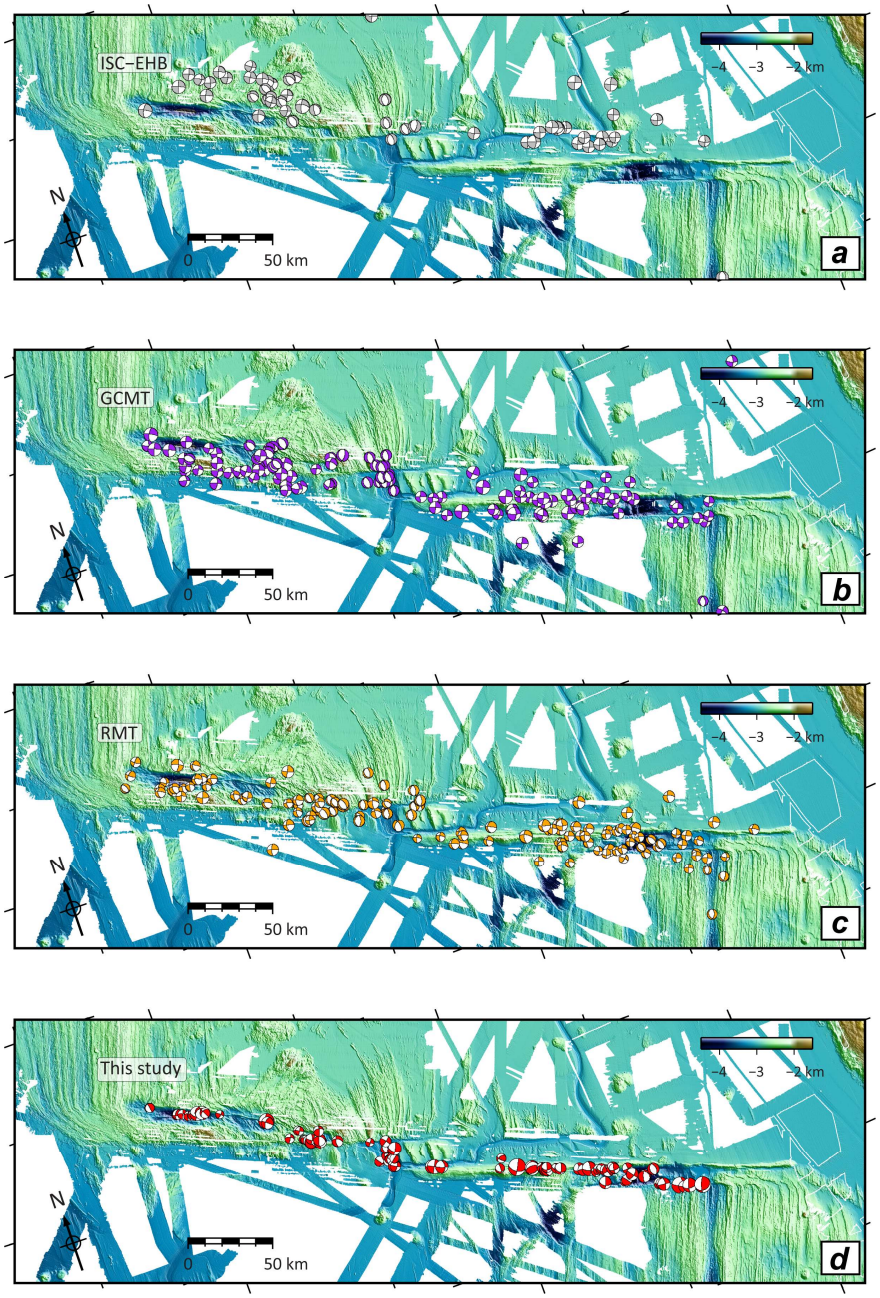

Figure S12. Focal mechanisms from (**a**) ISC-EHB (in grey; Engdahl, 2006) (**b**) GCMT (in purple; Ekström et al., 2012) (**c**) RMT (in yellow; Braunmiller & Nábělek, 2008) and (**d**) our local catalog in this study (in red).

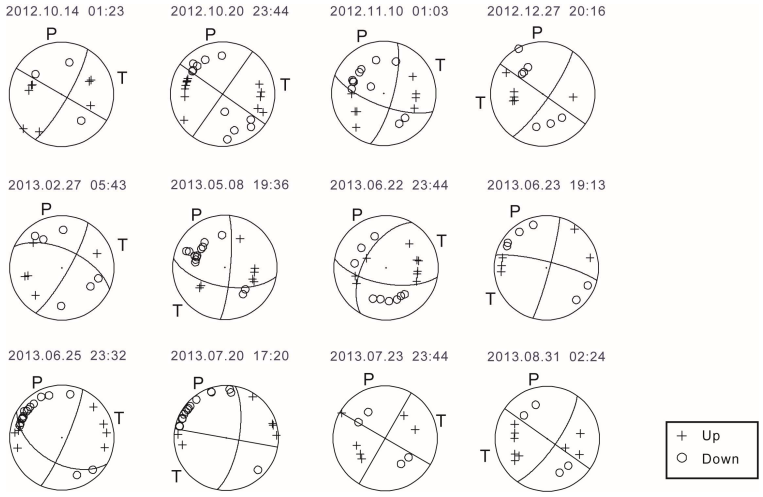

Figure S13. Examples of focal mechanisms of the local earthquakes with at least 10 first-motion polarities of P-phase onsets.

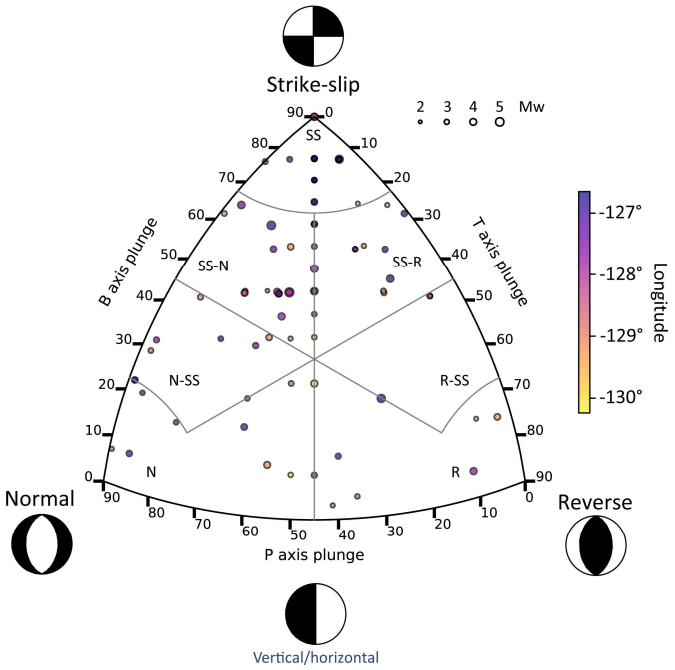

Figure S14. Ternary plot for the Focal mechanisms (Álvarez-Gómez, 2019) along the BTFS, constrained by the OBS network. This diagram indicates faulting styles of the BTFS. The major faulting style of the BTFS is strike-slip to transtensional (SS-N) rather than pure strike-slip. SS: Strike-slip; SS-N: Strike-slip-Normal; SS-R: Strike-slip-Reverse; N-SS: Normal-Strike-slip; R-SS: Reverse-Strike-slip; N: Normal; R: Reverse.

Table S1. Local seismicity catalog of the Blanco transform fault system (BTFS) derived in this study. Errx: Uncertainties in latitude (km); Erry: Uncertainties in longitude (km); Errz: Depth uncertainties (km).

date	time	latitude	longitude	depth	Errx	Erry	Errz	RMS	Ml	Mw
2012-09-26	07:42:40.00	043.023	-126.650	009.0	0.60	0.40	2.40	0.1	4.6	4.7
2012-09-29	06:16:56.60	043.796	-128.644	004.8	0.30	0.20	0.50	0.2	3.9	4.0
2012-09-30	17:30:34.20	043.251	-127.112	009.2	0.50	0.40	1.60	0.1	3.5	3.2
2012-10-02	11:54:43.50	044.133	-129.439	006.7	0.40	0.30	0.80	0.1	3.0	2.8
2012-10-02	13:08:46.90	044.146	-129.447	005.9	0.40	0.30	1.20	0.2	2.9	2.9
2012-10-02	13:49:24.20	044.145	-129.443	009.1	0.40	0.30	2.50	0.2	3.0	3.0
2012-10-02	17:05:06.80	044.148	-129.448	003.0	0.50	0.30	0.60	0.3	2.8	2.7
2012-10-02	17:21:59.90	044.164	-129.462	004.8	0.40	0.40	0.70	0.3	3.1	3.0
2012-10-02	18:03:31.80	044.159	-129.445	004.9	0.40	0.40	0.60	0.2	3.2	2.9
2012-10-02	18:50:52.50	044.168	-129.458	005.7	0.30	0.30	1.00	0.2	3.4	3.3
2012-10-02	20:58:08.90	044.158	-129.455	004.6	0.30	0.30	0.60	0.2	3.9	3.6
2012-10-03	00:44:13.80	044.155	-129.461	002.3	0.40	0.30	0.80	0.3	3.5	3.2
2012-10-03	01:38:30.70	044.147	-129.448	004.6	0.60	0.40	0.90	0.3	2.9	2.9
2012-10-03	02:12:44.50	044.151	-129.453	003.3	0.30	0.20	0.50	0.3	4.3	4.2
2012-10-03	02:24:05.70	044.156	-129.462	006.2	0.40	0.40	0.50	0.1	2.8	2.8
2012-10-03	06:23:19.00	044.163	-129.478	006.4	0.50	0.50	1.10	0.1	3.0	2.7
2012-10-03	08:08:26.30	044.168	-129.463	005.1	0.50	0.30	0.60	0.3	3.7	3.3
2012-10-03	08:16:36.60	044.170	-129.458	004.8	0.30	0.30	0.50	0.2	4.7	4.6
2012-10-03	08:41:22.30	044.164	-129.455	005.5	0.40	0.40	0.50	0.2	3.3	3.0
2012-10-04	13:07:22.20	044.148	-129.467	002.9	0.50	0.30	0.70	0.1	2.9	2.7
2012-10-04	19:26:35.80	044.155	-129.470	003.3	0.70	0.40	2.40	0.2	2.7	2.7
2012-10-05	20:51:21.90	043.634	-128.438	010.2	0.40	0.30	1.40	0.2	3.9	3.9
2012-10-05	21:25:30.20	044.163	-129.467	005.7	0.50	0.40	0.90	0.1	3.2	3.1
2012-10-06	10:41:31.70	044.164	-129.471	006.3	0.50	0.30	0.80	0.1	3.0	2.9
2012-10-12	18:56:33.30	043.873	-128.766	005.3	0.50	0.60	2.50	0.1	3.2	3.0
2012-10-14	01:23:43.30	043.049	-126.779	005.0	0.60	0.50	1.40	0.2	3.6	3.4
2012-10-20	23:44:49.90	043.708	-128.692	007.1	0.40	0.30	0.80	0.2	3.8	3.7
2012-10-21	22:37:57.60	043.947	-129.047	005.0	0.70	0.50	1.30	0.2	2.3	2.3
2012-10-22	12:11:34.50	043.757	-128.780	007.0	0.50	0.30	1.10	0.1	3.1	3.1
2012-10-22	12:37:21.70	043.704	-128.685	007.8	0.30	0.20	0.60	0.2	3.5	3.2
2012-10-23	10:20:57.70	043.758	-128.774	007.1	0.60	0.50	2.50	0.2	2.6	2.6
2012-10-24	23:33:27.80	044.006	-129.234	008.0	0.50	0.30	1.60	0.2	2.9	2.7
2012-11-03	01:52:20.90	043.182	-126.913	009.2	0.60	0.60	3.20	0.1	3.7	3.3
2012-11-07	13:06:50.10	044.305	-129.865	004.8	0.40	0.30	1.00	0.2	4.2	3.9
2012-11-10	01:03:27.40	043.324	-127.373	006.0	0.40	0.40	0.90	0.1	4.2	4.2
2012-11-13	21:54:16.70	044.176	-129.431	002.5	0.50	0.40	0.70	0.1	2.6	2.4
2012-11-13	21:57:55.90	044.174	-129.431	002.1	0.50	0.40	0.60	0.1	2.3	2.2
2012-11-14	07:10:11.90	043.404	-127.678	010.4	0.50	0.40	0.80	0.1	3.5	3.5
2012-11-14	08:44:06.10	043.405	-127.677	011.3	0.30	0.20	1.30	0.2	3.3	3.2

Table S1. (continued)

date	time	latitude	longitude	depth	Errx	Erry	Errz	RMS	Ml	Mw
2012-11-15	22:49:52.40	043.956	-129.038	006.5	0.70	0.60	1.30	0.1	2.1	2.5
2012-11-27	08:37:40.80	043.213	-127.096	006.3	0.40	0.20	0.90	0.2	3.8	3.6
2012-12-03	20:54:18.90	044.025	-129.298	003.5	0.80	0.60	2.30	0.2	2.4	2.2
2012-12-05	01:01:44.30	043.412	-127.669	012.4	0.40	0.30	2.20	0.1	3.7	3.4
2012-12-09	22:13:42.90	044.385	-130.031	019.1	0.60	0.60	2.90	0.2	2.6	2.9
2012-12-12	22:57:37.60	043.995	-129.198	006.3	0.40	0.30	1.10	0.3	2.9	3.0
2012-12-18	16:20:56.90	044.270	-129.711	005.1	0.40	0.50	0.90	0.1	3.0	2.9
2012-12-20	17:26:38.60	043.834	-128.789	002.0	0.60	0.60	0.90	0.3	2.9	2.6
2012-12-26	20:37:41.00	043.495	-127.985	007.8	0.50	0.40	1.10	0.4	2.9	2.5
2012-12-27	20:16:06.50	043.874	-128.799	002.5	0.60	0.40	1.50	0.2	2.7	2.6
2012-12-31	11:20:54.40	043.285	-127.267	009.1	0.40	0.30	1.00	0.1	3.4	3.2
2013-01-12	11:19:48.20	043.439	-127.759	004.5	0.40	0.20	0.80	0.2	4.1	4.3
2013-01-15	05:14:22.10	043.385	-127.621	011.1	0.30	0.20	0.90	0.2	3.2	3.1
2013-01-19	23:56:18.20	044.182	-129.567	005.1	0.50	0.40	0.60	0.1	2.9	2.9
2013-01-23	06:52:19.20	043.987	-129.202	005.0	0.40	0.50	1.80	0.2	3.2	3.2
2013-01-30	03:14:25.80	043.471	-127.858	004.4	0.50	0.30	1.20	0.3	4.6	5.2
2013-01-30	10:53:06.30	043.463	-127.832	004.9	0.60	0.50	1.10	0.1	2.4	2.2
2013-01-30	13:30:54.20	043.457	-127.831	004.1	0.50	0.30	0.90	0.1	3.0	2.9
2013-02-04	16:03:08.00	043.849	-128.688	008.0	0.40	0.40	1.70	0.1	3.3	3.4
2013-02-04	17:24:43.90	043.744	-128.673	005.2	0.60	0.50	0.80	0.1	2.5	2.7
2013-02-06	16:41:46.70	043.772	-128.716	008.0	0.50	0.40	0.80	0.1	3.0	3.1
2013-02-07	16:05:10.50	043.957	-129.074	004.6	0.50	0.40	1.10	0.1	2.8	2.8
2013-02-12	21:09:37.00	043.544	-127.942	006.2	0.40	0.40	1.20	0.1	3.1	2.9
2013-02-18	03:26:59.20	043.276	-127.249	010.0	0.40	0.40	1.70	0.1	3.7	3.5
2013-02-25	06:46:04.20	043.777	-128.712	006.6	0.40	0.50	0.70	0.1	2.7	2.6
2013-02-26	17:10:12.20	043.295	-127.335	006.8	0.50	0.40	1.00	0.1	2.9	2.8
2013-02-27	05:43:11.50	044.040	-129.341	006.4	0.40	0.40	2.60	0.1	3.0	2.8
2013-02-27	22:25:41.80	043.065	-126.804	005.3	0.50	0.30	1.10	0.3	4.9	4.9
2013-03-04	03:42:39.10	043.437	-127.763	008.4	0.30	0.20	1.20	0.1	3.9	4.0
2013-03-07	08:19:36.10	043.968	-129.138	004.7	0.30	0.30	0.70	0.2	4.1	3.8
2013-03-23	23:09:34.00	044.065	-129.263	007.0	0.60	0.40	2.20	0.1	2.6	2.7
2013-03-28	14:19:48.10	043.669	-128.557	010.0	0.50	0.40	1.30	0.2	2.6	2.7
2013-03-28	15:04:09.90	043.663	-128.546	008.7	0.70	0.80	1.80	0.1	2.3	2.2
2013-04-06	09:51:29.00	044.038	-129.149	004.3	0.80	0.70	1.50	0.1	2.1	2.2
2013-04-08	18:05:51.70	044.354	-130.023	001.7	0.50	0.60	5.30	0.1	3.0	2.9
2013-04-08	23:38:20.80	043.838	-128.679	005.3	0.60	1.00	1.80	0.1	1.7	2.2
2013-04-19	12:23:52.80	044.011	-129.246	007.5	0.50	0.40	2.00	0.1	2.9	2.7
2013-04-21	23:09:14.30	043.864	-128.745	004.5	0.90	0.80	2.30	0.1	2.0	2.3
2013-04-22	00:01:18.20	043.063	-126.815	016.3	0.70	0.60	3.10	0.1	3.3	3.3
2013-04-24	23:52:06.80	043.742	-128.722	005.7	0.60	0.50	0.90	0.1	3.0	2.9

Table S1. (continued)

date	time	latitude	longitude	depth	Errx	Erry	Errz	RMS	Ml	Mw
2013-04-25	22:50:56.50	043.277	-127.203	008.5	0.50	0.30	1.90	0.2	3.1	3.0
2013-04-29	19:09:12.20	043.398	-127.663	011.1	0.30	0.20	1.40	0.1	3.5	3.3
2013-05-05	10:14:10.70	043.390	-127.595	008.5	0.30	0.30	1.10	0.1	2.9	2.9
2013-05-06	13:18:08.50	043.046	-126.739	009.0	0.50	0.40	1.40	0.2	4.1	4.2
2013-05-07	23:53:34.10	044.336	-129.972	007.4	0.70	0.50	3.70	0.1	2.4	2.4
2013-05-08	19:36:52.90	043.343	-127.441	004.5	0.40	0.30	0.80	0.1	3.6	3.5
2013-05-10	03:12:43.30	044.276	-129.733	004.2	0.50	0.60	1.00	0.1	1.9	2.1
2013-05-10	08:35:35.70	043.750	-128.708	008.5	0.40	0.30	1.20	0.1	2.7	2.7
2013-05-11	10:25:12.50	043.887	-128.778	009.6	0.70	0.50	2.40	0.4	2.2	2.4
2013-05-15	23:56:45.70	043.192	-127.164	008.5	0.80	0.40	1.70	0.1	2.8	2.8
2013-05-21	20:28:27.80	043.993	-129.208	002.5	0.40	0.20	0.80	0.3	4.0	3.7
2013-05-25	04:26:21.20	044.287	-129.764	005.7	0.60	0.60	1.70	0.1	2.5	2.5
2013-05-25	05:50:55.80	044.327	-129.887	000.7	0.50	0.30	0.70	0.2	4.1	4.0
2013-05-25	11:50:53.00	044.333	-129.920	001.8	0.50	0.40	1.40	0.2	4.1	4.3
2013-05-25	23:56:23.50	044.298	-129.825	005.7	0.70	0.60	2.60	0.1	2.2	2.4
2013-05-26	09:38:52.90	044.320	-129.863	003.7	0.50	0.40	1.20	0.1	3.1	3.0
2013-05-26	16:05:13.70	044.331	-129.955	003.0	0.60	0.50	2.70	0.1	2.8	2.7
2013-05-29	18:07:26.20	044.025	-129.122	007.2	0.60	0.50	1.30	0.1	3.2	3.1
2013-05-31	12:58:51.70	043.513	-128.008	005.0	0.50	0.50	2.90	0.2	2.3	2.3
2013-06-01	22:27:38.80	044.000	-129.193	008.0	0.60	0.40	1.90	0.1	3.4	3.1
2013-06-05	11:13:54.00	043.979	-129.138	005.0	0.40	0.20	0.80	0.3	3.9	3.6
2013-06-05	22:09:57.40	043.198	-126.940	009.0	0.40	0.30	1.60	0.2	3.6	3.5
2013-06-09	09:06:47.70	043.983	-129.198	000.8	0.40	0.30	0.50	0.3	4.1	3.9
2013-06-14	23:46:36.90	043.811	-128.708	007.0	0.40	0.40	0.90	0.2	2.8	2.8
2013-06-16	22:27:05.80	044.361	-130.057	005.9	0.60	0.60	1.00	0.1	2.9	3.1
2013-06-19	22:23:59.80	043.379	-127.567	009.1	0.30	0.30	1.40	0.2	3.3	3.4
2013-06-22	07:08:01.60	043.114	-126.935	010.0	0.50	0.40	1.90	0.1	3.4	3.5
2013-06-22	23:44:35.50	044.363	-130.062	005.7	0.50	0.40	1.20	0.2	3.3	3.2
2013-06-23	19:13:37.70	043.110	-126.927	009.3	0.50	0.40	1.60	0.2	3.1	3.0
2013-06-25	23:32:40.10	043.224	-127.301	009.0	0.40	0.20	1.30	0.2	3.9	3.6
2013-06-27	00:03:20.70	043.433	-127.756	006.1	0.40	0.20	1.00	0.2	3.9	4.0
2013-06-28	13:46:24.90	043.192	-127.148	008.1	0.50	0.40	1.40	0.1	3.3	3.3
2013-07-01	10:38:49.40	044.385	-130.107	005.2	0.70	0.60	4.10	0.1	2.2	2.4
2013-07-02	01:16:08.70	043.281	-127.212	005.7	0.40	0.30	1.10	0.2	3.9	3.7
2013-07-04	09:15:10.10	044.445	-130.237	000.5	0.90	0.60	4.00	0.2	3.0	2.9
2013-07-04	23:02:38.70	043.764	-128.684	006.1	0.60	0.60	1.10	0.1	2.6	2.4
2013-07-07	00:09:49.20	043.851	-128.699	009.0	0.70	0.50	1.90	0.3	2.0	2.4
2013-07-07	23:41:23.10	043.412	-127.656	006.3	0.50	0.40	1.20	0.1	3.1	3.0
2013-07-16	21:20:12.00	043.298	-127.298	008.9	0.60	0.40	1.50	0.1	3.0	2.9
2013-07-20	03:48:16.70	043.420	-127.690	013.8	0.40	0.30	2.30	0.1	3.1	3.0

Table S1. (continued)

date	time	latitude	longitude	depth	Errx	Erry	Errz	RMS	Ml	Mw
2013-07-20	17:20:53.30	043.101	-126.908	010.0	0.50	0.40	1.70	0.1	3.7	3.7
2013-07-20	17:43:39.20	043.109	-126.910	008.2	0.60	0.40	1.60	0.1	3.0	2.9
2013-07-23	23:44:43.00	044.061	-129.253	003.8	0.60	0.50	2.20	0.1	2.4	2.5
2013-07-24	05:25:43.80	043.330	-127.415	009.6	0.50	0.50	1.70	0.1	3.6	3.5
2013-07-26	20:29:46.70	043.712	-128.675	008.0	0.60	0.70	1.40	0.2	2.3	1.9
2013-08-07	18:47:46.50	043.178	-127.020	008.0	0.50	0.30	1.30	0.2	3.1	3.0
2013-08-07	19:03:13.50	043.179	-127.020	009.5	0.40	0.30	1.20	0.1	3.8	3.7
2013-08-10	05:10:13.50	043.630	-128.421	005.9	0.40	0.20	0.80	0.2	4.3	4.2
2013-08-12	23:16:49.60	043.301	-127.289	006.0	0.40	0.30	1.00	0.1	3.1	2.9
2013-08-29	07:27:18.10	044.335	-129.950	007.0	0.60	0.50	1.30	0.1	2.6	2.6
2013-08-29	17:16:49.50	043.303	-127.316	006.3	0.50	0.40	0.90	0.1	2.8	2.8
2013-08-31	02:24:52.80	043.300	-127.311	006.2	0.50	0.50	1.00	0.1	3.2	3.2
2013-09-03	08:53:08.50	043.004	-126.596	015.4	0.60	0.50	2.90	0.3	3.2	3.2
2013-09-11	23:42:06.20	044.336	-129.985	007.8	0.50	0.50	1.30	0.1	2.9	2.9
2013-09-12	03:06:44.80	043.939	-129.017	006.3	0.50	0.40	1.30	0.1	3.3	3.3
2013-09-14	20:20:31.80	044.023	-129.310	002.2	0.60	0.50	2.10	0.1	2.5	2.2
2013-09-15	05:10:02.80	043.498	-127.977	010.0	0.30	0.20	1.40	0.2	2.9	2.9
2013-09-18	23:17:53.80	044.010	-129.243	004.9	0.60	0.40	2.30	0.1	2.7	2.6
2013-09-23	08:49:26.20	043.615	-128.369	010.0	0.30	0.20	1.00	0.2	4.0	3.8

CHAPTER 7

MANUSCRIPT #6

Seismological evidence of mantle shear zones in response to a northward migrating transform-transform-trench triple junction, northeast Pacific

Yu Ren [(1)], Dietrich Lange [(1)], and Ingo Grevemeyer [(1)]

(1) GEOMAR Helmholtz Centre for Ocean Research Kiel, Kiel, Germany

Pending submission to *Nature Communications*

This chapter contains a manuscript to be submitted to *Nature Communications*. Please note that the manuscript contains its own reference list and refers to its own figure and page numbers.

Seismological evidence of mantle shear zones in response to a northward migrating transform-transform-trench triple junction, northeast Pacific

Yu Ren [1], Dietrich Lange [1], and Ingo Grevemeyer [1]

[1] GEOMAR Helmholtz Centre for Ocean Research Kiel, Kiel, Germany

Correspondence to: Yu Ren (yren@geomar.de)

The offshore region of Cascadia offers a natural laboratory to study the interactions among mid-ocean ridges, oceanic transform faults, and subduction zones. Using deep-learning algorithms, we automated the detection of micro-seismicity by analyzing multi-year, large-scale OBS data from the Cascadia Initiative. Focusing specifically on areas seaward of the Cascadia deformation front, we identified sparse intraplate earthquakes offshore central Cascadia. In contrast, the southern region exhibits high levels of intraplate microseismicity, which align with reactivated spreading-related faults and correspond closely with spreading fabrics observed in seafloor bathymetry. A spatial trend of increasingly deeper earthquakes is observed with greater distance from the Gorda Ridge and decreasing proximity to the deformation front, driven by a combination of north-south compression and plate-bending extension. Additionally, clusters of deep micro-earthquakes, reaching depths of up to 40 km along the MTF, indicate the development of shear zones in the uppermost mantle, likely driven by active asthenospheric flow influenced by the northward migration of the Mendocino triple junction and advection due to the larger Pacific plate.

In the northeast Pacific, the oceanic Juan de Fuca (JdF) plate system subducts northeastward beneath the continental North American plate, exhibiting young plate ages (<10 Ma) at the onset of subduction. The oceanic domain of central and southern Cascadia encompasses diverse plate boundaries (Fig. 1), including the JdF and Gorda ridges (JdFR and GR), the Blanco and Mendocino transform faults (BTFS and MTF), and the Cascadia subduction zone (CSZ). Additionally, the presence of pseudofaults and propagator wakes evident in seafloor bathymetry and magnetic anomalies (Wilson, 1988; Dziak et al., 2001; Nedimović et al., 2009), associated with ridge propagation processes and changes in plate motion, further complicate the tectonics of this region.

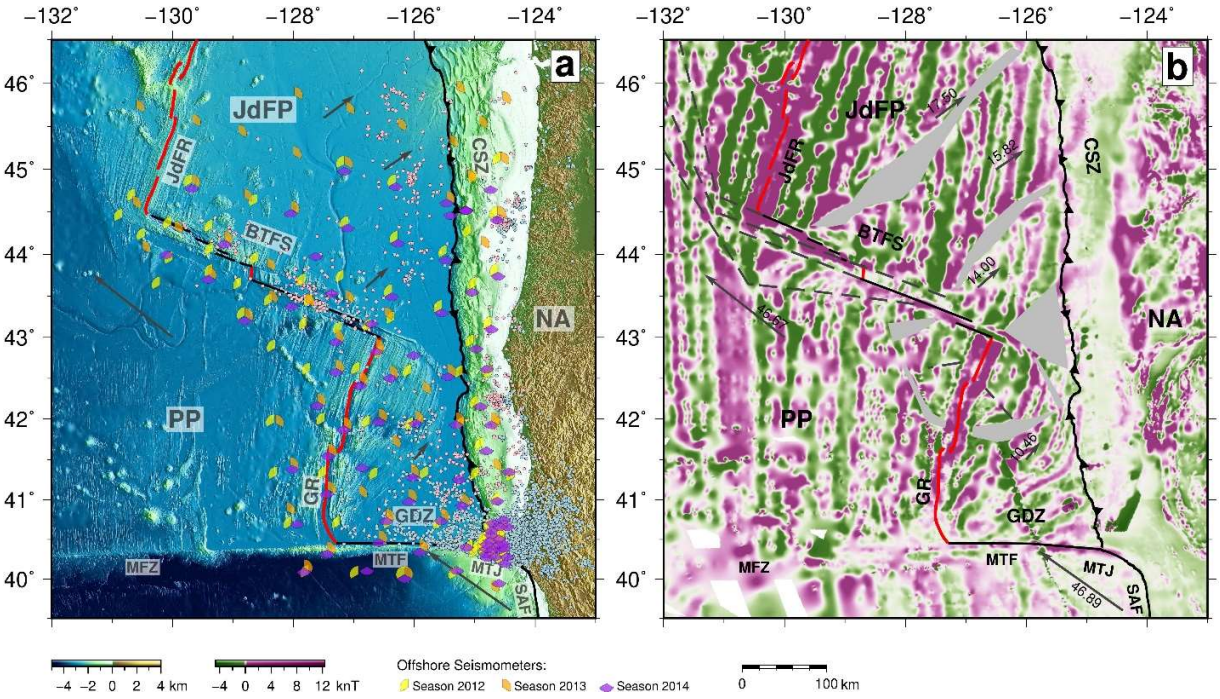

Fig. 1. Overview of the study area. (**a**) Distribution of offshore seismicity (circles in pink, Stone et al., 2018; in blue, Morton et al., 2023) and OBS (color-coded sectors) used in this study was plotted over seafloor bathymetry (Ryan et al., 2009). (**b**) Airborne magnetic anomaly (Bankey et al., 2002). Broken lines indicate pseudofault traces in response to plate motion changes and ridge propagation (Ren et al., 2023; Wilson, 1989). Gray shading outlines propagator wakes (Wilson, 1993; Nedimović et al., 2009). Red thick lines indicate segments of mid-ocean ridges. Black thin lines represent transform fault traces inferred from

local seismicity (Ren et al., 2023) and seafloor bathymetry. Arrows show plate motions in a no-net-rotation frame (GSRM v2.1; Kreemer et al., 2014) and the corresponding numbers in panel (**b**) indicate plate velocities in mm/yr. JdFP, Juan de Fuca plate; PP, Pacific plate; NA, North American plate; CSZ, Cascadia subduction zone; JdFR, Juan de Fuca ridge; GR, Gorda ridge; BTFS, Blanco transform fault system; GDZ, Gorda deformation zone; MTJ, Mendocino triple junction; MTF, Mendocino transform fault; MFZ, Mendocino fracture zone; SAF, San Andreas fault.

The spreading rate on the JdFR immediately north of the BTFS is 56 mm/yr, slightly higher than the 55 mm/yr rate on the northern GR (Riddihough, 1980). The BTFS, which connects the JdFR and GR, is a highly segmented transform fault system characterized by topographic highs and deep troughs, spanning approximately 350 km in total length (Embley & Wilson, 1992). Kinematic models (e.g., Wilson, 1993) indicated that a clockwise rotation of plate motion at ~5 Ma initiated the formation of the BTFS. Since then, the fault system has continued to evolve in response to multiple ridge propagation events. Recent local seismicity studies (e.g., Kuna, 2020) have revealed significant along-strike variations in deformation and stress patterns, indicating that the BTFS is an immature transform plate boundary still developing to accommodate relative plate motion between the Pacific and JdF plates (Ren et al., 2023).

Furthermore, different types of morphological features are readily evident at the intersections between the BTFS and the JdFR in the northwest and the GR in the southeast. For instance, while the southern end of the JdFR shows the typical axial high morphology, the GR is characterized by a rift valley. Spreading rates along the GR decrease southward from 55 mm/yr near the BTFS to 26 mm/yr approaching the MTF (Wilson, 1989). Newly produced lithosphere (0–7 Ma) slides past the old Pacific plate (27–32 Ma), forming the 215-km-long right-lateral MTF and its prominent fracture zone, which extends 3,000 km west into the central Pacific basin. At the eastern end of the MTF, the JdF, North American, and Pacific plates meet at the northward-migrating Mendocino triple junction (MTJ) that resulted from the subduction of the Pacific-Farallon ridge at ~28 Ma (Atwater & Stock, 1998). The MTJ connects the MTF, San Andreas fault (SAF) system, and CSZ, representing one of the most tectonically active features in southern Cascadia. However,

the east-west trending MTF is kinematically inconsistent with the current strike of the BTFS. The MTF restricts the southward movement of the JdF plate, leading to north-south compression and shortening across the GDZ (Wilson, 1986; Wang et al., 1997). In response, the GDZ has been deformed nonrigidly, reactivating and generating pervasive faults. Curved spreading fabric and magnetic anomalies in the GDZ have been documented in an area of broadly distributed seismic events (Silver, 1971; Dziak et al., 2001). Yet, the northern limit of the nonrigid deformation remains debated (Stoddard, 1987; Wilson, 1989; Chaytor et al., 2004) due to the lack of robust offshore seismic patterns.

Detailed seismic observations of the Cascadia subduction zone have been facilitated by regional seismic networks on land, such as the Pacific Northwest and the Northern California Seismic Networks, and the USArray. However, it has been documented that offshore seismicity constrained exclusively by land-based seismic networks are generally biased by 20–60 km (e.g., Sverdrup, 1986; Ren et al., 2023) due to large observational gaps in the oceanic domain. Fig. S1a shows striking mismatch between the ANSS seismic locations and tectonic features, especially in the vicinity of the BTFS and the GR. Based on the U.S. Navy Sound Surveillance system, hydro-acoustic tertiary (T-) waves have been utilized to better constrain the precision of event locations (e.g., Dziak et al., 2000, 2011). However, the hydro-acoustic locations are sensitive to seafloor topography (e.g., Braunmiller and Nábělek, 2008), thus might be biased by complex bathymetric features in the study area. Although a few local seismic catalogs based on the CI OBS dataset have been recently published (Stone et al., 2018; Kuna, 2020; Morton et al., 2023; Ren et al., 2023), they have been focused on regional subsets such as the BTFS or the Cascadia margin. In addition, in the broader offshore region west of the deformation front, generic velocity model has been used for event location and detection using traditional methods, leading to noticeable bias of the event locations. Therefore, in addition to the existing geophysical databases including multibeam bathymetry and magnetic anomaly, improved earthquake source parameters are therefore desired to systematically study faulting and deformation styles in this region. Here we report seismotectonics behavior of active tectonic features including the BTFS, GR, MTF, and the GDZ offshore Cascadia, constrained by automated micro-seismicity analysis.

Results

By leveraging the enormous CI OBS dataset and the deep learning picker, PickBlue, we obtained accurate focal parameters of 14,057 local events offshore central and southern Cascadia (Fig. S4a). Our three-year-long catalog spanning from 2012/09 to 2015/09 reveals abundant small earthquakes in the research area. The Ml and Mw of our detected events, range from 0.6 to 5.6 and 0.9 to 6.0, respectively. According to the Gutenberg-Richter distribution indicated by cumulative magnitude curves (Fig. S5c), our catalog is complete for events with a Ml greater than 2.4.

The distribution of P- and S-phase residuals (Fig. S4b-c) and the wadati diagram (Fig. S7) indicate that event locations constrained by automated phase picks exhibit fairly high quality. The DL picker, PickBlue, has superior performance in event detection capacity when applied to OBS data, compared to pickers trained with onshore data. Fig. S8 shows the comparison of event-detection capabilities between the onshore picker, EQTransformer (Mousavi et al., 2020), and the OBS picker, PickBlue (Bornstein et al., 2023). From a subset of four-month offshore recordings between September and December 2012, we detected 1765 local events using PickBlue, representing an approximately four-fold increase as compared with the 467 earthquakes identified by EQTransformer during the same timeframe. In addition, our catalog yields event counts 8.3 and 3.5 times greater than those in the ANSS Comprehensive Earthquake Catalog and a recent seismicity study by Morton et al. (2023), respectively. The greatly enhanced capability in detecting offshore events allowed us to uncover more detailed offshore seismic activities, such as those occurring around GR, MTF, and GDZ, which were largely absent in previous investigations.

Table 1
Quality classification and location uncertainties (68% confidence) of Cascadia offshore events.

Quality Class	Selection Criteria	Errors in lon, lat, & depth
A (excellent)	RMS < 0.5 sec, DIFF < 0.5 km, AE < 2.0 km, GAP < 180°	0.94 km, 0.90 km, 2.40 km
B (good)	RMS < 0.5 sec, DIFF < 0.5 km, AE < 2.0 km, GAP ≥ 180°	1.41 km, 1.47 km, 4.75 km
C (fair)	RMS < 0.5 sec, DIFF < 0.5 km, 2.0 km ≤ AE < 4.0 km	1.83 km, 1.67 km, 5.07 km
D (poor)	RMS ≥ 0.5 sec, or DIFF ≥ 0.5 km, or AE ≥ 4.0 km	3.52 km, 3.56 km, 8.98 km

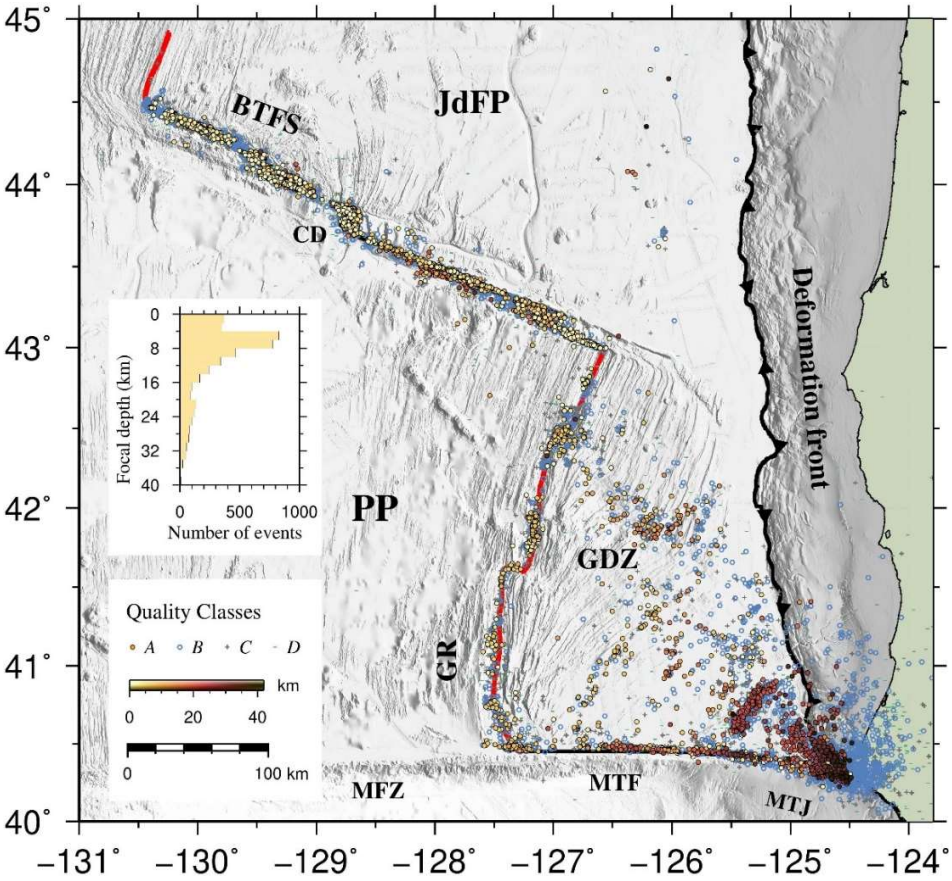

Fig. 2. Offshore seismic activity in central and southern Cascadia. Color-coded dots, blue open circles, crosses, and dashes indicate the even locations classified in quality class A (excellent), B (good), C (fair), and D (poor), respectively. The inset shows the focal depth distribution of quality class A events.

Furthermore, NonLinLoc computes hypocenter locations and provides uncertainty parameters such as RMS, DIFF (the difference between the maximum likelihood and the expectation hypocenter locations), and AE (the average length of the three axes of the 68% error ellipsoid). The located earthquakes could be further classified into various quality categories based on their uncertainties. Following Husen & Smith (2004), we defined four quality classes for our catalog (Fig. 2) based on the selection criteria indicated in Table 1. Earthquakes in quality classes A and B have reliable epicenter locations, accounting for 63% of the total events in our catalog. However, the focal depth of quality class B events is less well-constrained than that in quality class A, due to a larger GAP for station coverage. Making up 27% of the total catalog,

quality class C earthquakes show overall larger location uncertainties in epicenter locations and focal depth compared to quality class B events. Epicenter locations and focal depth in quality class D are poorly constrained, with notably irregular location uncertainties. To investigate active seismotectonics and deformation patterns in the research area, we particularly analyze focal parameters that are reasonably well-constrained, such as epicenter locations in quality classes A and B, and focal depth in quality class A.

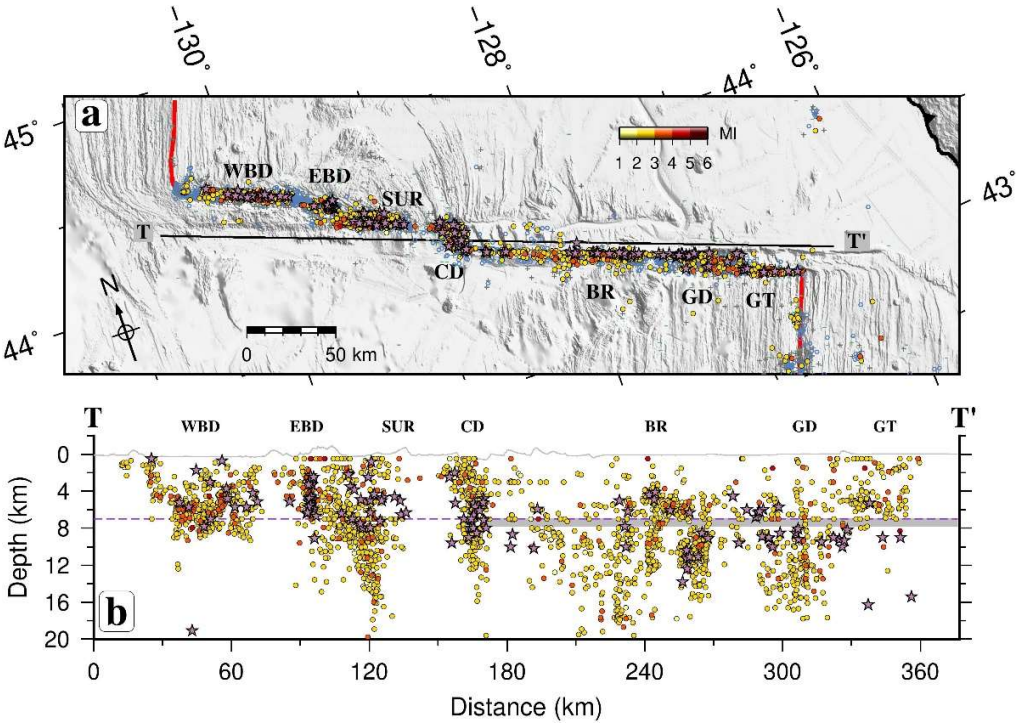

Fig. 3. Close-up view of the BTFS. (a) Local seismicity of the BTFS. (b) Along-strike vertical profile showing the focal depth distribution (4 times vertical exaggeration). Purple stars indicate earthquake locations derived manually by Ren et al. (2023). Dashed purple line shows the Moho discontinuity inferred from the minimum 1D velocity model (Fig. S3). Gray shading represents an aseismic layer near the Moho discontinuity (Kuna et al., 2019). WBD, West Blanco Depression; EBD, East Blanco Depression; SUR, Surveyor Depression; CD, Cascadia Depression; BR, Blanco Ridge; GD, Gorda Depression; GT, Gorda transform segment.

In addition, the highly segmented BTFS is among the best studied tectonic features offshore Cascadia. Recent local seismicity studies (Kuna, 2020; Ren et al., 2023) divided it into five transform segments (i.e., the West and East Blanco Depressions [WBD and EBD], Surveyor Depression [SUR], Blanco Ridge [BR], and Gorda transform [GT]). Based on OBS stations deployed along the BTFS (Nábělek & Braunmiller, 2012), Kuna (2020) exclusively utilized P-phase onsets to detect and locate small earthquakes. Source parameters, especially focal depth, might be therefore biased due to the lack of constraint from S-phases. Furthermore, based on both P- and S-wave arrivals manually picked from the same dataset, Ren et al. (2023) investigated precise locations, focal depth, and focal mechanisms of relatively strong events with phase readings manually derived from at least 15 stations. The events included in both our automated catalog and the manually-constructed catalog (Ren et al., 2023) exhibit a good consistency (Fig. 3), deviated by only 0.158 km, 0.351 km, 1.052 km in latitude, longitude, and focal depth, benchmarking the location quality of the deep-learning-based earthquakes.

Discussion

The offshore region of central and southern Cascadia is tectonically very active (Fig. 1), including a spectrum of active plate boundaries (i.e., JdFR, GR, BTFS, MTF, and CSZ) and a transform-transform-trench triple junction, MTJ. However, seismicity studies primarily based on land (e.g., Sverdrup, 1986; Braunmiller and Nábělek, 2008) or hydro-acoustic (e.g., Dziak et al., 2000, 2011) networks lead to biased earthquake locations that limited the understanding of seismotectonic behavior in this region. Although a few local seismic catalogs based on the CI OBS dataset have been recently published (Stone et al., 2018; Kuna, 2020; Morton et al., 2023; Ren et al., 2023), they have been focused on regional subsets such as the BTFS or the Cascadia margin. Our deep-learning-based seismic catalog for the first time provides detailed information of faulting and deformation in the offshore region of central and southern Cascadia, with a special focus on portions seaward of the Cascadia deformation front (CDF). Earthquake locations, especially those in quality classes A and B, show perfect alignment with morphological features in this region, where data quality and analysis have long been limited.

Offshore central Cascadia, sparse intraplate earthquakes with focal depths up to 40 km are observed within 150 km seaward of the CDF (Fig. 2), which has also been observed by a recent seismicity study (Morton et al., 2023). Previous active seismic studies (e.g., Nedimović et al., 2009; Han et al., 2016; Canales et al., 2017) have revealed normal faulting in the vicinity of this region in response to plate bending, providing a pathway for promoted cooling (Wu et al., 2023) that contributes to the origin of these intraplate events. However, the BTFS in the further seaward is much more seismically active, exhibiting focused seismicity along the entire fault system (Fig. 3). Our seismicity catalog reveals similar deformation patterns and patches with previous studies (Kuna, 2020; Ren et al., 2023), supporting along-strike variations in fault structure and slip modes. The eastern segments, including BR, GD, and GT, represent a mature transform fault system that has accommodated plate motion since ~0.6 Ma, while he western segments, including WBD, EBD, and SUR, remains an immature, evolving system adapting to regional tectonic forces (Ren et al., 2023). Additionally, our micro-earthquake catalog reveals deep clusters under SUR, BR, and GD, which might be related to magma upwelling within OTF systems (e.g., Rychert et al., 2021; Adimah et al., 2024).

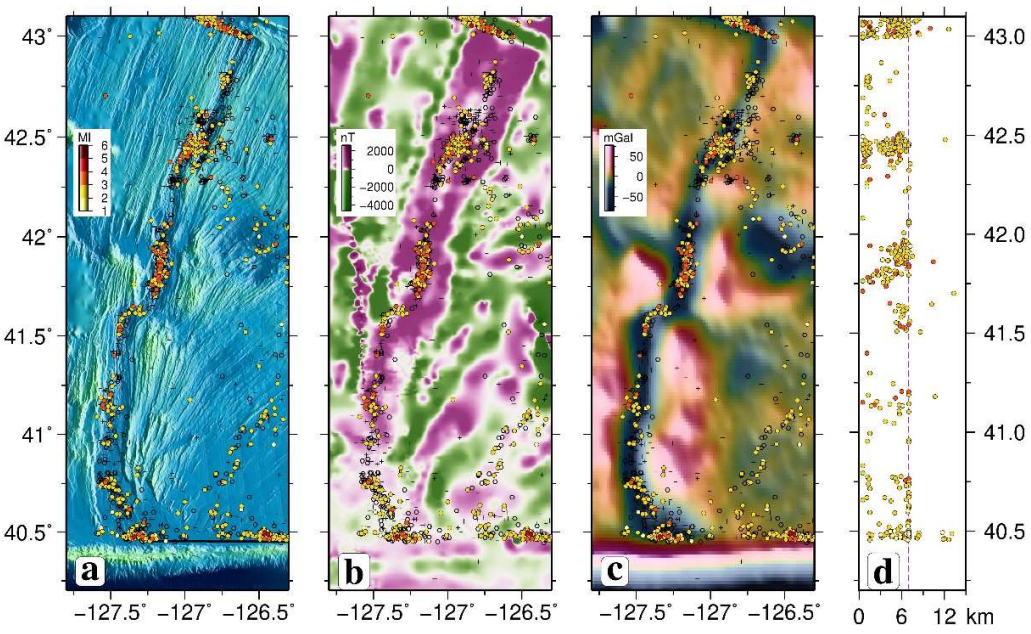

Fig. 4. Close-up view of the GR. Local seismicity is plotted over (a) Seafloor bathymetry (Ryan et al., 2009), (b) Airborne magnetic anomaly (Bankey et al., 2002), and (c) Free air gravity anomaly (Sandwell et

al., 2014). (d) Focal depth profile without vertical exaggerations. Dashed purple line shows the Moho discontinuity inferred from the minimum 1D velocity model (Fig. S3).

In the offshore region of southern Cascadia, structural and deformation characteristics become more complex from GR to CDF. Multidisciplinary geophysical data (Fig. 4) support the segmentation of the GR: northern (42.2°N – 43°N), central (41.7°N – 42.2°N), and southern (40.5°N – 41.7°N) segments (Riddihough, 1980). Although spreading rates along the GR decrease southward from 55 mm/yr near the BTFS to 26 mm/yr approaching the MTF (Wilson, 1989), focal depth distribution is rather homogenous, constrained mainly by brittle deformation in the crust (Fig. 4d), fitting into a compilation of focal depth ranges across slow- and ultraslow-spreading ridges (Grevemeyer et al., 2019). Moreover, in the northern and southern ends where the GR intersects adjacent transform faults, deep events occur, which has been observed in the vicinity of several ridge-transform intersections (Yu et al., 2021; Ren et al., 2023).

The GDZ is bounded by the GR in the west, the CDF in the east, and the MTF in the south. However, its northern boundary, or the northern limit of deformation, is under debated (Riddihough, 1980; Wilson, 1989; Chaytor et al., 2004; Bodmer et al., 2015). Within the GDZ, high levels of intraplate micro-seismicity highlight the complex tectonic interactions at work, as the GDZ deforms nonrigidly in response to the northward migration of the MTJ. The observed micro-earthquakes, especially those in quality A and B, are reasonably focused, aligning closely with spreading fabrics and magnetic anomalies (Fig. 5a), which provides for the first time, seismic evidence for the reactivation of spreading-related faults that accomplish the majority of the internal nonrigid deformation within GDZ. The strike-slip faulting indicated by focal mechanisms further supports the deformation model of Chaytor et al. (2004), characterized as left-lateral strike-slip motion. In addition, the spatial distribution of micro-events also highlights the northern boundary of the nonrigid GDZ, which aligns perfectly with the pseudofault traces between 42°N and 42.5°N (Fig. 5a).

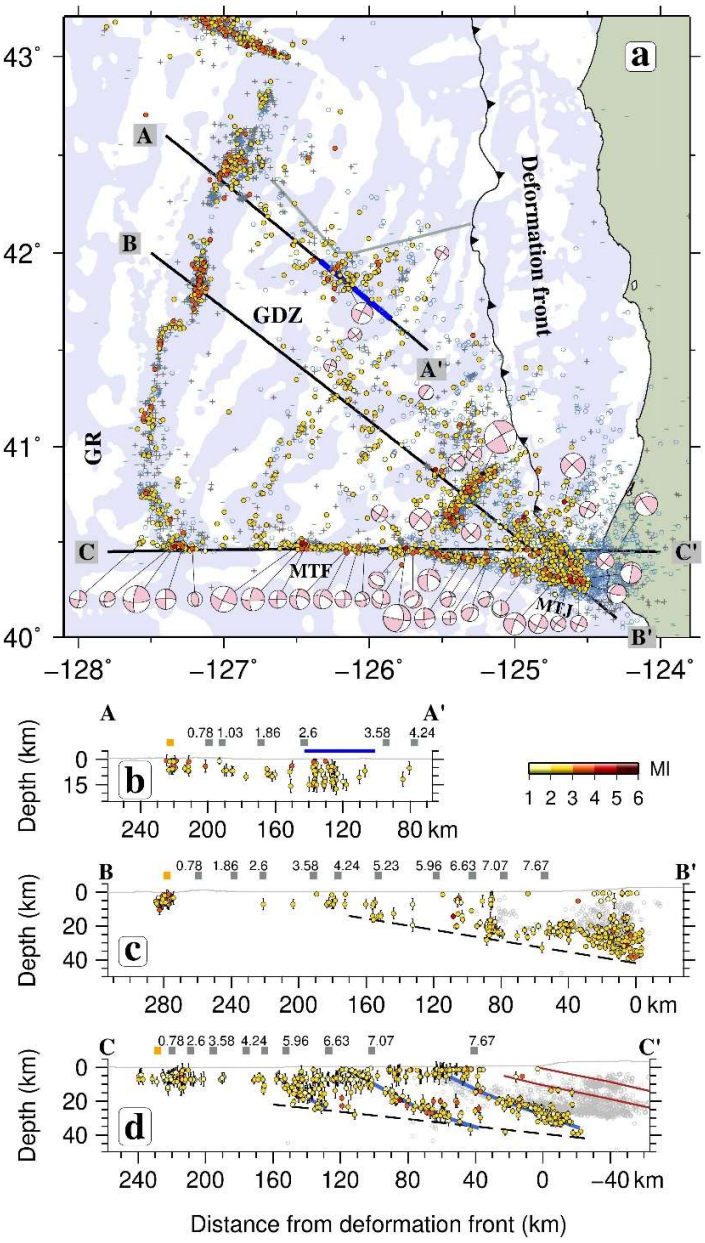

Fig. 5. Close-up view of the GDZ. (a) Local seismicity and focal mechanisms of the GDZ. The shaded and the open areas are normally and reversely magnetized, respectively (Bankey et al., 2002). Gray polylines to the north of 42°N mark the northern limit of nonrigid deformation in GDZ. Thick blue line indicates the intersection between the projection line AA' and the nearby propagator wakes (Fig. 1b). Focal depth cross sections (without vertical exaggerations) are shown along profiles (b) AA', (c) BB', and (d) CC'. Orange squares correspond to 0 Ma, while gray squares and numberings show isochrons in Ma. Gray

open circles show earthquake locations from Guo et al. (2021). Broken lines indicate the limit of brittle deformation. The subducting oceanic crust is bounded by red lines (Wang & Rogers, 1994) in panel (d), while blue lines mark the clusters of intermediate earthquakes at the MTF.

A general trend of increasingly deeper earthquakes is observed with greater distance from the GR and decreasing proximity to the deformation front (Fig. 5b, c, and d). This pattern aligns with recent findings that the lithosphere thickens with increasing distance (and plate age) from the GR (Wu et al., 2023). Nearing the CDF, the influence of plate bending intensifies (Nedimović et al., 2009; Han et al., 2016), resulting in deeper and denser seismic activity. Consequently, the maximum focal depth along the three cross-sections increases from ~7 km beneath the GR to ~40 km at the CDF. However, profile CC' reveals more complex dynamics within the MTF, displaying distinct seismotectonic behavior compared to other oceanic transform faults (e.g., McGuire et al., 2012; Wolfson-Schwehr et al., 2014; Kuna, 2020; Ren et al., 2023; Schlaphorst et al., 2023). Oceanic transform faults, commonly offsetting mid-ocean ridges (Grevemeyer et al., 2021; Ren et al., 2022), show limited focal depth ranges correlating with the 600°C isotherm (Abercrombie & Ekstrom, 2001; Roland et al., 2010). However, the MTF connects the southern segment of the GR and the CDF, representing a ridge-trench transform fault. Although both the BTFS and the MTF serve as prominent transform plate boundaries between the Juan de Fuca and Pacific plates, the east-west trending MTF is kinematically inconsistent with the current strike of the BTFS. This inconsistency results in the MTF impeding the southward motion of the Juan de Fuca plate, leading to north-south compression and shortening across the GDZ (Wilson, 1986; Wang et al., 1997) as the MTJ migrates northward along the west coast of North America (Furlong & Schwartz, 2004). Focal mechanism solutions further demonstrate along-strike variations in deformation styles (Fig. 5a). In addition to strike-slip faulting, reverse faulting is observed around the MTJ, and, interestingly, the western end of the MTF where it intersects the GR, which is uncommon, as ridge-transform intersections are often where shear stress interacts with spreading-axis tensile stress (Morgan & Parmentier, 1984). The reverse-faulting earthquakes in the west suggest ridge-parallel fault planes, possibly driven by magmatic intrusions (Olive et al., 2024) and complex stress state

(Wang et al., 1997). However, extensional strike-slip and dip-slip faulting dominate the central MTF between 125.5°W and 127°W. Similar features have been evidenced by a few local seismicity studies supporting extensional tectonics at oceanic transform faults (Yu et al., 2021; Ren et al., 2023). Moreover, deep earthquake clusters are observed underneath, revealing trenchward-dipping structures in the upper mantle (Fig. 5d, blue lines).

A few studies, using multi-channel seismic profiles across old, mature oceanic crust, have observed dipping reflectors mainly terminating at the Moho (e.g., Ranero et al., 1997; Han et al., 2016; Marcaillou et al., 2021), known as lower crust dipping reflectors (LCDRs) and interpreted as shear zones (Ranero et al., 1997; Kodaira et al., 2014) linked to mantle flow or plate reorganizations. However, our study, using passive seismic data, for the first time, revealed the dipping structures extending to the upper mantle up to 40 km at the MTF, the southern boundary of the GDZ. One possible interpretation is the asthenospheric deformation as the diffuse GDZ rotates clockwise to accommodate the relative motion between the JdF and Pacific plates. The spreading rates along the GR decrease southward from 55 mm/yr to 26 mm/yr caused a spacing problem (Wilson, 1989). The predicted north-south compression and shortening across the GDZ are accommodated mainly by the flexural slip along reactivated spreading-related faults at crustal depths (Chaytor et al., 2004). However, at asthenospheric depths, Bodmer et al. (2015), based on shear wave splitting observations, suggested that relative motion of the surrounding plates controls the upper mantle deformation beneath the GDZ. Therefore, we interpret the dipping structures as mantle shear zones developed in the vicinity of a weak transform fault (Wang et al., 1997; Cox et al., 2021), the MTF, as the MTJ migrates northward. This effect might promote cooling, facilitate chemical alteration/serpentinization, resulting in both a low-temperature and low-wave-speed lithosphere (Wu et al., 2023).

Methods

Offshore seismic data

The Cascadia Initiative (CI) was a community-based amphibious seismic and geodetic experiment that significantly enhanced the extent of observation in the offshore region of Cascadia. A total of about 25 cruises were carried out to deploy and recover OBS during the course of four CI expedition seasons (2011–2014), spanning from July 2011 to October 2015 (Toomey et al., 2014). Each expedition season commenced during the summer and extended for a duration of around 11–15 months, during which over 60 OBS were deployed offshore Cascadia. In addition, there were several principal-investigator-driven experiments (e.g., Nábělek & Braunmiller, 2012; 2013) that complemented the CI expeditions.

During the 2011 expedition season, OBS were mostly deployed to the north of our study region. We thus exclusively utilized OBS data from seasons 2012 to 2014 to investigate the offshore micro-seismicity in central and southern Cascadia between July 2012 and October 2015. We obtained continuous seismic recordings from a total of 238 OBS stations (Fig. 1). The station spacing was approximately 40–60 km, with the exception of certain focused arrays such as the dense array sites near the Mendocino triple junction (e.g., Chen & McGuire, 2016; Gong & McGuire, 2018).

Earthquake phase detection and association

We utilized the PickBlue (Bornstein et al., 2023), an integration of adapted DL models of EQTransformer (Mousavi et al., 2020) and PhaseNet (Zhu & Beroza, 2019), for effective and efficient seismic phase picking on the massive CI OBS dataset. The picker provides arrival times of P- and S-phases and their corresponding confidence values. The confidence values, defined as the peak values in the time series of probabilities for phase picks, could be used as indicators of pick quality (Bornstein et al., 2023). In order to eliminate the low-quality picks and outliers, we exclude picks with confidence values below 0.6. Fig. S2 depicts seismograms and picked phases of two local events. Arrival times of 2,253,059 P-phases and 1,405,180 S-phases were obtained from the entire OBS dataset.

We further associated the phase picks using REAL (Zhang et al., 2019). The velocity model used in the association step was adapted from Ren et al. (2023). The search range spans 120 km in depth and is bounded

by a station that records the earliest phase at a 1.5° radius. The search grid has a horizontal spacing of 0.1° and a vertical spacing of 5 km. The thresholds for P- and S-arrivals were 4 and 1, respectively. We identified a total number of 14,074 candidate earthquakes with initial locations.

Velocity models and event relocation

A minimum one-dimensional (1D) velocity model for the offshore central Cascadia region between 43° and 45°N was already constrained by Ren et al. (2023). We further inverted for a minimum 1D velocity model for the offshore region in southern Cascadia (40°–43°N) using VELEST (Kissling et al., 1994). We selected 91 well-locatable events offshore southern Cascadia with a large number of observations (> 15 P- and S-arrivals) and a maximum station azimuthal gap up to 180°. We constructed 10,737 initial P-wave velocity models and then performed inversions to identify the 1D P-wave velocity model with the lowest root-mean-square (RMS) residual. Thereafter, we determined the 1D minimum S wave velocity model using an additional iteration of inversions using various initial Vp/Vs ratios (e.g., Husen et al., 1999; Lange et al., 2007). The final 1D velocity model with minimum RMS residuals among all output models is shown in Fig. S3. Our 1D velocity model for the offshore southern Cascadia region closely resembles the one offshore central Cascadia, with the exception of a noticeably higher Vp/Vs ratio in the topmost layer within 1.5 km beneath the seafloor.

By leveraging the non-linear oct-tree grid-search algorithm (NonLinLoc, Lomax et al., 2000), we relocated local earthquakes with a combination of minimum 1D velocity models above (Fig. S3) for the entire region. NonLinLoc utilizes the computation of probability density functions (PDF) for each event to estimate location uncertainties. The preferred earthquake location was defined as the maximum likelihood point of the complete non-linear location PDF. In addition, station correction terms (Husen et al., 1999) were calculated and iteratively updated to account for non-modeled three-dimensional wave propagation effects below the OBS network (Grevemeyer et al., 2019). In total, we obtained 14,057 local events with an overall RMS misfit of 0.13 s (Fig. S4).

Magnitude calculation and focal mechanism solutions

We estimated the local magnitudes (Ml) following Hutton & Boore (1987), and calculated the moment magnitudes (Mw) using an automated procedure described by Ottemöller & Havskov (2003). The magnitude estimates we obtained are in good agreement with those in the ANSS catalog (Fig. S5a-b). Our magnitudes show 53 and 130 common estimates that deviate by -0.21 and 0.10 units for Mw and Ml, respectively, when compared to the ANSS catalog.

First motion polarities of P-phase onsets were manually identified to determine focal mechanisms (Reasenberg & Oppenheimer, 1985). We selected events with a minimum of 10 polarities and an azimuthal gap below 180°, and obtained focal mechanisms of 54 events in the vicinity of the GDZ in addition to 84 events of the BTFS (Ren et al., 2023). Exemplary focal mechanism solutions determined from first motion polarities are shown in Fig. S6.

Data Availability

Seismic data used in this study, which are archived at the IRIS Data Management Center (http://www.iris.edu), were provided by instruments from the Ocean Bottom Seismic Instrument Center (https://obsic.whoi.edu/). Bathymetric data are available via https://www.gmrt.org/GMRTMapTool/. Airborne magnetic anomaly data are available from the USGS Mineral Resources Program (https://mrdata.usgs.gov/magnetic/).

Code Availability

The implementation of the deep learning picker, PickBlue, is from the SeisBench toolbox (Woollam et al., 2022). All plots are made with GMT (Wessel & Smith, 1998) and Matplotlib (Hunter, 2007).

Acknowledgements

The authors wish to thank all persons who contributed to data collection in the four CI expedition seasons.

Author contributions

Y. Ren accessed seismological data from various temporary offshore networks and generated a high-quality micro-earthquake catalog using advanced machine-learning-based algorithms. I. Grevemeyer and D. Lange supervised the study, refined its overall scope, and provided input on the interpretation and discussion of the results. Y. Ren drafted the initial manuscript, and all authors contributed to editing the manuscript.

Competing interests

The authors declare no competing interests.

References

Abercrombie, R. E., & Ekstrom, G. (2001). Earthquake slip on oceanic transform faults. Nature, 410,74–77. https://doi.org/10.1038/35065064

Adimah, N. I., Tan, Y. J., & Russell, J. B. (2024). Shear-wave velocity structure of the Blanco oceanic transform fault zone. Geophysical Journal International, 239(2), 1287-1312. https://doi.org/10.1093/gji/ggae318

Atwater, T., & Stock, J. (1998). Pacific-North America Plate Tectonics of the Neogene Southwestern United States - an update. International Geological Review, 40(5), 375–402. https://doi.org/10.1080/00206819809465216

Bankey, V., Cuevas, A., Daniels, D., Finn, C., Hernandez, I., Hill, P., et al. (2002), Digital Data Grids for the Magnetic Anomaly Map of North America. USGS Open File Report 2002-414. https://doi.org/10.3133/ofr02414

Bodmer, M., Toomey, D. R., Hooft, E. E., Nábělek, J., & Braunmiller, J. (2015). Seismic anisotropy beneath the Juan de Fuca plate system: Evidence for heterogeneous mantle flow. Geology, 43(12), 1095-1098. https://doi.org/10.1130/G37181.1

Bornstein, T., Lange, D., Münchmeyer, J., Woollam, J., Rietbrock, A., & Barcheck, G., et al. (2024). PickBlue: Seismic phase picking for ocean bottom seismometers with deep learning. Earth and Space Science, 11, e2023EA003332. https://doi.org/10.1029/2023EA003332

Canales, J. P., Carbotte, S. M., Nedimović, M. R., & Carton, H. (2017). Dry Juan de Fuca slab revealed by quantification of water entering Cascadia subduction zone. Nature Geoscience, 10(11), 864–870. https://doi.org/10.1038/ngeo3050

Chaytor, J. D., Goldfinger, C., Dziak, R. P., & Fox, C. G. (2004). Active deformation of the Gorda plate: Constraining deformation models with new geophysical data. Geology, 32(4), 353-356. https://doi.org/10.1130/G20178.2

Chen, H., Yang, H., Zhu, G., Xu, M., Lin, J., & You, Q. (2022). Deep outer-rise faults in the Southern Mariana Subduction Zone indicated by a machine-learning-based high-resolution earthquake catalog. Geophysical Research Letters, 49, e2022GL097779. https://doi.org/10.1029/2022GL097779

Chen, X., & McGuire, J. J. (2016). Measuring earthquake source parameters in the Mendocino triple junction region using a dense OBS array: Implications for fault strength variations. Earth and Planetary Science Letters, 453, 276–287. https://doi.org/10.1016/j.epsl.2016.08.022

Duarte, C. M., Chapuis, L., Collin, S. P., Costa, D. P., Devassy, R. P., & Eguiluz, V. M., et al. (2021). The soundscape of the Anthropocene ocean. Science, 371(6529), eaba4658. https://doi.org/10.1126/science.aba4658

Dziak, R.P., Fox, C.G., Bobbitt, A.M., & Goldfinger, C. (2001). Bathymetric Map of the Gorda Plate: Structural and Geomorphological Processes Inferred from Multibeam Surveys. Marine Geophysical Researches, 22, 235–250. https://doi.org/10.1023/A:1014606407111

Dziak, R. P., Hammond, S. R., & Fox, C. G. (2011). A 20-year hydroacoustic time series of seismic and volcanic events in the Northeast Pacific Ocean. Oceanography, 24(3), 280–293. http://dx.doi.org/10.5670/oceanog.2011.79

Embley, R. W., & Wilson, D. S. (1992), Morphology of the Blanco Transform Fault Zone-NE Pacific: Implications for its Tectonic Evolution. Marine Geophysical Researches, 14, 25–45. https://doi.org/10.1007/BF01674064

Fisk, M. R., Duncan, R. A., Fox, C. G., & Witter, J. B. (1993). Emergence and petrology of the Mendocino Ridge. Marine Geophysical Researches, 15, 283–296. https://doi.org/10.1007/BF01982386

Fox, C. G., & Dziak, R. P. (1999). Internal deformation of the Gorda Plate observed by hydroacoustic monitoring. Journal of Geophysical Research, 104(B8), 17603–17615. https://doi.org/10.1029/1999JB900104

Furlong, K. P., & Schwartz, S. Y. (2004). Influence of the Mendocino triple junction on the tectonics of coastal California. Annual Review of Earth and Planetary Sciences, 32(1), 403-433. https://doi.org/10.1146/annurev.earth.32.101802.120252

Gong, J., Fan, W., & Parnell-Turner, R. (2022). Microseismicity indicates atypical small-scale plate rotation at the Quebrada transform fault system, East Pacific Rise. Geophysical Research Letters, 49, e2021GL097000. https://doi.org/10.1029/2021GL097000

Gong, J., & Fan, W. (2022). Seismicity, fault architecture, and slip mode of the westernmost Gofar transform fault. Journal of Geophysical Research: Solid Earth, 127, e2022JB024918. https://doi.org/10.1029/2022JB024918

Gong, J., & McGuire, J. J. (2018). Interactions between strike-slip earthquakes and the subduction interface near the Mendocino Triple Junction. Earth and Planetary Science Letters, 482, 414–422. https://doi.org/10.1016/j.epsl.2017.11.022

Grevemeyer, I., Hayman, N. W., Lange, D., Peirce, C., Papenberg, C., Van Avendonk, H. J. A., et al. (2019). Constraining the maximum depth of brittle deformation at slow- and ultraslow-spreading ridges using microseismicity. Geology, 47(11), 1069–1073. https://doi.org/10.1130/G46577.1

Grevemeyer, I., Reston, T. J., & Moeller, S. (2013). Microseismicity of the Mid-Atlantic Ridge at 7° S – 8° 15′ S and at the Logatchev Massif oceanic core complex at 14° 40′ N – 14° 50′ N. Geochemistry, Geophysics, Geosystems, 14, 3532 – 3554. https://doi.org/10.1002/ggge.20197

Grevemeyer, I., Rüpke, L. H., Morgan, J. P., Iyer, K., & Devey, C. W. (2021). Extensional tectonics and two-stage crustal accretion at oceanic transform faults. Nature, 591, 402–407. https://doi.org/10.1038/s41586-021-03278-9

Guo, H., McGuire, J.J. & Zhang, H. (2021). Correlation of porosity variations and rheological transitions on the southern Cascadia megathrust. Nature Geoscience, 14, 341–348. https://doi.org/10.1038/s41561-021-00740-1

Han, S., Carbotte, S. M., Canales, J. P., Nedimović, M. R., Carton, H., Gibson, J. C., & Horning, G. W. (2016). Seismic reflection imaging of the Juan de Fuca plate from ridge to trench: New constraints on the distribution of faulting and evolution of the crust prior to subduction. Journal of Geophysical Research: Solid Earth, 121(3), 1849–1872. https://doi.org/10.1002/2015JB012416

Husen, S., & Smith, R. (2004). Probabilistic Earthquake Relocation in Three-Dimensional Velocity Models for the Yellowstone National Park Region, Wyoming. Bulletin of the Seismological Society of America, 94(3), 880–896. https://doi.org/10.1785/0120030170

Kodaira, S., Fujie, G., Yamashita, M., Sato, T., Takahashi, T., & Takahashi, N. (2014). Seismological evidence of mantle flow driving plate motions at a palaeo-spreading centre. Nature Geoscience, 7(5), 371-375. https://doi.org/10.1038/ngeo2121

Kuna, V. M., Nábělek, J. L., & Braunmiller, J. (2019), Mode of slip and crust–mantle interaction at oceanic transform faults. Nature Geoscience, 12, 138–142. https://doi.org/10.1038/s41561-018-0287-1

Kuna, V. M. (2020), Investigation of Slip and Tectonics of the Blanco Transform Fault Using High-resolution Ocean Bottom Seismic Data. Ph.D. thesis, Oregon State University.

Kreemer, C., G. Blewitt, & E. C. Klein (2014). A geodetic plate motion and Global Strain Rate Model. Geochemistry, Geophysics, Geosystems, 15, 3849–3889. https://doi.org/10.1002/2014GC005407

Lomax, A., Virieux, J., Volant, P., & Berge-Thierry, C. (2000). Probabilistic Earthquake Location in 3D and Layered Models. In: Advances in Seismic Event Location, Thurber, C.H., Rabinowitz, N. (Eds), vol 18, pp. 101–134. Springer, Dordrecht. https://doi.org/10.1007/978-94-015-9536-0_5

Marcaillou, B., Klingelhoefer, F., Laurencin, M., Lebrun, J. F., Laigle, M., Lallemand, S., ... & Graindorge, D. (2021). Pervasive detachment faults within the slow spreading oceanic crust at the poorly coupled Antilles subduction zone. Communications Earth & Environment, 2(1), 203. https://doi.org/10.1038/s43247-021-00269-6

McGuire, J. J., Collins, J. A., Gouédard, P., Roland, E., Lizarralde, D., Boettcher, M. S., et al. (2012). Variations in earthquake rupture properties along the Gofar transform fault, East Pacific Rise. Nature Geoscience, 5(5), 336–341. https://doi.org/10.1038/ngeo1454

McKenzie, D., Jackson, J., & Priestley, K. (2005). Thermal structure of oceanic and continental lithosphere. Earth and Planetary Science Letters, 233(3-4), 337–349. https://doi.org/10.1016/j.epsl.2005.02.005

Morgan, J.P., & Parmentier, E.M. (1984). Lithospheric stress near a ridge-transform intersection. Geophysical Research Letters, 11, 113–116. https://doi.org/10.1029/GL011i002p00113

Morton, E. A., Bilek, S. L., & Rowe, C. A. (2023). Cascadia subduction zone fault heterogeneities from newly detected small magnitude earthquakes. Journal of Geophysical Research: Solid Earth, 128, e2023JB026607. https://doi.org/10.1029/2023JB026607

Mousavi, S. M., Ellsworth, W. L., Zhu, W., Chuang, L. Y., & Beroza, G. C. (2020). Earthquake transformer—An attentive deep-learning model for simultaneous earthquake detection and phase picking. Nature Communications, 11(1), 3952. https://doi.org/10.1038/s41467-020-17591-w

Nábělek, J., & Braunmiller, J. (2012). Plate Boundary Evolution and Physics at an Oceanic Transform Fault System [Data set]. International Federation of Digital Seismograph Networks. https://doi.org/10.7914/SN/X9_2012

Nábělek, J., & Braunmiller, J. (2013). Seismicity, Structure and Dynamics of the Gorda Deformation Zone [Data set]. International Federation of Digital Seismograph Networks. https://doi.org/10.7914/SN/Z5_2013

Nedimović, M. R., Bohnenstiehl, D. R., Carbotte, S. M., Canales, J. P. & Dziak, R. P. (2009). Faulting and hydration of the Juan de Fuca plate system. Earth and Planetary Science Letters, 284(1–2), 94–102. https://doi.org/10.1016/j.epsl.2009.04.013

Niksejel, A., & Zhang, M. (2024). OBSTransformer: a deep-learning seismic phase picker for OBS data using automated labelling and transfer learning. Geophysical Journal International, 237(1), 485–505. https://doi.org/10.1093/gji/ggae049

Olive, J. A., Ekström, G., Buck, W. R., Liu, Z., Escartín, J., & Bickert, M. (2024). Mid-ocean ridge unfaulting revealed by magmatic intrusions. Nature, 1-6. https://doi.org/10.1038/s41586-024-07247-w

Ranero, C. R., Reston, T. J., Belykh, I., & Gnibidenko, H. (1997). Reflective oceanic crust formed at a fast-spreading center in the Pacific. Geology, 25(6), 499-502. https://doi.org/10.1130/0091-7613(1997)025%3C0499:ROCFAA%3E2.3.CO;2

Ren, Y., Geersen, J., & Grevemeyer, I. (2022). Impact of spreading rate and age-offset on oceanic transform fault morphology. Geophysical Research Letters, 49, e2021GL096170. https://doi.org/10.1029/2021GL096170

Ren, Y., Lange, D., & Grevemeyer, I. (2023). Seismotectonics of the Blanco transform fault system, northeast Pacific: Evidence for an immature plate boundary. Journal of Geophysical Research: Solid Earth, 128, e2022JB026045. https://doi.org/10.1029/2022JB026045

Riddihough, R. P. (1980). Gorda plate motions from magnetic anomaly analysis. Earth and Planetary Science Letters, 51(1), 163–170. https://doi.org/10.1016/0012-821X(80)90263-0

Roland, E., Behn, M. D., & Hirth, G. (2010), Thermal‐mechanical behavior of oceanic transform faults: Implications for the spatial distribution of seismicity. Geochemistry, Geophysics, Geosystems, 11, Q07001. https://doi.org/10.1029/2010GC003034

Ruppert, N. A., Barcheck, G., & Abers, G. A. (2022). Enhanced regional earthquake catalog with Alaska amphibious community seismic experiment data. Seismological Research Letters, 94(1), 522–530. https://doi.org/10.1785/0220220226

Ryan, W. B. F., Carbotte, S. M., Coplan, J. O., O'Hara, S., Melkonian, A., Arko, R., et al. (2009). Global multi-resolution topography synthesis. Geochemistry, Geophysics, Geosystems, 10, Q03014. https://doi.org/10.1029/2008GC002332

Rychert, C. A., Tharimena, S., Harmon, N., Wang, S., Constable, S., Kendall, J. M., ... & Schlaphorst, D. (2021). A dynamic lithosphere–asthenosphere boundary near the equatorial Mid-Atlantic Ridge. Earth and Planetary Science Letters, 566, 116949. https://doi.org/10.1016/j.epsl.2021.116949

Sandwell, D. T., Müller, R. D., Smith, W. H. F., Garcia, E., & Francis, R. (2014), New global marine gravity model from CryoSat-2 and Jason-1 reveals buried tectonic structure. Science, 346(6205), 65–67. https://doi.org/10.1126/science.1258213

Schlaphorst, D., Rychert, C. A., Harmon, N., Hicks, S. P., Bogiatzis, P., Kendall, J. M., & Abercrombie, R. E. (2023). Local seismicity around the Chain Transform Fault at the Mid-Atlantic Ridge from OBS observations. Geophysical Journal International, 234(2), 1111-1124. https://doi.org/10.1093/gji/ggad124

Silver, E. A. (1971). Tectonics of the Mendocino Triple Junction. GSA Bulletin, 82(11), 2965–2978. https://doi.org/10.1130/0016-7606(1971)82[2965:TOTMTJ]2.0.CO;2

Stone, I., Vidale, J. E., Han, S., & Roland, E. (2018). Catalog of offshore seismicity in Cascadia: Insights into the regional distribution of microseismicity and its relation to subduction processes. Journal of Geophysical Research: Solid Earth, 123, 641–652. https://doi.org/10.1002/2017JB014966

Sverdrup, K. A. (1986). Multiple-event relocation of earthquakes on and near the Gorda Ridge. Geophysical Research Letters, 13, 674–677. https://doi.org/10.1029/GL013i007p00674

Toomey, D. R., Allen, R. M., Barclay, A. H., Bell, S. W., Bromirski, P. D., Carlson, R. L., et al. (2014). The Cascadia Initiative: A sea change in seismological studies of subduction zones. Oceanography, 27(2), 138–150. https://doi.org/10.5670/oceanog.2014.49

VanderBeek, B. P., & Toomey, D. R. (2019). Pn tomography of the Juan de Fuca and Gorda plates: Implications for mantle deformation and hydration in the oceanic lithosphere. Journal of Geophysical Research: Solid Earth, 124, 8565–8583. https://doi.org/10.1029/2019JB017707

Wang, K., & Rogers, G. C. (1994). An explanation for the double seismic layers north of the Mendocino triple junction. Geophysical Research Letters, 21(2), 121–124. https://doi.org/10.1029/93gl03538

Wang, K., He, J., & Davis, E. E. (1997). Transform push, oblique subduction resistance, and intraplate stress of the Juan de Fuca Plate. Journal of Geophysical Research, 102(B1), 661–674. https://doi.org/10.1029/96JB03114

Wilson, D. S. (1986). A kinematic model for the Gorda deformation zone as a diffuse southern boundary of the Juan de Fuca plate. Journal of Geophysical Research, 91(B10), 10259-10269. https://doi.org/10.1029/JB091iB10p10259

Wilson, D. S. (1988). Tectonic history of the Juan de Fuca Ridge over the last 40 million years. Journal of Geophysical Research, 93(B10), 11863–11876. https://doi.org/10.1029/JB093iB10p11863

Wilson, D. S. (1989). Deformation of the so‐called Gorda plate. Journal of Geophysical Research, 94(B3), 3065-3075. https://doi.org/10.1029/JB094iB03p03065

Wilson, D. S. (1993), Confidence intervals for motion and deformation of the Juan de Fuca Plate. Journal of Geophysical Research, 98(B9), 16053–16071. https://doi.org/10.1029/93JB01227

Wolfson-Schwehr, M., Boettcher, M. S., McGuire, J. J., & Collins, J. A. (2014). The relationship between seismicity and fault structure on the Discovery transform fault, East Pacific Rise. Geochemistry, Geophysics, Geosystems, 15(9), 3698–3712. https://doi.org/10.1002/2014GC005445

Wu, M., Wang, H., Zhang, S., & Ritzwoller, M. H. (2023). Plate age and uppermost mantle structure across the Juan de Fuca and Gorda plates. Journal of Geophysical Research: Solid Earth, 128, e2023JB026494. https://doi.org/10.1029/2023JB026494

Xiao, Z., Wang, J., Liu, C., Li, J., Zhao, L., & Yao, Z. (2021). Siamese earthquake transformer: A pair-input deep-learning model for earthquake detection and phase picking on a seismic array. Journal of Geophysical Research: Solid Earth, 126(5), e2020JB021444. https://doi.org/10.1029/2020JB021444

Yu, Z., Singh, S. C., Gregory, E. P. M., Maia, M., Wang, Z., & Brunelli, D. (2021), Semi-brittle seismic deformation in high-temperature mantle mylonite shear zone along the Romanche transform fault. Science Advances, 7(15), eabf3388. https://doi.org/10.1126/sciadv.abf3388

Zhu, W., & Beroza, G. C. (2019). Phasenet: A deep-neural-network-based seismic arrival-time picking method. Geophysical Journal International, 216(1), 261–273. https://doi.org/10.1093/gji/ggy423

Nature Communications

Supporting Information for

Seismological evidence of mantle shear zones in response to a northward migrating transform-transform-trench triple junction, northeast Pacific

Yu Ren [(1)], Dietrich Lange [(1)], and Ingo Grevemeyer [(1)]

(1) GEOMAR Helmholtz Centre for Ocean Research Kiel, Kiel, Germany

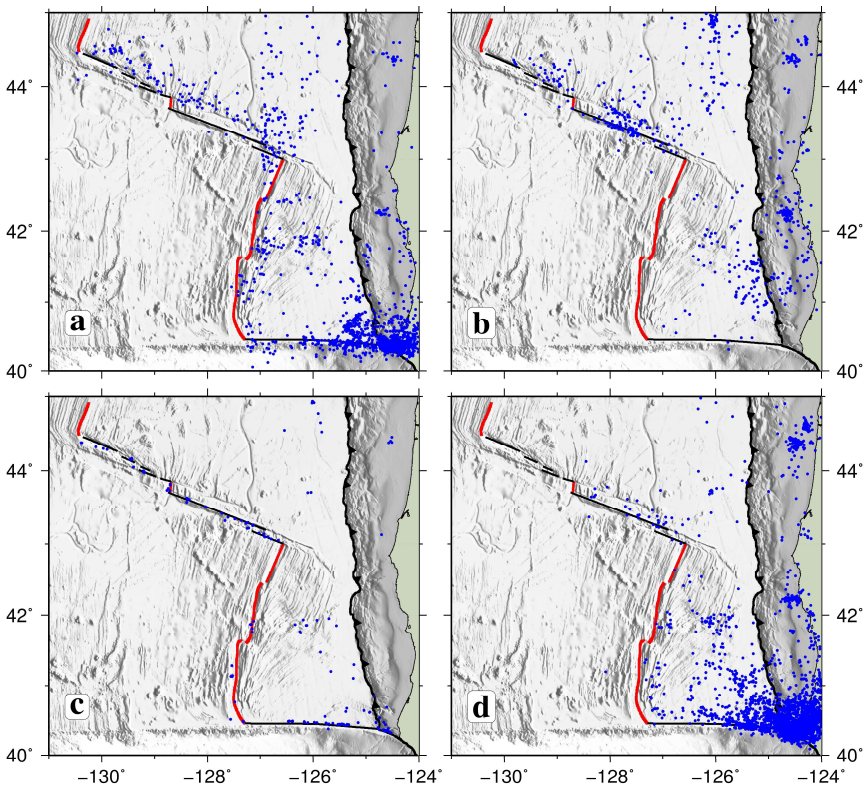

Figure S1. Earthquake catalogs of the study area. Blue dots show event locations. (**a**) ANSS Comprehensive Earthquake Catalog (2012/09–2015/09); (**b**) Stone et al., 2018; (**c**) VanderBeek and Toomey, 2019; (**d**) Morton et al., 2023.

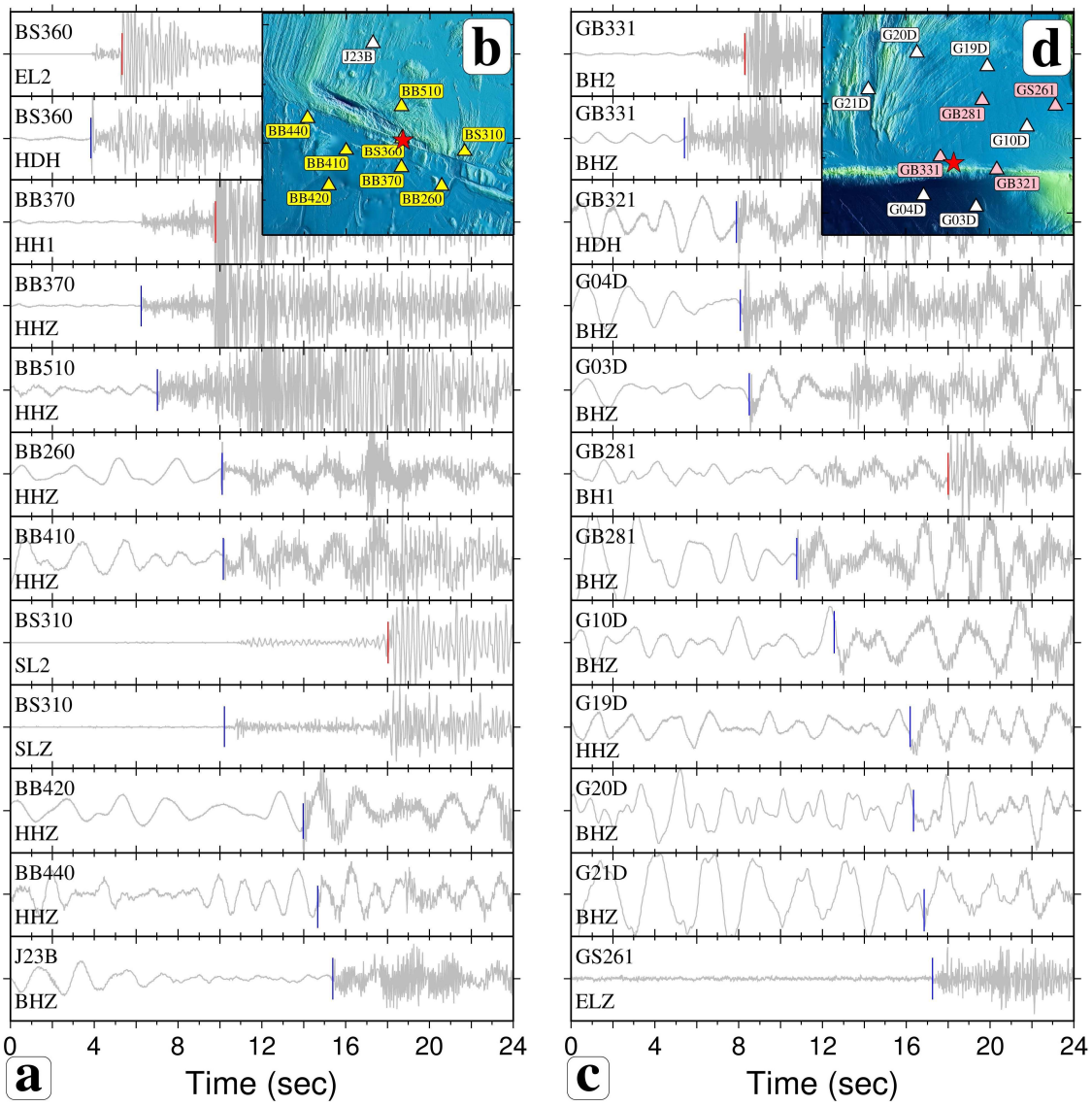

Figure S2. Seismograms and phase picks of two local events recorded by OBS stations. (**a**) P- and S-phase arrivals of a local earthquake (2012/09/30, 7:13:45.0, Ml 2.4) at the western BTFS, and (**b**) spatial distribution of their corresponding OBS stations. (**c**) P- and S-phase arrivals and (**d**) OBS station distribution in the vicinity of a local event (2015/03/14, 0:6:0.3, Ml 2.0) at the Mendocino transform fault. HH1, BH1, BH2, SL2, and EL2 are horizontal channels; HHZ, BHZ, SLZ, and ELZ are vertical channels; HDH is hydrophone channel. The onsets of P- and S-phase arrivals are marked in blue and red, respectively. White, yellow, and pink triangles indicate locations of OBS under network code 7D, X9, and Z5, respectively. Red stars show locations of the two local earthquakes.

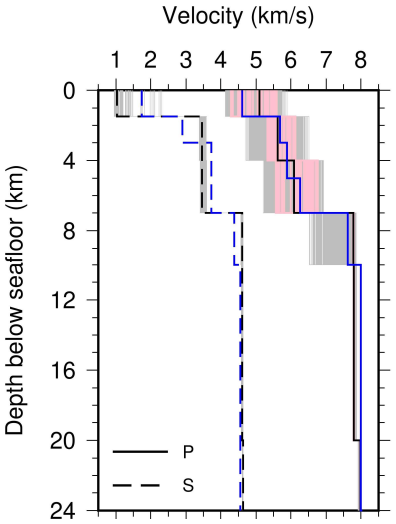

Figure S3. Minimum 1D velocity models of the study region. Black lines indicate the minimum 1D velocity model for the offshore southern Cascadia region (40° – 43°N) among all output models (gray lines). Red lines show 800 models with the lowest RMS. Blue lines indicate the 1D velocity model for the offshore central Cascadia region (43° – 45°N) (Ren et al., 2023). The inferred depth of seismological Moho is 7 km.

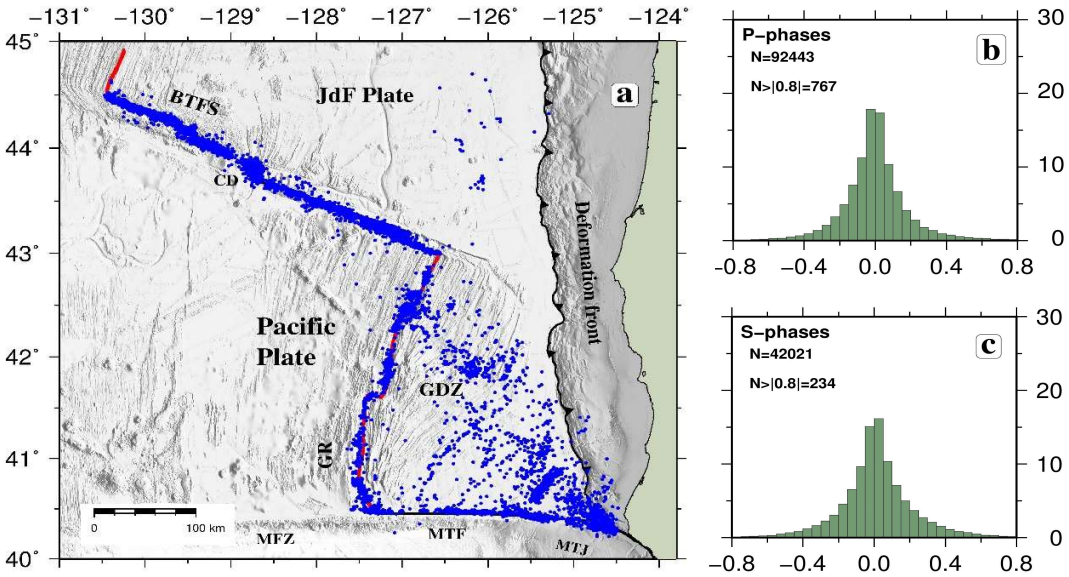

Figure S4. Relocated local events and residuals of the location procedures in this study. (**a**) Distribution of local events from the relocated seismic catalog. (**b**) P- and (**c**) S-phase residuals of the location procedures. Blue dots show event locations. N, number of phases.

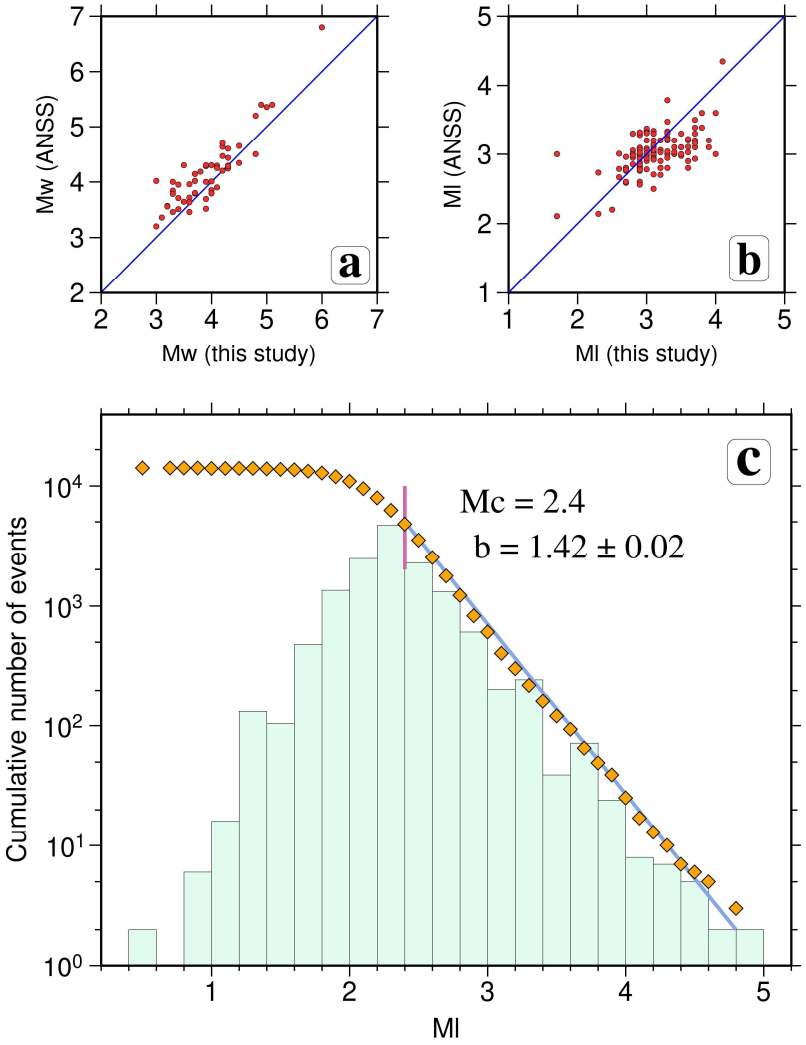

Figure S5. Properties of the magnitude estimates in this study. Comparison of the (**a**) moment and the (**b**) local magnitudes for the common events in both ANSS and our local catalogs. Blue lines indicate one-to-one relationship between both catalogs. (**c**) Magnitude-frequency distribution of our local seismicity catalog.

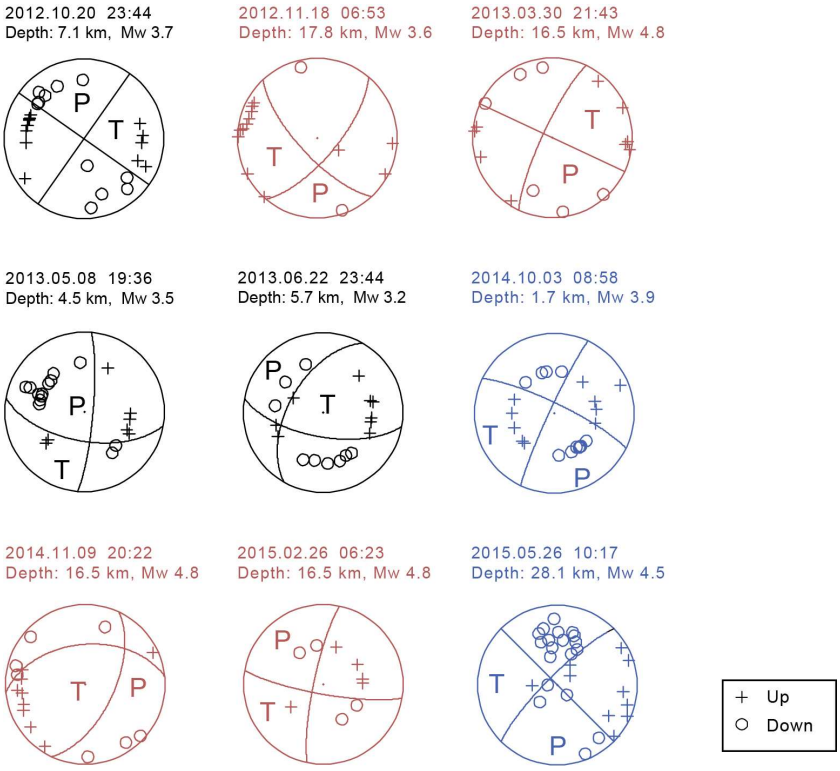

Figure S6. Exemplary focal mechanism solutions determined from first motion polarities. Events of the BTFS, MTF, and GDZ are in black, red, and blue, respectively.

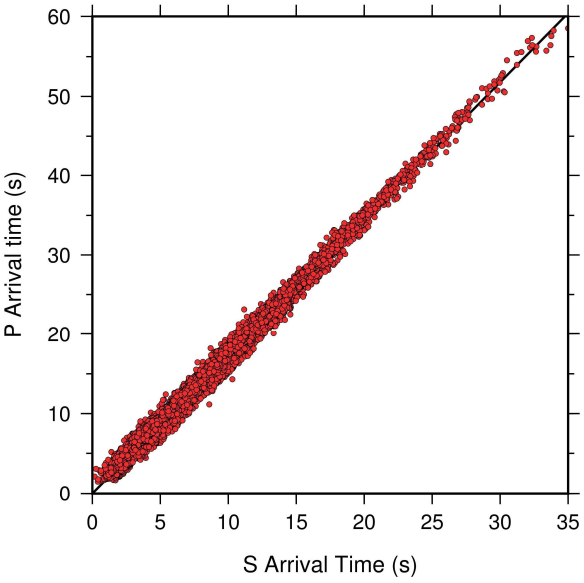

Figure S7. Wadati diagram of P-phase onsets versus S-phase onsets, yielding Vp/Vs ratio at around 1.725 for offshore Cascadia regions.

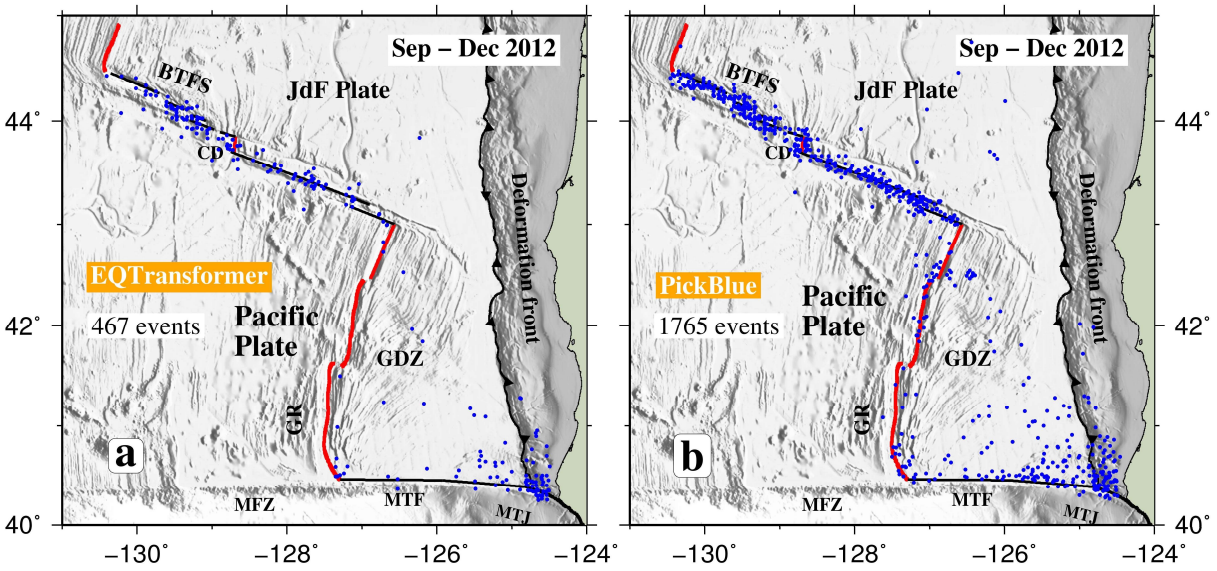

Figure S8. Distribution of earthquakes detected by (**a**) EQTransformer and (**b**) PickBlue from OBS data between September and December, 2012. Earthquake locations are preliminary results of the event association process, shown as blue dots.

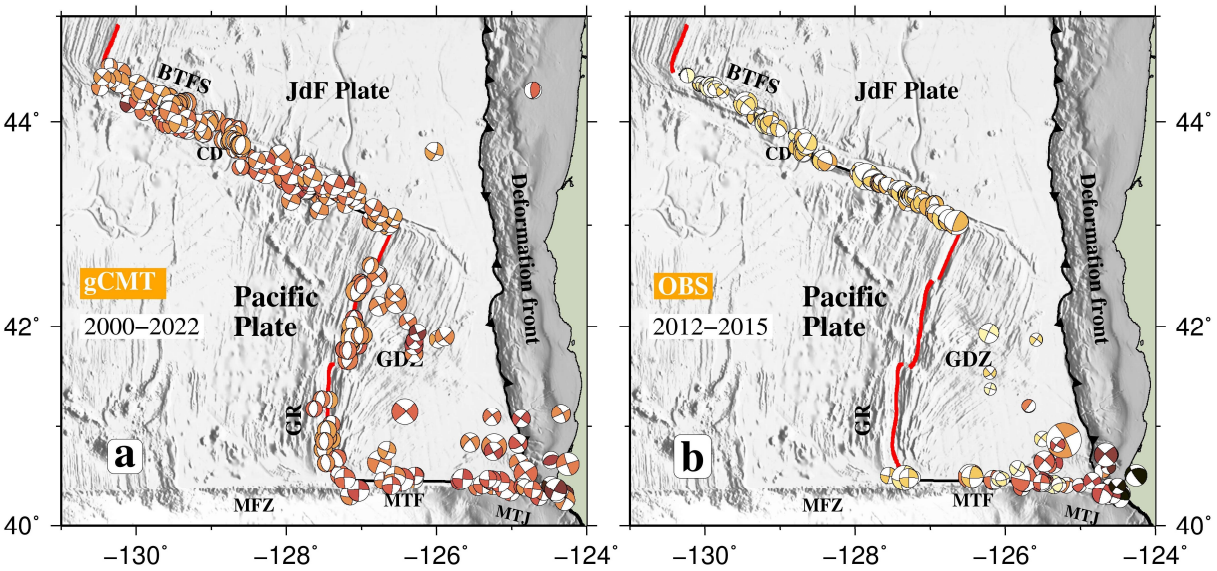

Figure S9. Focal mechanisms in the research area from (**a**) gCMT catalog (Ekström et al., 2012) from 2000 to 2022, and (**b**) our local seismic study constrained by OBS instruments.

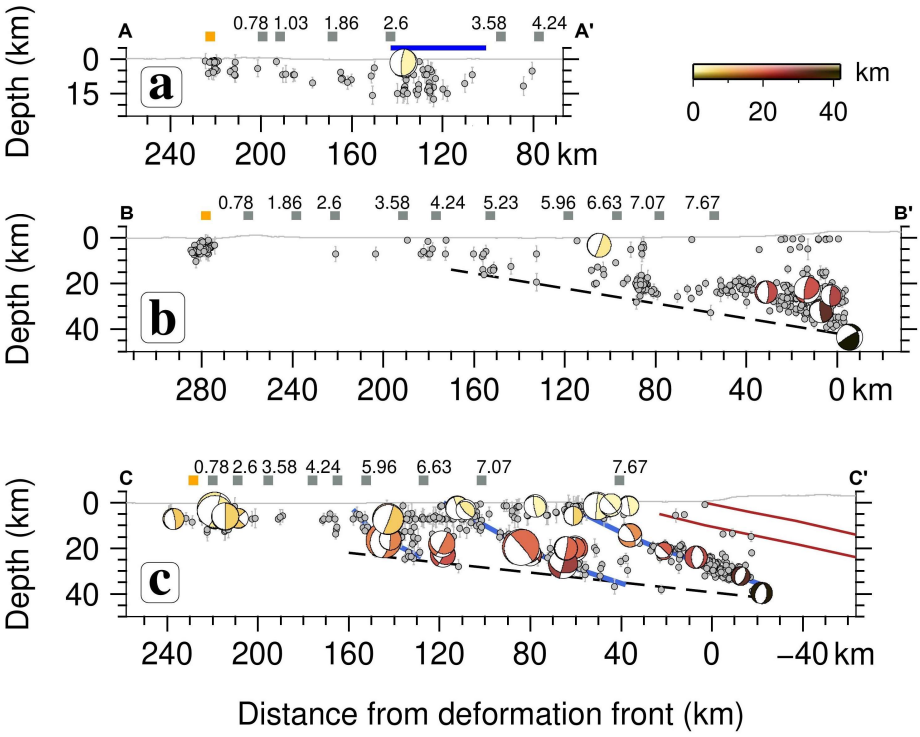

Figure S10. Focal mechanisms and earthquakes in cross-sectional view along profiles (**a**) AA', (**b**) BB', and (**c**) CC' of Fig. 5.

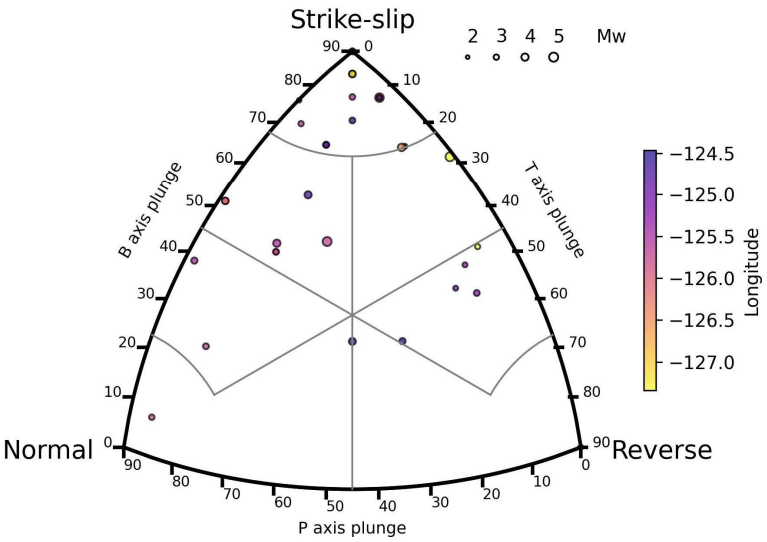

Figure S11. Ternary plot for focal mechanisms in the vicinity of the MTF.

CHAPTER 8

CONCLUSION AND OUTLOOK

8.1 Conclusion

Since the advent of plate tectonic theory, OTFs have traditionally been regarded as simple, conservative strike-slip boundaries where lithosphere is neither created nor destroyed. However, recent advances in marine geophysics and geodynamic simulations suggest that OTFs exhibit significantly more complex dynamics than previously assumed. To deepen the understanding of OTF systematics, the initial phase of this doctoral project systematically investigated the morphology (Chapter 2), gravity anomalies (Chapter 3), and mantle rheology (Chapter 4) of OTF systems using global geophysical databases.

Morphological analysis indicates that OTFs at ultraslow- and slow-spreading ridges generally exhibit large age offsets and are characterized by long, wide, and deep transform valleys. In contrast, OTFs corresponding to higher spreading rates generally have small age offsets and display highly complex morphologies. The correlation between parameterized morphology and spreading rate is found to be weak, while a more robust relationship that transform valleys get deeper and wider with increasing age offset, links surface deformation to tectonic extension predicted by geodynamic models (Grevemeyer et al., 2021). Scattered observations at small age offsets (<5 Myr) suggest that these hotter, more ductile OTFs are more prone to modification by secondary tectonic processes, accommodating higher spreading rates compared to their large-age-offset counterparts.

Mantle rheology significantly influences the steady-state temperature field of OTF systems by affecting mantle flow dynamics beneath the oceanic lithosphere. Differing rheological assumptions alter the thermal correction terms applied during residual mantle Bouguer anomaly (RMBA) calculations, leading to discrepancies in computed values. Compared to plate cooling models, isoviscous models underpredict RMBAs within the transform deformation zones and overpredict them in the far field at older plate ages. To refine these estimates, three-dimensional geodynamic models incorporating nonlinear viscoplastic rheology were employed for RMBA calculations. The computed RMBA for OTF systems across the full range of spreading rates reveal systematic differences in crustal thickness between OTFs and their adjacent FZs, evidenced by larger RMBAs in transform deformation zones compared to associated FZs. These observations suggest thinner crust beneath active transform valleys due to extension and mantle upwelling, as differences in plate strength produce increasingly oblique boundaries at depth. In contrast, FZs are characterized by thicker crust resulting from multi-stage accretion and hydrothermal alteration.

Leveraging near-field observations from dedicated research cruises, this doctoral project further conducted multiple case studies to explore the seismotectonics of OTFs and their geodynamic implications (Chapters 5, 6, and 7).

The Oceanographer transform fault, offsetting the Mid-Atlantic Ridge, spans 120 km and features a ~10 km-wide transform valley with FZs extending hundreds of kilometers. Data from recent research cruises, including multibeam bathymetry and passive seismic recordings, reveal that the fault is segmented by a small pressure ridge within the transform valley, evident in both morphology and seismicity. Near the RTI, widespread seismicity extends across the inside corner, with normal faulting parallel to the transform fault, providing seismological evidence of tectonic extension. In contrast, strike-slip motion dominates farther from the RTIs, aligning with predictions from plate tectonic theory.

In the northeast Pacific, the Blanco transform fault system (BTFS) spans 350 kilometers of highly segmented OTFs. Unlike many other OTFs, the BTFS lacks prominent FZ traces. Previous kinematic models suggested that a clockwise rotation of plate motion around ~5 Ma initiated the formation of the BTFS, which has since evolved through multiple ridge propagation events. In the eastern segment, stresses are predominantly accommodated by brittle deformation in the lower crust and uppermost mantle. Conversely, in the western segment, plate motions are accommodated by brittle deformation at temperatures below 600°C and mantle creep. At the western RTI, bathymetry reveals magma-robust features, including J-shaped ridges extending beyond the transform valley. By contrast, the eastern RTI displays magma-poor features, with truncated J-shaped ridges terminating at the Gorda Depression. Furthermore, seismic slip vectors highlight the contrasting maturity of the two segments. In the eastern BTFS, stresses align closely with the direction of plate motion, signifying a mature transform fault system that has accommodated plate motion since ~0.6 Ma. In the western BTFS, however, stresses are clockwise skewed, reflecting ongoing reorganization and adaptation to far-field stress changes. These observations suggest that the BTFS comprises two distinct transform systems: the eastern segment represents a mature plate boundary with stabilized dynamics, while the western segment remains an immature, evolving system adapting to regional tectonic forces.

Although both the BTFS and the Mendocino transform fault (MTF) serve as prominent transform plate boundaries between the Juan de Fuca and Pacific plates, the east-west trending MTF is kinematically inconsistent with the current strike of the BTFS. This inconsistency results in the MTF impeding the southward motion of the Juan de Fuca plate, which, in turn, induces internal nonrigid deformation within its southern portion, known as the Gorda deformation zone (GDZ). Within the GDZ, high levels of intraplate micro-seismicity highlight the complex tectonic interactions at work. Reactivated

spreading-related faults, driven by a combination of north-south compression and plate-bending extension, align closely with spreading fabrics observed in seafloor bathymetry. A spatial trend of increasingly deeper earthquakes is observed with greater distance from the Gorda Ridge and decreasing proximity to the deformation front. Additionally, clusters of deep micro-earthquakes, reaching depths of up to 40 km along the MTF, indicate the development of shear zones in the uppermost mantle, likely driven by active asthenospheric flow influenced by the northward migration of the Mendocino triple junction and advection due to the larger Pacific plate.

In summary, this thesis provides robust evidence for tectonic extension and multi-stage magmatic accretion at OTF systems, fundamentally challenging the conventional view that OTFs are purely strike-slip, conservative plate boundaries. Additionally, the BTFS and MTF in the northeast Pacific demonstrate more intricate dynamics driven by secondary tectonic processes, offering new insights into the segmentation and evolution of OTFs.

8.2 Outlook

As evidence increasingly challenges the traditional concept of OTFs, many open questions persist regarding the dynamics of mid-ocean ridges and transforms, including:

(I) What controls the geometry of mid-ocean ridges and spacing, segmentation, and orientation of their discontinuities (including OTFs, overlapping spreading centers, and non-transform offsets)?

(II) What are possible geodynamic scenarios for past, present and future development of transform valleys and their adjacent FZs?

(III) How do detachment faults influence the dynamics of asymmetric accretion at OTFs?

Addressing these questions requires a combined observational and model-based approach. Multidisciplinary near-field datasets should be compiled to provide a comprehensive understanding of global mid-ocean ridges. Parameterization techniques similar to those used in previous chapters could be applied to further investigate tectonic parameters relevant to questions (I) and (III). For question (II), estimating the volume of lithosphere missing in the transform valley due to tectonic extension and the volume created through multi-stage accretion could offer valuable insights into the evolution of transform valleys and adjacent FZs. Additionally, three-dimensional geodynamic models (e.g., Tian et al., 2023) can be employed to further constrain the dynamics of these evolving systems through geological time, offering a temporal framework to understand their complex processes.

Moreover, the superior performance of deep-learning-based earthquake detection algorithms, as demonstrated in Chapter 7, highlights their potential for identifying hidden seismic signals from massive OBS datasets. It paves the way for uncovering previously undetected seismicity in global amphibious seismic datasets. The same deep-learning-driven workflow can be extended to seismic recordings from other tectonic features, such as the shallow offshore regions of subduction zones (SZs).

As the incoming plate bends into the trench, it fractures, producing faults that serve as conduits for water to hydrate the plate prior to subduction. The hydration, particularly through bending-related faults, plays a crucial role in regulating global water cycles and influencing the modes of fault slip in SZs. Despite decades of numerical models aimed at simulating this process (e.g., Rüpke et al., 2004; van Keken et al., 2011), key aspects remain poorly understood due to a lack of observational constraints on the extent and depth of hydration. Imaging the seismic velocity structure, sensitive to rock composition and fluid content, is widely used to estimate the hydration state of the incoming plate. Yet, previous studies have typically been limited to regional scales and/or suffered considerable uncertainties due to challenges in processing large-scale offshore seismic datasets with traditional techniques (e.g., Niksejel and Zhang, 2024). Recent advances in seismology have led to several machine learning tools that effectively address these challenges, indicating that far more water might be subducted than previously indicated by numerical models (Cai et al., 2018). A global assessment is thus required to measure the extent of plate hydration and its impact on key SZ processes.

Leveraging the deep-learning-based workflow, seismic events can be effectively detected, located, and characterized across amphibious seismic datasets from SZs in Alaska, Cascadia, Chile, Hikurangi, Japan, Java, and Mariana. The resulting high-resolution seismic catalogs, combined with shipborne bathymetry and published controlled-source seismic images, provide a foundation for mapping the spatial distribution and geometry of plate fabric and bending-related faults in the downgoing plate. Constrained by the precise locations of detected earthquakes, local earthquake travel time tomography could be further performed to refine the velocity structure of the crust and upper mantle, allowing for the quantification of both the depth and magnitude of plate hydration. By correlating faulting and plate hydration with other SZ parameters such as slab age, thermal state, and convergence rate, this work has the potential to uncover fundamental patterns in SZ dynamics that have previously been obscured due to data limitations.

In addition, the interdisciplinary approach of transforming scientific data into visual arts, as presented in the Appendix, offers new opportunities for both scientific exploration and public engagement. This approach enhances the accessibility of complex scientific findings, making them more understandable and appealing to a broader audience.

8.3 References

Cai, C., Wiens, D. A., Shen, W., & Eimer, M. (2018). Water input into the Mariana subduction zone estimated from ocean-bottom seismic data. *Nature*, 563, 389–392. https://doi.org/10.1038/s41586-018-0655-4

Grevemeyer, I., Rüpke, L. H., Morgan, J. P., Iyer, K., & Devey, C. W. (2021). Extensional tectonics and two-stage crustal accretion at oceanic transform faults. *Nature*, 591, 402–407. https://doi.org/10.1038/s41586-021-03278-9

Niksejel, A., & Zhang, M. (2024). OBSTransformer: a deep-learning seismic phase picker for OBS data using automated labelling and transfer learning. *Geophysical Journal International*, 237(1), 485–505. https://doi.org/10.1093/gji/ggae049

Rüpke, L. H., Morgan, J. P., Hort, M., & Connolly, J. A. (2004). Serpentine and the subduction zone water cycle. *Earth and Planetary Science Letters*, 223(1–2), 17–34. https://doi.org/10.1016/j.epsl.2004.04.018

Tian, X., Behn, M. D., Ito, G., Schierjott, J. C., Kaus, B. J. P. & Popov, A. A. (2024). Magmatism controls global oceanic transform fault topography. *Nature Communications*, 15, 1914. https://doi.org/10.1038/s41467-024-46197-9

van Keken, P. E., Hacker, B. R., Syracuse, E. M., & Abers, G. A. (2011). Subduction factory: 4. Depth-dependent flux of H2O from subducting slabs worldwide. *Journal of Geophysical Research*, 116(B1), B01401. https://doi.org/10.1029/2010jb007922

Appendix A

MANUSCRIPT #7

Bridging Science and Art: Auralization and Visualization of Ocean Soundscape

Yu Ren [1,4], Tian Wu [2,4], Chuanzhi Li [3,4], Pengfei Yao [4], and Weiwei Ding [5,6]

(1) GEOMAR Helmholtz Centre for Ocean Research Kiel, Kiel, Germany
(2) Muthesius University of Fine Arts and Design, Kiel, Germany
(3) Institute for Advanced Ocean Study, Ocean University of China, Qingdao, China
(4) Deep Sea Light Team, Kiel, Germany
(5) Second Institute of Oceanography, MNR, Hangzhou, China
(6) School of Oceanography, Shanghai Jiao Tong University, Shanghai, China

Published in 2024 in *iScience*, 27(9),110696

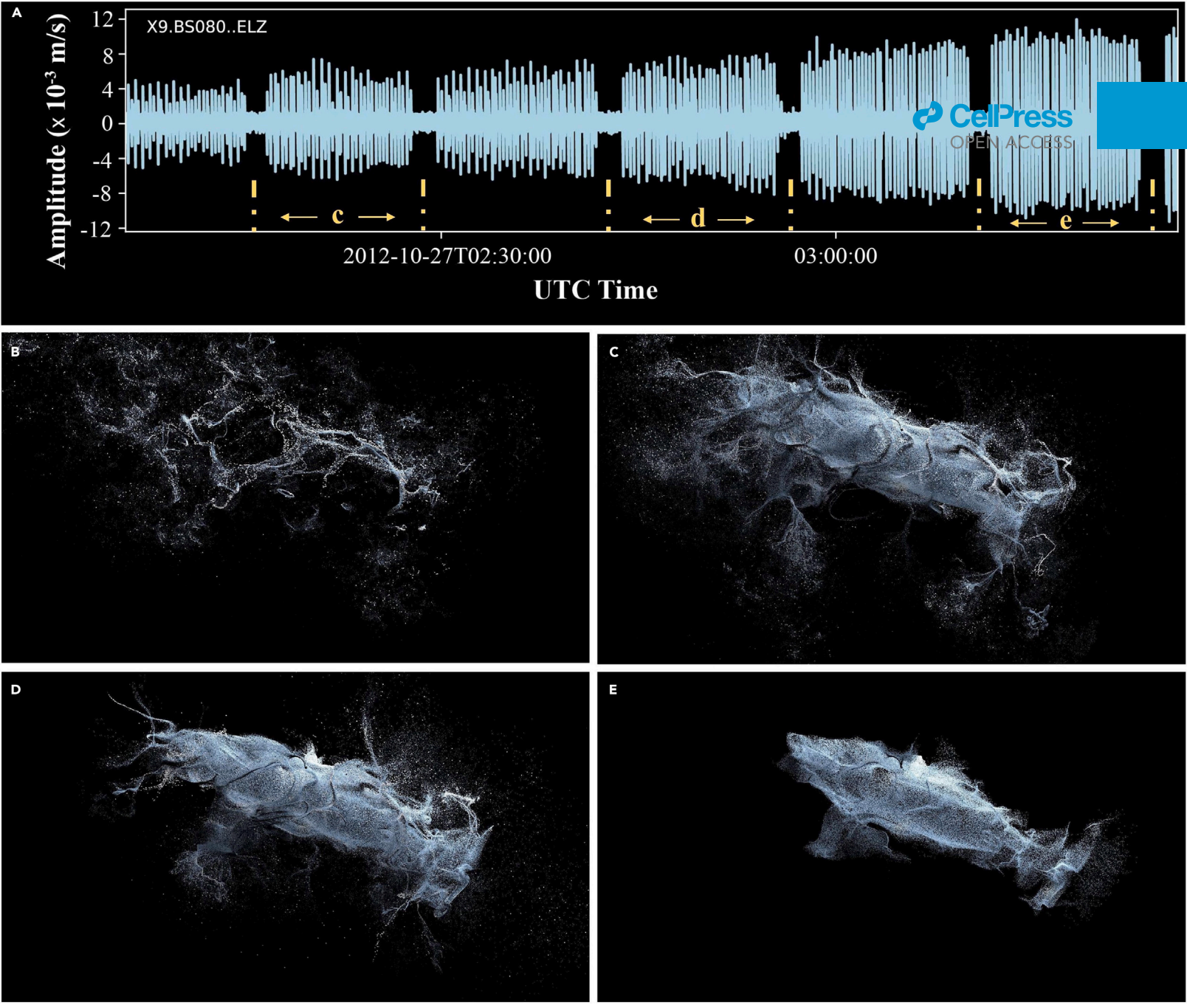

Backstory

Bridging science and art: Auralization and visualization of the ocean soundscape

Yu Ren,[1,4,*] Tian Wu,[2,4] Chuanzhi Li,[3,4] Pengfei Yao,[4] and Weiwei Ding[5,6]

As a group of researchers and artists, we have collaborated on a science-art project that converts seismic and hydroacoustic data into immersive digital artworks, revealing the hidden realm of ocean soundscape. We integrated artistic methodologies to produce soundtracks and videos from seismic waveforms

Above image: Digital art images visualizing fin whale songs in the northeast Pacific Ocean. (A) Seismic time series data of the fin whale song recorded at the vertical component (ELZ) of OBS station BS080 under the network code X9. Labels and broken lines indicate short segments of the whale song used to produce art images in c–e. Note that b corresponds to an earlier time window representing weaker energy level and lower amplitude of the seismic waveform prior to the recordings in A. (B–E) Art visuals created based on the variation in the amplitudes of the seismic waveforms. The higher the amplitude, the greater the energy level of the whale song, resulting in a more accurate silhouette of the fin whale.

recorded in the ocean, which enables the general public to gain a multisensory experience of the scientific data studied by specialists. Through exhibitions in multiple venues, our interdisciplinary approach was well received by diverse audiences, showcasing the potential for creative representations of scientific information.

Beginnings

Geoscientists commonly use visual representations such as graphs and tables to explain their research to both their colleagues and individuals without specialized knowledge in the field. Nevertheless, visualizing the mechanisms of our Earth system concealed under intricate geoscientific data has proven to be a difficult task for the geoscience community.[1] Due to its universal nature, the field of art has experienced significant progress in the utilization of scientific data visualization during the past decades.[2] The connection between science and art is becoming increasingly important in finding innovative methods to make geoscience more accessible to the public.[3]

A collective of early-career researchers and artists have collaborated on a science-art project known as Deep Sea Light to reveal the hidden realm of sounds in the ocean. This project aims to combine geoscience and digital art in order to create an immersive experience that appeals to a broader audience.[4] We produced soundtracks and digital art videos depicting various underwater scenarios, such as whale songs, earthquake swarms, and submarine eruptions, detected and extracted from extensive seismic and hydroacoustic datasets. The process of auralization and visualization of the ocean soundscape serves as a connection between the realms of science and art, allowing artists to convert scientific datasets into visually captivating and scientifically stimulating artworks. This interdisciplinary approach not only opens new avenues for scientific investigation and communication but also enhances public engagement. The digital artworks we created were exhibited in several venues in 2023, attracting diverse audiences that included schoolchildren, scholars, artists, politicians, and the general public.

Art and science

The sounds of the ocean

The ocean was assumed to be a quiet place. However, with the increasing number of underwater monitoring experiments,[5] a hidden realm of sounds in the ocean has been progressively revealed. The soundscape of the ocean is a complex mixture of biotic sounds (e.g., vocalizations from marine mammals and fish), abiotic sounds from natural phenomena like wind and waves, and anthropogenic sounds resulting from human activities. Sounds in the ocean are of utmost importance in the underwater world, exerting a significant influence on the behavior and communication patterns of diverse marine organisms.[6,7]

Ocean-bottom seismometer (OBS) and hydrophone arrays are commonly used for both seismological research and hydroacoustic monitoring. Between 2011 and 2015, over 300 OBSs were deployed and recovered offshore the Cascadia subduction zone, offering valuable opportunities to study local seismicity,[8] structures,[9] and biotic sounds (e.g., blue whale vocalizations[10]) in the northeast Pacific Ocean. While these scientific findings are vital for understanding our Earth system, they can be challenging for individuals without expertise in the field to comprehend and engage with. Taking advantage of the extensive seismic and hydroacoustic datasets, our project aims to explore new dimensions of scientific data representation by integrating artistic methodologies.

Creating digital artworks

We first extracted some of the most common sounds recorded by OBS arrays in the northeast Pacific Ocean, for example digital seismic waveform of fin whale calls. These vocalizations consist of frequency-modulated sweeps that decrease in frequency from around 40 to 13 Hz, with a central frequency of approximately 20 Hz. To make the fin whale vocalizations audible to humans, we increased the speed of the digital waveform data (following the study by Kilb et al.[11]) by a factor of 10 (Audio S1).

Further, we analyzed the spectrums of seismic waveforms and saved them as RGBa visuals. RGBa images consist of pixels, each of which is defined by four parameters: the three R, G, and B values that determine the color, and an alpha channel value that specifies the transparency of that particular pixel. We then utilized the Touch Designer software to convert the RGBa values of the analyzed spectrums into the positions of numerous particles within a three-dimensional xyz coordinate system. Through this approach, we can effectively depict the sounds in a three-dimensional manner and showcase various scenarios to the audience. A series of art images created from seismic waveforms shows the varying levels of discretization in the particles that compose the fin whale's shape. When the distance between the whale and the OBS station is far away, the particles become dispersed because the energy of the whale calls received by the OBS is relatively low. This corresponds to the relatively low amplitude of the seismic waveforms prior to the beginning time of the seismic whale song in Image 1a. An

[1]GEOMAR Helmholtz Centre for Ocean Research Kiel, Kiel, Germany
[2]Muthesius University of Fine Arts and Design, Kiel, Germany
[3]Ocean University of China, Qingdao, China
[4]Deep Sea Light Team, Kiel, Germany
[5]Key Laboratory of Submarine Geosciences, Second Institute of Oceanography, Ministry of Natural Resources, Hangzhou, China
[6]School of Oceanography, Shanghai Jiao Tong University, Shanghai, China
*Correspondence: yren@geomar.de
https://doi.org/10.1016/j.isci.2024.110696

Digital artworks exhibited for various target audiences. Our team utilized (A) high-resolution projectors at the Jinan International Biennale, (B) a small monitor array for schoolchildren on Ocean Science Day 2023, and (C) video wall systems at a science-art exhibition in the Blue Planet Science Fiction Film Festival 2023, to showcase our digital art videos corresponding to different sources of sound in the ocean.

increase in the amplitude of the whale calls recorded at the station results in a more accurate silhouette of the fin whale. At the peak amplitude of the seismic waveforms, the particles became more densely packed, allowing us to clearly see the characteristic shape of the fin whale portrayed by our artist colleagues. Utilizing spectrum analysis and dynamic imaging techniques on the seismic waveforms allows for the conversion of scientific information into artistic images and videos (Video S1).

We further produced digital art videos totaling 10 min in length, based on the detection and extraction of 11 types of sounds in the Pacific Ocean (Figure S1), including whale songs, earthquake swarms, submarine eruptions, shipping, etc. The soundtracks and videos were carefully designed to capture the essence of the ocean soundscape while also delivering a visually pleasing and emotionally engaging experience.

Exhibition and public engagement

Our digital artworks were exhibited in several venues in 2023, attracting a diverse audience that included schoolchildren, scholars, artists, politicians, and the general public. We chose diverse methods to present our artworks to cater to different target audiences. At the Jinan International Biennale in early 2023, we showcased our videos and soundtracks utilizing high-resolution projectors and a professional audio array. This setup ensured that the sounds and visuals were perfectly synchronized, creating a harmonious experience for the audience. This was widely appreciated by both artists and the wider community. Our artworks attracted over 300,000 visits throughout the duration (3 months) of the Jinan International Biennale.

In June 2023, we participated in the science communication events on Ocean Science Day held by the Second Institute of Oceanography, Ministry of Natural Resources in China. We used a small monitor array to play our art videos. This option is not only cost-effective compared to professional projectors or video walls but also very convenient because it allows for easy switching between different sounds in the ocean on separate screens.

In addition, our digital artworks have been displayed alongside traditional art forms such as sculpture and light art. In November 2023, we curated a public exhibition on the interactions between earth science and art during the Blue Planet Science Fiction Film Festival in Nanjing, China. We used video wall systems to showcase our digital art videos depicting sounds in the ocean in a 450 square meter exhibition hall. In addition to our digital art videos, we also crafted sculptures symbolizing glaciers and built light installations representing devastating earthquakes and the rising sea level. This exhibition showcases a diverse range of artistic representations that demonstrate the potential of integrating science and art, as well as the underlying social values they embody. Furthermore, video documentary footage of the artworks has been incorporated into a dedicated webpage on a Chinese social media platform (in Chinese, www.zhihu.com/xen/market/ecom-page/1753104503861940225; Video S2), allowing users to access and watch the artworks online.

Challenges and opportunities

Interpreting the world through art and science

While art and science are commonly perceived as distinct disciplines, they have a common objective of observing and interpreting the world. We expanded the ways in which data can be represented by combining science and art. This collaboration has resulted in the creation of digital artworks that not only capture the essence of the ocean soundscape but also deliver a visually pleasing and emotionally engaging experience. Our artworks highlight the potential of integrating artistic methodologies with scientific data to reveal the hidden realm of sounds in the ocean.

Moreover, the collaboration between the two fields has the potential to generate novel approaches, offering fresh perspectives and insights that foster further investigation.[12,13] Our artworks provide new dimensions of scientific data representation, while the creation of the artworks is also driven by the analysis of scientific datasets. Due to technical constraints, our digital artworks were produced based on a limited number of sound detections in the ocean. Therefore, one of our ongoing tasks is to improve the capability of detecting and visualizing the sounds and/or events from extensive datasets using advanced techniques like artificial intelligence.

Moving forward, our goal is to broaden our collaborative endeavors to encompass additional domains within the field of geoscience. We hope to further integrate earth science and digital art in order to generate additional avenues for public engagement and education, ultimately cultivating a stronger bond between human societies and the ever-changing systems of our planet.

Our artworks provide new dimensions of scientific data representation, while the creation of the artworks is also driven by the analysis of scientific datasets.

We hope to further integrate earth science and digital art in order to generate additional avenues for public engagement and education, ultimately cultivating a stronger bond between human societies and the ever-changing systems of our planet.

ACKNOWLEDGMENTS

To learn more about our recent artworks, please visit www.instagram.com/deep_see_light/. Our science-art project benefited from the 2022 Beacon Prize sponsored by Zhihu Incorporation. Y.R. was supported by the China Scholarship Council (grant 201904910466). This manuscript benefited greatly from conversations with Helene-Sophie Hilbert, Sibiao Liu, and Maochuan Zhang.

SUPPLEMENTAL INFORMATION

Supplemental information can be found online at https://doi.org/10.1016/j.isci.2024.110696.

REFERENCES

1. Rodrigues, J., Castro, C., Costa e Silva, E., and Pereira, D.I. (2023). Geoscientists' views about science communication: predicting willingness to communicate geoscience. Geosci. Commun. *6*, 15–25. https://doi.org/10.5194/gc-6-15-2023.
2. Crameri, F., Shephard, G.E., and Heron, P.J. (2020). The misuse of colour in science communication. Nat. Commun. *11*, 5444. https://doi.org/10.1038/s41467-020-19160-7.
3. Barrett, N., and Mair, K. (2014). Aftershock: A science–art collaboration through sonification. Org. Sound *19*, 4–16. https://doi.org/10.1017/S1355771813000368.
4. Wu, T., Ren, Y., Liu, S., Li, C., Yao, P., and Hu, X. (2023). What can we see by illuminating the ambient deep sea? In EGU General Assembly 2023, Vienna, Austria, *EGU23*EGU General Assembly 2023, Vienna, Austria, p. 7514. https://doi.org/10.5194/egusphere-egu23-7514.
5. Lu, Z., Zhu, X., Du, X., and Li, J. (2024). Development and Prospect of Deep-Sea Environmental Noise Monitoring Technology. Earth Sci. *49*, 2120–2130. https://doi.org/10.3799/dqkx.2023.162.
6. Tyack, P.L. (2008). Implications for marine mammals of large-scale changes in the marine acoustic environment. J. Mammal. *89*, 549–558. https://doi.org/10.1644/07-MAMM-S-307R.1.
7. Duarte, C.M., Chapuis, L., Collin, S.P., Costa, D.P., Devassy, R.P., Eguiluz, V.M., Erbe, C., Gordon, T.A.C., Halpern, B.S., Harding, H.R., et al. (2021). The soundscape of the Anthropocene ocean. Science *371*, eaba4658. https://doi.org/10.1126/science.aba4658.
8. Ren, Y., Lange, D., and Grevemeyer, I. (2023). Seismotectonics of the Blanco transform fault system, northeast Pacific: Evidence for an immature plate boundary. JGR. Solid Earth *128*, e2022JB026045. https://doi.org/10.1029/2022JB026045.
9. Kuna, V.M., and Nábělek, J.L. (2021). Seismic crustal imaging using fin whale songs. Science *371*, 731–735. https://doi.org/10.1126/science.abf3962.
10. Wilcock, W.S.D., and Hilmo, R.S. (2021). A method for tracking blue whales (Balaenoptera musculus) with a widely spaced network of ocean bottom seismometers. PLoS One *16*, e0260273. https://doi.org/10.1371/journal.pone.0260273.
11. Kilb, D., Peng, Z., Simpson, D., Michael, A., Fisher, M., and Rohrlick, D. (2012). Listen, Watch, Learn: SeisSound Video Products. Seismol Res. Lett. *83*, 281–286. https://doi.org/10.1785/gssrl.83.2.281.
12. Jacobsen, E. (2016). Seismic wave videos combine sight and sound. Eos *97*, 5. https://doi.org/10.1029/2016EO060261.
13. Rees, K.V. (2024). The soil zones of Saskatchewan: Creating art to visualize the concept. iScience *27*, 109335. https://doi.org/10.1016/j.isci.2024.109335.

iScience

Supporting Information for

Bridging Science and Art: Auralization and Visualization of Ocean Soundscape

Yu Ren [1,4], Tian Wu [2,4], Chuanzhi Li [3,4], Pengfei Yao [4], and Weiwei Ding [5,6]

(1) GEOMAR Helmholtz Centre for Ocean Research Kiel, Kiel, Germany
(2) Muthesius University of Fine Arts and Design, Kiel, Germany
(3) Institute for Advanced Ocean Study, Ocean University of China, Qingdao, China
(4) Deep Sea Light Team, Kiel, Germany
(5) Second Institute of Oceanography, MNR, Hangzhou, China
(6) School of Oceanography, Shanghai Jiao Tong University, Shanghai, China

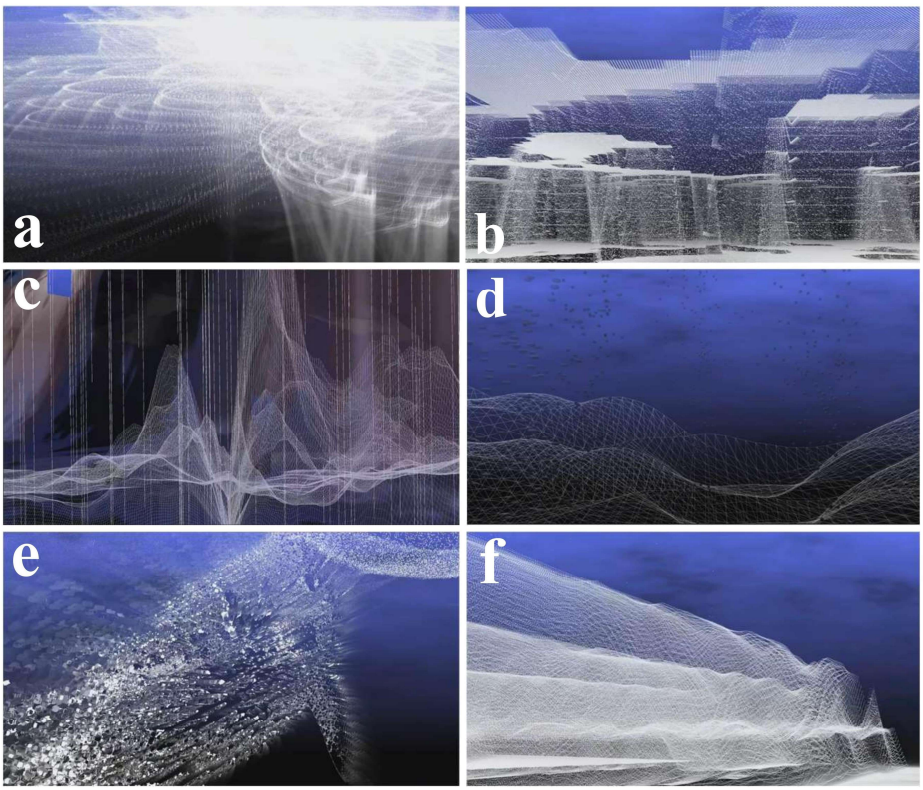

Figure S1. Artistic representations of common sounds, such as **(a)** ship noise, **(b)** active seismic investigation, **(c)** earthquakes, **(d)** hydrothermal venting, **(e)** blue whale songs, and **(f)** large storms in the Pacific Ocean.

Audio S1. Fin whale vocalizations recorded at OBS station BS080 in the northeast Pacific Ocean (via https://www.sciencedirect.com/science/article/pii/S2589004224019217#mmc2). Fin whale calls recorded by seismic stations in the northeast Pacific sped up 10 times to be audible to humans.

Video S1. Art video created based on the seismic whale song recorded at the OBS station BS080 (via https://www.sciencedirect.com/science/article/pii/S2589004224019217#mmc3). Video resolution is compressed to 480p due to file size limitations of the submission system.

Video S2. Video documentary footage of our science-art exhibition (via https://www.sciencedirect.com/science/article/pii/S2589004224019217#mmc4) in the Blue Planet Science Fiction Film Festival 2023, Nanjing, China. Video resolution is compressed to 480p due to file size limitations of the submission system.

Acknowledgements

Many thanks to…

… Ingo Grevemeyer for your invaluable supervision and unwavering support at every level. I am, and will always be, deeply grateful for your introduction to the fascinating realm of transform faults, your encouragement to challenge existing knowledge, and your guidance in bringing projects to the finishing line. Your keen observational skills and remarkable critical thinking continue to inspire my passion for scientific research. I am looking forward to continued collaborations with you on many exciting research topics in the future.

… Dietrich Lange for guiding me into the world of seismology and for dedicating your time to assist with numerous technical aspects. I have greatly benefited from your valuable advice, constructive input, and thoughtful perspectives on scientific work. The seismological skills you have taught me form the backbone of my career, and I am deeply grateful for your guidance and support.

… Jacob Geersen for your training, support, and encouragement throughout my doctoral project. Your guidance began six years ago when you supported my application for the CSC scholarship, enabling me to pursue my PhD in Germany. With great patience, you mentored me in morphology parameterization and taught me the art of scientific writing during the preparation of my first paper. During the challenging times of the Corona pandemic, you regularly invited me to lunch and lifted my spirits on difficult days.

… Morelia Urlaub for supporting the final phase of my PhD and for providing me with wonderful opportunities to contribute to various exciting projects. I greatly enjoyed working with diverse datasets and look forward to delving deeper into the OBS dataset on the southeastern flank of Mount Etna. Collaborating with you as a co-instructor for courses at Kiel University has also been a thoroughly rewarding experience.

… all colleagues who contributed to this work and helped develop new research ideas, with special thanks to Sibiao Liu, Ming Chen, Yueyang Xia, Anouk Beniest, Ingo Klaucke, Colin Devey, Lars Rüpke, and Jason P. Morgan.

… all my friends and colleagues in Kiel for helping my family integrate into local life, assisting us in finding new apartments, and showing incredible kindness when my son Timo was born. I would also like to extend my gratitude to all the colleagues and crew members of research cruise M170 for the wonderful moments shared both on land and at sea.

… the China Scholarship Council and the CASCO project of the Helmholtz Association for financing my doctorate. I am also grateful to Zhihu Incorporation for financially supporting my *Deep Sea Light* team in transforming scientific data into immersive digital artworks. Additional thanks to Projekt DEAL for providing Open Access funding for several papers published as part of this thesis.

… my dear mum, Hui, and my wonderful wife, Hong, for your boundless love and constant support. A special thanks to my son, Timo, for ensuring I spend less time working. I love you 3000.